Dissertation
submitted to the
Combined Faculties for the Natural Sciences and for Mathematics
of the Ruperto-Carola University of Heidelberg, Germany
for the degree of
Doctor of Natural Sciences

presented by

Ricardo Bruno, da Costa Pereira de Carvalho
born in Lisbon, Portugal
Oral-examination:

Quantitative analysis of centriolar satellites and control of ciliogenesis by centrosome associated kinases

Referees:

Summary

Centrioles nucleate two types of cellular structures: the centrosome and the cilium. Because of the signaling activity that takes place in centrosomes and cilia, these centriole based organelles are central in maintaining cellular homeostasis, control cell fate, growth, and cell cycle progression. Centrosomes are composed of a pair of centrioles enveloped by a protein mesh that nucleates microtubules and serves as the cell's microtubule organizing center. The older centriole of the pair is called the mother centriole and is decorated at its distal tip with a nine-fold symmetric ring of proteinaceous appendages. Cilia are antenna-like projections of the plasma membrane that surround a microtubule-based structure called axoneme which is nucleated by the mother centriole. Ciliogenesis starts at the G1/G0 phase of the cell cycle by a mechanism that is not entirely understood. For cilia to emerge, it is necessary that a mature centriole contacts a membrane or vesicle and attaches to it. After that, for the axoneme to grow, there is a need to remove from the mother centriole the inhibitory factors that prevent abnormal centriole size in proliferating cells. The overall aim of my work was to shed light onto some of the regulatory events controlling the onset of cilia formation. For this, I investigated the role of two microtubule-associated kinases and developed methods that allowed the analysis of centrosome/cilia associated components using large fluorescence-based datasets.

Our lab has identified MARK4 and TTBK2, among others, as positive regulators of cilia formation. I show that MARK4 is associated with purified centrosomes and regulates the levels of the centrosomal protein ODF2 at the sub-distal appendages of the mother centriole. Using fluorescence microscopy and in vivo pull downs, I show that TTBK2 interacts with the distal appendage component Cep164 via the N-terminal WW-domain of Cep164. Although MARK4 and TTBK2 seem to be associated with different appendage proteins, previous studies have shown that MARK4 and TTBK2 are necessary for the removal of CP110 and Cep97 (inhibitory factors of axoneme extension) from the distal tip the mother centriole. Presented here is the finding that MARK4 interacts with Cep97 in vivo, and it phosphorylates CP110 in vitro. Since the depletion of both MARK4 and TTBK2 causes bigger deficiencies in ciliogenesis and CP110 removal from the mother centriole than the single depletion of either kinase, I could not assign them a hierarchy of importance in the same pathway for cilia biogenesis. The most satisfactory explanation for the results is that MARK4 and TTBK2 action on ciliogenesis is exerted in separate and synergistic pathways.

In the vicinity of centrosomes and cilia, protein complexes, named centriolar satellites, are thought to play crucial roles in centriole duplication and cilia formation. Recently it was found that autophagic degradation of the OFD1 protein pool that localizes to the centriolar satellites sets ciliogenesis in motion. Here, I report that MARK4 is required for autophagic activation in human retinal epithelial cells. I then pursued the idea that the defect of MARK4 depleted cells to ciliate could be due to persistent OFD1 at the centriolar satellites. I postulated that if this hypothesis was correct, co-depleting ODF1 and MARK4 should rescue the ciliogenesis defect observed upon a single MARK4 depletion. Indeed, I found that cells lacking MARK4 and OFD1 had a higher probability to ciliate than cells lacking MARK4 alone. This finding involves MARK4 in the autophagy-induced OFD1 degradation from the centriolar satellites at the onset of ciliogenesis.

Little is known about how the spatial distribution of the centriolar satellites around the centrosome is determined. My aim was to develop quantitative methods to compare centriolar satellite behavior based on the information gathered through the analysis of large datasets of fluorescence microscopy images. With the data obtained, I present two methods that proved well-suited for comparing the centriolar satellite organiza-

tion around the centrosome of a subset of satellite proteins, namely PCM1, OFD1, and Cep290. My data revealed that during the serum starvation process used to induce ciliogenesis in cultured cells, a drastic reorganization of satellite particles loaded with OFD1 occurs. However, the same does not happen with centriolar satellite particles containing either the scaffold protein PCM1 or Cep290. My observations indicate that the protein composition of centriolar satellite particles is regulated according to the proliferative state of the cell.

Together, my work contributed to the understanding of MARK4 and TTBK2 function during ciliogenesis. Furthermore, I anticipate that the development of the quantitative tools for the analysis of centriole satellites will allow the systematic study of these protein complexes that has been lacking so far.

Zusammenfassung

Es gibt zwei Arten von zellulären Strukturen bei deren Organisation Zentriolen eine zentrale Funktion einnehmen: das Zentrosom und das Cilium. Diese zentriolenbasierten Zellorganellen sind dank ihrer Schlüsselposition bei der Signalübertragung wichtig für den Erhalt der zellulären Homöostase, der Kontrolle des Zellschicksals, des -wachstums und des Fortschreitens des Zellzyklusses. Zentrosome bestehen aus einem Paar Zentriolen, die von einem Eiweißmantel umgeben sind und als Organisationseinheit für die Ausrichtung von Mikrotubuli dienen. Die ältere wird als Mutterzentriole bezeichnet und ist an ihrem distalen Ende mit Proteinfortsätzen bestückt. Cilien sind antennenartige zytoplasmatische Ausstülpungen der Plasmamembran mit einem inneren, aus Mikrotubulibündeln bestehenden, Skelett, dem sogenannten Axonem. Die Ciliogenese beginnt in der G1/G0 Phase des Zellzykluss durch einen Mechanismus der weitgehend unbekannt ist. Für die Bildung eines Ciliums ist es notwendig, dass eine Zentriole Verbindung mit einem Vesikel eingeht.

Die Größe der Mutterzentriole in proliferierenden Zellen ist durch inhibierende Faktoren geregelt, diese müssen entfernt werden damit das Axonem wachsen kann. Das übergreifende Ziel meiner Arbeit war es einige der regulatorischen Ereignisse zu erforschen, die die Ciliogenese in Gang setzen. Hierfür untersuchte ich die Rolle zweier microtubuliassoziierter Kinasen und entwickelte eine Methode die, basierend auf Fluoreszenzmikroskopiedatensätzen, die Analyse von Zentrosome/Cilia abhängigen Komponenten ermöglicht.

MARK4 und TTBK2 wurden in unserer Arbeitsgruppe al. Mit meiner Arbeit zeige ich dass MARK4 mit aufgereinigten Zentrosomen assoziiert und die Menge an ODF2 an den subdistalen Fortsätze der Mutterzentriole reguliert.

Mit Hilfe von Floureszenzmikroskopie und in vivo „pull downs“ konnte ich zeigen, dass TTBK mit dem subdistalen Fortsatzprotein Cep164 über dessen N-terminale WW-Domain interagiert. MARK4 und TTBK2 scheinen mit unterschiedliche subdistalen Fortsatzkomponenten zu interagieren auch wenn frühere Studien haben gezeigt dass die Proteinkinasen MARK4 und TTBK2 notwendig sind um die inhibierenden Faktoren CP110 und Cep97 vom distalen Ende der Mutterzentriole zu entfernen. In der vorliegenden Arbeit wird gezeigt, dass in lebenden Zellen MARK4 direkt mit Cep97 interagiert und CP110 in vitro phosphoryliert. Es konnte dabei keine Hierarchie der beiden Kinasen MARK4 und TTBK2 im Signaltransduktionsweg der Ciliogenese festgestellt werde, da die Verminderung beider Kinasen zusammen einen stärkeren Phänotyp erzeugt als die Verminderung der einzelnen. Die plausibelste Erklärung für dieses Resultat ist eine separate und synergetische Funktion von MARK4 und TTBK2 bei der Ciliogenese.

In der Umgebung der Zentrosomen und Cilien kann man die sogenannten zentriolären Satelliten finden, Proteinkomplexe bei denen man davon ausgeht, dass sie eine wichtige Rolle bei der Zentriolenduplikation sowie bei der Ciliogenese spielen. Der autophagieabhängige Abbau von OFD1, einem Protein das sich an den zentriolären Satelliten befindet, ist laut einer aktuellen Studie dafür verantwortlich, dass die Ciliogenese in Gang gesetzt wird. Hier wird gezeigt, dass MARK4 für die Aktivierung von Autophagie in humanen retinalen Epithelzellen notwendig ist. Ich postuliere, dass der Ciliogenesedefekt in Abwesenheit des MARK4-Proteins darauf begründet ist, dass OFD1 an den zentriolären Satelliten verbleibt. Nach dieser Hypothese sollte die Verminderung von OFD1 und MARK4 dem Ciliogenesedefekt entgegen wirken, der durch die MARK4-Depletion erzeugt wird. Die Tatsache, dass die Depletion beider Faktoren dazu führt dass die Wahrscheinlichkeit einer Zelle ein Cilium auszubilden höher ist als wenn nur MARK4 vermindert ist, stütz

diese Hypothese. Auf diesen Ergebnissen beruhend kann man davon ausgehen, dass MARK4 eine zentrale Rolle beim autophagieinduzierten Abbau von OFD1 an den zentriolären Satelliten zu Beginn der Ciliogenese spielt.

Bisher ist wenig bekannt wie die räumliche Verteilung von zentriolären Satelliten um das Zentrosom geregelt wird. Die Entwicklung einer quantitativen Methode auf der Basis von umfangreichen Fluoreszenzmikroskopiedatensätzen ermöglichte das Verhalten von zentriolären Satellitenproteinen (PCM1, OFD1 und Cep290) zu analysieren und zu vergleichen. Die Analyse zeigte, dass bei der durch die Zugabe von serumfreien Kulturmedium initiierten Ciliogenese eine drastische Neuorganisation von OFD1-beladenen Sattelitenpartikeln statt fand. Das Gleiche gilt jedoch nicht für zentrioläre Satelliten die mit den Scaffoldproteinen PCM1 und Cep290 beladen sind. Meine Analysen deuten darauf hin, dass die Proteinzusammensetzung von zentriolären Satelliten je nach Proliferationsstatus der Zellen reguliert wird.

Im Gesamten trägt meine Arbeit dazu bei die Funktionen von MARK4 und TTBK2 bei der Ciliogenese besser zu verstehen. Des weiteren gehe ich davon aus, dass es die von mir entwickelte, quantitativen Methode ermöglicht zentriolären Satelliten systematisch zu untersuchen und Bedeutung ihrer Dynamik besser zu verstehen.

Table of contents

I. Introduction

I.I. The centrioles and the centrosomes

Centrioles are involved in cell division, microtubule organization, environment sensing and locomotion (Bettencourt-Dias and Glover, 2007; Goetz and Anderson, 2010; Nigg and Raff, 2009). They have a cylindrical shape and are formed by nine tubulin microtubule triplets organized as shown in Figure 1A and B. Centriole microtubules are very stable, able to resist cold and drug treatments that render cytoplasmic microtubules depolymerized. Fluorescence recovery after photobleaching experiments revealed that there is little turnover between centriole and cytoplasmic tubulin (Pearson et al., 2008). These findings are consistent with the fact that centriolar microtubules are heavily modified by acetylation, polyglutamylation, detyrosination and contain Δ2-tubulin (Janke et al., 2011), hallmarks of very stable microtubules. Centrioles have a typical diameter of 250 nm and a length that ranges from 150 to 500 nm, depending on the cell type and cell cycle stage (Gönczy, 2012; Winey and O'Toole, 2014). The centriole is asymmetrically polarized along its long axis: the base where procentriole biogenesis starts and where the tubulin microtubules minus end is located is referred to as the proximal end; the apex that in mature human centriole is decorated with proteinaceous appendages and where the tubulin microtubules plus end is located is known as distal end (Figure 1C).

Centrioles are conserved in the Eukaryota domain although they are absent in some Fungi, Amoebozoa, Alveolates and most notably in Angiosperms (Carvalho-Santos et al., 2011). Centrioles can be found by themselves (Ross and Normark, 2015) or as part of larger organelles: centrosomes and cilia. The centrosome as its name suggests is usually located near the cell center, close to the nucleus and away from the

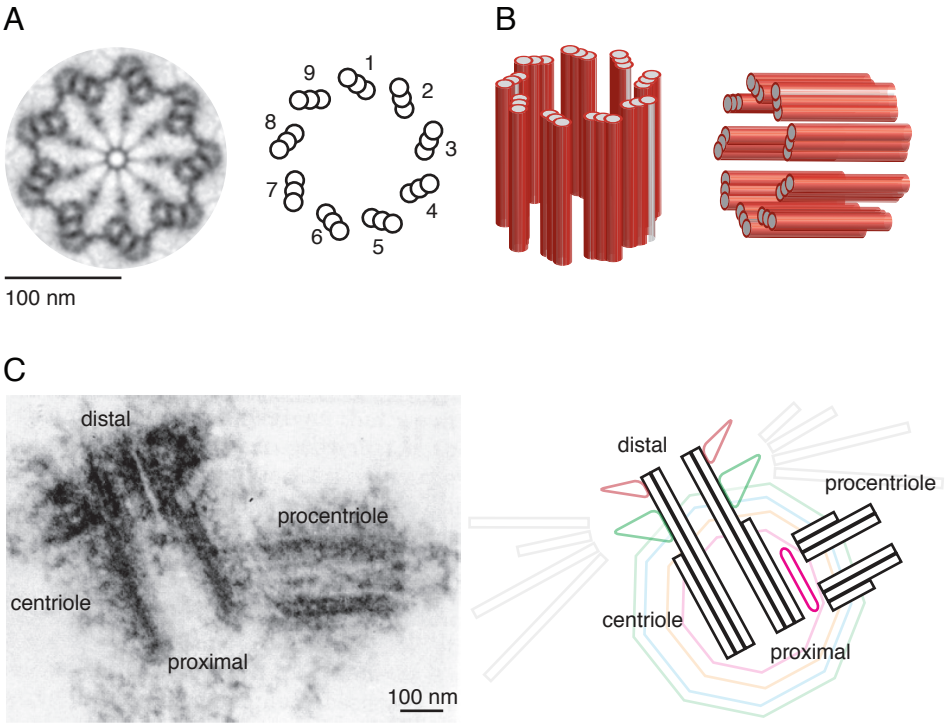

Figure 1: **Structure of the human centriole**. (A) Electron micrograph and schematic representation of the cross section of a human centriole showing the ninefold symmetric arrangement of the microtubule triplets. (B) 3D representation of an orthogonal pair of centrioles. (C) Electron micrograph and schematic representation of the longitudinal section of a centriole and a procentriole. Indicated are the distal and proximal ends of the centriole. (A and C) Adapted from Gönczy, P. Towards a molecular architecture of centriole assembly. Nature Reviews Molecular Cell Biology 13, 425–435 (2012).

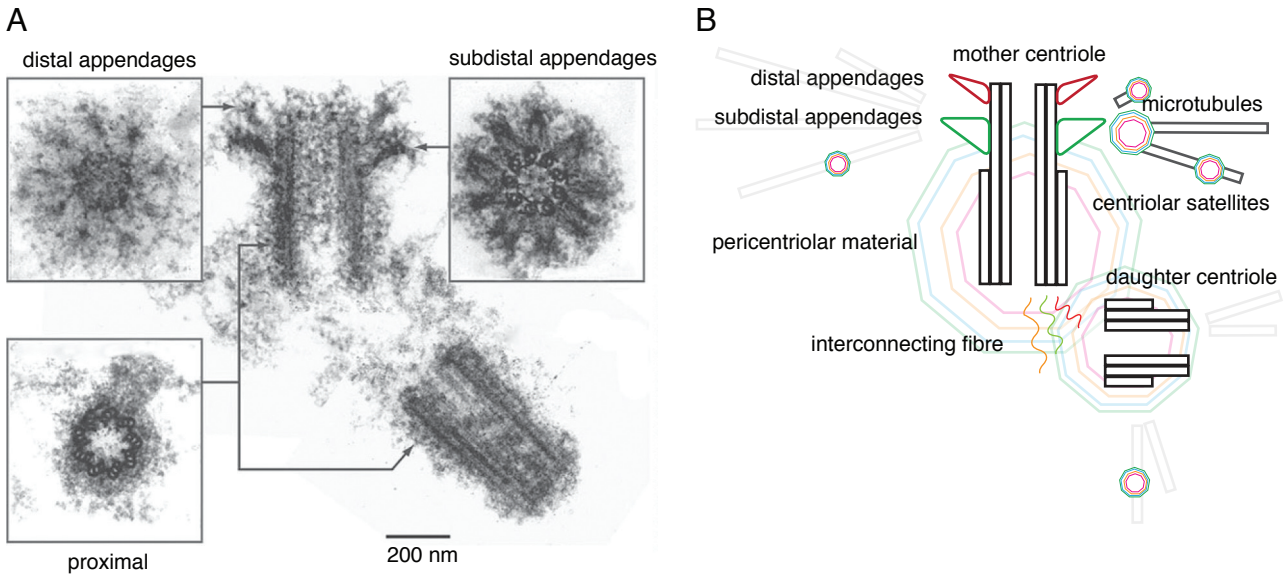

Figure 2: **Structure of the human centrosome**. (A) Electron micrograph of a longitudinal section of an isolated centrosome and informative cross sections of the proximal section of the centrioles as well as the distal and sub distal appendages of the mother centriole. Adapted from Winey, M. & O'Toole, E. Centriole structure. Philosophical transactions of the Royal Society of London. Series B, Biological sciences 369, 20130457- (2014). (B) Schematic representation of the mammalian centrosome during the G1 stage of the cell cycle. Microtubules are represented as black bounded rectangles and the centrioles are represented in longitudinal section showing the microtubule triplets at the proximal end and duplets at the distal end. The mother centriole has distal (red) and sub distal (green) appendages whereas the daughter centriole has not. The centriole pair is connected by interconnecting fibres, represented by wiggly colourful lines, and enveloped by the pericentriolar material, represented by concentric colourfull polygons around the centrioles.

plasma membrane (Boveri, 1887; Burakov et al., 2003). A normal mature human centrosome of a first gap phase (G1) cell is represented in Figure 2. It is composed of two centrioles, daughter and mother, so called if their genesis occurred respectively in the previous cell cycle or before. In the centrosome, centrioles are connected by interconnecting fibers composed mainly of centrosomal Nek2-associated protein 1(C-Nap1) and rootletin (Fry et al., 1998; Yang et al., 2002).

As previously mentioned, centrioles can be decorated with proteinaceous modifications at their distal ends. They are exclusive to the mother centriole and are referred to as distal or sub-distal appendages, as shown in Figure 2. Distal and sub-distal appendages are protrusions structured in a nine-fold symmetric ring around the centriole and are central in the cilia formation process, the other skin of the centriole that will be covered below. Proteins that localize to the distal appendages do it in a hierarchical way. The centrosomal protein of 83 kDa (Cep83) is required for the localization of centrosomal protein 123 (Cep123) and sodium channel and clathrin linker 1 (SCLT1). The latter is necessary for the localization of fas-binding factor 1 (FBF-1) and centrosomal protein of 164 kD (Cep164) (Tanos et al., 2013). Localization studies using super-resolution microscopy showed that Cep164 is organized in a ring-like structure with nine-fold symmetry at the distal end of the mother centriole of Henrietta Lacks (HeLa) cells (Sillibourne et al., 2011). The oral-facial-digital syndrome 1 (OFD1) protein is localized to the distal end of the mother centriole and also to the centriolar satellites. It is necessary for the assembly of the distal appendages, namely the recruitment of Cep164 (Singla et al., 2010). Mutations in the OFD1 protein are associated with the ciliary disease orofaciodigital syndrome 1 (Ferrante et al., 2001).

Sub-distal appendages are essential to maintaining a proper microtubule anchorage and organization at the centrosome (Dammermann and Merdes, 2002; Delgehyr et al., 2005; Guarguaglini et al., 2005; Mogensen et al., 2000; Quintyne et al., 1999). They are reported to be required for proper alignment of the cilium basal body at the cell cortex in multi-ciliated epithelial cells (Tsukita et al., 2012). Outer dense fiber pro-

tein 2 (ODF2), also known as cenexin, was reported to localize at both the distal and sub-distal appendages, being essential for their assembly (Ishikawa et al., 2005; Nakagawa et al., 2001). However, its distal localization is hard to detect, being much more prominent in the sub-distal appendages for whom it is a standard marker (Azimzadeh and Marshall, 2010; Brito et al., 2012). In mouse cells, the absence of ODF2 leads to impairment of primary cilia formation (Ishikawa et al., 2005) and discoordination of motile ciliary beating (Tsukita et al., 2012). Other sub-distal appendage proteins include ninein (Mogensen et al., 2000), centrosomal protein of 170 kDa (Cep170) (Guarguaglini et al., 2005), ε-tubulin (Chang et al., 2003), and centriolin (Gromley et al., 2003). Upon depletion of ninein, centriolin or ε-tubulin, ciliation was found to be impaired (Graser et al., 2007; Mikule et al., 2007).

A vital part of the centrosome is the pericentriolar material (PCM) that embeds the centrioles and acts as the primary microtubule organizing center (MTOC) of metazoan cells (Gould, 1977; Woodruff et al., 2014). It is believed that the PCM consists of a structural scaffold of fibrous proteins that embeds the γ-tubulin ring complexes that cap the minus ends of PCM-derived microtubules (Moritz et al., 1995; Schnackenberg et al., 1998; Woodruff et al., 2014). Some of the proteins that are localized at the PCM include pericentrin, spindle-defective protein 2 (spd-2), centrosomal protein of 152 kDa (Cep152) or centrosomin (Doxsey et al., 1994; Pelletier et al., 2004; Vaizel-Ohayon and Schejter, 1999; Varmark et al., 2007). The protein sequence of PCM proteins is abundant in predicted coiled-coil domains. Coiled-coil domains are intertwined α-helices, known for mediating protein-protein interactions (Lupas et al., 1991). So far untested is the hypothesis that the PCM scaffold is assembled from the numerous interactions between the coiled-coil domains (Woodruff et al., 2014). Advances in sub-diffraction light microscopy allowed to shed light into the surprising substructure within the PCM (Fu and Glover, 2012; Lawo et al., 2012; Mennella et al., 2012; Sonnen et al., 2012). It was found that interphase PCM proteins are distributed in concentric toroids around the centrioles. The toroids of the different proteins can overlap or occupy strictly separated domains within the PCM and can reach an outer radius of 100 nm from the centriole wall (Fu and Glover, 2012; Lawo et al., 2012; Mennella et al., 2012; Sonnen et al., 2012).

The first observations of centriolar satellites (CS) were made using electron microscopy (EM) by independent laboratories in the 1960s. Centriolar satellites are visible by EM as small electron dense granules of approximately 70 to 100 nm that cluster around the centrosome. They were observed next to newly forming daughter centrioles, associated with microtubules originating from the centrosome or around assembling basal bodies of motile cilia in epithelial cells (Anderson and Brenner, 1971; Bärenz et al., 2011; Bernhard and de Harven, 1960; de-Thé, 1964; Hori and Toda, 2016; Peterson and Berns, 1978; Sorokin, 1968; Steinman, 1968; Tollenaere et al., 2015). The proximity of the electron dense particles to newly formed centriolar structures hinted that these granules could be somehow involved in procentriole or cilia assembly. However, further characterization of the precise function and composition of CSs had to wait until the 1990s[1].

I.II. The centriole cycle

Because of its importance for mitotic spindle nucleation and therefore for genomic stability, the number of centrosomes in the cell and its duplication process are tightly regulated. After each cell division, a newly

[1] Chapter 1 of this thesis is entirely dedicated to the quantitative study of centriolar satellites. Refer to the Chapter 1 specific introduction for more details about centriolar satellite biology.

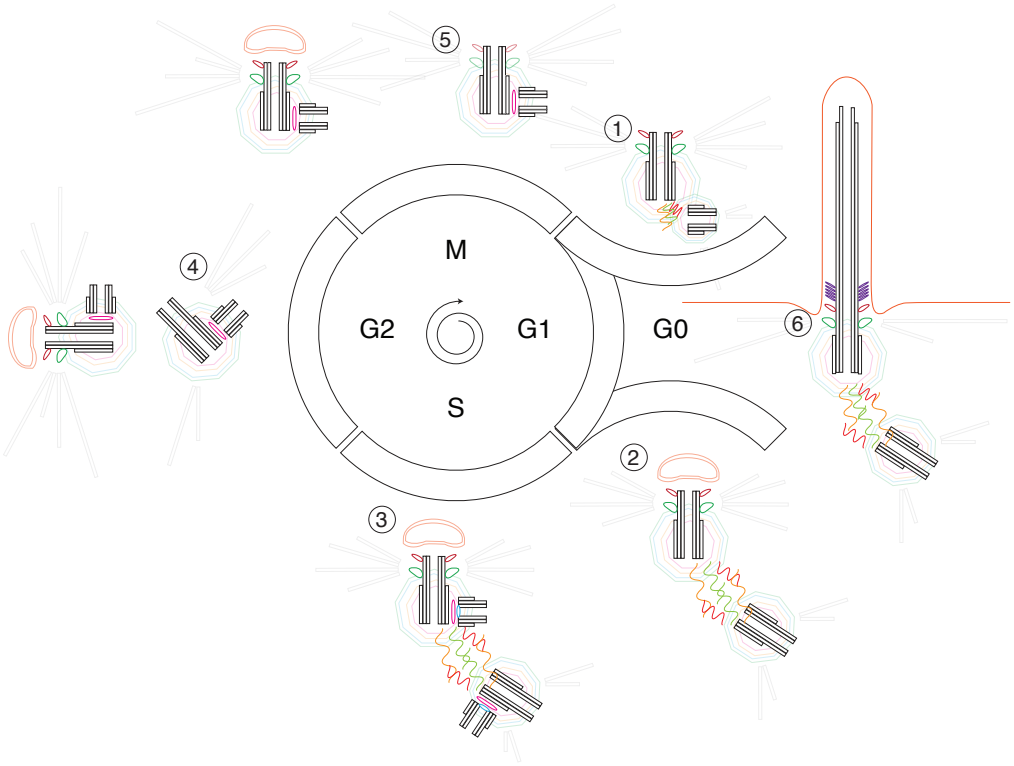

Figure 3: **The centriole cycle**. Schematic representation of the main stages in centriole duplication, centrosome maturation and cilia formation during the cell cycle. (1) At the end of mitosis cells inherit one fully matured centrosome with a mother centriole equipped with distal and sub distal appendages and a disengaged daughter centriole. (2) During G1 and on the G1 to S phase transition the centrioles further disengage and the daughter centriole grows until it reaches the same size as the mother centriole. If the mother centriole was a ciliary basal body during G1 or G0 it can keep a ciliary vesicle associated with its distal appendages throughout the rest of the cell cycle. (3) Centrioles are duplicated during S phase as one procentriole is formed at the proximal end of each centriole. (4) In G2 phase the procentrioles elongate, pericentriolar material is recruited to the centrioles and as cells approach M phase the protein tether that connects the two parental centrioles is disassembled and two centrosomes are separated. (5) Centrosomes migrate to opposite sides of the cell and assemble a bipolar mitotic spindle on the onset of M phase. After cytokinesis each daughter cell inherits one centrosome. (6) If after mitosis cells enter a quiescent phase, the so called G0 phase, it is probable that they form a primary cilium with the mother centriole becoming the basal body that nucleates the ciliary axoneme.

formed cell inherits one centrosome containing two disengaged centrioles, one of them, the mother centriole, with distal and sub-distal appendages (Figure 3, 1). During the G1 phase of the cell cycle, the daughter centriole is extended, it disengages further from the mother centriole albeit maintaining a link with it, starts to accumulate PCM and nucleate microtubules (Figure 3, 2). As the cell enters the synthesis (S) phase, the centriole duplication process begins. A nine-fold symmetry structure, capable of self-assembling called the cartwheel serves as a template for the tubulin microtubule triplets of what will constitute the procentriole (Fırat-karalar and Stearns, 2014; Nigg and Stearns, 2011) (Figure 3, 3). The formation of the cartwheel is initiated by an activation of Polo-like kinase 4 (PLK-4) (Kim et al., 2013; Ohta et al., 2014) that precedes the recruitment of spindle assembly abnormal protein 6 homolog (SAS6) (van Breugel et al., 2011; Kitagawa et al., 2011; Nakazawa et al., 2007) and SCL-interrupting locus protein (STIL) (Cottee et al., 2015; Stevens et al., 2010). SAS6 and STIL's intrinsic oligomerization properties serve as the template for the cartwheel nine-fold symmetry. Centriole elongation follows, depending on centrosomal P4.1-associated protein (CPAP) (Kohlmaier et al., 2009; Tang et al., 2009) for deposition of centriolar microtubules and CP110 (Schmidt et al., 2009; Spektor et al., 2007) together with OFD1 (Singla et al., 2010) for the regulation of centriolar length. During the second gap phase (G2), the centrosomes are separated when the kinase activity of never in mitosis A-related kinase 2 (NEK2) exceeds the phosphatase activity of type 1γ phosphatase and leads to the

phosphorylation of the centriole linker proteins C-Nap1 and rootletin (Fry et al., 1998; Helps et al., 2000; Mardin et al., 2011). Once the link is broken, the two centrosomes are separated through the recruitment of the kinesin-related motor Eg5 to the centrosomes (Bertran et al., 2011). Nucleated by what was at the beginning of the cell cycle the daughter centriole, a new fully functional centrosome matures (Figure 3, 4). During mitosis, the centrosomes are positioned at opposing sides of the mitotic spindle and each new cell inherits one mature centrosome (Figure 3, 5). During the mitotic (M) phase, the mother centrioles lose their distal appendages (Schmidt et al., 2012; Ye et al., 2014) while the daughter centrioles are still orthogonally attached to them. It is only during mitosis that the centrioles are disengaged through the action of the mitotic polo-like kinase 1 (PLK-1) and the protease separase of sister chromatid separation fame (Tsou et al., 2009). It has been proposed that centriole disengagement during mitosis marks the licensing step necessary for the next centriole duplication cycle (Conduit et al., 2015; Nigg and Stearns, 2011; Tsou and Stearns, 2006). Mitotic exit triggers the maturation of the distal and sub-distal appendages of the mother centriole (Nigg and Stearns, 2011). If, after mitosis, the cell exits the cell cycle and remains quiescent in an exit of G1 (G0) state, there is the possibility of cilia formation (Figure 3, 6).

I.III. The cilium

The cilium is the second type of organelle nucleated by a centriole and shown in Figure 4. The cilium is an antenna-like organelle that projects itself from the cell surface to the extracellular environment for a specific molecule, force or light detection or to exert a force on the extracellular medium, either to move through it or to move it. The cilium axoneme is the part of the cilium that protrudes from the cell surface and it is composed of a nine-fold symmetric arrangement of duplet tubulin microtubules. These tubulin microtubules are extended from the mother centriole and provide the scaffold of the cilium around which intra flagellar transport (IFT; see below) systems, membrane interacting proteins, septins and others give shape to the cilium and assure its maintenance and function. Even though the diversity is enormous, cilia are divided into two categories according to their axoneme structure: motile and primary cilia. In motile cilia, the axonemal microtubules are decorated with dynein complexes and radial spokes that act in a coordinated fashion to achieve ciliary movement (Lindemann and Lesich, 2010). Furthermore, motile cilia have a central tubulin microtubule doublet in the center of the axoneme in a so-called 9+2 arrangement. That 9+2 arrangement contrasts with the 9+0 arrangement of primary cilia because primary cilia do not have the central microtubule doublet or dynein motors associated with its axoneme (Goetz and Anderson, 2010; Nigg and Raff, 2009). The cilium basal body is the mature mother centriole that besides the nucleation of the axoneme's microtubule duplets, can interact with ciliary vesicles and anchors the axoneme to the plasma membrane. It derives from the centrosome's mother centriole whose distal appendages are converted into transition fibers or alar sheets (Anderson and Brenner, 1971) and the sub-distal appendages that are used to orient the cilium within the cell surface (Mazo et al., 2016; Tsukita et al., 2012).

The transition zone is distal to the basal body and located where the axoneme, the basal body, the plasma and the ciliary membranes intersect (Garcia-Gonzalo and Reiter, 2016; Nachury et al., 2010; Reiter et al., 2012). Interactome studies were able to identify two distinct transition zone protein complexes: the nephronophthisis (NPHP) complex and the Meckel syndrome (MKS) complex. The NPHP complex includes nephrocystin-1 (NPHP1), nephrocystin-4 (NPHP4) and RPGR-interacting protein 1-like protein (RPGRIP1L)

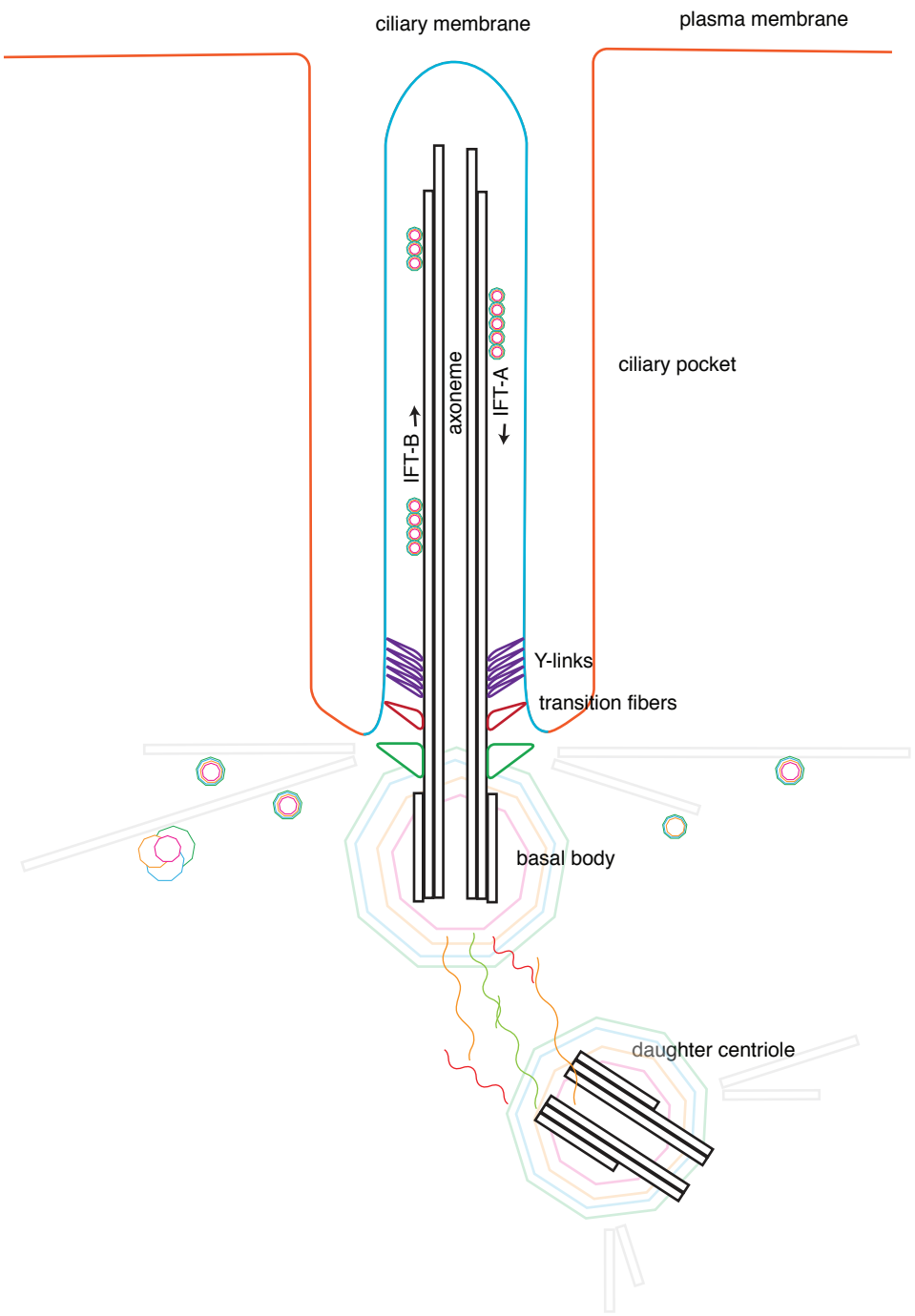

Figure 4: **The structure of the cilium**. Schematic representation of the longitudinal section of a primary cilium where the basal body and daughter centriole, the ciliary pocket, the transition zone with its Y-links, the axoneme, both the IFT-A and IFT-B complexes and the ciliary and plasma membranes are indicated.

and is mostly involved in the ciliopathy nephronophthisis (Garcia-Gonzalo and Reiter, 2016). The MKS complex features the Teutonic proteins 1, 2 and 3, the three B9 domain proteins, coiled-coil proteins and transmembrane proteins. It is mostly involved in Meckel and Joubert syndromes (Garcia-Gonzalo and Reiter, 2016).

Structurally, the transition zone is composed of transition fibers, Y-links and the ciliary necklace (Garcia-Gonzalo and Reiter, 2016; Reiter et al., 2012; Ringo, 1967). The transition fibers are derived from the distal appendages of the mother centriole and interact directly with ciliary vesicles and the ciliary membrane, mediating the contact between the centrosome and the ciliary and plasma membranes (Joo et al., 2013; Schmidt et al., 2012; Sillibourne et al., 2013; Tanos et al., 2013). Transition fiber proteins such as Cep164,

FBF-1 and Cep83 are known to participate in the recruitment to the transition zone of IFT-B complex (see below) proteins IFT88, IFT54 and IFT20, respectively (Cajánek and Nigg, 2014; Schmidt et al., 2012; Wei et al., 2013; Ye et al., 2014). Due to the obstruction of the basal body lumen with centrin-2 containing structures (Fisch and Dupuis-Williams, 2011), the spaces between transition fibers are considered a likely passage for macromolecules that enter or exit the cilium (Garcia-Gonzalo and Reiter, 2016).

Distal to the contact of the transition fibers with the ciliary membrane is an additional anchorage of the tubulin nucleated structures (basal body + axoneme) to the membrane via centrosomal protein of 290 kDa (Cep290) containing (Craige et al., 2010) structures called Y-links. Freeze-fracture EM of the location where the Y-shaped protein structures contact the ciliary membrane reveals a spiral of beads around the ciliary membrane that is referred to as the ciliary necklace (Gilula and Satir, 1972; Heller and Gordon, 1986; Lambacher et al., 2015).

At the interface of the axoneme with the extracellular medium, it is the ciliary membrane. The ciliary membrane is continuous with the plasma membrane. However, its lipid and protein composition is thoroughly regulated and different from the rest of the cell (Rohatgi and Snell, 2010). It is common to find in EM images, the cilium base sunk into the cell surface. This depression originates the so-called ciliary pocket if the invagination is of modest size as is the case in motile cilia of ciliated protozoans (Benmerah, 2013) or a ciliary pit in the case of submerged cilia (Fisher and Steinberg, 1982; Mazo et al., 2016; Rattner et al., 2010; Sorokin, 1962). The ciliary pocket was reported to be a hotspot for exocytosis and clathrin-dependent endocytosis of ciliary receptors (Benmerah, 2013; Clement et al., 2013). It is believed that the sorting of lipids and integral membrane proteins to the ciliary membrane is performed in the transition zone and ciliary pocket (Benmerah, 2013; Garcia-Gonzalo and Reiter, 2016; Nachury et al., 2010; Reiter et al., 2012) and is maintained thanks to a septin-containing diffusion barrier located at the base of the cilium that constrains the movement of membrane-bound components between the cilium and the rest of the plasma membrane (Hu and Nelson, 2011; Hu et al., 2010; Reiter et al., 2012).

I.IV. Ciliogenesis

Ciliogenesis starts when vesicles containing ciliary cargo are derived from the trans-Golgi network and are transported to the centrosome or when the centrosome attaches to the plasma membrane directly (Sorokin, 1968) as shown in Figure 5. Distal appendages have been reported to mediate the docking of vesicles to the mother centriole in the initial steps of cilia formation (Joo et al., 2013; Schmidt et al., 2012; Sillibourne et al., 2013; Tanos et al., 2013). The protein Cep164 specifically localizes to the distal appendages, and it is essential for ciliogenesis (Graser et al., 2007). With the help of the protein chibby homolog 1, Cep164 interacts with Rab-3A-interacting protein (Rabin8) to activate Ras-related protein Rab-8A (Rab8A) and by doing so it allows the docking of the ciliary membrane or vesicle to the basal body (Burke et al., 2014; Feng et al., 2012; Knödler et al., 2010; Lu et al., 2015; Schmidt et al., 2012; Westlake et al., 2011). The small GTPase Rab8A mediates vesicle trafficking to the cilium and is essential for cilia formation (Nachury et al., 2007; Yoshimura et al., 2007). Also located at the distal appendages of the mother centriole and essential for ciliogenesis for its role in vesicle attachment is the Cep123 protein (Sillibourne et al., 2013).

Downstream of ciliary vesicle docking to the basal body are Tau-tubulin kinase 2 (TTBK2) and microtubule-associated protein (MAP)/microtubule affinity-regulating kinase 4 (MARK4). These centrosomal pro-

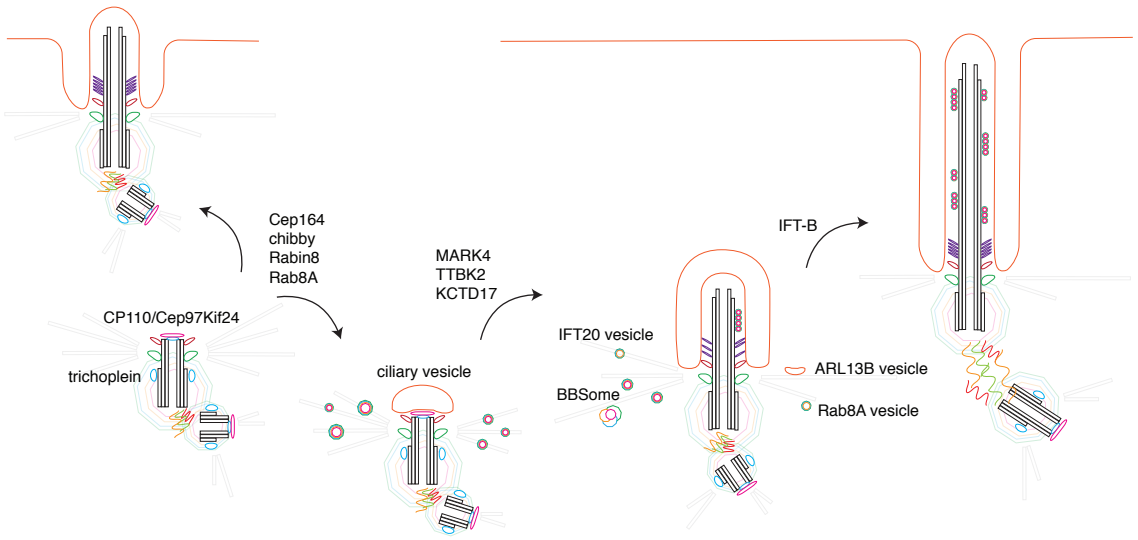

Figure 5: **Ciliogenesis**. Schematic representation of the main stages of cilia biogenesis. Ciliogenesis is inhibited in proliferating cells by the action on the centrioles of the CP110/Cep97/Kif24 complex and trichoplein. Through interaction with the distal appendages, the mother centriole docks to the plasma membrane or to a ciliary vesicle. Upon CP110 and trichoplein removal becomes a basal body and axoneme extension starts. With further traffic to the cilium and incorporation regulated by IFT, BBsome, Rab8A and ARL13B, the cilium is extended. Eventually the ciliary vesicle fuses with the plasma membrane and the ciliary membrane is exposed to the extracellular environment. For further details consult the text where this Figure is embedded.

tein kinases play a role upstream of the displacement of the centriolar coiled-coil protein of 110 kDa (CP110) from the distal tip of the centrosome and subsequent axoneme extension[2] (Cajánek and Nigg, 2014; Goetz et al., 2012; Kuhns et al., 2013). The complex formed by CP110 / centrosomal protein of 97 kDa (Cep97) and its association with kinesin-like protein Kif24 (Kif24) is considered one of the most important negative regulators of mother centriole to basal body transition (Bettencourt-Dias and Carvalho-Santos, 2008; Seeley and Nachury, 2010; Tsang and Dynlacht, 2013). The CP110 complex with Cep97 and Kif24 is localized at the distal end of the centrioles (Kobayashi et al., 2011; Spektor et al., 2007). When overexpressed, CP110, Cep97 and Kif24 suppress cilia formation whereas their depletion leads to aberrant ciliogenesis or abnormal centrosomal growth in the case of cells unable to ciliate for other reasons (Kleylein-Sohn et al., 2007; Kobayashi et al., 2011; Kohlmaier et al., 2009; Schmidt et al., 2009; Spektor et al., 2007). CP110 stability is regulated by Cep97 and ciliation requires the complex of these two proteins to be asymmetrically removed from the mother centriole, but not the daughter centriole, before axoneme extension can be observed (Spektor et al., 2007). The mechanism proposed for ciliary axoneme extension inhibition by the CP110-Cep97 complex is centered on the finding that Kif24, a member of the microtubule depolymerizing kinesin family capable of depolymerizing centriolar microtubules, interacts with CP110 and its degradation helps to trigger ciliogenesis (Kobayashi et al., 2011).

As CP110, trichoplein has also been shown to regulate cilia biogenesis (Ghossoub et al., 2013; Goto et al., 2016; Inoko et al., 2012; Izawa et al., 2015; Kasahara et al., 2014). Originally identified as a keratin-binding protein, trichoplein exerts an activating effect on the centriolar Aurora kinase A, itself a negative regulator of ciliogenesis (Inoko et al., 2012). It is localized at the subdistal/medial region of both centrioles, but upon serum starvation, it is removed specifically from mother centriole when the cilium is formed (Kasahara et al., 2014). Less trichoplein, less Aurora kinase A activity. It has been shown that a decrease, even induced

[2] Chapter 3 of this thesis is entirely dedicated to the study of how MARK4 and TTBK2 interact upstream of the CP110 degradation from the mother centriole. Refer to the Chapter 3 specific introduction for more details about MARK4 and TTBK2 kinases.

by ectopic depletion, in Aurora kinase A activity is enough to activate cilia formation in proliferating cells (Inoko et al., 2012). Trichoplein is targeted for degradation upon ubiquitination by a cullin-3-RING E3 ubiquitin-protein ligase bound to the BTB/POZ domain-containing protein KCTD17 (KCTD17) substrate adaptor protein. Ultrastructural analysis of cells depleted of KCTD17 shows that those cells do not have a centrosome-vesicle docking defect. The problem is that they fail to extend the ciliary axoneme (Kasahara et al., 2014). Trichoplein was involved in the recruitment of microtubules to the centrioles via interaction with ninein and ODF2 in non-ciliated HeLa cells (Ibi et al., 2011).

It was reported that the degradation either ectopic or naturally via autophagy of the set of CSs that contain OFD1 promotes cilia formation (Tang et al., 2013). Therefore it was proposed that another negative regulator of ciliogenesis be the OFD1 protein pool that is localized to the centriolar satellites and that inducible autophagy was an activator of cilia formation[3].

Essential for axoneme growth and maintenance is the intra flagellar transport or IFT (Figure 4), the highly conserved cargo transport process first discovered in the green algae *Chlamydomonas reinhardtii* (Kozminski et al., 1993). It consists in the active transport of cargo along the axoneme microtubules in the direction of the cilium tip (anterograde) by the IFT-B complex and towards the cytoplasm (retrograde) by the IFT-A complex (Lechtreck, 2015; Pedersen and Rosenbaum, 2008; Taschner and Lorentzen, 2016). Since ribosomes are absent from cilia, there is no protein synthesis within the cilium, proteins necessary for axoneme growth and maintenance need to be shuttled inside at the same time that turnover products need to be brought out of the cilium (Lechtreck, 2015; Taschner and Lorentzen, 2016). The cargo can include tubulin, other protein components of the axoneme and even membrane proteins that associate with scaffold protein complexes particular to the anterograde or retrograde direction of transport, complex B and complex A respectively (Lechtreck, 2015; Pedersen and Rosenbaum, 2008). For its role in protein transport to the cilium, IFT has been implicated in the regulation of ciliary length (Silverman and Leroux, 2009). The IFT cargo and scaffold complex are assembled in trains that are then transported along the axonemal microtubules by motor proteins specific for each complex. The plus-end directed kinesin-2 motor is the responsible for the anterograde movement of IFT-B cargo complex. As for IFT-A retrograde movement, the motor proteins responsible are the minus-end directed cytoplasmic dyneins. The first time a link was established between human disease and mutations in cilia-associated proteins was when it was found that a mutation in the mice homolog of the C. reinhardtii IFT88 protein was responsible for the polycystic kidney disease prevalent in that murine model (Pazour et al., 2000).

Ciliary membrane proteins can be delivered from the Golgi apparatus to cilia with the help of IFT20 (Follit, 2006; Follit et al., 2009; Omori et al., 2008) or via the Bardet–Biedl syndrome complex (BBSome) (Nachury et al., 2007). The BBSome consists of eight proteins that form a coat like structure and mediate the traffic of integral membrane proteins to the ciliary membrane (Nachury et al., 2007). The BBSome may not be essential for cilia formation, but when its function of delivery of membrane ciliary proteins to the cilium is compromised the results are defects in cell signaling, embryogenesis, and organogenesis that manifest as the ciliopathy known as Bardet–Biedl syndrome. The small GTPase ADP-ribosylation factor-like protein 13B

[3] Chapter 2 of this thesis will focus in investigating the interplay between autophagy, centriolar satellites and ciliogenesis. Refer to the Chapter 2 specific introduction for more details about the role of autophagy and OFD1's centriolar satellites regulation in cilia formation.

(ARL13B) also localizes to cilia. However, its trafficking role is still obscure even though it is known to be required for correct axoneme structure (Caspary et al., 2007).

I.V. Cilia in signaling and human pathologies

The “raison d'être” (Silverman and Leroux, 2009) of primary cilia is the concentration, in a subset of cytoplasm and plasma membrane that is independent of the rest of the cell, of molecular machinery to receive and/or to transmit information (Hilgendorf et al., 2016; Ishikawa and Marshall, 2011; Malicki and Johnson, 2016; Nachury, 2014; Silverman and Leroux, 2009; Singla and Reiter, 2006). Therefore, it is not surprising to realize that cilia are major signaling hubs. Hedgehog (Hh) signaling was one of the first pathways to be linked with primary cilia and fulfills a central role in development, namely in patterning, morphogenesis, and growth of tissues and organs (Briscoe and Thérond, 2013; Goetz and Anderson, 2010). Hh signaling depends on the coordinated movement in and out of the cilium of the major signaling components such as Sonic hedgehog (Shh) receptor Protein patched homolog 1 (PTCH1), the class F G protein-coupled receptor (GPCR) Smoothened (Smo), Suppressor of Fused (SuFu) and the Glioma (Gli) transcription factors. In the absence of Shh, SuFu inhibits the transcriptional activity of the Gli transcription factors on the Hh target genes. The binding of Shh to PTCH1 triggers the exit of PTCH1 from the cilium in parallel with the entry Smo and the activation of Gli mediated transcription of Hh target genes (Corbit et al., 2005; Goetz and Anderson, 2010; Haycraft et al., 2005; Hilgendorf et al., 2016; Nachury, 2014; Schou et al., 2015). Besides Hh signaling, there are many components of other pathways that are in the primary cilium. Examples include class A and B GPCRs (Hilgendorf et al., 2016; Schou et al., 2015), receptor tyrosine kinases (Christensen et al., 2011), transforming factor beta (TGF-β) receptors (Clement et al., 2013), notch (Ezratty et al., 2011), Wingless/Int (Wnt) (May-Simera and Kelley, 2012; Veland et al., 2009), purinergic signaling (Masyuk et al., 2008), receptors for extracellular matrix proteins (McGlashan, 2006; Seeger-Nukpezah and Golemis, 2012) or ion channels of the transient receptor potential (TRP) family (Phua et al., 2015). The expanding number of receptors and signaling pathways implicated with cilia raise the question of how cilia receive and transmit multiple signals simultaneously. Moreover, this issue is even more interesting if we consider that many signaling pathways use the same downstream effector molecules. The idea that cilia are not just a platform to orchestrate signaling pathways but are also responsible for the integration multiple signals into specific outputs has gained support in recent years (Hilgendorf et al., 2016; Malicki and Johnson, 2016; Nachury, 2014).

Either because cilium structure is compromised or the protein composition necessary for its correct function is abnormal, ciliary defects are responsible for a group of diseases known as ciliopathies. Defects in motile cilia often lead to chronic bronchitis, sinusitis, male sterility and situs inversus (Afzelius, 1976; Gerdes et al., 2009; Nigg and Raff, 2009) and for historical reasons are referred to as primary ciliary dyskinesias or PCDs. Diseases associated with primary cilia are genetically heterogeneous disorders that share many overlapping clinical manifestations. Defects in primary cilia manifest themselves through a broad spectrum of pathologies that include polydactyly, cranio-facial abnormalities, brain malformation, situs inversus, obesity, diabetes, and polycystic kidney disease (Braun and Hildebrandt, 2016; Gerdes et al., 2009; Nigg and Raff, 2009; Valente et al., 2013; Waters and Beales, 2011). The most notable ciliopathies include nephronophthisis (NPHP), polycystic kidney disease (PKD), Bardel Biedl syndrome (BBS), Meckel Gruber syndrome

(MKS), Joubert syndrome (JS), Alström syndrome (ALMS), retinal degeneration (RPGR), and orofaciodigital syndrome (OFD).

II. Aims of this study

Centrosome and cilia biology intersect many aspects of human life. Expanding our knowledge about cilia and centrosome biology can provide useful insights to prevent prenatal lethality and other severe human pathologies. Advances in RNAi screening and genome-wide sequencing have allowed the identification of a vast number of proteins that are involved in centrosome biology and, play a role in cilia formation, maintenance, and function in human health.

Centriolar satellite particles have been enigmatic constituents of animal cells. Understanding of the individual composition of each particle is still lacking due to the methodological difficulty in purifying centriolar satellites to homogeneity. Regarding their structure and function, the particles small size and apparently chaotic distribution throughout the cell have precluded a quantitative approach to their study. My aim here was to develop quantitative methods to use in the study of centriolar satellite biology. To achieve this goal, I developed computational analysis pipelines that allow investigation of sizeable fluorescence microscopy datasets in a fast and unbiased way. With the data obtained, it was possible to quantify and compare alterations introduced in centriolar satellite dispersal.

Our lab identified MARK4 as a positive regulator of ciliogenesis, and my goal was to understand better the molecular details of that regulation. I reckoned that MARK4's influence could be exerted in two non-exclusive ways: via autophagy regulation and via CP110-Cep97 complex removal from the basal body.

The finding that MARK4 depletion leads to autophagy defects and that autophagy has been found to have a functional link with ciliogenesis via degradation of the OFD1 protein that localizes to the centriolar satellites, primed me to investigate if MARK4 is involved in the autophagy activation necessary for ciliogenesis. I found that that was the case. Moreover, artificial degradation of OFD1 from the centriolar satellites was able to rescue MARK4’s defect in cilia formation.

We previously published that cells depleted of MARK4 are less probable to ciliate. Associated with MARK4 depletion was the failure of cells in removing CP110 from the basal bodies. As a follow up on these studies, my aim was to identify physical and regulatory interactions between MARK4, CP110, and Cep97 that may explain the inability of MARK4 depleted cells to ciliate. Moreover, I wanted to know if there is a functional overlap in the regulation of the localization of the CP110-Cep97 complex at the basal body with TTBK2. I found that indeed MARK4 interacts with the CP110-Cep97 complex in vivo and that both CP110 and Cep97 are MARK4's in vitro substrates. When double-depleted, MARK4 and TTBK2 show a more severe phenotype regarding cilia loss than the single-depletions, indicating a synergistic role for the two kinases in the control of the early steps of cilia formation.

Due to the diverse nature of the three subjects mentioned above, the contents of this thesis are divided into three chapters:

Chapter 1: Quantitative microscopy methods for centriolar satellite analysis;

Chapter 2: MARK4 at the crossroads of autophagy and ciliogenesis;

Chapter 3: MARK4 and TTBK2 interplay with CP110 and Cep97.

A literature review of the relevant molecular details to understand each section will be provided in a chapter specific introduction and then results will be presented and discussed. I hope this thesis is useful for you.

III. Chapter 1: Quantitative microscopy methods for centriolar satellite analysis

III.I. Introduction

The modern use of the term “satellite” to refer to centriolar satellite (CS) particles came from the first live cell imaging study to report on CSs (Kubo et al., 1999). Kubo et al. (Kubo et al., 1999) used the term “satellites” since the CS particles continuously moved in the vicinity of the centrosome as planetary satellites do around another celestial body. To this day CSs remain poorly understood (Bärenz et al., 2011; Hori and Toda, 2016; Tollenaere et al., 2015). The protein pericentriolar material 1 (PCM1) was the first component of the centriolar satellites to be identified and characterized (Balczon et al., 1994; Kubo et al., 1999). It is regarded as the scaffold protein for CSs (Bärenz et al., 2011; Hori and Toda, 2016; Tollenaere et al., 2015). It is believed that PCM1's structural role is achieved through homo-oligomerisation and binding to other components considering that PCM1 is a large protein and rich in internal coiled-coil domains (Hori and Toda, 2016) available for interaction. Today, more than 100 proteins were identified as CS components (Bärenz et al., 2011; Hori and Toda, 2016; Tollenaere et al., 2015).

An undisturbed microtubule organization is essential for CS localization. Microtubule destabilization employing nocodazole or cold treatments results in CS particles dispersion from the vicinity of the centrosome towards the cell periphery (Dammermann and Merdes, 2002; Kim et al., 2008; Kubo et al., 1999; Lopes et al., 2011). Likewise, interference with microtubule machinery has the effect of disturbing CSs (Gupta et al., 2015). As usual for microtubule-associated entities, CSs are not static within the cell. However, contrary to planetary satellites, centriolar satellites movement does not originate from the force of gravity, and it is not orbital. Instead, dynein is involved, at least in part, on CS drive. Dynein was shown to interact with CS components (Kim et al., 2004) and perturbation of dynein functions by over-expression of dynamitin (Burkhardt et al., 1997) results in the dispersion of CSs (Dammermann and Merdes, 2002; Lopes et al., 2011). Nonetheless, the precise mechanism that explains CS movement within the cell and specifically how CS are distributed in the vicinity of the centrosome remains to be unveiled.

Although CS accumulate at the vicinity of centrosomes in a microtubule-dependent manner, most of CS components are not integral components of the centrosome. Essential elements of the centrosome or the cilium, the proteins OFD1 and Cep290 were shown to be CS localized and also necessary for CS formation and maintenance (Kim et al., 2008; Lopes et al., 2011; Romio et al., 2003; Valente et al., 2006). Contrary to other proteins such as ninein, centrin (Dammermann and Merdes, 2002) or NEK2 (Hames et al., 2005), both OFD1’s and Cep290’s centrosomal localization does not depend on PCM1 (Kim et al., 2008; Lopes et al., 2011).

Besides interacting with PCM1, OFD1 is a master organizer of CS structure, centriole architecture and ciliogenesis (Lopes et al., 2011; Singla et al., 2010). Some of the OFD1 roles include recruitment and assembly of essential components to the distal appendages of the mother centriole, namely Cep164 (Singla et al., 2010), and an inhibition of ciliogenesis that is reversible by autophagy or ectopic degradation of OFD1 (Tang et al., 2013). Cep290 interacts with PCM1, it is required for Rab8A localization to the primary cilium (Kim et al., 2008), and it is another example of a protein that shares localization between CS and the centrosome or cilium.

Hori and Toda (Hori and Toda, 2016) report that perturbation of PCM1 or PLK-4 leads to abnormal pericentriolar patterns of CS localization. This altered distribution of CS particles throughout the cell can affect the transport and regulation roles of CSs in centriole duplication, cellular stress response or ciliogenesis. However, the study of the distribution of chaotic cellular structures such as CSs has confronted the scientific community with the difficulty of accurately and meaningfully quantify variables such as shape, compactness or degree of spatial clustering of cellular objects. Until now, manual quantification of complex variables would not be exhaustive and could not be assumed to be unbiased. Qualitative classification of phenotypes, on the other hand, does not allow comparisons of results between different experiments and makes reproducibility very challenging. In previous publications, the way CS are dispersed around the centrosome has been referred to as "clustered", "organized" or a similar qualitative term. Beyond the difficulty in reproducing such qualifications, they make it tough to compare different kinds and degrees of "unclustered" or "disorganized" CS.

I propose to analyze centriolar satellite distribution through the cell in a quantitative way. For that, I developed a computational method to extract a wide array of variables from large microscopy datasets (up to 18,000 image files in this study but it is possible to upscale). The data that can be extracted from the microscopy images via automated computational processing includes object segmentation such as determination of the cell borders or identification of a cilium, centrosome or CS granule. It also includes background correction, pixel intensity measurement of a region of interest (ROI) and various useful statistical and mathematical operations. Once a comprehensive list of features for a large number of cellular objects is obtained, some cell biology patterns that were hidden can be revealed. We start by observing the strong relation between cell size and the number of CS particles. Next, I propose two data visualization diagrams that summarize data collected from large datasets and in a fast and intuitive way allow to trace changes in CSs that are hidden by their chaotic nature. Finally, I explain how to use Wiener entropy (WE) to quantify, using a single value per cell, the degree of spatial dispersal of CSs around the centrosome.

III.II. Results

III.II.I. Automated cilia and centrosome segmentation and classification

Using the machine learning capabilities of image segmentation software, we obtain for any given pixel of the γ-tubulin/polyglutamylated tubulin micrographs, a probability value for that pixel to be or not part of an object that we defined as "centrosome/cilium" (Figure 6Aa-b). By thresholding this probability map we can extract objects whose pixels meet the threshold conditions that we identified and set as satisfactory in the machine learning stage (Figure 6Ac). We can then extract geometric and pixel intensity data from this objects and teach the software to classify different objects as centrosomes or cilia (Figure 6Ad). The resulting binary images with the centrosomes and cilia masks can then be used for further quantification of cilia and centrosomes related parameters such as measuring fluorescence intensity values or geometric variables regarding their shape and position within the cell.

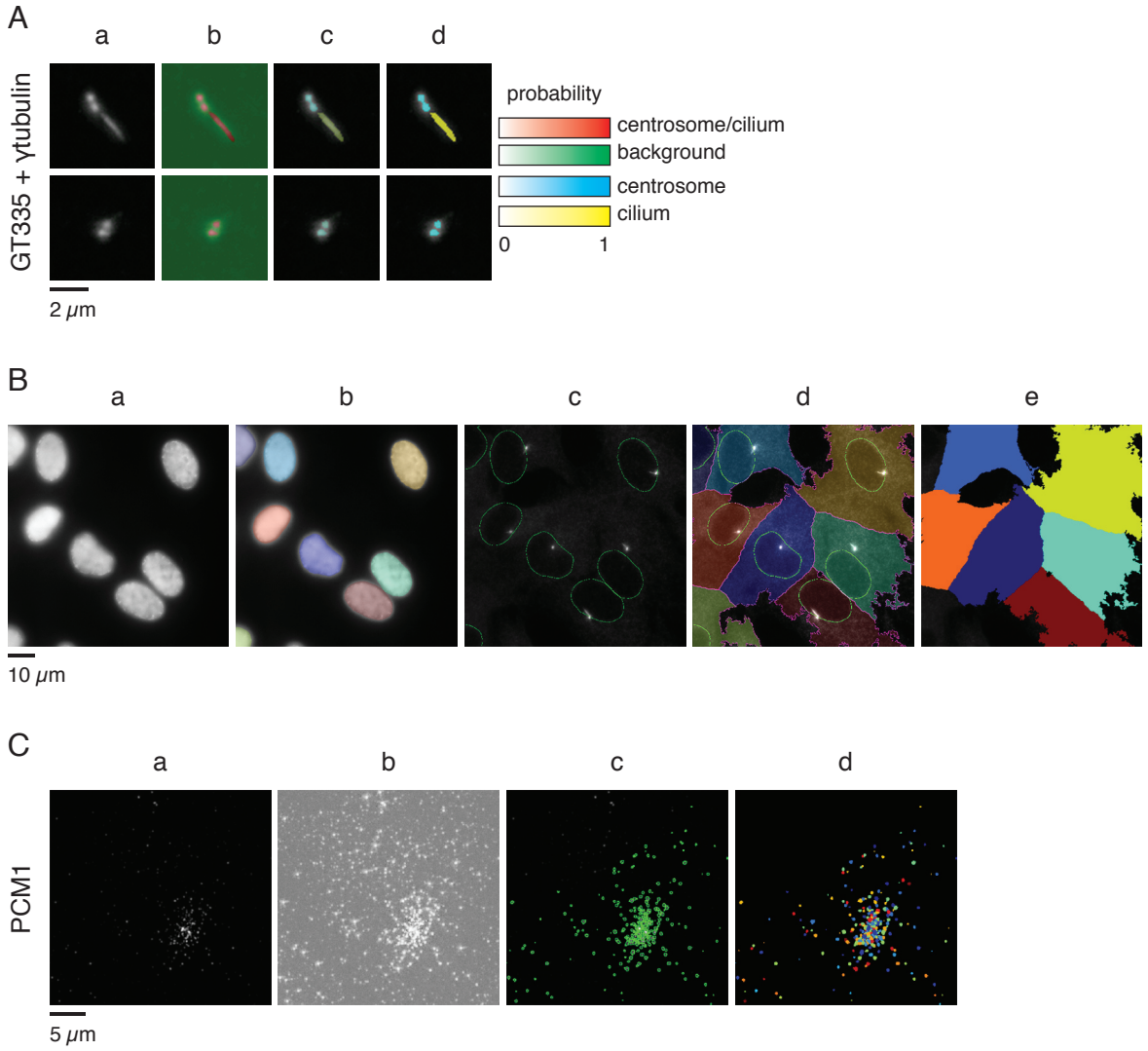

Figure 6: **Segmentation of centrosomes, cilia, cells and centriolar satellites**. (A) machine learning steps for the segmentation of centrosomes and cilia: a, monochrome image of centrosomes and cilia after tophat filter treatment; b, the probability that each pixel belongs to the background or to a centrosome or cilium is indicated in green and red colors respectively; c, image after thresholding for centrosome and cilium where the blue color indicates the probability of the object to be a centrosome and the yellow color the probability of being a cilium; d, final binary image of centrosomes and cilia. (B) steps for cell area segmentation: a, monochrome, maximum intensity projected images of cell nuclei; b, segmentation of cell nuclei where different colors represent different nuclei; c, outline of nuclei used as seeds to segment the cell area using a median intensity projection of gamma-tubulin and polyglutamylated tubulin staining; d, result of the cell area segmentation; e, final binary image of the cell areas. The colors are used for illustrative purposes and were chosen arbitrarily by the software used for segmentation.

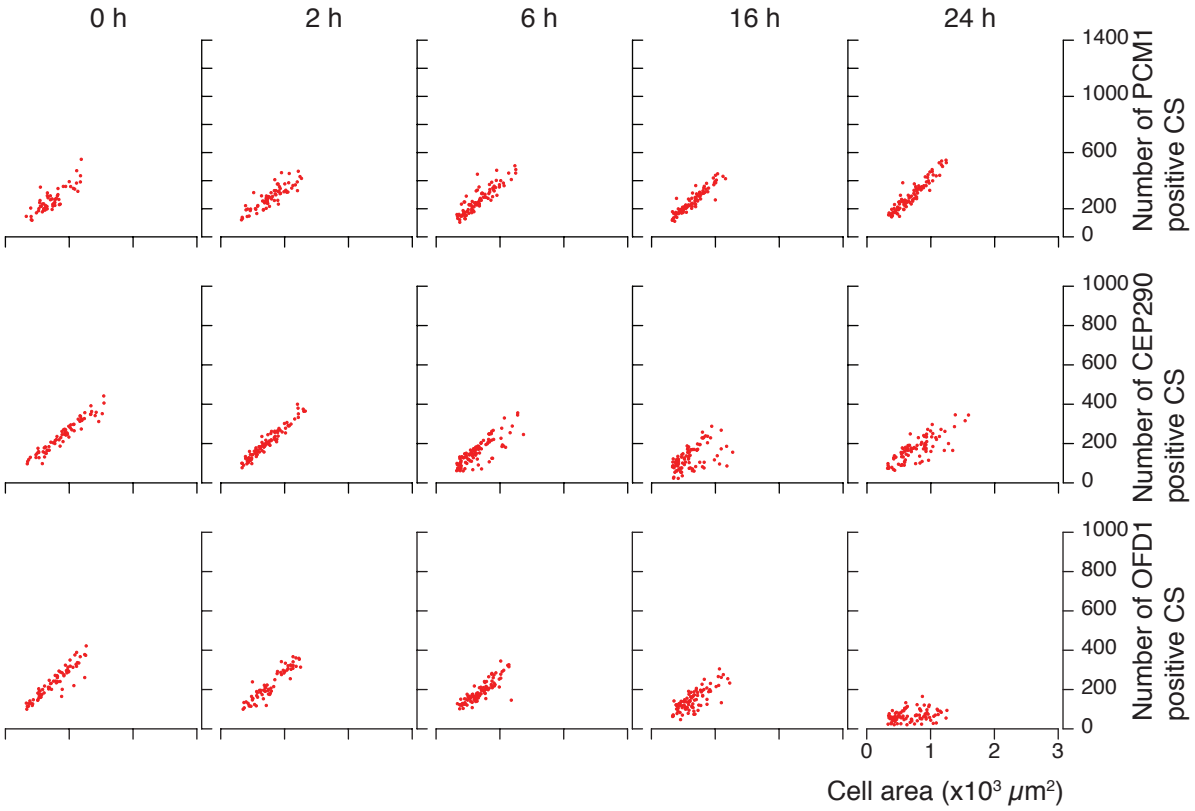

Figure 7: **Centriolar satellite number has high correlation with cell size**. RPE1 cells were serum starved for 24 hours, samples were taken at the indicated time points and resulting immunofluorescence microscopy images were processed as described in Methods. The data points plotted refer to the values for each cell of the cell area and number of CSs obtained by automated quantification. One representative experiment out of two is shown. $57<N_{PCM1}<95$, $72<N_{Cep290}<103$, $70<N_{OFD1}<97$.

III.II.II. Automated cell segmentation

I used the maximum intensity projected images of the DAPI channel to identify the cell nuclei (Figure 6Ba-b). Using these nuclei as input objects and the median intensity projection of the γ-tubulin/polyglutamylated tubulin images as the base image, I identified the cell boundaries (Figure 6Bc-d). The identified objects were further filtered to eliminate too small or too large cells and cells with abnormal numbers of centrosomes and cilia.

III.II.III. Automated centriolar satellite segmentation

To segment the dot-like signals of the centriolar satellites I used the predetermined cell shapes as masking objects and tophat filtered, maximum intensity projections of the centriolar satellite images as the input image (Figure 6Ca-b). It is critical for the detection of small intensity variations that will allow distinguishing clumped objects that the microscopy conditions are well optimized to the objects that will be analyzed. In this case, I chose the 488 nm emission channel and a 100×/1.45 NA objective so that by using a smaller wavelength and a high numerical aperture I could obtain maximum resolution. The use of a 16-bit EM-CCD camera allows for high sensitivity and dynamic range without compromising acquisition rate in situations such as these where confocality is a minor issue. After taking the acquisition parameters of the image mentioned above in consideration, I used a RobustBackground thresholding method and Laplacian of Gaussian method to identify and distinguish clumped CSs. It is shown in Figure 6Cc-d that I was able not only to segment isolated CS particles, granules or foci (interchangeable terms) but also made possible to

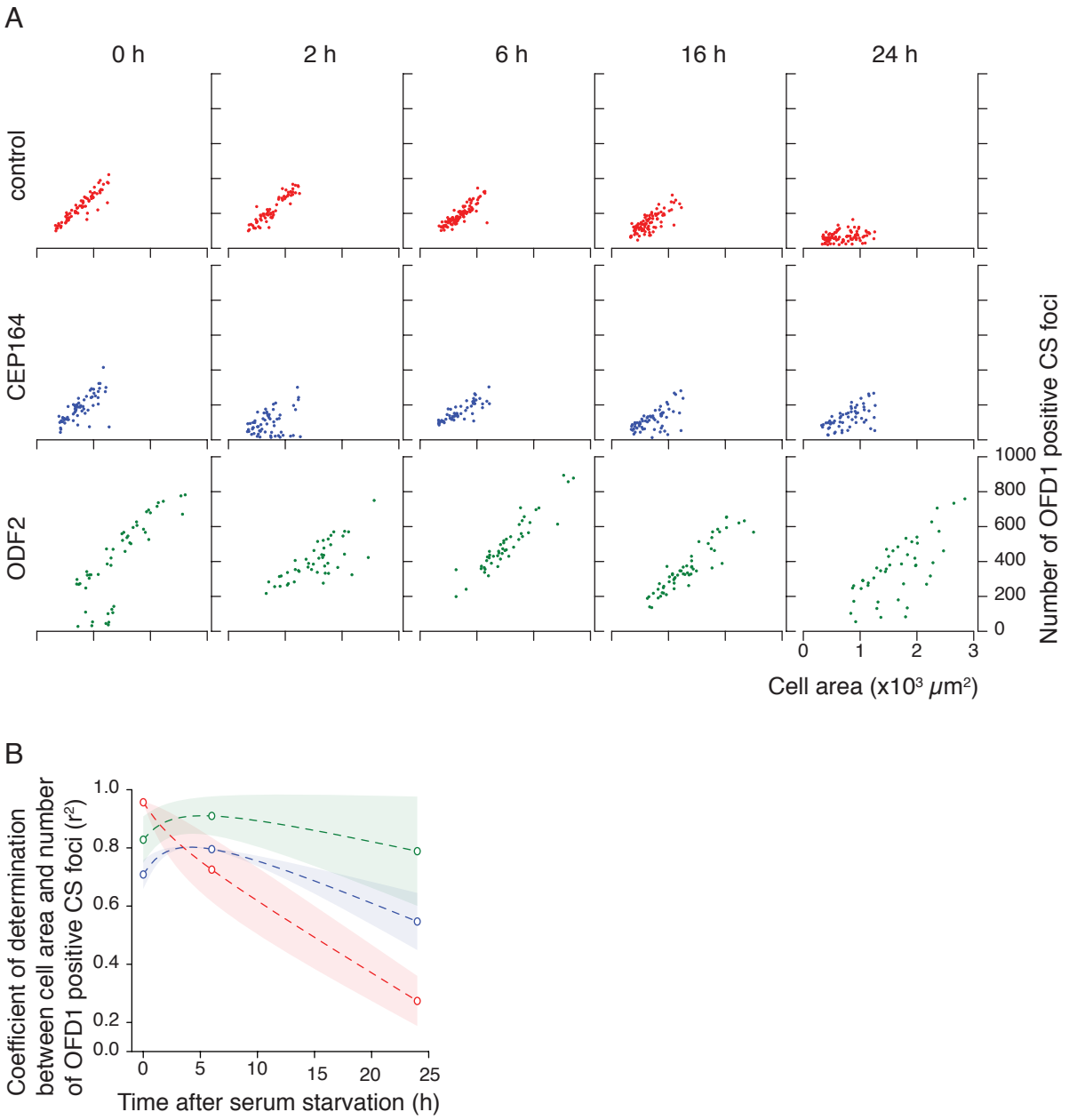

Figure 8: **Correlation between cell size and number per cell of OFD1 positive CS particles decreases upon serum starvation**. (A and B) RPE1 cells, control, CEP164 and ODF2 depleted, were serum starved for 24 hours, samples were taken at the indicated time points and resulting immunofluorescence microscopy images were processed as described in Methods. (A) The data points plotted refer to the values for each cell of the cell area and number of CSs obtained by automated quantification. Data corresponding to control is the same as presented in Figure 6. (B) Quantification of the coefficient of determination of the conditions and time points presented in A. Data shown is the average of three independent experiments and shaded area around the dashed lines corresponds to the SEM. One representative experiment out of two is shown. $67<N_{control}<97$, $54<N_{Cep164}<63$, $45<N_{ODF2}<57$.

distinguish individual particles that appear to be clumped in the CS cloud that localizes to the vicinity of the centrosome.

III.II.IV.Correlation between the number of CS particles and cell size

I wanted to know how the number of CS particles correlated to the cell size. In Figure 7 I plotted a dot for each cell, with the number of CS foci and the cell area as coordinates. We can see that there is a strong positive correlation between these two variables: as cells grow, the number of CS particles in the cells increases proportionally. For human retinal pigment epithelium cells immortalized with telomerase reverse transcriptase (RPE1) cells, the coefficient of determination (r^2) values can be as high as 0.85 for OFD1 CSs

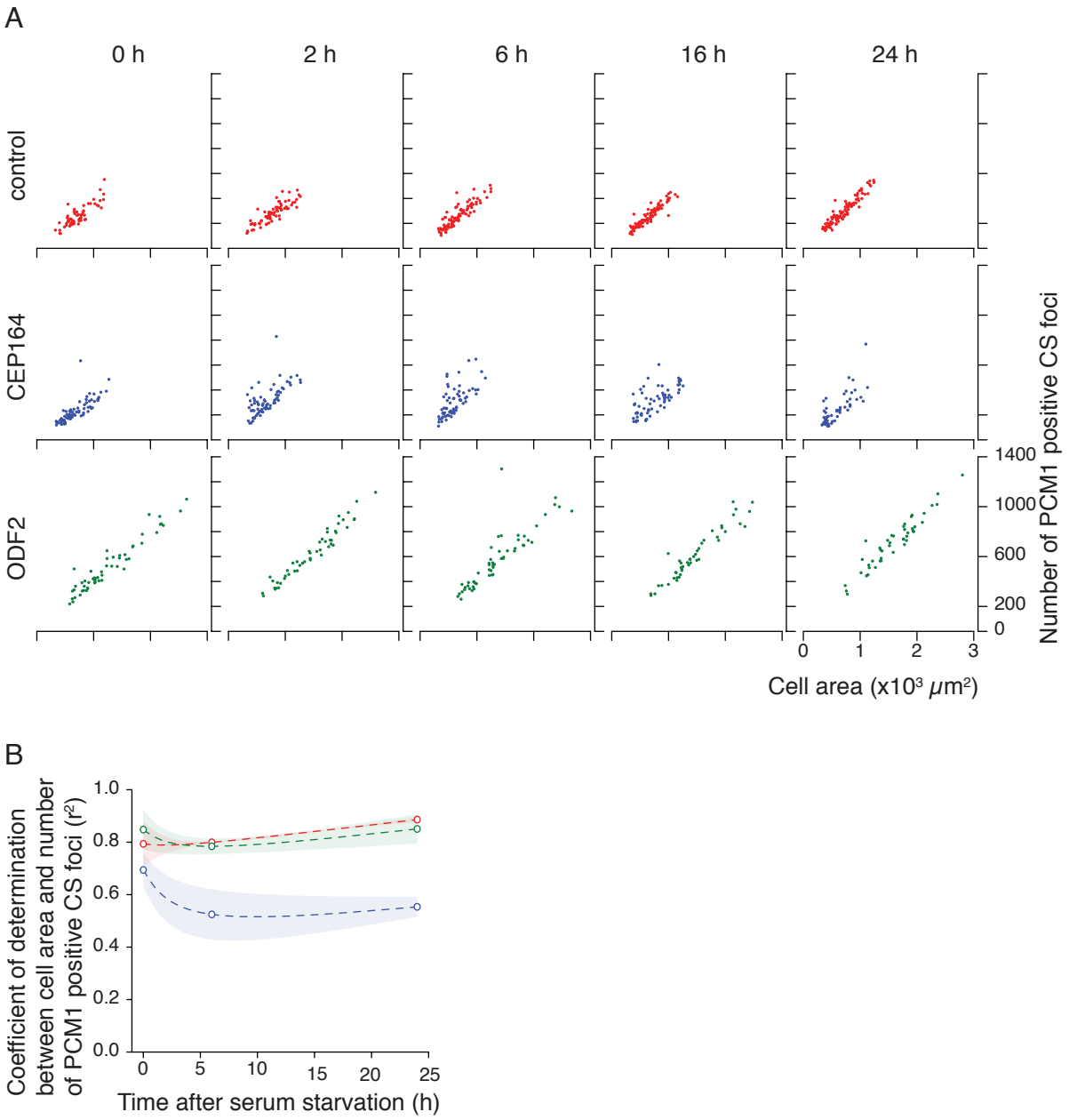

Figure 9: **Correlation between cell size and number per cell of PCM1 positive CS particles increases upon serum starvation**. (A and B) RPE1 cells, control, CEP164 and ODF2 depleted, were serum starved for 24 hours, samples were taken at the indicated time points and resulting immunofluorescence microscopy images were processed as described in Methods. (A) The data points plotted refer to the values for each cell of the cell area and number of CSs obtained by automated quantification. Data corresponding to control is the same as presented in Figure 6. (B) Quantification of the coefficient of determination of the conditions and time points presented in A. Data shown is the average of three independent experiments and shaded area around the dashed lines corresponds to the SEM. One representative experiment out of two is shown. $57<N_{control}<95$, $53<N_{Cep164}<76$, $45<N_{ODF2}<54$.

in cycling cells. The extent of the correlation between cell area and the number of CS foci (corrACS) depends on the CS protein studied and its dynamics throughout the ciliation process. For PCM1 positive CS particles, it increases during the serum starvation period necessary for ciliation to occur. The same does not happen to Cep290 and OFD1, where the correlation mentioned above drops during serum starvation. In the case of OFD1, the decline of the corrACS is quite substantial. As seen in Figure 7, after 24 hours of serum starvation, all the cells have approximately the same (low) number of OFD1 CSs irrespective of their cell size. This observation is in agreement with the report that OFD1 CSs are degraded during serum starvation (Tang et al., 2013).

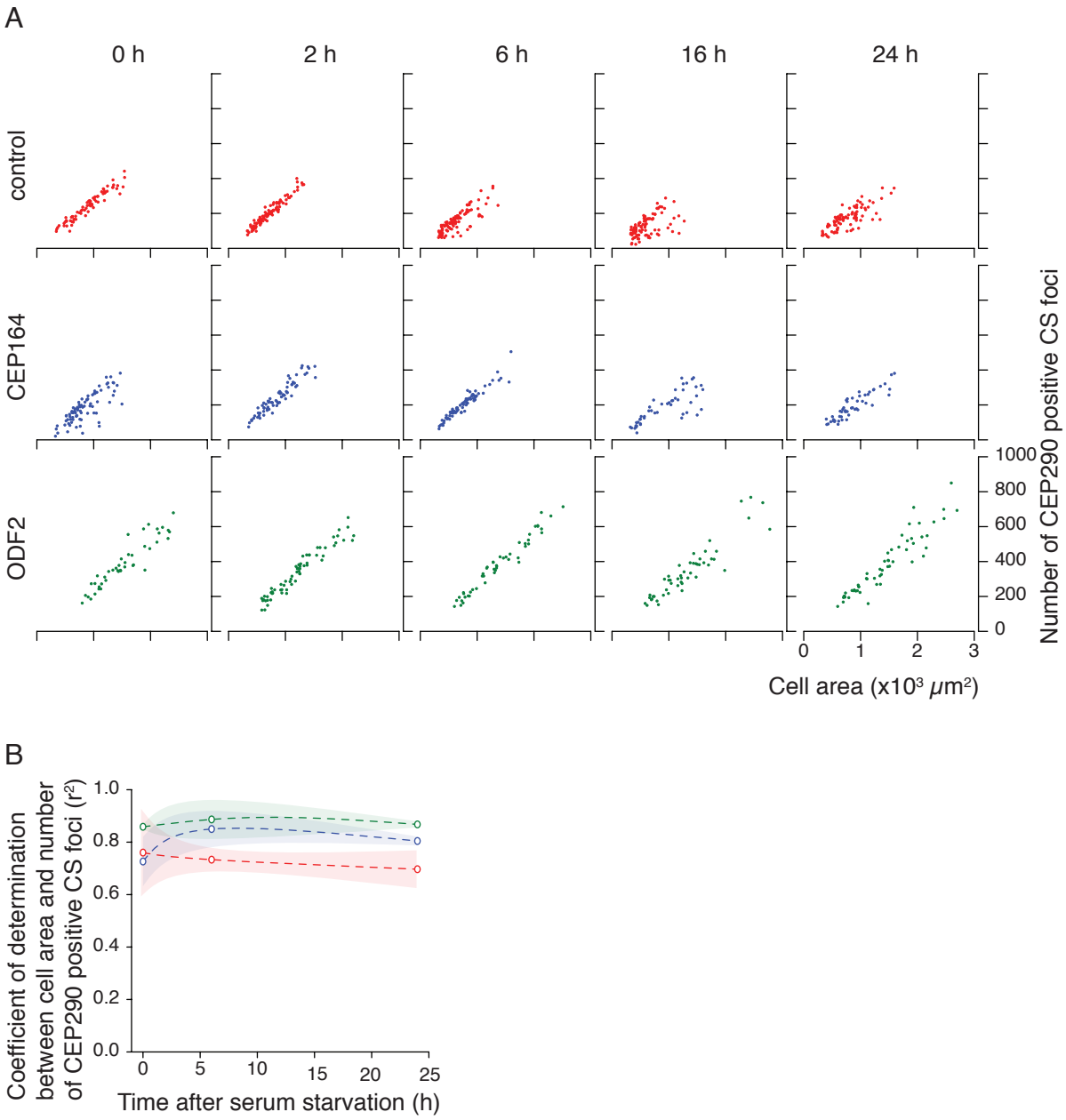

Figure 10: **Correlation between cell size and number per cell of CEP290 positive CS particles is stable upon serum starvation**. (A and B) RPE1 cells, control, CEP164 and ODF2 depleted, were serum starved for 24 hours, samples were taken at the indicated time points and resulting immunofluorescence microscopy images were processed as described in Methods. (A) The data points plotted refer to the values for each cell of the cell area and number of CSs obtained by automated quantification. Data corresponding to control is the same as presented in Figure 6. (B) Quantification of the coefficient of determination of the conditions and time points presented in A. Data shown is the average of three independent experiments and shaded area around the dashed lines corresponds to the SEM. One representative experiment out of two is shown. $72<N_{control}<103$, $48<N_{Cep164}<80$, $43<N_{ODF2}<64$.

Next, I aimed at analyzing the influence of centriolar appendage proteins in CS organization. To know how CSs dynamics are affected by the integrity of the distal and sub-distal appendages of the mother centriole, I analyzed RPE1 cells depleted of Cep164 or ODF2 respectively. Cells lacking Cep164 are not able to ciliate due to a defect in ciliary vesicle attachment (Schmidt et al., 2012) and possibly carry defects in distal appendage structure. Depletion of ODF2 also causes ciliogenesis defects and severely disrupts sub-distal appendage formation (Ishikawa et al., 2005; Kuhns et al., 2013). In Figure 8, we can contrast what happens in control, Cep164 and ODF2-depleted cells regarding the corrACS of OFD1 positive CS. Both Cep164 and ODF2-depleted cells have lower values for their corrACS of OFD1 CS foci than control-depleted cells when the cells are kept in serum rich conditions (Figure 8A, quantification in B). As we have seen (Figure 7), in

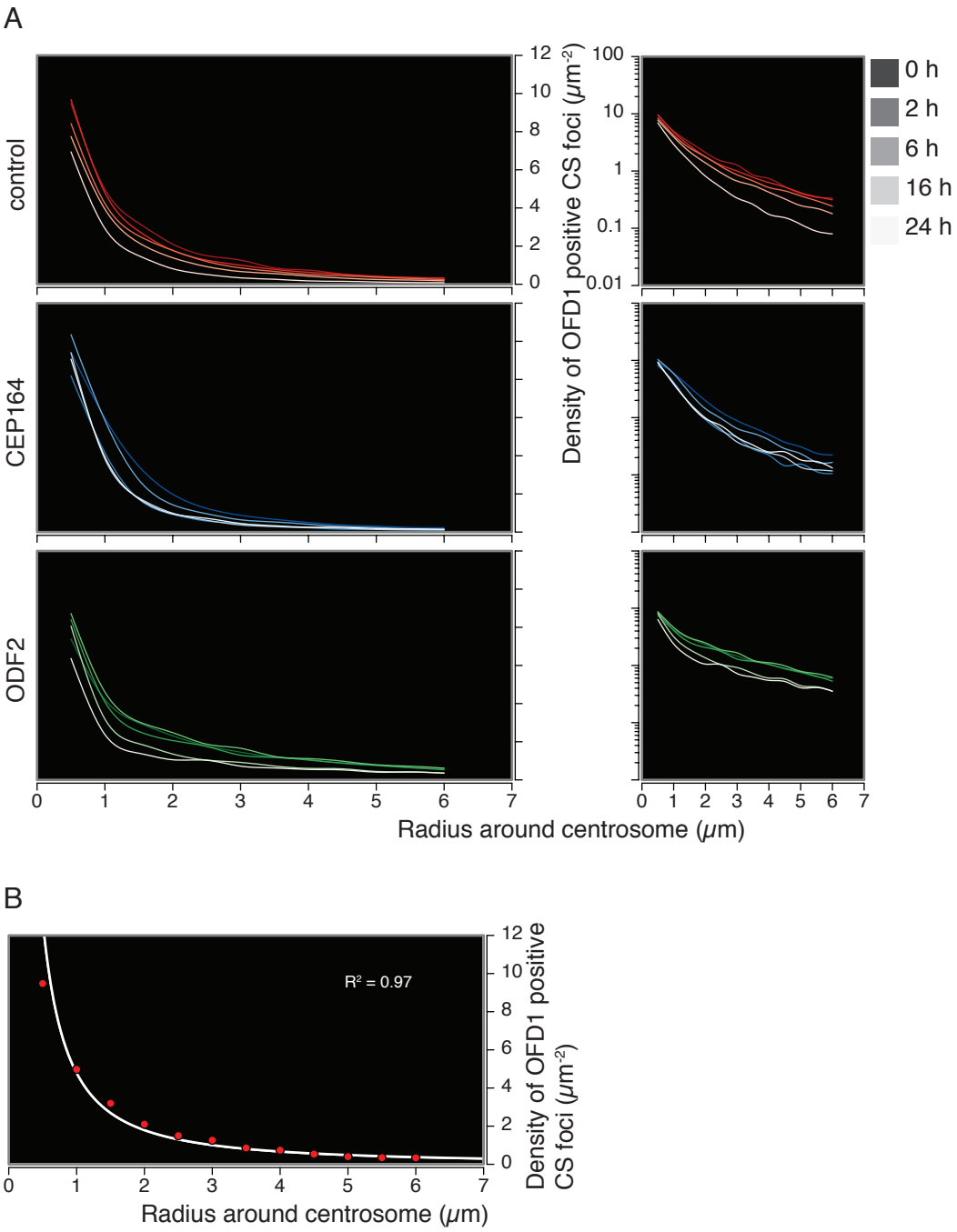

Figure 11: **Profile of OFD1 CS particle density around the centrosome in control, CEP164 and ODF2 depleted cells**. (A and B) RPE1 cells, control, CEP164 and ODF2 depleted, were serum starved for 24 hours, samples were taken at the indicated time points and resulting immunofluorescence microscopy images were processed as described in Methods. (A and B) Plot of the density of OFD1 positive granules as a function of the distance to the nearest centrosome. In the left panel, the density of OFD1 foci is represented in a linear scale, in the right panel, in a logarithmic scale. After calculating the CS foci density in concentric rings around the centrosomes, that density value was plotted in function of the radius of the outer circumference of the corresponding concentric ring. (A) The curves shown are interpolated from these data points using a natural cubic spline function. Shades of grey associated with the time points make the correspondence with different hues of the colors chosen to illustrate different depletion conditions. (B) The line shown was fitted to the data points using a Power function. The R^2 indicated is the coefficient of determination found for this fit. One representative experiment out of two is shown. $67<N_{control}<97$, $54<N_{Cep164}<63$, $45<N_{ODF2}<57$.

control-depleted cells subjected to serum starvation, the corrACS of OFD1 CSs drops to very low values after 24 hours of treatment. This decline is less pronounced in Cep164-deficient cells and especially in ODF2-depleted cells (Figure 8). If we look at Figure 8A, we notice that ODF2-depleted cells can achieve much larger cell areas than control or Cep164-depleted cells. Even so, for ODF2-depleted cells, the corrACS is

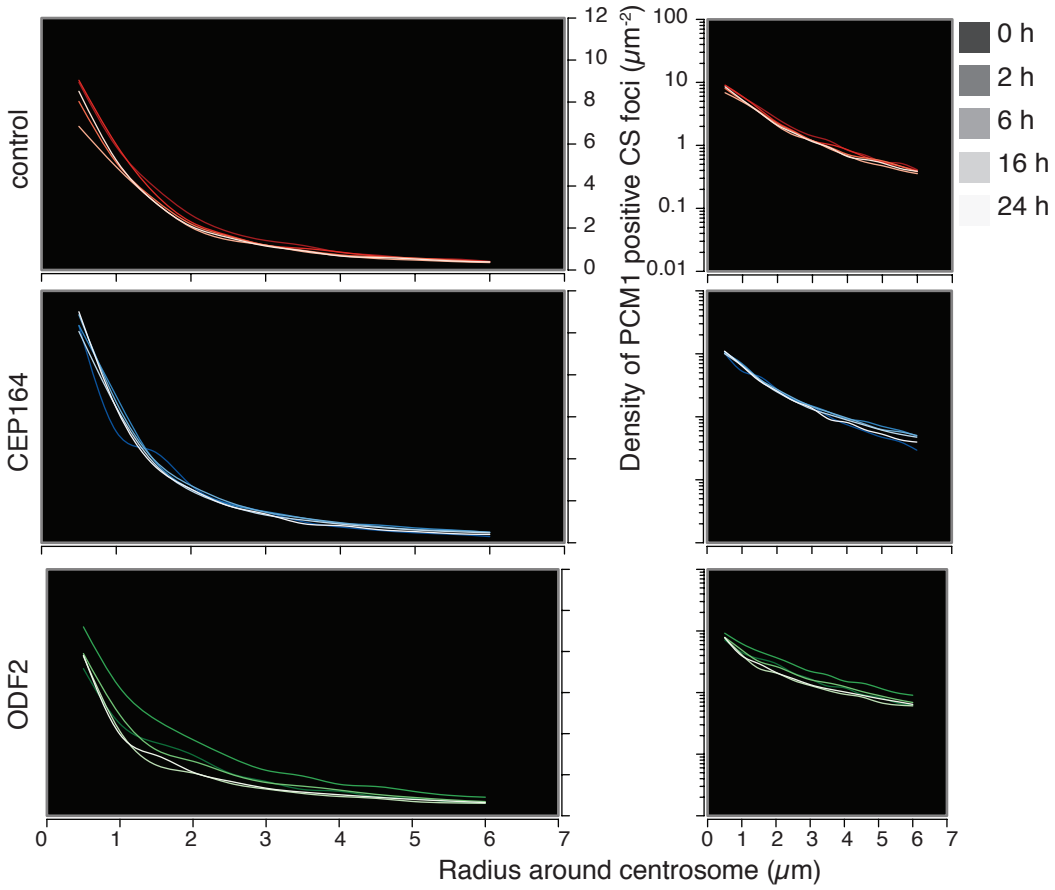

Figure 12: **Profile of PCM1 CS particle density around the centrosome in control, CEP164 and ODF2 depleted cells**. (A and B) RPE1 cells, control, CEP164 and ODF2 depleted, were serum starved for 24 hours, samples were taken at the indicated time points and resulting immunofluorescence microscopy images were processed as described in Methods. Plot of the density of PCM1 positive granules as a function of the distance to the nearest centrosome. In the left panel, the density of PCM1 foci is represented in a linear scale, in the right panel, in a logarithmic scale. After calculating the CS foci density in concentric rings around the centrosomes, that density value was plotted in function of the radius of the outer circumference of the corresponding concentric ring. The curves shown are interpolated from these data points using a natural cubic spline function. Shades of grey associated with the time points make the correspondence with different hues of the colors chosen to illustrate different depletion conditions. One representative experiment out of two is shown. $57<N_{control}<95$, $53<N_{Cep164}<76$,

over 0.80 throughout the length of the experiment. Therefore, the drop in corrACS for OFD1 CS foci seems to be dependent on ODF2 and to a lesser extent on Cep164.

Regarding PCM1 CSs, in control and ODF2-depleted cells, a tendency for the increase in the corrACS is observed as serum starvation progresses (Figure 9). For Cep164-depleted cells, a drop in the corrACS is seen in the first few hours after the serum is washed away from the cells. After the initial slump, the correlation stabilizes at values above 0.50 (Figure 9).

Cep290 CS particle number is also strongly correlated with the cell size (Figure 10). However, from the three CS proteins chosen for analysis in this thesis, Cep290 is the one that after the cells are serum starved registers fewer changes in the corrACS. Both for control, Cep164 and ODF2-depleted cells the corrACS of Cep290 foci does not vary significantly throughout 24 hours of serum starvation.

III.II.V. Profile of centriolar satellite density around the centrosome

To better compare CS distribution around the centrosome in different cells and experimental conditions, I calculated the CS foci density in concentric rings around the centrosomes and plotted that density value in function of the radius of the outer circumference of that concentric ring. Figure 11A shows this plot

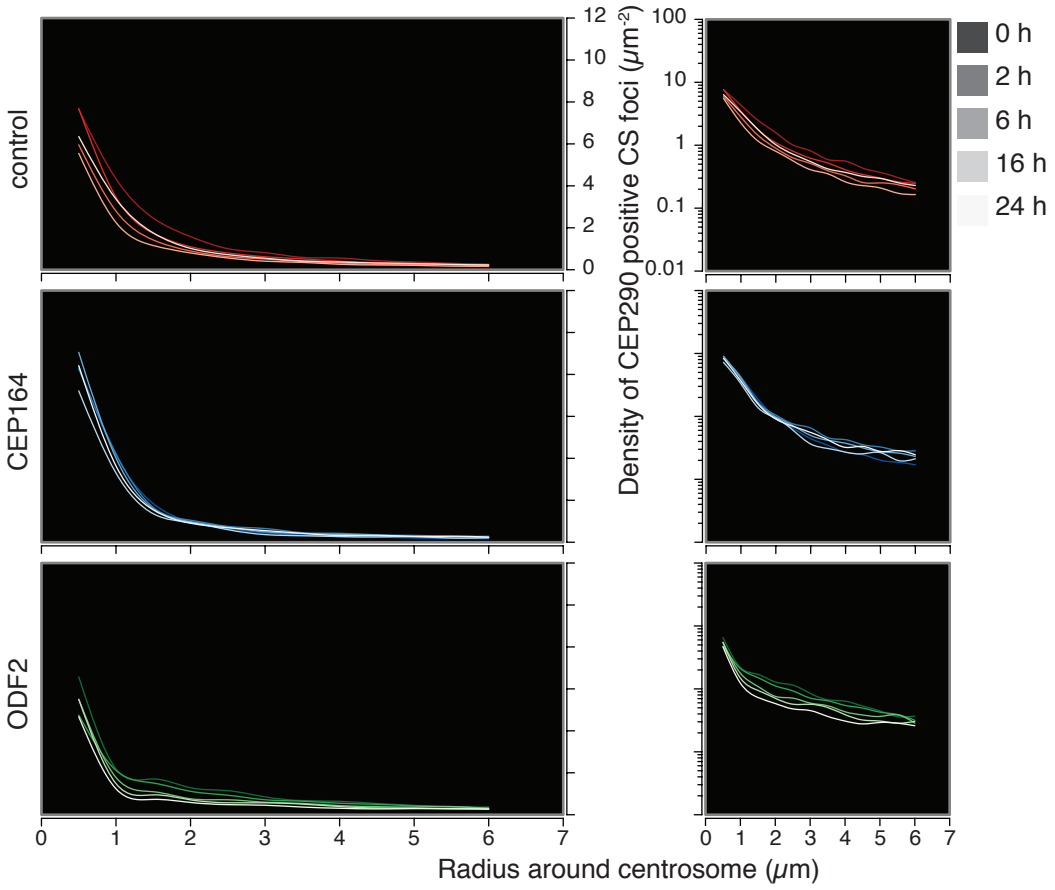

Figure 13: **Profile of CEP290 CS particle density around the centrosome in control, CEP164 and ODF2 depleted cells**. (A and B) RPE1 cells, control, CEP164 and ODF2 depleted, were serum starved for 24 hours, samples were taken at the indicated time points and resulting immunofluorescence microscopy images were processed as described in Methods. Plot of the density of CEP290 positive granules as a function of the distance to the nearest centrosome. In the left panel, the density of CEP290 foci is represented in a linear scale, in the right panel, in a logarithmic scale. After calculating the CS foci density in concentric rings around the centrosomes, that density value was plotted in function of the radius of the outer circumference of the corresponding concentric ring. The curves shown are interpolated from these data points using a natural cubic spline function. Shades of grey associated with the time points make the correspondence with different hues of the colors chosen to illustrate different depletion conditions. One representative experiment out of two is shown. $72<N_{control}<103$, $48<N_{Cep164}<80$, $43<N_{ODF2}<64$.

where I interpolated the values using a natural cubic spline function. After smoothing out the interpolation of the density values, the result can be interpreted as an empirically determined abstraction of a conical section of the density of CS around the centrosome. This way of representation allows us to, in a fast and intuitive way, evaluate fluctuations in the CS distribution profile around the centrosome and it is amenable to a power law curve fit with remarkably high coefficients of determination (Figure 11B), which can be useful for modeling applications of this method. For OFD1 CSs we can see in Figure 11 that in control serum-starved cells, there is a drop in CS density near the centrosome in all time points. The same can be seen in regions more distant from the centrosome (Figure 11)A. In the nearest proximity of the centrosome, the density variation is significant regarding absolute values. If we compare the order of magnitude of the change, the difference is more dramatic in regions peripheral about the centrosome. Figure 11 shows that in control-depleted cells, a single drop of CS density in ranges from 3 to 6 µm away from the centrosome takes place only during the final stages of cilia formation (24 hours after serum starvation). We can see that in these cells, the drop of OFD1 CS granules happens very gradually close to the centrosome and suddenly, just during the final stages of cilia formation, away from the centrosome.

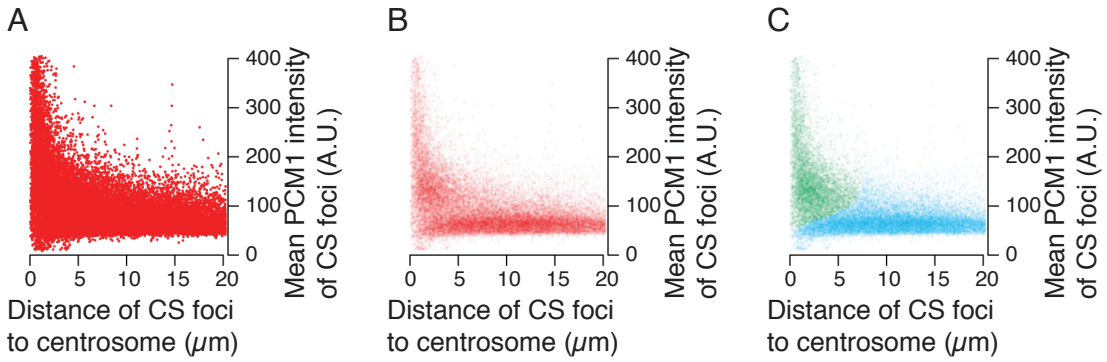

Figure 14: **Centrosome satellite fluorescence intensity vs. distance of CS foci to the nearest centrosome plot**. (A, B and C) RPE1 cells were serum starved for 24 hours and samples for immunofluorescence microscopy images were processed as described in Methods. Plot, for each CS particle detected, of mean fluorescence intensity as a function of the distance to the centrosome. (B and C) The point corresponding to the data of each CS particle is colored with a 5% transparency. The more saturated the color chosen to illustrate the experimental condition is, more densely distributed are the data points in that area of the graph. (C) Color code of the two regions of B with more data point density: green corresponds to central region, cyan corresponds to distal region. See Results for further details regarding this classification.

Cells depleted of Cep164 show fewer changes in OFD1 CS density around the centrosome. There is also a variation in the OFD1 CS density around the centrosome profile, but it is more erratic, increasing and decreasing in the same scale during the length of the experiment. This behavior is the same if we consider the order of magnitude of the change: erratic fluctuations of the density profile around the centrosome. For ODF2-depleted cells, the density profile around the centrosome consists of a sharp drop (from a relatively small value) within 1 µm of radius around the centrosome and a plateau from there to 3 µm away, followed by a steady decrease as the distance to the centrosome increases further. In these cells, this unique distribution of the density of OFD1 CSs is maintained throughout the serum starvation process even though the total levels of OFD1 granules decrease during this period.

The density profile for PCM1 CS foci is shown in Figure 12. In contrast to OFD1, the density profile in control-depleted cells does not change during serum starvation. In Figure 12 it is also visible that in Cep164-depleted cells, the PCM1 density profile around the centrosome does not significantly change over time. However, the PCM1 foci density is much higher near the centrosome in Cep164-depleted cells than in control-depleted cells. Regarding cells depleted of ODF2, these cells have the lowest and shallower density profile around the centrosome of PCM1 CSs. ODF2 depletion is the only treatment that leads to a significative reduction in PCM1 CS density around the centrosome. This decrease happens in the first hours of serum starvation, and it is noticeable both close to the centrosome and in peripheral regions. In ODF2-depleted cells it is also noticeable that the drop in the density profile does no happen as a smooth transition for all time points as in control and Cep164-depleted cells, but it is more inconstant in a region between 1 and 3 µm away from the centrosome.

As for Cep290 CS density distribution around the centrosome profile, the results are presented in Figure 13. In the picture, we can see that in control cells there is a decrease and then an increase in CS density around the centrosome as the serum starvation stimulus progresses in time. As we have seen for PCM1 granules, Cep290 CS foci density is not so dynamic in Cep164-depleted cells as it is in control-depleted cells. In ODF2-depleted cells, the density values next to the centrosome are the lowest in all the experimental conditions, but they seem to have the same dynamics as control-depleted cells. Once again it is visible in ODF2-depleted cells that there is some CS density plateau between 1 and 3 µm away from the centrosome.

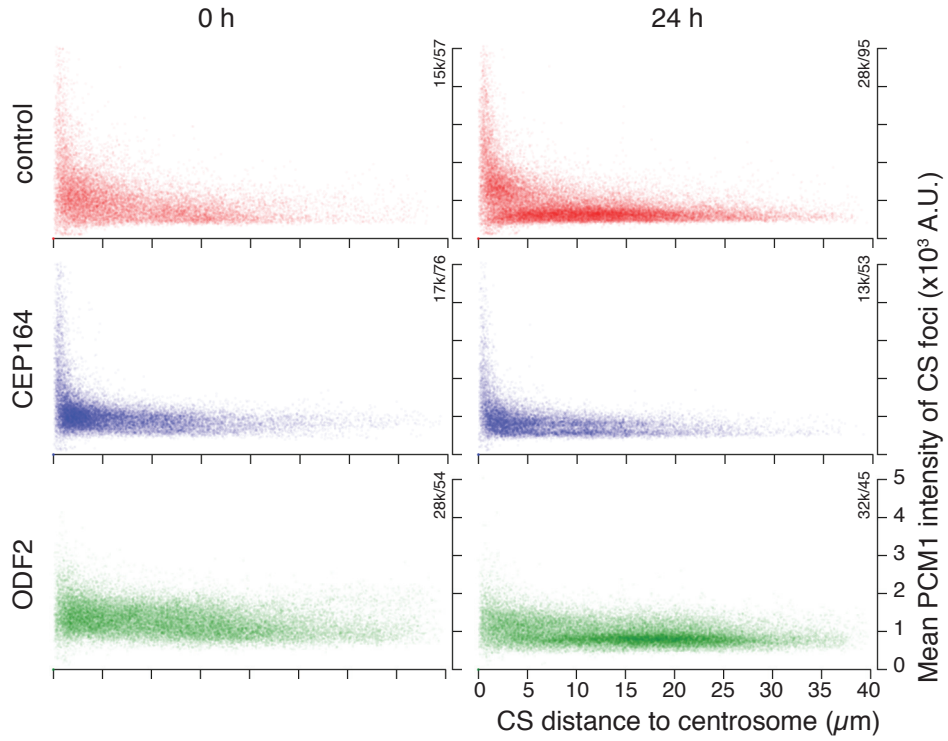

Figure 15: **PCM1 centrosome satellite fluorescence intensity vs. distance of CS foci to the nearest centrosome plot**. RPE1 cells, control, CEP164 and ODF2 depleted, were serum starved for 24 hours. Samples were taken before and after starvation and resulting immunofluorescence microscopy images were processed as described in Methods. For each CS particle detected, the mean fluorescence intensity is plotted as a function of the distance to the centrosome. The point in the graph corresponding to the data of each CS particle is colored with a 5% transparency so that the more saturated the color chosen to illustrate the experimental condition is, more densely distributed are the data points in that area of the graph. One representative experiment out of two is shown. Numbers on the upper right corner of the plots correspond to $N_{satellites}/N_{cells}$. k is equal to 1000.

However, for Cep290 foci in ODF2-depleted cells this plateau has two steps: the first from 1 to 2 µm and the second from 2 µm to 3 µm away from the centrosome.

III.II.VI. Central and peripheral centriolar satellites

Due to the randomness inherent to CS spatial localization and fluorescence intensity of each CS foci, I wondered if it was possible to unveil a level of information that relates these two variables and that is hidden from our visual perception by that same apparent randomness. In Figure 14, is shown the plot of the mean fluorescence intensity for PCM1 positive particles in function of the distance of that particle to its nearest centrosome. In Figure 14A we see that both, the brightest and the dimmest CS foci are localized near the centrosome and that as the distance to the centrosome increases, the intensity values of individual CS granules converge to a value different from zero. If as in Figure 14B, we make the single scatter plot dots 5% transparent so that as the data points stack over populated regions of the graph the saturation of the dot color increases. It is revealed another layer of information to the graph: the relative abundance of CS particles with a particular position and intensity. In Figure 14B we can see that the distribution of CS particles according to their distance to the centrosome and mean fluorescence intensity is not as homogeneous as Figure 14A would make us suppose. We can see that there are regions of the graph shown in Figure 14B where the values for the CS foci tend to accumulate. Others, in between these clustering areas, the data point density is more rarefied. In Figure 14C the two more distinct density regions are highlighted regarding the distance to

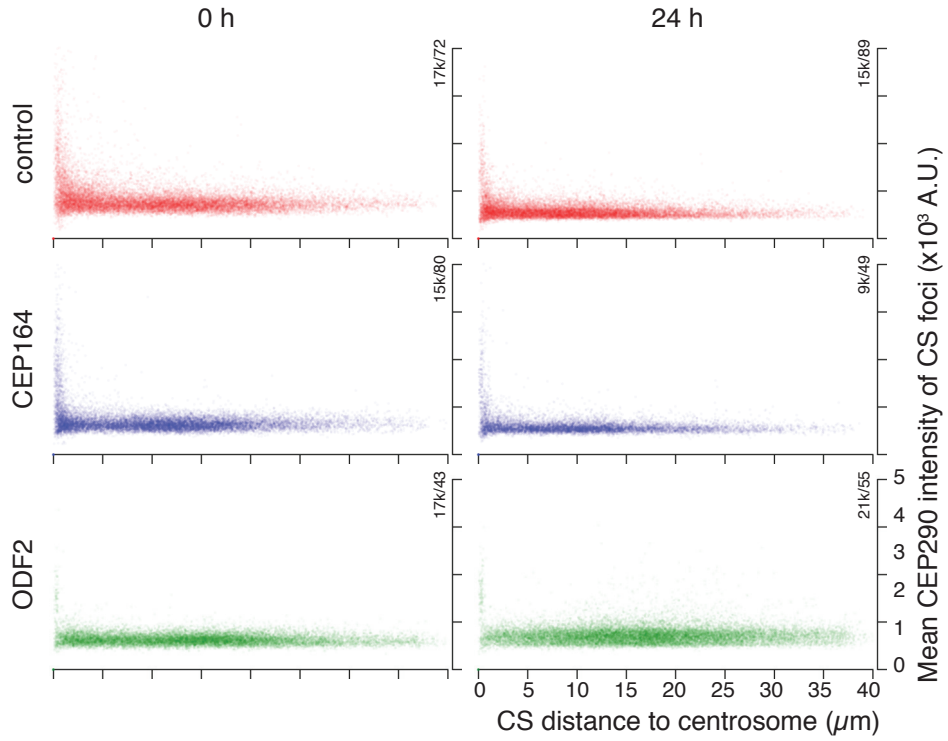

Figure 16: **CEP290 centrosome satellite fluorescence intensity vs. distance of CS foci to the nearest centrosome plot**. RPE1 cells, control, CEP164 and ODF2 depleted, were serum starved for 24 hours. Samples were taken before and after starvation and resulting immunofluorescence microscopy images were processed as described in Methods. For each CS particle detected, the mean fluorescence intensity is plotted as a function of the distance to the centrosome. The point in the graph corresponding to the data of each CS particle is colored with a 5% transparency so that the more saturated the color chosen to illustrate the experimental condition is, more densely distributed are the data points in that area of the graph. One representative experiment out of two is shown. Numbers on the upper right corner of the plots correspond to $N_{satellites}/N_{cells}$. k is equal to 1000.

centrosome vs. fluorescence intensity of individual CS foci. The green labeled dots in the graph of Figure 14C are near the centrosome, and I named them as "central" CSs. The fluorescence intensity values for this class of CSs vary from very low to very high. Labeled cyan in the same panel is the group of CS with relatively small and homogeneous fluorescence intensity values, that are evenly distributed throughout the cell area, and that I named "peripheral" CSs.

Using this data visualization tool, we can characterize the behavior of CS particles regarding their distance to the centrosome vs. mean fluorescence intensity during the serum starvation process that leads to cilia formation. In Figure 15 it is plotted the distance to the centrosome vs. mean fluorescence intensity for PCM1 positive CS particles in control, Cep164 and ODF2-depleted cells, before and after 24 hours of serum starvation. For control-depleted cells growing under serum rich conditions there is not a clear separation regarding central or peripheral CSs but once growth factors are removed the separation of these classes of CSs becomes more evident. Once serum starvation begins, the central and the peripheral group become more defined (data not shown) and as withdrawal continues up to 24 hours we can see in Figure 15 that the peripheral group increases in comparison to the central group. Cep164-depleted cells have a very well defined central group before they are subjected to serum starvation. Upon serum removal, Cep164-depleted cells tend to have more CSs that fall in the peripheral group classification but as time goes by this peripheral group of CSs never gets so preponderant as in control-depleted cells. One interesting feature of the central group of CSs in Cep164-depleted cells is the appearance of two bands that are noticeable at the time point

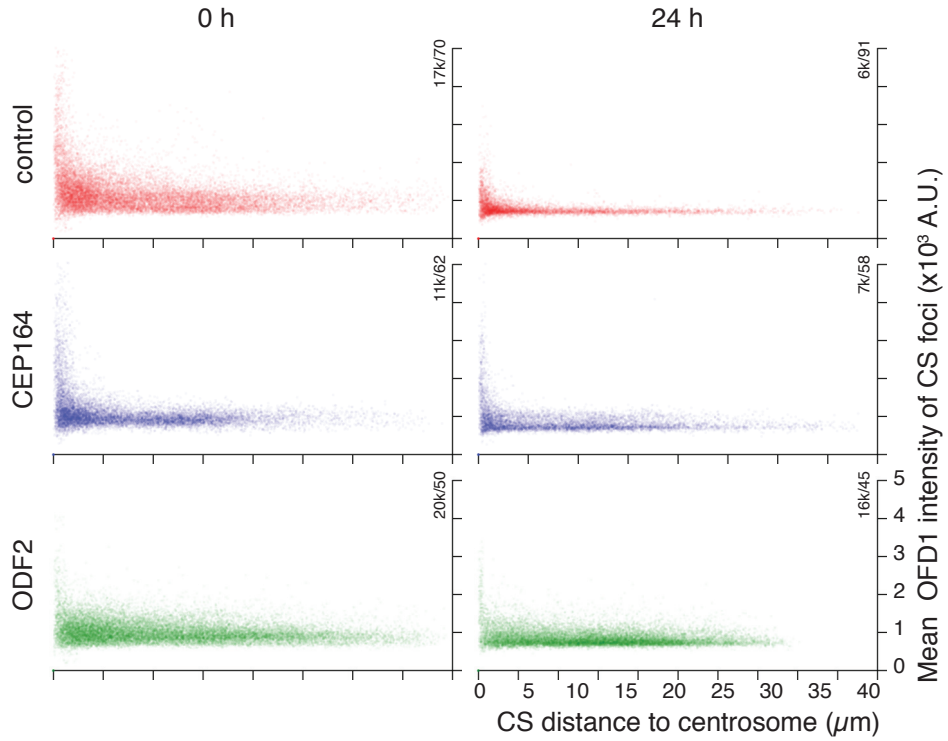

Figure 17: **OFD1 centrosome satellite fluorescence intensity vs. distance of CS foci to the nearest centrosome plot**. RPE1 cells, control, CEP164 and ODF2 depleted, were serum starved for 24 hours. Samples were taken before and after starvation and resulting immunofluorescence microscopy images were processed as described in Methods. For each CS particle detected, the mean fluorescence intensity is plotted as a function of the distance to the centrosome. The point in the graph corresponding to the data of each CS particle is colored with a 5% transparency so that the more saturated the color chosen to illustrate the experimental condition is, more densely distributed are the data points in that area of the graph. One representative experiment out of two is shown. Numbers on the upper right corner of the plots correspond to $N_{satellites}/N_{cells}$. k is equal to 1000.

corresponding to 24 hours after serum starvation. These lines suggest the existence of sub-pools of CSs that share the same localization in peripheral regions about the centrosome, but their intensity values tend to fall within two particular values. As for ODF2-depleted cells, the plot of the distance to the centrosome vs. mean fluorescence intensity of PCM1 positive CS presented in Figure 15 shows that in these cells there is a broad distribution of fluorescence intensity values irrespective of the distance to the centrosome. Contrary to what happens in control or Cep164-depleted cells, ODF2-depleted cells do not exhibit PCM1 CS foci with very high fluorescence intensity values near the centrosome. In ODF2-depleted cells, the enrichment of the peripheral group in proportion to the central group of CSs is only detected in late stages of serum starvation (Figure 15 and data not shown).

If we contrast Figure 16 with Figure 15 we find that for Cep290 CSs the distribution range for fluorescence intensity it is not as broad as it is for PCM1 CSs. Figure 16 shows that Cep290 CSs have similar gray values independent of the distance to the centrosome. As expected for a CS protein, there are more Cep290 positive particles close to the centrosome than in the cell periphery. The notable exception is when cells are ODF2-depleted and serum starved for 24 hours. In these conditions, the highest density of data points is no longer at small distances to the centrosome but has shifted to bigger distance values. Note however that in the plot of Figure 16 corresponding to the same conditions, we can see near the centrosome the remnants of the central CSs. Some of these data points that stand out because they have a higher intensity than the more abundant peripheral CSs correspond in fact to the centrosomal Cep290. If we compare the central CSs

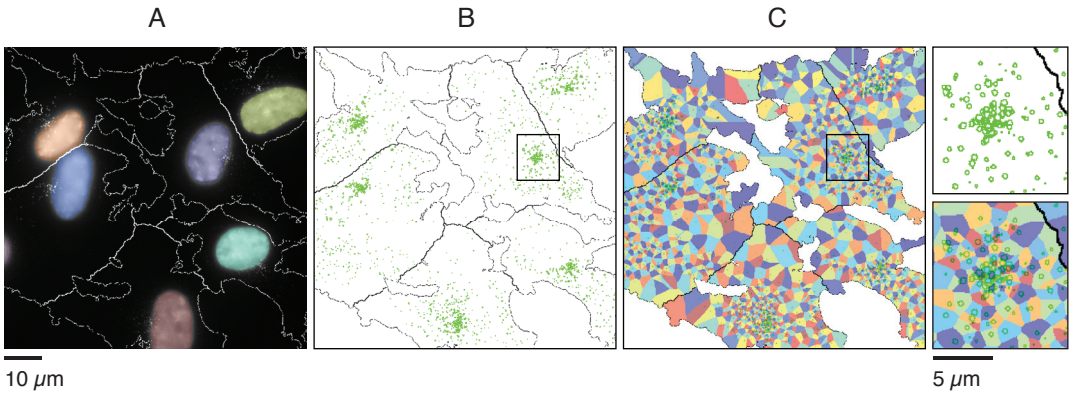

Figure 18: **Voronoi tiling of the cell area using centriolar satellites as seeds**. (A) representation of the cell area with different colored nuclei indicating the different cells; (B) cell areas and centriolar satellites used for Voronoi tiling; (C) binary image of the Voronoi tiling result. Regions within the black boxes are depicted with higher magnification on the right. The colors are used for illustrative purposes and were chosen arbitrarily by the software used for segmentation.

of the control-depleted cells and ODF2-depleted cells we conclude that the depletion of the sub-distal appendage protein does not influence the fluorescence intensity of centrosomal Cep290. The distribution of fluorescence intensity values for both conditions has the same magnitude range with similar maximums around 2 x103 A.U. and averages of 1.2 x103 A.U.

For OFD1 positive CS particles, we can see in Figure 17, that there is a sharp decrease in the total number of CS particles. In 70 cycling (0h) control-depleted cells I detected 16,698 CS granules whereas in 91 serum starved (24 hours) cells I detected 6029 CS foci. The dispersal of the fluorescence intensity values for the remaining CSs is largely reduced upon serum starvation. In the same panel it is visible that after 24 hours of serum starvation, most of the data points are localized close to the centrosome. The same transition from dispersal to a high concentration in the centrosome vicinity of OFD1 CS granules is also observed in cells depleted of Cep164 or ODF2 (Figure 17).

The methods of visualization and analysis of CS spatial context data here presented, the density profile and the intensity distribution around the centrosome, allowed to identify and distinguish different CS phenotypes of dispersal presented by cells with defective distal and sub-distal appendages.

III.II.VII.Quantification of CS dispersal using an entropy value

To score each cell with a single value corresponding to the degree of dispersal of the centriolar satellite particles, I borrowed the concept of Wiener entropy. WE is a measure of randomness that can be applied to the quantification of texture variation on speckled images (Woodhouse, 2001). It is defined as the ratio between the geometric and arithmetic means of a given set, and I borrowed it from the fields of digital audio signal processing and radar imaging (Aldaz, 2010; Tchernichovski et al., 2000; Woodhouse, 2001). Besides mathematical advantages, using entropy to quantify and describe the visual density of cellular structures facilitates the analysis of the results since cellular structures such as CSs that present themselves as having some local density usually have a higher degree of organization (lower entropy) than structures that appear evenly dispersed (higher entropy).

To calculate the WE of the CSs of each cell I propose a method that involves a Voronoi tessellation of the cell area using the CSs as seeds. A Voronoi tessellation is the division of a plane based on the distance to a particular set of points of that plane. Those unique points are called seeds, and the plane is divided ac-

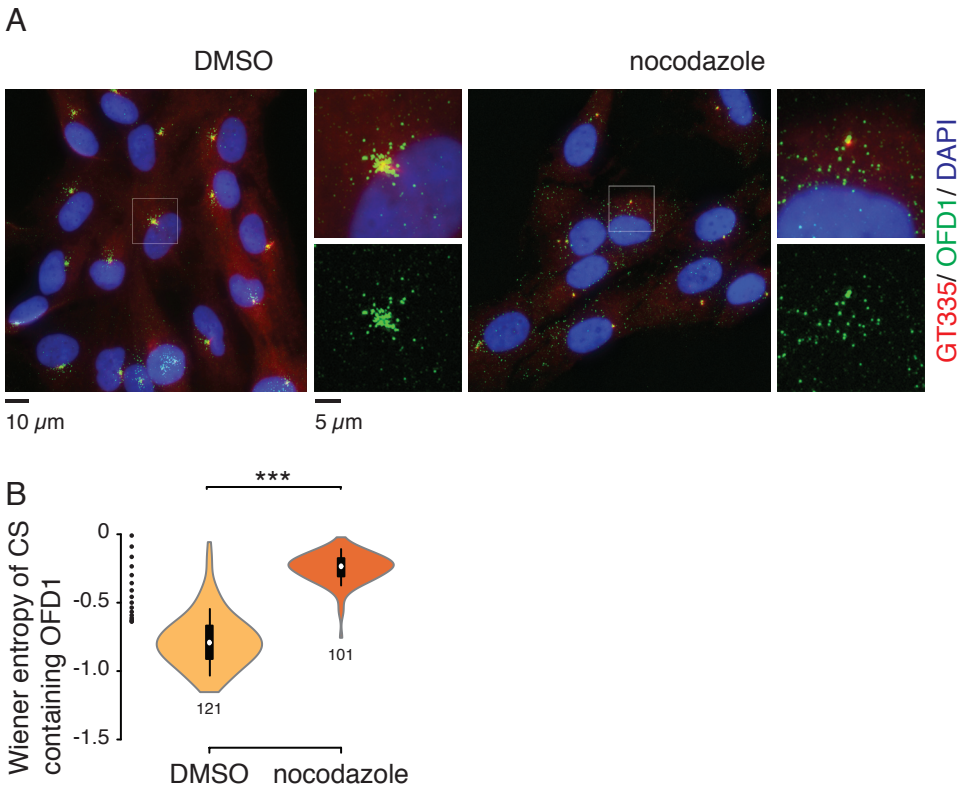

Figure 19: **Centriolar satellite dispersal caused by nocodazole treatment can be quantified in terms of Wiener entropy**. (A) RPE1 cells were serum starved for 24 hours and then treated with 6 μg/mL nocodazole or DMSO for 1 hour at 37 °C. After the treatment cells were fixed and stained for polyglutamylated tubulin (GT335), OFD1 and DAPI. Regions within the white boxes are depicted at higher magnification on the right. (B) violin plot of the Wiener entropy of the centriolar satellites containing OFD1 for cells either treated with DMSO or nocodazole. Diagram on the right side of the y-axis ilustrates the degree of dispersal. *** corresponds to $p<0.001$. Label under the violin corresponds to N. One representative experiment out of three is shown.

cording to the nearest-neighbor rule: each point is associated with the region of the plane closest to it (Voronoi, 1908). These areas around each seed are called tiles. In our case, the plane to be divided is the cell area and the seeds are the CS particles, both obtained by computational analysis from high resolution, high definition, micrographs. Having segmented the cells and CS (Figure 6B and C and Figure 18A and B) it was possible to create a Voronoi tilling of the cell area using the CS as input objects (Figure 18C). After performing the Voronoi tessellation, the area of each tile was measured, and the WE value for each cell was obtained by calculating the ratio of the geometric (GM) to the arithmetic (AM) mean of the area of the tiles in any given cell. If all the CSs were homogeneously distributed in the cell, that state of CS organization would correspond to the case where the entropy is at its maximum. In this situation, the area of the tiles obtained by Voronoi tessellation of the cell area would, by definition, be the same. In this case of maximum entropy, GM=AM and the highest value for WE is obtained. Other CS particle spatial distributions, where the homogeneity is lowered by bringing CS particles to be confined to smaller areas, have higher organization and therefore lower entropy. In these circumstances, the AM-GM inequality kicks in and GM will always be smaller than AM leading to WE values to be between 0 and 1. As CSs get close to each other, the space between the CSs that are in the center is smaller. At the same time, the space around the edge CSs gets bigger. The result is an increasing AM-GM inequality as the CSs are more concentrated, leading to lower values of WE. Given the properties of real numbers, the GM/AM ratio is not linear but tends to be compressed as the WE values tend to 0. The base 10 significant of the GM/AM ratio is used to expand the scale to be between 0

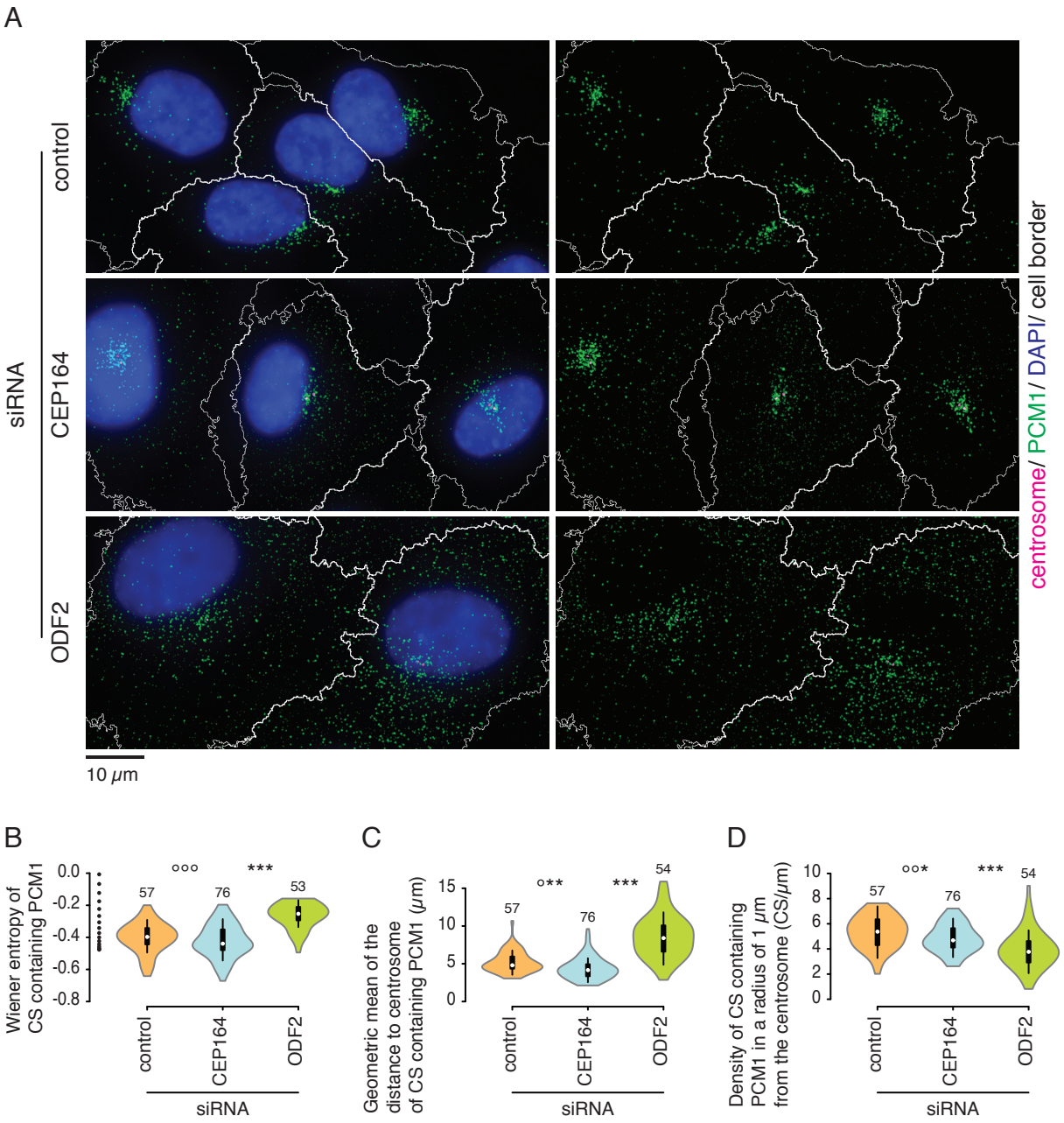

Figure 20: **Comparison of quantification of centriolar satellite dispersal by Wiener entropy, geometric mean distance to the centrosome and density 1 μm around the centrosome**. (A-D) RPE1 cells, treated with control, Cep164 or ODF2 siRNAs, were serum starved for 24h and stained for gamma-tubulin + polyglutamylated tubulin (GT335), PCM1 and DAPI. (A) transformed images used by the automated image analysis pipeline described in the Methods section. Due to high dynamic range, pixel intensity values of PCM1 are log transformed to allow the visualization of both the brightest and the faintest granules. (B-D) violin plot of (C) the Wiener entropy, (B) geometric mean distance to the centrosome and (D) density 1 μm around the centrosome of centriolar satellites containing OFD1. (B) Diagram on the right side of the y-axis ilustrates the degree of dispersal. (B-D) *** corresponds to p<0.001, °** corresponds to p<0.01, °°* corresponds to p<0.05, °°° corresponds to non statistically significant. Label over the violin is the value of N. One representative experiment out of two is shown.

and minus infinity (Tchernichovski et al., 2000). With this system of measurement, we know that the difference of 5 to 10 is the same as from 10 to 15 and can directly compare results obtained for CS distribution in different cells or treatments. Wiener entropy is a unit-less Pure number.

To demonstrate that this measurement can be used to distinguish between "clustered" and "uncluttered" CSs, I treated cells with either DMSO or nocodazole and imaged OFD1 containing CSs. Because of the association between CSs and microtubules (Dammermann and Merdes, 2002), nocodazole treatment is known to lead to the dispersal of several CS proteins (Kim et al., 2008; Lopes et al., 2011). We can see in

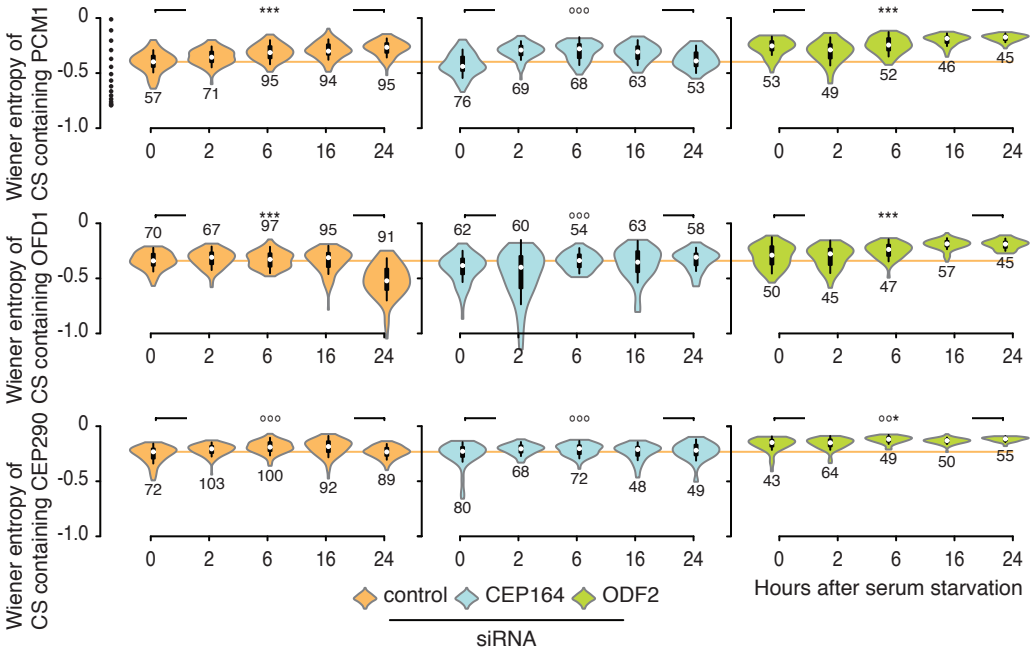

Figure 21: **Centriolar distal and sub-distal appendages have different roles in regulating centriolar satellite architecture dynamic upon serum starvation**. Violin plot of the Wiener entropy of PCM1, OFD1 and CEP290 centriolar satellites in RPE1 cells, treated with control, Cep164 or ODF2 siRNAs and serum starved for 24h. Samples were taken at the indicated time points and resulting immunofluorescence microscopy images were processed as described in Methods. Diagram on the right side of the y-axis ilustrates the degree of dispersal. *** corresponds to p<0.001, °°* corresponds to p<0.05, °°° corresponds to non statistically significant. The number on the head or at the foot of the violin is N. One representative experiment out of two is shown.

Figure 19A that in DMSO-treated cells, OFD1 positive satellites are concentrated around the centrosome whereas in cells treated with nocodazole the satellites are redistributed throughout the cytosol in an almost uniform way. Using the image analysis pipeline explained above, I calculated the WE for each cell. As shown in Figure 19B the WE of cells treated with nocodazole is much higher than the entropy of cells treated with DMSO.

To validate the WE value as a reliable indicator of CS organization around the centrosome I analyzed the dispersion of PCM1 CSs in cells depleted of control, Cep164 and ODF2 mRNAs. By doing this, I would be introducing perturbations to the organization of distal and sub-distal appendage of the mother centriole. I had preliminary indications that interference with Cep164 and ODF2 would induce differences in CS order that would be possible to distinguish using WE as a measurement. As seen in Figure 20A, cells lacking Cep164 do not have significant disruption of their PCM1 CS cellular layout when compared to control-depleted cells, but ODF2 depletion leads to a dramatic dispersal of the PCM1 CSs. I used an automated image analysis protocol to perform a comparison analysis of three different methods to quantify the degree of dispersal of the CS: the WE of the CSs, the geometric mean of the distance of each CS to the nearest centrosome and the density of CSs 1 µm around the centrosome (Figure 20B-D). Quantification shows that cells subjected to ODF2 depletion have a CS geometry with significantly higher values of WE than the control cells (Figure 20B). Both the mean distance of each CS to the nearest centrosome and the density of CSs 1 µm around the centrosomes are consistent with the WE quantification results shown in Figure 20B and to what is apparent in the micrographs of Figure 20A. Centriolar satellites of cells lacking ODF2 have higher mean distances to the closest centrosome than control cells (Figure 20C). Regarding the density of CSs near the centrosome, ODF2 cells have a significantly lower median value than control (Figure 20D). For

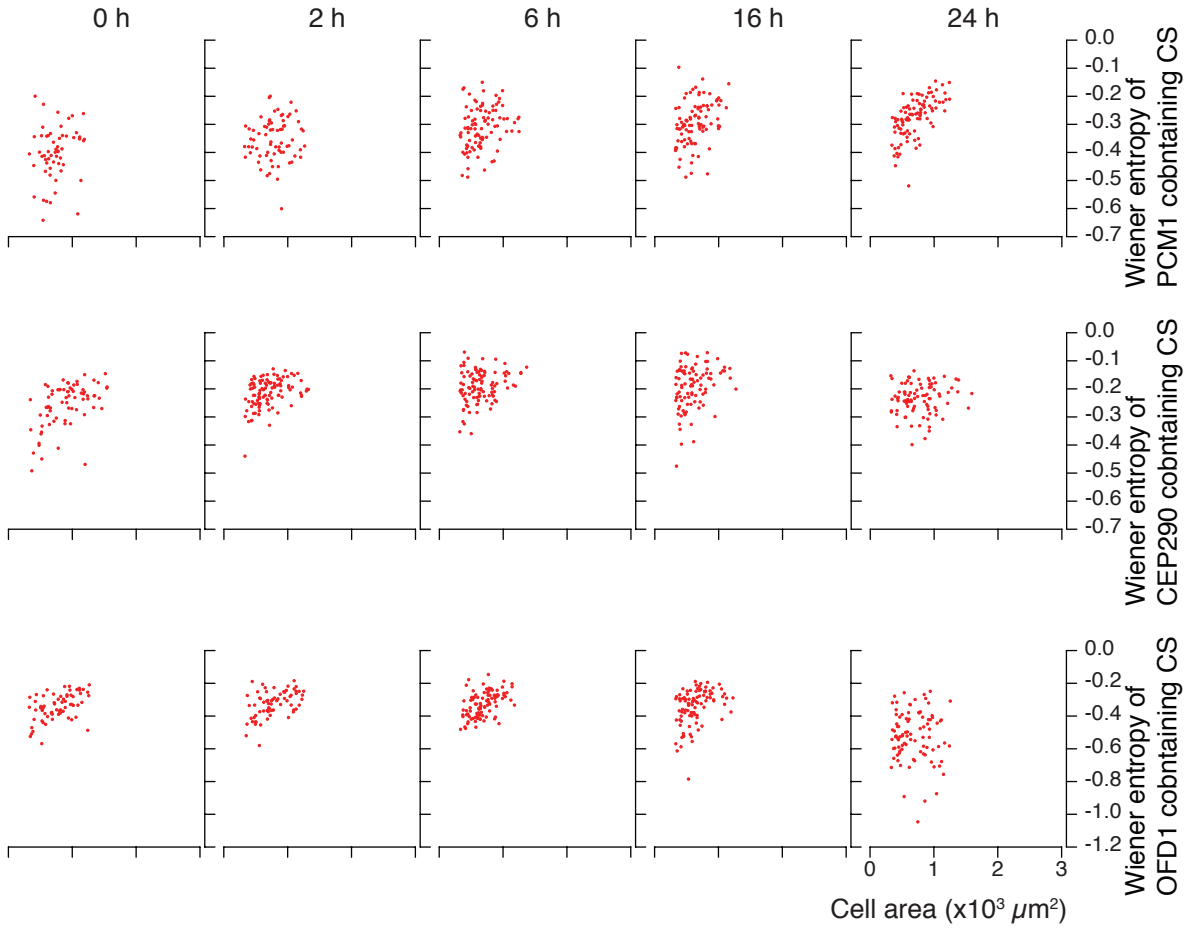

Figure 22: **Cell size and clustering of CS particles are not correlated in RPE1 cells**. (A and B) RPE1 cells, control, CEP164 and ODF2 depleted, were serum starved for 24 hours, samples were taken at the indicated time points and resulting immunofluorescence microscopy images were processed as described in Methods. (A) The data points plotted refer to the values for each cell of the cell area and Wiener entropy of CSs obtained by automated quantification. One representative experiment out of two is shown. $57<N_{PCM1}<95$, $72<N_{Cep290}<103$, $70<N_{OFD1}<97$.

Cep164, comparison of CSs clustering around the centrosome with control-depleted cells reveals a statistical difference between the two depletion conditions if we take the mean distance to the centrosome (Figure 20C) or the density next to the centrosome (Figure 20D) but not in WE (Figure 20B). This difference in results most likely reflects a property of WE that is its independence from a reference point (such as the centrosome in this case). This aspect will be discussed in more detail below (Discussion section of this chapter).

Considering how the depletion of Cep164 and ODF2 have opposite effects on CS localization patterns when cells are grown in serum rich conditions, I further investigated how the CS degree of dispersal evolved upon serum starvation. In Figure 21 we can see the evolution of WE values at different time points for different CS localized proteins after the cells were serum starved. We can see that as the cells adapt to the no serum conditions and undergo cilium formation, the dispersal of the different CS proteins varies differently according to the CS protein and with the integrity of the distal and sub-distal appendages. In control-depleted cells, the clustering around the centrosome of PCM1 granules decreases whereas OFD1 particles are found to be more concentrated around the centrosome. For control cells, Cep290 CSs do not appear to change much its degree of CS dispersal over time. The depletion of Cep164 does not lead to a significant difference in satellite dispersal compared to control cells in any of the considered CS markers in cells that are grown in serum rich conditions (t=0). However, opposed to what happens to control-depleted cells, the degree of dispersal of the PCM1 and OFD1 CS proteins changed little after Cep164-depleted cells were subjected to

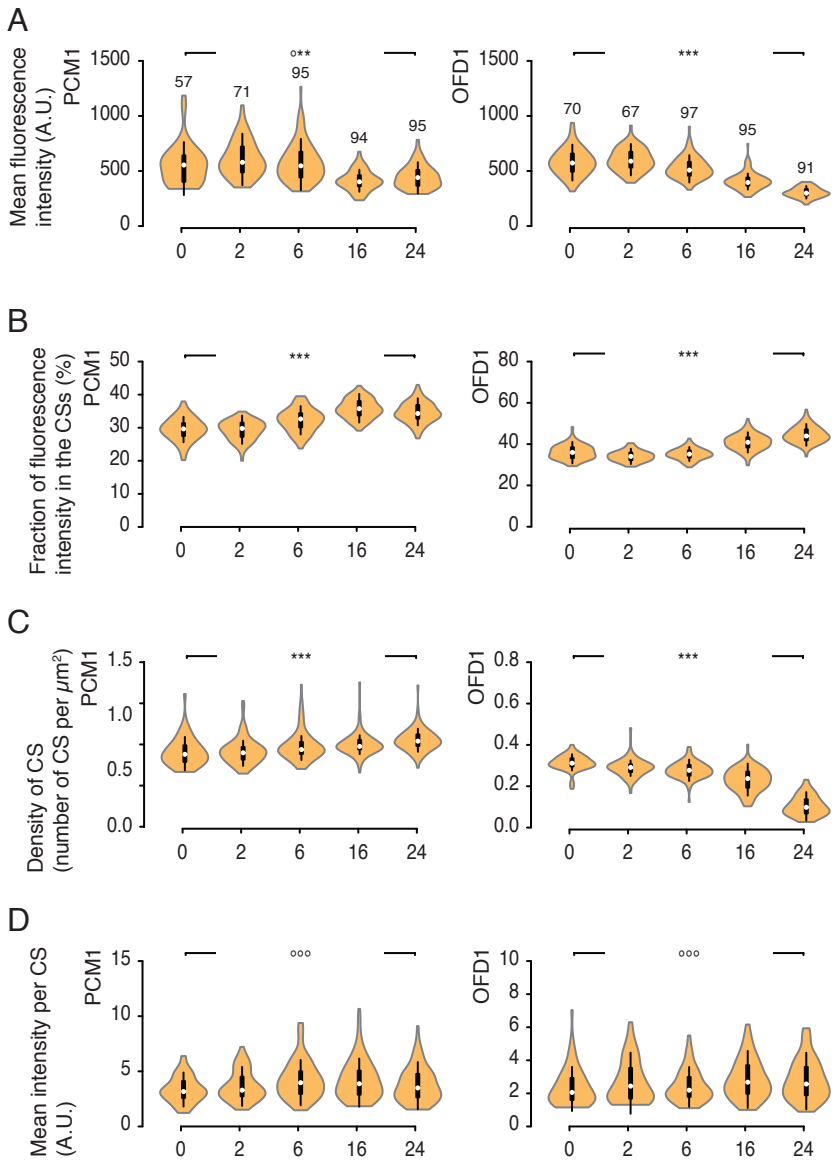

Figure 23: **Centriolar satellite architecture is dynamic upon serum starvation**. (A-D) RPE1 cells were serum starved for 24 hours, samples were taken at the indicated time points and resulting immunofluorescence microscopy images were processed as described in Methods. (A) violin plot of the mean fluorescence intensity of PCM1 and OFD1 in the whole cell. (B) violin plot of the fraction of the total intensity of PCM1 and OFD1 that is specifically localized at the centriolar satellites. (C) violin plot of the PCM1 and OFD1 centriolar satellites density per cell area. (D) violin plot of the mean intensity per PCM1 and OFD1 centriolar satellite granule. (A.U.) arbitrary units. *** corresponds to $p<0.001$, °** corresponds to $p<0.01$, °°°, not statistically significant. (A-D) values of N indicated on top of the violins of panel A. One representative experiment out of two is shown.

serum-free conditions. Regarding the importance of sub-distal appendage integrity for satellite organization, ODF2-depleted cells have a higher dispersion around the centrosome of PCM1, OFD1, and Cep290 and for all CSs markers the dispersal increases upon serum starvation.

To understand better the relation between CS proteins and cell size, I plotted, for each cell, the cell area in function of WE for that cell. The results are shown in Figure 22 and do not reveal any strong correlation between these two variables.

III.II.VIII.Application of the quantification to previously reported phenomena

Centriolar satellite architecture dynamics have been previously reported in the context of ciliogenesis, specifically regarding PCM1 (Kobayashi et al., 2014) and OFD1 (Tang et al., 2013). Kobayashi et al., report that in untreated RPE1 cells, the number of cells with PCM1 granules around the centrosome decreases gradually with the onset of serum starvation and increasing number of ciliated cells. This granule disappearance was not accompanied by a reduction in PCM1 levels in cell lysates, what suggests some reorganization of these proteins triggered by serum starvation which may govern or be governed by cilia formation. I observed that in untreated RPE1 cells, the mean fluorescence intensity of PCM1 decreased slightly during the 24 hours of serum starvation (Figure 23). However, as it is visible in the same column of Figure 23, the fraction of the PCM1 fluorescence signal that was detected in the CS increased. By segmenting the CSs and measuring the total cell size, I calculated the CSs density per cell. I found that during the serum starvation period the density of CSs increased (Figure 23). The growth in the ratio of PCM1 fluorescence signal in the CSs to the total PCM1 fluorescence is explained by the formation of new PCM1 containing CS particles and not by an enrichment of PCM1 in the CSs already present in the cell. This conclusion is supported by the fact that the mean intensity of each PCM1 containing CS did not change upon serum starvation. The explanation for the previously reported decrease in PCM1 granules around the centrosome can not be attributed to PCM1 protein degradation but instead to a rearrangement in CSs distribution around the centrosome. As previously shown in Figure 22, increase in WE for PCM1 CSs indicates that the CSs that contain this protein have a more dispersed structure after serum starvation.

Tang et al., document the autophagy-dependent degradation of OFD1 at the CSs upon serum deprivation and how OFD1 at the CSs degradation promotes cilia formation. Regarding OFD1 breakdown, I fond that OFD1 mean fluorescence intensity values drastically decrease after serum starvation (Figure 23), indicating that the OFD1 levels are indeed reduced in cells that underwent ciliogenesis. At the same time, as it is visible in the same column of Figure 23, the density of OFD1 granules in the cells drops to very low values (which is in line with what was previously published by Tang). Also, the fraction of the OFD1 fluorescence signal that is incorporated in the CSs increases. During the serum starvation process that leads to cilia formation, the levels of OFD1 per single centriolar satellite did not change (Figure 23). These methods give tools to the cell biologist that allow detecting CS behaviour in a spatial and timely manner.

III.III. Discussion

The use of automated image analysis to segment and extract high-content information of cilia, centrosomes and centriolar satellites captured in big immunofluorescence microscopy datasets allows to collect data of a large variety of variables such as fluorescence intensities, the number of features or geometric coordinates of those features. A large number of observations for each experimental condition lends robustness to hypothesis testing allowing to separate what is a population phenotype from minor variations inherent to the sampling process.

In principle, a large cell should have more CS particles than a small cell. The correlation between cell size and the number of CS particles (corrACS) measures how closely to the population average, the number of CS particles in one cell scales up with the cell size. This measurement can provide valuable information about CS integrity in a given population. Here I presented the corrACS for three CS proteins: PCM1, Cep290, and OFD1. It is remarkable that the number of CSs particles is linked to the cell size in such a fast manner. I found that the corrACS is not the same for all the CS proteins and moreover, it varies upon serum starvation. The corrACS increases upon serum withdrawal for PCM1 and at the same time decreases for OFD1 and Cep290. These corrACS changes are notable results since they show that even though PCM1 is believed to serve as the platform for CS particles, the composition of the particles is differently regulated depending on the CS protein. It begs the question of how this regulation is accomplished. Do PCM1 CS particles function as a platform for other CS proteins to be loaded and unloaded? Or does a PCM1-containing CS particle have a particular fixed composition such as the formation of new CS particles demands the degradation of old ones? Hopefully, when used for distinct CS proteins simultaneously, the corrACS can be used to know more about CS biogenesis, modification, and degradation. The observation that OFD1 corrACS drops significantly upon serum starvation is in agreement with the report that OFD1 CSs disappear during serum starvation-induced ciliogenesis (Tang et al., 2013). The decline in corrACS is explained by the fact that OFD1 CS particles dissipate regardless of the cell size.

My results suggest that ablation of the integrity of distal or sub-distal appendages of the mother centriole does not have an impact in the OFD1 corrACS when cells are in serum-rich growth conditions. However, once serum starvation starts, the corrACS falls apart. The change in OFD1 corrACS that is observed in control-depleted cells can not be reproduced in Cep164 and even less in ODF2-depleted cells. Since the cell sizes did not vary during the serum starvation process, this result implicates a role for distal and sub-distal appendages in OFD1 CS disappearance upon serum starvation.

As for PCM1 CSs, the corrACS drop observed for Cep164 but not for control or ODF2-depleted cells indicates that Cep164 has some role in the coupling of the cell size and the number of PCM1 positive CS particles a cell bears. The corrACS of PCM1 CSs is the same for control, and ODF2-depleted cells even though the cells of both groups have radically different sizes. We can thus conclude that the role of the sub-distal appendages in CS regulation does not touch the balance between CS number and cell size.

Not much change was observed in the corrACS of Cep290 positive CS particles during the serum starvation process either for control or distal/sub-distal deficient cells. From these results, we can conclude that Cep290 loaded CS particles do not share the same fate of OFD1 positive particles. Is it because Cep290 and OFD1 never share the same PCM1 platform and only the OFD1 loaded particles are degraded, or it is because OFD1 is selectively subtracted to the PCM1 scaffold? Single-molecule approaches such as

Förster resonance energy transfer (FRET) or live-cell imaging with single particle tracking could be useful for answering these questions.

To have a more clear picture of CS organization, we need to take into consideration more than just the number of CSs in a cell. We also need to know how are the CSs particles distributed around the centrosome. Here I smooth out the inherent to CS density variation by averaging, for all the cells in a given condition, the CS density values in concentric rings, 0.5 µm of radius around the centrosome. By applying a natural cubic spline function to an interpolating line between the data points, it was possible to represent the CS particle density in function of the distance to the nearest centrosome. The resulting profile synthesizes how the CS density of a given CS protein drops around the centrosome. The resulting diagram allows evaluating in an unbiased and quantitative way if the CS particles are more concentrated or dispersed around the centrosome, if there are any plateau regions or if the drop fits a linear, exponential, or power function. This information will be useful for modeling purposes and model formulation considerations. Here I found that, in serum rich conditions, the empirical distribution of OFD1 CSs in cells subjected to a control mRNA depletion is best approximated by a power law of the form:

$f(x)=x^P$ where P is constant.

With this tool, I analyzed the impact of interfering with the distal or sub-distal appendages on the CS profile around the centrosome for different CS proteins during the serum starvation process that leads to ciliogenesis. For OFD1 containing CSs in control-depleted cells, as previously observed and reported (Tang et al., 2013), there is a significant drop in CS density throughout the serum starvation process. The overall shape of the curve did not change much during the starvation process (Figure 11) except for the last time point (24 hours) where the density away from the centrosome suffers a sharp drop. This change in density profile shows that, in control-depleted cells, at the final stages of ciliogenesis there is not just an overall decrease in OFD1 CS density but that the edge of the CS cloud is closer to the centrosome.

Depletion of Cep164 leads to a lack of response of the cell regarding OFD1 CS degradation once the cell is subjected to serum starvation. I register fluctuations in OFD1 levels but not of the magnitude and direction observed for control-depleted cells. Consistent with results presented in Chapter 2, probably the OFD1 role in promoting ciliogenesis is only put into play after the ciliary vesicle docking step is realized. When Cep164 is not present, vesicle docking to the mother centriole is not possible, and therefore the cell does not progress to further stages of cilium assembly, in this case, OFD1 CS degradation.

The profile of OFD1 CSs in ODF2-depleted cells is somehow unique because it unveils the existence of a CS density plateau between 1 and 3 µm from the centrosome. This observation would be impossible to achieve without the image analysis processing presented here. The biological significance of this plateau is hard to ascertain, but its appearance invites to revisit the study of CSs using EM, this time with state of the art fixation techniques that have significantly evolved since the 1970s in their ability to preserve the specimen.

The profile obtained from the analysis of CSs stained against PCM1 showed these to be more static than the previously analyzed OFD1 CSs for control, and Cep164-depleted cells but not for ODF2-depleted cells. Cells lacking ODF2 and subjected to serum starvation show a rapid response to the withdrawal stimulus. Also, the density levels of PCM1 CSs drop in the middle of the cell, that is, between 1 and 3 µm from the centrosome. It is, therefore, tempting to speculate that this region between 1 and 3 µm, outside the inner

realm of the centrosome, may represent a critical stage where CS regulation takes place in cells devoid of ODF2. This result shifts the focus of analysis of CS control away from the centrosome and suggests that CS can be modulated not only from the centrosome but also from the cell periphery.

It is important to take into consideration the fluorescence intensity of the individual CS particles and how is it correlated with the distance from the centrosome to complement the information that was gathered so far concerning the spatial organization of the CSs. I wanted to know if behind the manifest noisy localization, hides some order regarding CS particle size, more precisely, if the size distribution of the CS is uniform or it has steps or optimal values, a consequence of CS structure. I used fluorescence intensity as a proxy measurement for CS particle size since CS particles are smaller than the diffraction limit of light microscopy. Regardless of their real size, the point spread function (PSF) of CS particles minor than 200 nm in size will always have the same dimensions. On the other side, the fluorescence intensity of that PSF is related to the number of epitopes the secondary antibodies labeled with fluorescent probes that originate that PFS can recognize. And larger CS particles, more CS protein, more epitopes, more secondary antibodies, more fluorescent probes and presto: more fluorescence intensity. To better understand this aspect of CS biology, I plotted the mean intensity of each CS particle as it was detected by the image analysis pipeline in all the cells in a given condition in function of the distance of that particle to the centrosome. By using the transparency of the data points in the representation, we were able to discern that there are different regimes of intensity and distance to the centrosome of CS particles, namely, a central group of CSs and a peripheral group of CSs. The central group of CSs has a wide intensity distribution, but it is confined to about 5 μm from the centrosome whereas the peripheral group has a limited fluorescence intensity range but is spatially distributed throughout the cell.

For PCM1 CSs we observed that in control-depleted cells grown in serum rich conditions the central and peripheral groups of CSs are indistinguishable, but upon serum starvation, the separation between these two regimes of fluorescence intensity vs. the distance to the centrosomes becomes more apparent. This remodeling indicates a radical change in PCM1 CS character that was not obvious either by looking at the cells or by using the previous methods so far described. It principally shows that in control-depleted cells subjected to 24 hours of serum starvation, the peripheral PCM1 CSs fluorescence intensity falls into a single range of values with apparently a normal distribution. In the case of Cep164-depleted cells, 24 hours of serum starvation leads to the dissolution of a clearly defined central group of PCM1 CSs into a two banded peripheral group of CSs. This result indicates that upon Cep164 depletion followed by serum starvation, the PCM1 peripheral CSs size tends to fall into two discrete categories. Considering that control cells responded to the serum starvation stimulus by enriching themselves with peripheral PCM1 CSs of a unique size, we can conclude that Cep164 has an influence on the particle size of PCM1 CSs that are way from the centrosome and distributed throughout the cell periphery. Cells depleted of ODF2 and grown in serum rich medium have much less PCM1 CSs near the centrosome when compared control-depleted cells. On the other side, Cep164-depleted cells have much more. Is this an indication that the distal appendages of the mother centriole are necessary for PCM1 CS movement away from the centrosome whereas the sub-distal appendages are essential for CS movement to the centrosome? The answer to this question could be obtained through live-cell imaging.

If we use the same diagram to plot the results obtained for Cep290 CSs, we conclude that for this protein the fluorescence intensity values per CS particle are much more restricted than for PCM1 CS particles. For control, Cep164 and ODF2-depleted cells the results are similar and show that in these cells the intensity of Cep290 CSs is uniform throughout the cell and that are rare bright CS particles close to the centrosome, as was the case for PCM1 CSs. The implication of this result is that even tough PCM1 CS scaffold particles can have different sizes, the amount of Cep290 loaded into them is not proportional to the amount of PCM1 in the particle. Naturally, this analysis does not constitute a definitive proof for this hypothesis, but biochemical, immunofluorescence microscopy and live cell imaging experiments could provide useful additional data in its support or against it. An extreme case of CS dispersal is Cep290 CSs in ODF2-depleted cells subjected to serum starvation since, contrary to what happens to control or Cep164-depleted cells, the highest density of CS particles does not occur close to the centrosome but in the cytoplasm. For Cep290 CS particles, Cep164 does not seem to play a significant role in its size or spatial distributions since its CS particle mean fluorescence intensity vs. distance to the nearest centrosome plot data point cloud is identical to that of control-depleted cells under the same serum conditions.

We could see that regardless of being depleted of Cep164 or ODF2, RPE1 cells respond the same way (even if the intensity is not the same) to serum starvation concerning the size and localization of OFD1 loaded CSs: there are more particles with lower intensity values and more concentrated near the centrosome. This result is consistent with what was previously reported (Tang et al., 2013) and presented in this thesis: most OFD1 CS particles are degraded upon serum starvation at the same time that the ones that resist degradation are more concentrated close to the centrosome.

Another way to summarize the data for comparison and interpretation is to refer to CS dispersal as a value in a scale of dispersion.To my knowledge, very few studies used Voronoi tessellations to quantify spatial density as I did here. Even those that used it did it either for graphical representation purposes (Cauda et al., 2012; Prodanov et al., 2007) or (spatial) data clustering determination (Andronov et al., 2016; Levet et al., 2015). In most cases, the estimation of local densities has been done using Ripley's L function. However, it is a computing intensive method and impractical to perform in sizeable datasets. Moreover, since there is the irregular cell border to take into account when it is time to perform the necessary edge correction, using Ripley's L function to obtain a value per cell that quantifies how dispersed the CSs are is not a straightforward process (Andronov et al., 2016; Jafari-mamaghani et al., 2010; Kiskowski et al., 2009).

Comparison of CSs WE between control and Cep164 indicates that depletion of the distal appendage protein does not have a major effect (Figure 20B) but what we see in Figure 20A may suggest otherwise. It is arguable that cells Cep164-depleted have CSs more tightly clustered to the centrosome than control-depleted cells, and the WE measurements are failing to detect it, but that is not what is happening. The difference in CS dispersal in not quantitative but qualitative: as CSs are repositioned in the cell, small, local clusters can be formed independently of the centrosomes as is visible in Figure 20A and as was previously reported (Kim et al., 2008; Stowe et al., 2012). The local decrease in entropy caused by these many small clusters balances the large entropy increase that occurs next to the centrosome. That is why the CSs cellular layout difference, measured as WE, between control and Cep164-depleted cells is not significant. This apparent paradox highlights one interesting property of WE to quantify CSs disposition in the cell: its independence from a reference point. Besides the computational challenges of determining centrosomal coordinates and

calculation of a broad array of distances, analyzing CS dispersal in the cell having the centrosome as the only reference point can lead to misinterpretation of biological data by not taking into consideration the overall cellular arrangement of CSs. The independence of WE from a reference point can be an advantage in other applications when it needs to be quantified the degree of clustering of cellular structures visible as spots in fluorescence microscopy. These structures include lysosomes, chromosomal centromeres or mitochondria, among many others, where there is no clear reference point around which these cellular structures are clustering.

When we use WE to follow how CS dispersal changes during serum starvation we find that different CS proteins behave differently and not all of them follow the same tendencies as the CS scaffold protein PCM1. In control-depleted cells, PCM1 CSs are more dispersed during serum starvation whereas OFD1 CSs get more concentrated around the centrosome and Cep290 CSs dispersal status does not change. According to the CS paradigm, interaction with PCM1 is a condition sine qua non for a protein to be considered a CS protein (Bärenz et al., 2011; Hori and Toda, 2016; Tollenaere et al., 2015). However, we observe changes in some CS proteins dispersal that are in the opposite direction of what happens to PCM1, as is the case of OFD1 or do not follow the changes in PCM1 cellular distribution, as is the case for Cep290. These changes in opposite directions of the dispersal of CS proteins imply first that there are CS particles that have distinct compositions and second that CS structure regarding the proteins that are assembled in one CS particle can be modulated. One example of such modulation is the disappearance and higher concentration around the centrosome of OFD1 particles to allow cilia formation. Centriolar satellites in cells depleted of Cep164 do not change their WE throughout serum starvation, therefore implicating once again Cep164 or distal appendage integrity in CS distribution. Also implied in CS cellular distribution but in the opposite direction is ODF2 or sub-distal appendage integrity. In cells depleted of ODF2, all the CS proteins here analyzed had an increase in their WE and therefore in their dispersal throughout the cell.

Changes in protein composition of the CSs can prove challenging to measure using the traditional immunoblot method since detection in small changes of protein make-up, in this case of CSs, can be masked by the heterogeneity of the sample. To overcome this problem, I propose a single cell based analysis where instead of measuring all the sample, the protein composition and localization is measured by high resolution and high definition microscopy allied to automated image analysis procedures. Using such techniques as here described, I revisited some previous reports related to CSs dynamics during the serum starvation process. Regarding the claims of Kobayashi et al. (Kobayashi et al., 2014), we observed that the mean intensity of each PCM1 containing CS did not change upon serum starvation. We can conclude that the increase in the ratio of PCM1 fluorescence signal in the CSs to the total PCM1 fluorescence is explained not by an enrichment of PCM1 in the CSs already present in the cell but by the formation of new PCM1 containing CS particles. The explanation for the previously reported decrease in PCM1 granules around the centrosome can not be attributed to PCM1 protein degradation but instead to a rearrangement in CSs distribution around the centrosome. Regarding CS OFD1 degradation reported by Tang et al., we were able to confirm that there is not only a decrease in OFD1 fluorescence signal upon serum starvation, but there is also a reduction in the number of OFD1 CS particles per unit of area of the cell. At the same time, it is interesting to observe that from the OFD1 that is still in the cell after 24 hours of serum starvation there is a higher fraction of OFD1 in the CS particles than before the cells were subjected to serum-free conditions. At least in RPE1

cells, contrary to what was reported for mouse embryonic fibroblasts (MEFs) (Tang et al., 2013), OFD1 CS do not completely disappear from the vicinity of the centrosome. Using the image analysis here described I were able to replicate results and conclusions previously obtained by other studies and were able to provide new tools that hopefully will enable further exploration of CS biology and its understanding.

IV. Chapter 2: MARK4 at the crossroads of autophagy and ciliogenesis

IV.I. Introduction

IV.I.I. Regulation of autophagosome formation

Eukaryotic cells have vesicular organelles specialized in bulk digestion using hydrolytic enzymes that are called lysosomes. The substrates of the lysosome are delivered to it either from the cell exterior, as is the case of a phagocytized bacterium or from within the cell, as it happens during stress or starvation. Cells recognize changes in the cell context and respond by engulfing organelles or dysfunctional protein complexes to be delivered to the lysosome for degradation in double-membrane vesicles, called autophagosomes. This process is called macroautophagy (henceforward referred to as autophagy). The process of autophagosome formation is initiated at the phagophore assembly site (PAS in Figure 24) also known as isolation membrane where the uncoordinated-51-like kinase (ULK) complex and the class III phosphatidylinositol-3-kinase (PI3K) assemble. At the PAS, the activated ULK complex, composed of ULK1 or ULK2, autophagy-related protein (ATG) 13, FAK family kinase interacting protein of 200 kDa (FIP200) and ATG101, stimulates the class PI3K complex (also known as Beclin 1 complex). The Beclin 1 complex (composed of vacuolar protein sorting 34 (VPS34), protein of 150 kDa (p150), Beclin 1 and ATG14), promotes the production of an autophagosome specific pool of phosphatidylinositol 3-phosphate necessary for phagophore nucleation. Autophagosome expansion is achieved by the action of the ATG12-ATG5-ATG16 complex that is recruited to the phagophore

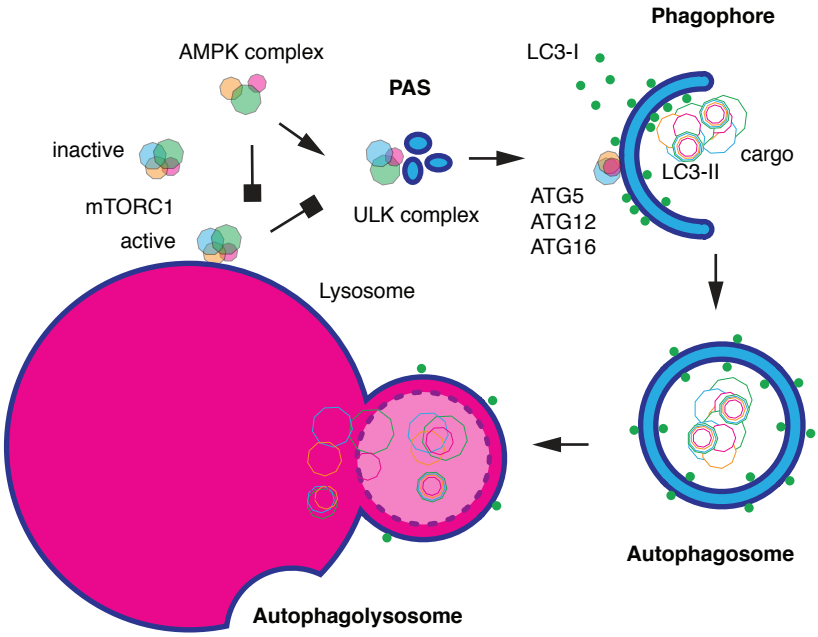

Figure 24: **The mammalian autophagy pathway**. Macroautophagy initiation starts at the phagophore assembly site (PAS) with the activation of the ULK complex by the AMPK kinases. Subsequent phagophore membrane elongation requires that the ubiquitin-like conjugation complex formed by ATG5, ATG12 and ATG16 converts cytoplasmic LC3-I in membrane bond LC3-II. LC3-II interacts with the cargo to be engulfed in the autophagosome that is delivered to the lysosome forming the autophagolysosome where the cargo is recycled into its carbohydrate, protein and lipid constituents. The mTORC1 is active when it localises at the lysosome and inactive when is cytosolic. When active, it inhibits the ULK complex and therefore autophagy. The AMPK complex activates autophagy by contracting mTORC1's inhibition and activating the ULK complex. Adapted from Kaur, J. & Debnath, J. Autophagy at the crossroads of catabolism and anabolism. Nature reviews. Molecular cell biology 16, 461–472 (2015) and Stolz, A., Ernst, A. & Dikic, I. Cargo recognition and trafficking in selective autophagy. Nature cell biology 16, 495–501 (2014).

membrane where it functions as an E3-like ligase and conjugate phosphatidylethanolamine to the microtubule-associated protein 1 light chain 3 (LC3) protein. LC3 exists in two forms: LC3-I that is soluble in the cytoplasm and LC3-II that is tightly associated with the autophagosomal membrane. By interacting with cargo and cargo-adaptor proteins, LC3 recruits autophagy substrates into the autophagosomes for degradation (Kaur and Debnath, 2015; Lamb et al., 2013; Stolz et al., 2014).

The bulk digestion of intracellular components achieved by the autophagic process plays a critical role in nutrient mobilization and hence an important part in the control of cellular metabolism and homeostasis. Currently, it is believed that the regulation node where coordination between autophagic activity with nutrient levels and proliferation cues occurs is the interaction of ULK, AMP-activated protein kinase (AMPK) and mammalian target of rapamycin (TOR) complex 1 (mTORC1) complexes.

The TOR kinase was first identified as the target of the anti-fungal drug rapamycin that inhibits the growth of *Saccharomyces cerevisiae* (Heitman et al., 1991). A highly conserved kinase, the mammalian version mTOR, exists in two complexes with related but distinct functions. mTORC1 regulates cell growth through coordination of protein anabolism, nucleotide biogenesis, lipogenesis, glycolysis and autophagy, and mTORC2 that controls cell growth through regulation of lipogenesis, glucose metabolism, actin cytoskeleton and apoptosis (Betz and Hall, 2013). In an amino acid (a.a.) rich environment, mTORC1 is recruited to the lysosome by activated Ras-related GTP-binding protein (Rag) GTPases dimers (Sancak et al., 2008, 2010). There, mTORC1 binds Ras homolog enriched in brain (Rheb) to form an active holoenzyme (Inoki et al., 2003a; Tee et al., 2003). Upon a.a. deprivation, the Rag dimers are switched to an inactive conformation that no longer keeps mTORC1 at the lysosomal surface (Kim et al., 2008a). It is believed that this loss of interaction with active Rheb renders the mTORC1 complex inactive (Demetriades et al., 2014). When cells are under optimal growth conditions, mTORC1 complex phosphorylates the autophagy promoter ULK kinase, preventing the formation of the ULK complex and therefore autophagy initiation (Ganley et al., 2009; Jung et al., 2009; Kamada et al., 2010; Kim et al., 2011; Utani, 2010).

As its name indicates, AMPK is a sensor of intracellular levels of adenosine nucleotides that activates its kinase domain when there is a decrease in the ATP to AMP and ADP ratio (Alers et al., 2012; Hardie et al., 2012; Mihaylova and Shaw, 2011). Being ATP the energy source of the cell, AMPK is an energy-sensing kinase complex that activates catabolic processes such as glucose uptake and metabolism at the same time that inhibits several anabolic pathways such as protein, carbohydrate and lipid biosynthesis (Hardie, 2007). Several studies were able to confirm the direct interaction between AMPK and ULK1 and the positive effect on the ULK1 activity of AMPK phosphorylation (Egan et al., 2011; Heitman et al., 1991; Lee et al., 2010; Shang et al., 2011). The fact that AMPK phosphorylates the mTORC1 subunits Regulatory-associated protein of mTOR (Raptor) and Tuberous Sclerosis Complex 2 (TSC2) rendering the kinase complex inactive (Gwinn et al., 2008; Inoki et al., 2003b) and hence unable to repress UKL1, gives prominence to AMPK as a regulatory keystone of autophagy.

Besides the regulation of autophagy in response to nutrient levels, cellular quality control and homeostasis is another important function of autophagy that needs to be tightly controlled by the cell. Even in situations where the cell does not have nutritional or energetic constraints, a basal level of autophagy is always observed (Kraft et al., 2010; Murrow and Debnath, 2012). Murine models with a tissue-specific knockout of Atg5 or Atg7 accumulate abnormal mitochondria and ubiquitinated protein aggregates in those tissues

(Ebato et al., 2008; Komatsu et al., 2005; Mizushima and Hara, 2006; Raben et al., 2008). Therefore, two types of autophagy have been defined: basal autophagy that is responsible for cell maintenance and homeostasis, and inducible autophagy that occurs when the cell is subjected to an acute stress event such as nutrient deprivation (Kraft et al., 2010; Murrow and Debnath, 2012).

Conserved mechanisms have evolved to concentrate, in a microtubule-dependent manner (Kimura et al., 2008), cytoplasmic aggregates that can cause cell toxicity. These aggregates concentrate at a special cell location in the vicinity of the centrosome that is called the aggresome (Chung et al., 2001; Corboy et al., 2005; Webb et al., 2004), where the autophagic machinery gets recruited for its disassembly (Chin et al., 2010; Iwata et al., 2005a, 2005b). The localization and coordination of the autophagosomes and lysosomes have been shown to be regulated and central for the proper function of this cellular scrap yard (Korolchuk et al., 2011; Zaarur et al., 2014).

IV.I.II. Autophagic regulation of ciliogenesis

Autophagy and ciliogenesis have been showing to be functionally related (Lam et al., 2013; Orhon et al., 2016; Pampliega et al., 2013; Tang et al., 2013). The current understanding is that basal and inducible autophagy have distinct substrate specificities. Basal autophagy represses cilia biogenesis by degrading ciliary components, whereas induced autophagy promotes it by degrading ciliogenesis inhibitors. Serum starvation of cultured cells is a stimulus used to study these two apparently unrelated phenomena: ciliogenesis and autophagy. Both for autophagy studies and ciliogenesis essays, the removal of the animal serum present in the growth medium of cultured cells is the method we use to bring about our subjects of investigation. It is thou somehow unsurprising that both phenomena are related. According to Orhon et al. (Orhon et al., 2014), when cells grow in serum rich medium, basal autophagy represses ciliogenesis by degrading IFT20 (Pampliega et al., 2013). According to these authors, this basal degradation of an essential component for ciliogenesis is the mechanism through which basal autophagy keeps ciliogenesis in check. On another publication, Tang et al. (Tang et al., 2013) provide an alternative and possibly complementary explanation for the role of autophagy in ciliogenesis that involves the interaction of the protein OFD1 with LC3. The mentioned article reports that in MEFs, the OFD1 pool that specifically localizes at the CSs is degraded by autophagy and the failure to do so by $Atg^{-/-}$ cells is the cause for the probability to be ciliated 24 hours after serum starvation to be lower in these cells than in WT. Reinforcing the idea that the undegraded upon serum starvation CS pool of OFD1in $Atg5^{-/-}$ MEFs is the culprit of these cells cilia formation defect, Tang et al. achieve the rescue of ciliogenesis by ectopically degrading OFD1's CS pool using RNA interference. On a later review, Orhon et al. (Orhon et al., 2014) try to conciliate the two mechanisms by proposing that upon serum withdrawal, starvation-induced autophagy is activated and its substrate specificity is shifted from IFT20 to the OFD1 pool that localizes in the CSs. The effects of this substrate specificity change seem to enable cilia formation: IFT20 is not degraded and can incorporate the IFT-B complex whereas the CS pool of OFD1 is degraded and its inhibitory role in ciliogenesis is dissipated.

IV.I.III.MARK4's role in autophagy and ciliogenesis

The microtubule-associated protein (MAP)/microtubule affinity regulating kinase 4, MARK4 (Kato et al., 2001; Kuhns et al., 2013; Rovina et al., 2014; Trinczek et al., 2004), has been found to be implicated both

in ciliogenesis (Kuhns et al., 2013) and in inducible autophagy (Zaarur et al., 2014). Regarding ciliogenesis, depletion of MARK4 negatively affects the loss of the CP110-Cep97 complex from the basal bodies at the same time that vesicle attachment to the mother centriole does not appear to be affected (Kuhns et al., 2013). These results assign MARK4 a role that coincides with the period between vesicle fusion and CP110 displacement from the mother centriole. This period is pivotal in cilia biogenesis since only after these two events is the axoneme allowed to grow (Goetz and Anderson, 2010; Kuhns et al., 2013; Schmidt et al., 2012; Sillibourne et al., 2013; Spektor et al., 2007). On the side of autophagy regulation, cells depleted of MARK4 were reported to have defects in clustering the lysosomes around the aggresome and concomitantly fail to degrade the ubiquitinated protein aggregates there located (Zaarur et al., 2014). Additionally, MARK4 was found to be a negative regulator of the mTORC1complex, which as already mentioned, is a negative regulator of autophagy. Finally, MARK4 is an AMPK related kinase (Lizcano et al., 2004) and recently the liver kinase B1 (LKB1)-AMPK pathway has been implicated in the crosstalk between ciliogenesis and autophagy (Orhon et al., 2016). I, therefore, postulated that MARK4 might contribute to ciliogenesis by regulating autophagy and therefore OFD1 degradation from the centriolar satellites. The aim of this study was to investigate whether MARK4's role in ciliogenesis is played through regulation of inducible autophagy. If MARK4, has a role in regulating the inducible autophagy process that degrades the OFD1 CSs that inhibit ciliogenesis, then we should expect to find an excess of OFD1 in MARK4-depleted cells. Moreover, it would be possible to rescue the ciliogenesis defect caused by MARK4 depletion by performing an OFD1 CS co-depletion.

IV.II. Results

IV.II.I. MARK4 is a positive regulator of inducible autophagy

To investigate whether MARK4 regulates autophagy, I used RPE1 cells stably expressing YFP-LC3. In the YFP-LC3 RPE1 cells it is possible to identify autophagy induction by visualizing the formation of fluorescent puncta that correspond to LC3-II rich autophagosomes. I thus compared the number of YFP-LC3 puncta formed in control and MARK4-depleted cells before (t=0) and after serum starvation (Figure 25A and B). As expected (Alpadi et al., 2012; Badr et al., 2011; Kabeya et al., 2003), the number of YFP-LC3 puncta increased upon serum withdrawal in control-depleted cells. The amount of YFP-LC3 increased upon MARK4 depletion and serum starvation, but the number of puncta stayed significantly bellow the control in all time points (Figure 25B). To confirm that in the first hours of serum starvation, control cells exhibit an autophagic burst that is significantly diminished in MARK4-depleted cells, I analyzed the ratio of LC3-I to LC3-II by immunoblot, as autophagy induction increases the levels of LC3-II. To induce autophagy to a maximum, I treated control and MARK4 siRNA-treated cells with the proteasome inhibitor MG132 (inductor of autophagic response). The exposures presented in Figure 25C attest that cells lacking MARK4 are not able to deliver such robust autophagic response to the serum starvation stimulus as control treated cells. The same was true for the autophagic response to MG132 (Figure 25C).

Since MARK4 has an effect regarding the ability of cells to form de novo autophagic vesicles, I also wanted to investigate if MARK4 kinase knock-down could have an effect on degradation activity. Autophagic degradation activity is often known as autophagic flux (Alpadi et al., 2012; Loos et al., 2014). From the many ways used to quantify autophagic flux (Alpadi et al., 2012), I chose a microscopy coupled with automated image analysis approach. For this, I cultured RPE1 cells stably expressing mCherry-EGFP-LC3. As previously mentioned, LC3BII decorates autophagic vesicles, and it goes through all the autophagosome cycle until its recycling when the autophagosome fuses with the lysosome. The tandem tagged LC3 with mCherry and EGFP will fluoresce in both red and green wavelengths when it is free in the cytoplasm or when it is incorporated in the autophagosomes. However, when the autophagosome fuses with the lysosome, the low lysosomal pH leads to the loss of EGFP but not mCherry fluorescence signal, due to change in EGFP protein conformation. In this situation, LC3 will only fluoresce in the red wavelength. In Figure 26A is shown that under microscopy, RPE1 cells stably expressing mCherry-EGFP-LC3 and fixed for fluorescence microscopy analysis exhibit yellow and red puncta. These, correspond to autophagosomes in different stages of the autophagic degradation cycle: yellow dots are early autophagosomes (where both mCherry and EGFP are fluorescent) and red dots that correspond to late autophagosomes after lysosomal fusion (where EGFP is unfolded and only mCherry is fluorescent). The ratio of yellow to red puncta in any single cell gives us a quantification of the autophagic flux in that cell. Using wide-field high-resolution microscopy and an automated image analysis pipeline described in Materials & Methods, I quantified the autophagic flux in cells treated with control or MARK4 siRNAs. To follow the autophagic flux dynamics through the serum starvation response, I fixed cells for imaging before and after serum starvation. In control cells, autophagic flux peaks 6 hours after serum starvation and undergoes a steady decrease after this time (Figure 26). In MARK4-depleted cells, however, the flux peak happens immediately after the serum starvation stimulus is applied and stays quite high through the serum starvation process.

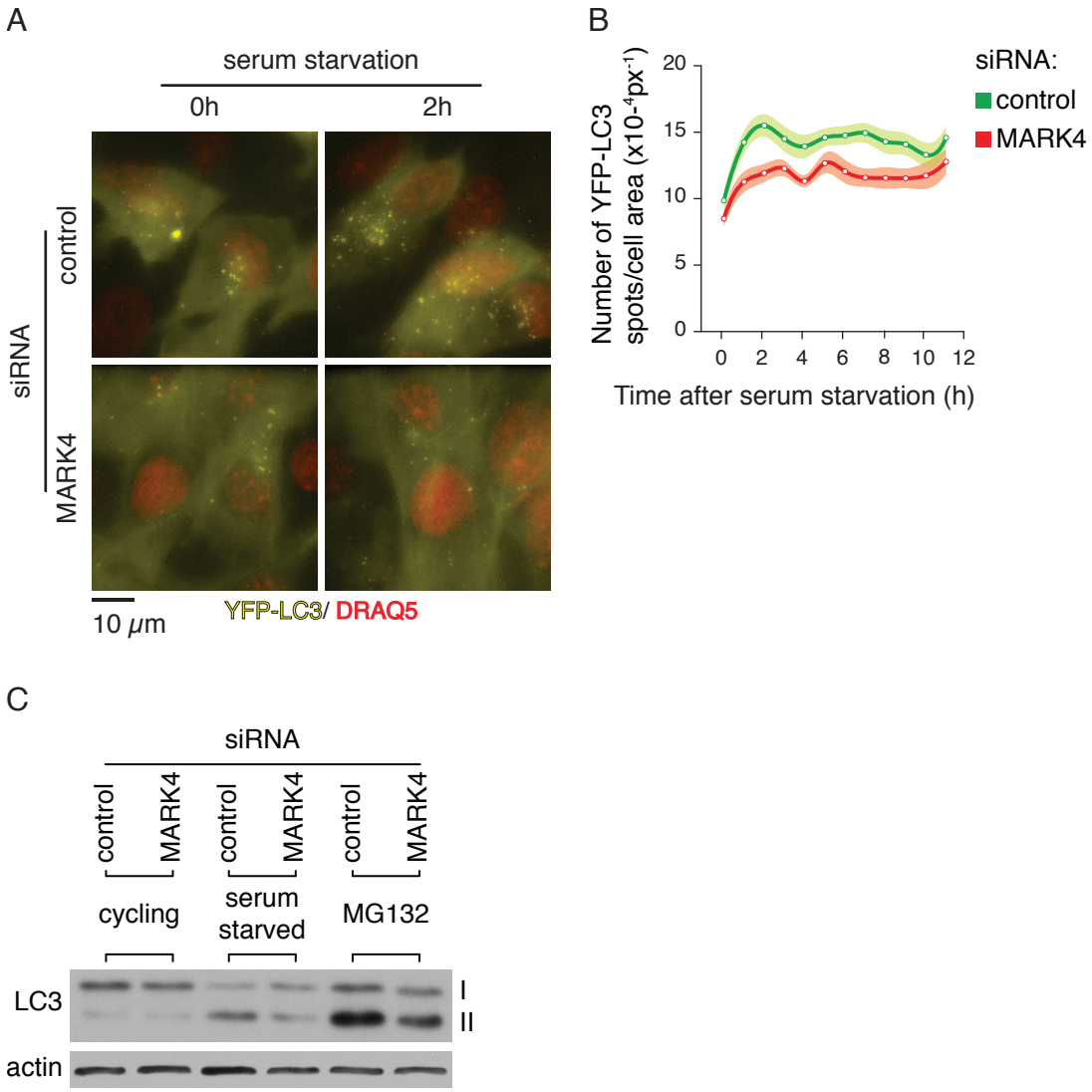

Figure 25: **MARK4 depleted cells are not capable of a full scale autophagic response to serum starvation**. (A and B) RPE1 cells stably expressing YFP tagged LC3B protein, treated with control or MARK4 siRNA, were serum starved and imaged for 12 hours. (A) Sample images of cells just before serum starvation (0h) or 2 hours after serum starvation (2h). Nuclear staining used for live cell imaging was DRAQ5. (B) Autophagic vesicle number and cell area were determined using an automated image analysis protocol detailed in Materials & Methods. Shaded area around the line defined by the vesicle density at a certain time point corresponds to the SEM. Data shown is the combination of three independent experiments. $115<N_{control}<138$, $106<N_{MARK4}<150$. (C) Total cell extracts of RPE1 cells treated with control or MARK4 siRNA in the presence of serum, without serum or treated with proteasome inhibitor MG132 were analyzed by immunobloting. I and II indicate the LC3B forms as they run in the SDS-PAGE. Actin served as a loading control. One representative experiment out of three is shown.

IV.II.II.MARK4 is a negative regulator of mTOR kinase activity

I next asked how MARK4 influences the autophagic response to serum starvation. It was previously documented that MARK4 can phosphorylate Raptor (Li and Guan, 2013), a key component of the mTORC1 protein complex. An active mTORC1 complex is known to inhibit autophagy activation. To have an idea of mTOR activity status and thus its influence on autophagic response to serum withdrawal, I started by analyzing whether mTOR localization was affected by MARK4 depletion. Recall that the mTORC1 complex localized to the lysosome is catalytically active and therefore phosphorylates the ULK complex inhibiting autophagosome formation. In Figure 27A it is shown how MARK4 depletion leads to a stronger colocalization of mTOR and lysosomal marker Lysosomal-associated membrane protein 1 (LAMP1) proteins when the cells are grown in serum-rich media. Upon serum starvation, both control and MARK4-depleted cells exhibit a marked mTOR lysosomal localization. If we attend to the colocalization of mTOR and LAMP1 concerning

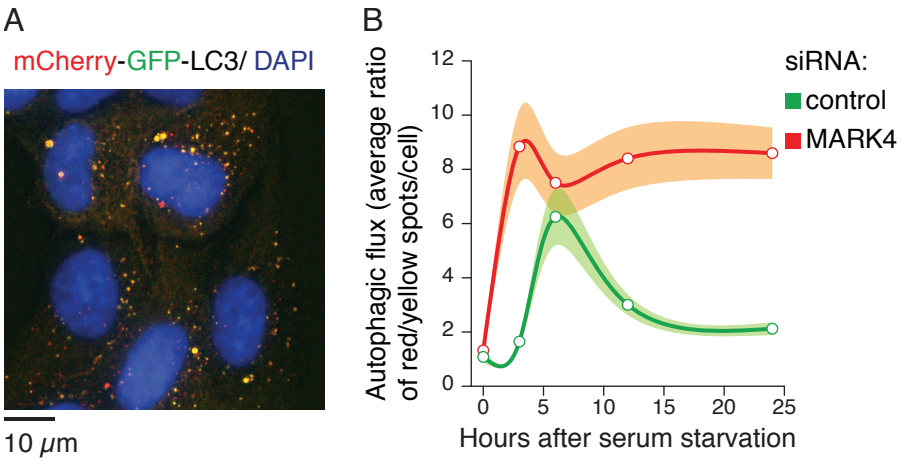

Figure 26: **MARK4 depleted cells have altered autophagic flux**. (A and B) RPE1 cells stably expressing mCherry and EGFP tagged LC3B protein were treated with control or MARK4 siRNA and serum starved for 24 hours. Cells were fixed and stained with DAPI for DNA visualization. (A) Illustrative example of RPE1 cells stably expressing mCherry-EGFP tandem tagged LC3B. (B) Autophagic flux in control and MARK4 depleted cells in the time points indicated by a white circle. Autophagic flux is measured by the amount of mCherry-GFP-LC3 incorporated into lysosomes (red signal only) per amount of mCherry-GFP-LC3 incorporated into autophagosomes (yellow signal reflection of mCherry-GFP colocalization). Classification of red and yellow vesicles was performed using the automated image analysis pipeline detailed in Material & Methods. Shaded area around the line defined by the vesicle ratio at a certain time point corresponds to the SEM. Data shown is the combination of three independent experiments. $90<N_{control}<196$, $102<N_{MARK4}<208$. One representative experiment out of three is shown.

Pearson's R value for the correlation between the red and green intensities at each pixel, we can see in Figure 27B that MARK4-depleted cells have as high signal overlap when grown in serum rich than in serum-free conditions. In Figure 27C we see that upon serum starvation, in control-depleted cells, the kinase activity of mTOR towards its model substrate Ribosomal protein S6 kinase (S6K) is substantially decreased. Given the high lysosomal localization of mTOR in MARK4-depleted cells, it would be expectable to find, after serum starvation, a significant mTOR activity. Indeed, a significant residual activity is still detected when cells are depleted of MARK4 (Figure 27C). Regarding mTOR regulation via Raptor phosphorylation the results are paradoxical: when MARK4 kinase is knocked-down, cells exhibit higher phosphorylation on S792 of Raptor than control cells (Figure 27C).

IV.II.III.MARK4 depletion leads to abnormal lysosomal positioning

One striking effect of MARK4 depletion in RPE1 cells that is visible in Figure 27A and Figure 28A is the positioning of lysosomes in dense perinuclear clusters. This effect of MARK4 depletion is noticeable either in cells grown in serum-rich media or cells subjected to serum starvation (Figure 28A). Using the clustering quantification method described in Material & Methods, I quantified the degree of geometric clustering of the lysosomes for each cell in the conditions presented in Figure 28A and B. Quantification shows that the level of perinuclear concentration of the lysosomes is always higher in MARK4-depleted cells compared with control cells. This observation is valid both for cells grown in serum-rich media or under serum starvation conditions. When cells are stimulated to condense its lysosomes by inhibition of the proteasome by the addition of MG132 to the growth medium, the difference between control and MARK4 depletion is smaller. In these conditions, in MARK4-depleted cells, the lysosomes are less densely packed around the centrosomes as in the control-depleted cells also subjected to MG132 treatment. This result is consistent with what was previously reported by Zaarur et al. (Zaarur et al., 2014) where they found that MARK4-depleted cells were

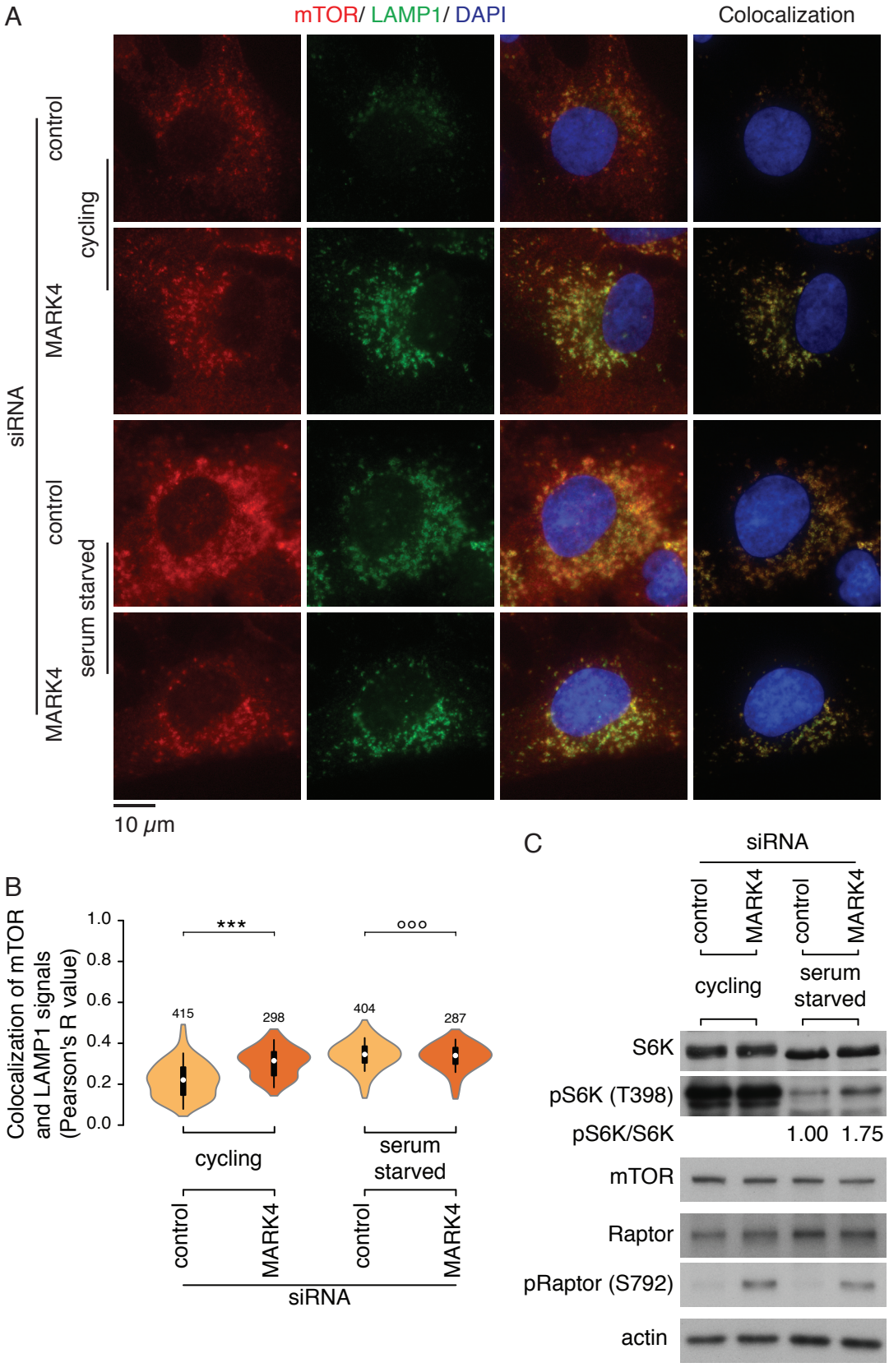

Figure 27: **MARK4 influences mTOR localization and activity response to serum starvation**. (A, B and C) RPE1 cells, treated with control or MARK4 siRNA, were taken for analysis either while grown in complete medium or after being serum starved for 24 hours. (A) Cells were stained for mTOR, LAMP1 and DAPI. Colocalization column shows the area of each cell where the green and red signal merge into the yellow color indicative of colocalization. (B) Violin plots showing the quantification of the degree of colocalization of the mTOR and LAMP1 signals as determined by the automated image analysis protocol detailed in Materials & Methods. *** corresponds to $p<0.001$, °°° corresponds to not significant. Data shown is the combination of three independent experiments. The number over the violin is N. (C) Total cell extracts of control and MARK4 depleted RPE1 cells were analyzed by immunoblotting. pS6K/S6K is the ratio of integrated pixel intensity after background subtraction of the pS6K and S6K bands. Actin was used as loading control. One representative experiment out of three is shown.

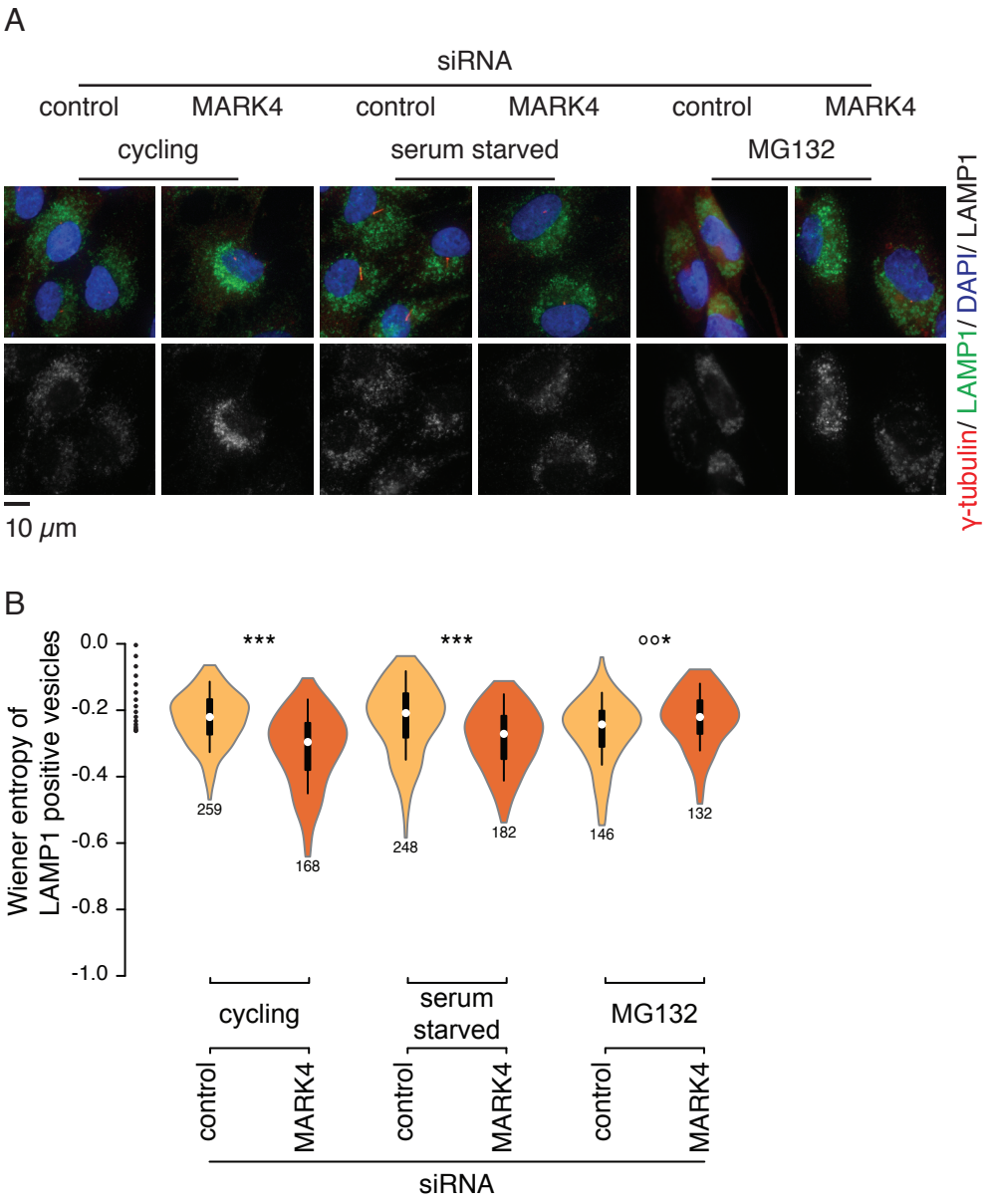

Figure 28: **MARK4 depletion disturbs lysosomal localization**. RPE1 cells treated with control or MARK4 siRNA in the presence of serum, without serum or treated with proteasome inhibitor MG132 were fixed and stained against γ-tubulin, LAMP1 and with DAPI. (A) Representative maximum intensity projections of fluorescence micrographs for the localization patterns of LAMP1. (B) Violin plot of the Wiener entropy quantification of the spatial organization of LAMP1 positive vesicles as determined by automated image analysis protocol detailed in Materials & Methods. Diagram on the right side of the y-axis illustrates the degree of dispersal. The number under the violin is N. One representative experiment out of three is shown.

less efficient than control-depleted cells to dispose of the lysosomes around the aggresome when this lysosomal positioning was promoted by proteasome inhibition with MG132.

The peculiar lysosomal positioning phenotype of cells depleted of MARK4 inspired the hypothesis that MARK4 could affect lysosomal positioning and inducible autophagy via its role in cytoskeleton regulation (Bulinski et al., 1997; Rovina et al., 2014; Semenova et al., 2014; Zaarur et al., 2014). One of the cytoskeleton components that has been previously identified as one of the factors that influences lysosomal positioning and autophagosome formation is the intermediate filament vimentin (Styers, 2004; Toivola et al., 2005). Figure 29 shows that cells depleted of MARK4 have much fewer vimentin fibers in the cytoplasm than cells treated with control siRNA.

IV.II.IV.MARK4 is critical for MAP4 dissociation from the microtubules upon serum starvation

Another possible explanation for abnormal lysosome positioning and incomplete autophagic response to serum starvation in MARK4-depleted cells is an anomaly in MAP4 regulation. MAP4 has been implicated both in ciliogenesis (Ghossoub et al., 2013) and control of organelle positioning (Bulinski et al., 1997; Semenova et al., 2014). M ARK4 is a known regulator of MAP4 by phosphorylating MAP4's microtubule-binding domain. This phosphorylation leads to the dissociation of MAP4 from microtubules and in some cell lines, increased microtubule dynamics (Drewes et al., 1997; Trinczek et al., 2004).

Immunofluorescence microscopy of cycling or serum starved cells treated with control siRNA (Figure 30) shows that cells subjected to serum starvation have a decrease in the levels MAP4 associated with microtubules. The same does not occur when cells are depleted of MARK4. We can see in Figure 30 that cycling MARK4-depleted cells do not have a different amount of MAP4 associated with the microtubules when compared with cycling cells that were control-depleted. On the contrary, upon serum starvation, MARK4-depleted cells have an increase in microtubule-associated MAP4 instead of the decrease observed in control cells.

Could the MAP4 accumulation on microtubules be the cause for the ciliogenesis defect in MARK4-depleted cells subjected to serum starvation? According to the mechanism proposed by Semenova et al. (Semenova et al., 2014)) MARK4 depletion and its effect of decreasing MAP4 phosphorylation and consequent accumulation on the microtubules should lead to inhibition of minus-end directed microtubule transport and stimulation of plus-end transport. If so, we would expect that cargos whose transport is dependent on microtubules and dynein-dynactin, such as CSs (Dammermann and Merdes, 2002), to be more dispersed away from the centrosome in MARK4-depleted cells when compared to control cells. Recall that in metazoans the centrosome is the microtubule organizing center and because of that, the minus-end of microtubules tends to be oriented towards the centrosome and the plus-end towards the cell periphery. We observed that a broad range of CS proteins has disturbed localization in MARK4-depleted cells. We can see in Figure 31A-F that CS proteins PCM1, Cep290 and WD repeat-containing protein 8 (WDR8) have its CS granules much more dispersed around the centrosome than control-depleted cells.

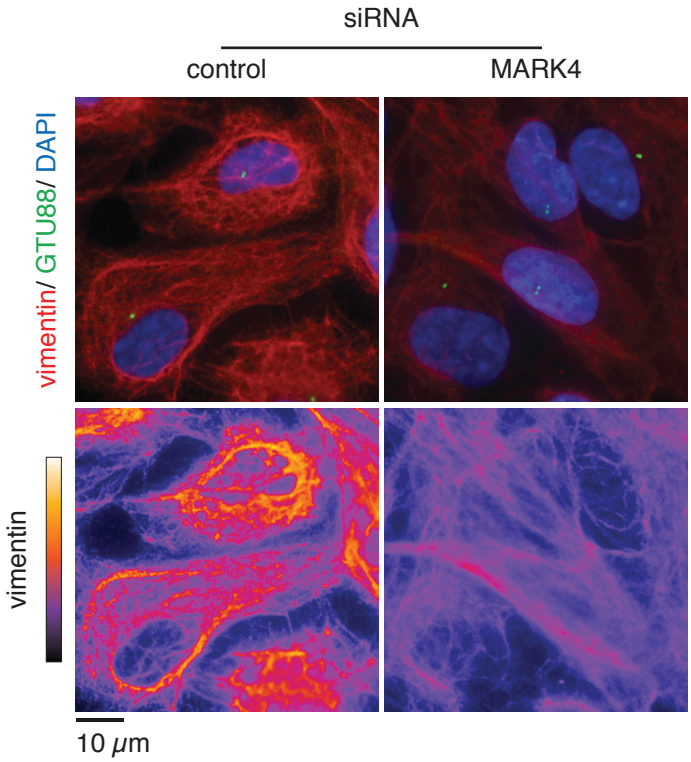

Figure 29: **MARK4 depletion leads defective vimentin cytoskeleton**. RPE1 cells treated with control or MARK4 siRNA in the presence of serum or serum starved for 24 hours were fixed and stained against vimentin, γ-tubulin (GTU88) and with DAPI. Lower row shows vimentin staining using a polychromatic lookup table with the scale shown on the box on the left side. Representative micrographs of one representative experiment out of three are shown.

In Figure 32A we can see that a striking difference between cells treated with control or MARK4 siRNAs is OFD1 CS dispersal. Both in cycling and serum-starved control treated RPE1 cells, OFD1 satellites are more concen-

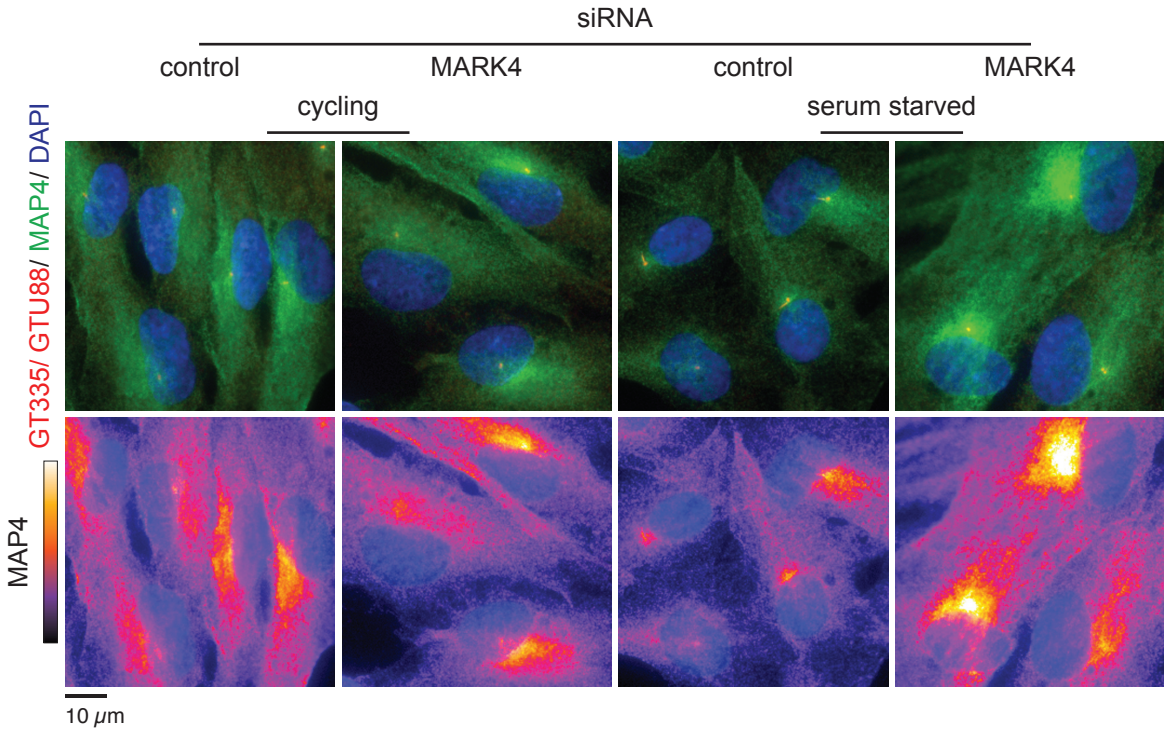

Figure 30: **MARK4 depletion leads to MAP4 accumulation at the microtubules**. RPE1 cells treated with control or MARK4 siRNA in the presence of serum or serum starved for 24 hours were fixed and stained against polyglutamilated tubulin (GT335), γ-tubulin (GTU88), MAP4 and with DAPI. Lower row shows MAP4 staining using a polychromatic lookup table with the scale shown on the box on the left side. Representative micrographs of one representative experiment out of three are shown.

trated around the centrosome than in MARK4-depleted cells, where OFD1 satellites can be observed scattered throughout the cytosol. Quantification of CS Wiener entropy (WE) (see Chapter 1 for more details about this method) shown in Figure 32B confirms this observation.

The observed dispersion and inability to concentrate OFD1 CSs around the centrosome is consistent with a compromised minus-end-directed transport of the centriolar satellite granules in MARK4-depleted cells. I reasoned that an inhibited minus-end directed transport caused by an abnormal MAP4 abundance on the microtubules could have an impact on ciliogenesis by inhibiting the transport to the basal body of cargo, such as IFT complexes or vesicular structures, essential for cilia formation and extension. To investigate the plausibility of this mechanism, I hypothesized that the ciliogenesis defect observed in the absence of MARK4 could be rescued by depleting MAP4. Figure 33A shows that the depletion of MAP4 was sufficient but not complete, especially in the case of cells with lowered levels of MARK4. It is important to only partially deplete MAP4 since, as observed in Figure 33B and previous publication (Ghossoub et al., 2013), MAP4 depletion by itself has the effect of reducing the number of cells able to form cilia. As we can see in Figure 33B, even taking in consideration the adverse effects that MAP4 depletion has on ciliogenesis, its co-depletion with MARK4 does not rescue the defect on ciliogenesis.

IV.II.V.Autophagy-deficient cells ciliate faster but in lower numbers than control

Since, to my best knowledge, no characterization of the role of autophagy on ciliogenesis in RPE1 cells has been published, I set to investigate the impact of autophagy deficiency, caused by ATG5 depletion, on the probability of cells to ciliate once subjected to serum starvation. A cell depleted of ATG5 has a limited capacity of converting LC3-I into LC3-II, therefore to form autophagosomes and to have a normal autophagic

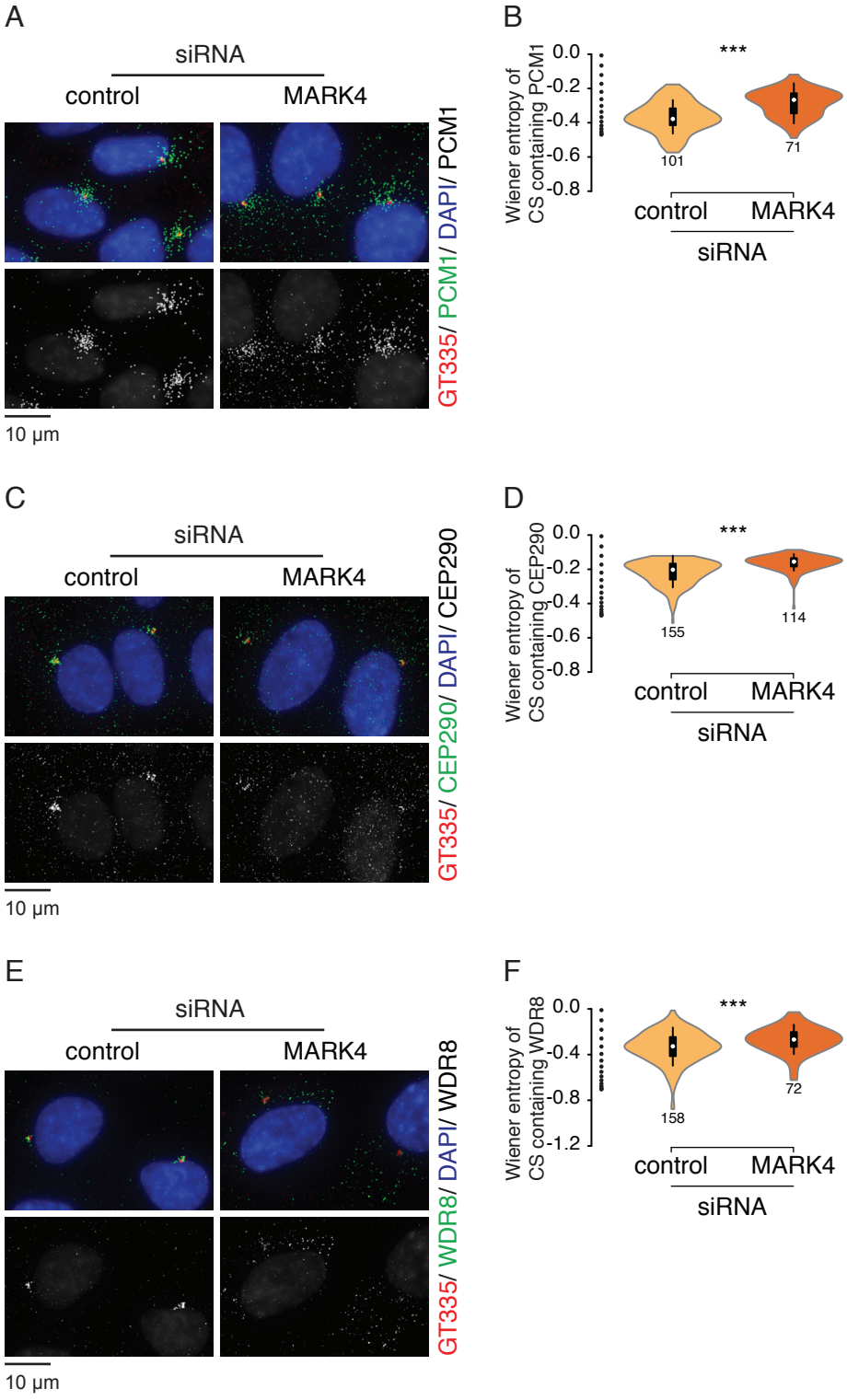

Figure 31: **MARK4 depletion causes centriolar satellite proteins to be more dispersed around the centrosome**. RPE1 cells treated with control or MARK4 siRNA and serum starved for 24 hours were fixed and stained against polyglutamilated tubulin (GT335), PCM1, CEP290, WDR8 and with DAPI. (A, C, and E) Transformed images used by the automated image analysis pipeline described in the Material & Methods section. Due to high dynamic range, pixel intensity values of (A) PCM1, (C) CEP290 and (E) WDR8 are log transformed to allow the visualization of both the brightest and the faintest granules. (B, D and F) Violin plot of the Wiener entropy quantification of the spatial organization of (B) PCM1, (D) CEP290 and (F) WDR8 positive foci as determined by automated image analysis protocol detailed in Materials & Methods. *** corresponds to $p<0.001$. Diagram on the right side of the y-axis illustrates the degree of dispersal. The number under the violin is N. Representative micrographs and quantification of one representative experiment out of three are shown.

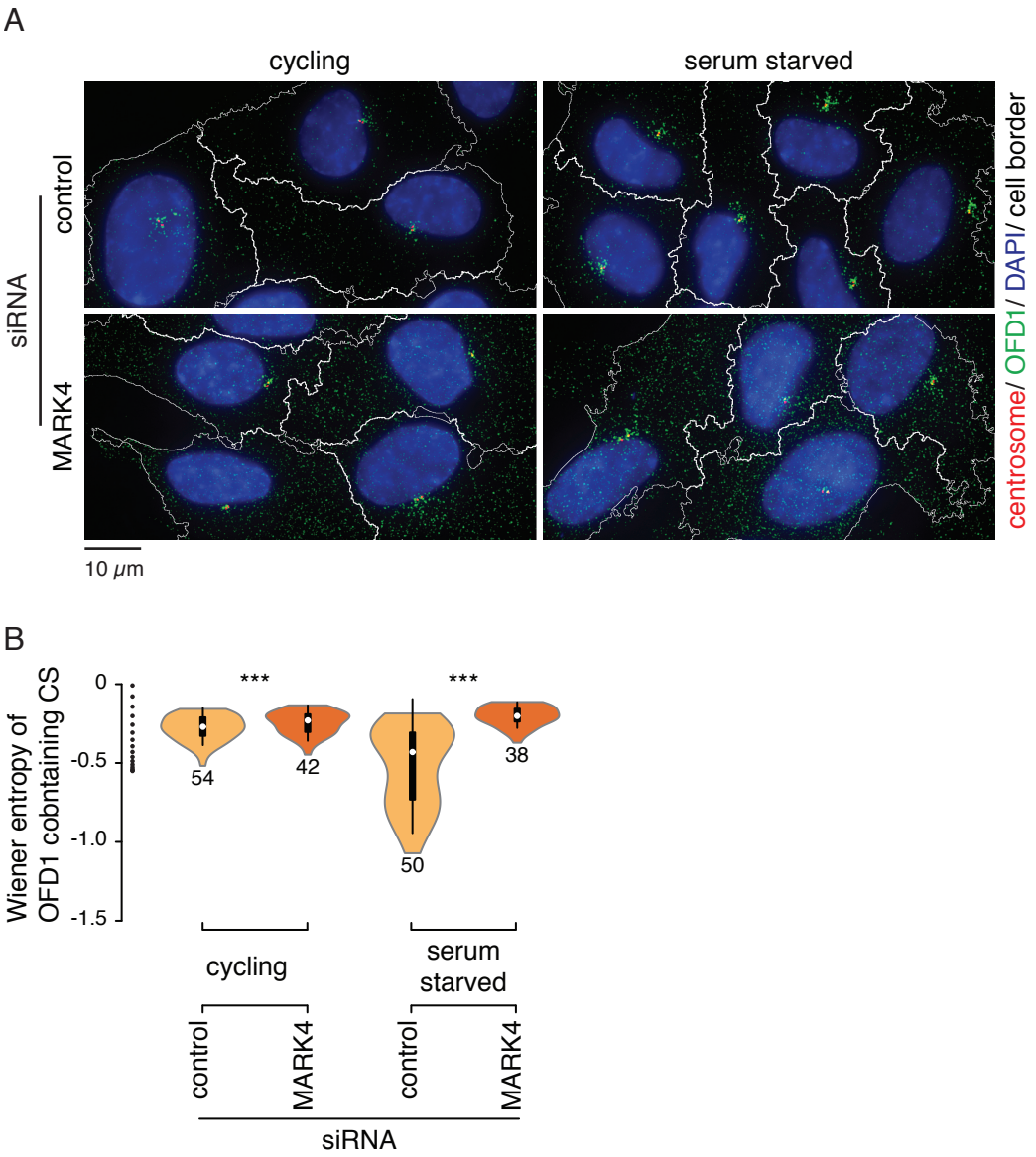

Figure 32: **MARK4 depleted cells are not able to concentrate OFD1 centriolar satellites around the centrosome**. (A and B) RPE1 cells treated with control or MARK4 siRNA in the presence of serum or serum starved for 24 hours were fixed and stained against polyglutamilated tubulin (GT335), γ-tubulin (GTU88), OFD1 and with DAPI. (A) Transformed images used by the automated image analysis pipeline described in the Material & Methods section. Due to high dynamic range, pixel intensity values of OFD1 are log transformed to allow the visualization of both the brightest and the faintest granules. (B) Violin plot of the Wiener entropy quantification of the spatial organization of OFD1 positive foci as determined by automated image analysis protocol detailed in Materials & Methods. *** corresponds to p<0.001. Diagram on the right side of the y-axis ilustrates the degree of dispersal. Label under the violin is the value of N. Representative micrographs and quantification of one representative experiment out of three are shown.

response. In Figure 34A we can see that the depletion of ATG5 leads to a decreased autophagic response to serum starvation. The quantification of the autophagosome density performed using the automated image analysis protocol detailed in Material & Methods and shown in Figure 34B reveals that ATG5-depleted cells have a significantly lower amount of autophagosomes than control-depleted cells both in serum supplemented and free media. Serum-starved cells depleted of ATG5 are still able to respond to serum removal by producing new LC3-II positive autophagosomes but not to the same degree as control-depleted cells. The defective incorporation of LC3-II in the newly formed autophagosomes is evident in Figure 34C-D. In Figure 34C we can see that both in cycling and serum starved cells, there is a lower ratio of LC3-II to total LC3 in ATG5- than in control-depleted cells. However, the highest LC3-II to total LC3 ratio drop is observed when

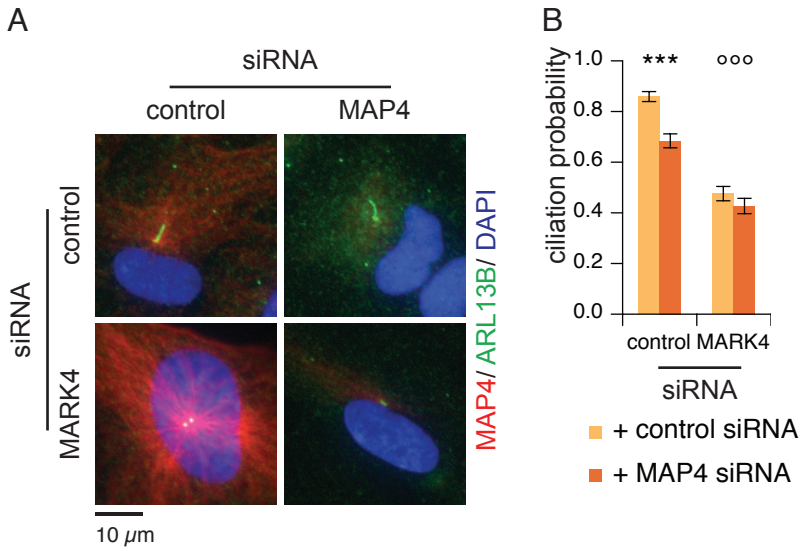

Figure 33: **MAP4 co-depletion with MARK4 does not rescue MARK4 depleted cells ciliogenesis defect**. (A and B) RPE1 cells treated with control or MARK4 siRNA for 24 hours were further treated with control or MAP4 siRNA for 12h and serum starved for 24 hours. (A) Cells were fixed and stained against MAP4, ARL13B and with DAPI. Representative fluorescence micrographs of one representative experiment out of three are shown. (B) Quantification of the probability of a cell to ciliate under the indicated treatments. *** corresponds to $p<0.001$, °°° corresponds to not significant. Data shown is the combination of three independent experiments. $N_{control}$=312, 285; N_{MARK4}=311, 267.

siRNA treated cells are subjected to serum starvation, that is, when inducible autophagy is activated. In Figure 34A we can see that there is an increase in the green signal that is dispersed throughout the cytoplasm (and not in the autophagosomes) in ATG5-depleted cells that were serum starved for 2 hours. It appears that cells can mobilize LC3 to deal with the serum starvation response, but the lack of ATG5 renders them unable to convert it into LC3-II. Confirming this hypothesis is the fact that the median of the mean fluorescence intensity per autophagosome increases in control treated cells subjected to serum starvation but remains unchanged when ATG5-depleted cells are serum deprived (Figure 34D). Regarding the ability of autophagy-defective cells to ciliate, we can see in Figure 34E that a significant proportion of ATG5-depleted cells are more probable to be ciliated in serum-rich medium (t=0) when compared with control-depleted cells. Upon serum starvation, the probability that ATG5-depleted cells are ciliated increases sharply in the first hours and reaches its maximum just 6 hours after serum removal whereas for control-depleted cells the growth in probably to be ciliated is linear, and this probability keeps increasing throughout the 24 hours that the experiment took.

IV.II.VI.OFD1 is degraded upon serum starvation both via autophagy and proteasome pathways

To understand how OFD1 protein abundance upon serum starvation is regulated in RPE1 cells, I quantified OFD1 by immunoblot in cycling cells and cells subjected to 12h of serum starvation (Figure 35A and B). To estimate OFD1 abundance, I calculated the ratio of integrated pixel intensities of OFD1 to loading control bands in the image and divided all values by the proportion of the "cycling-mock" condition for normalization. Figure 35A shows how the efficiency of OFD1 knock-down translates in the disappearance of the OFD1 specific band (OFD1 KD).

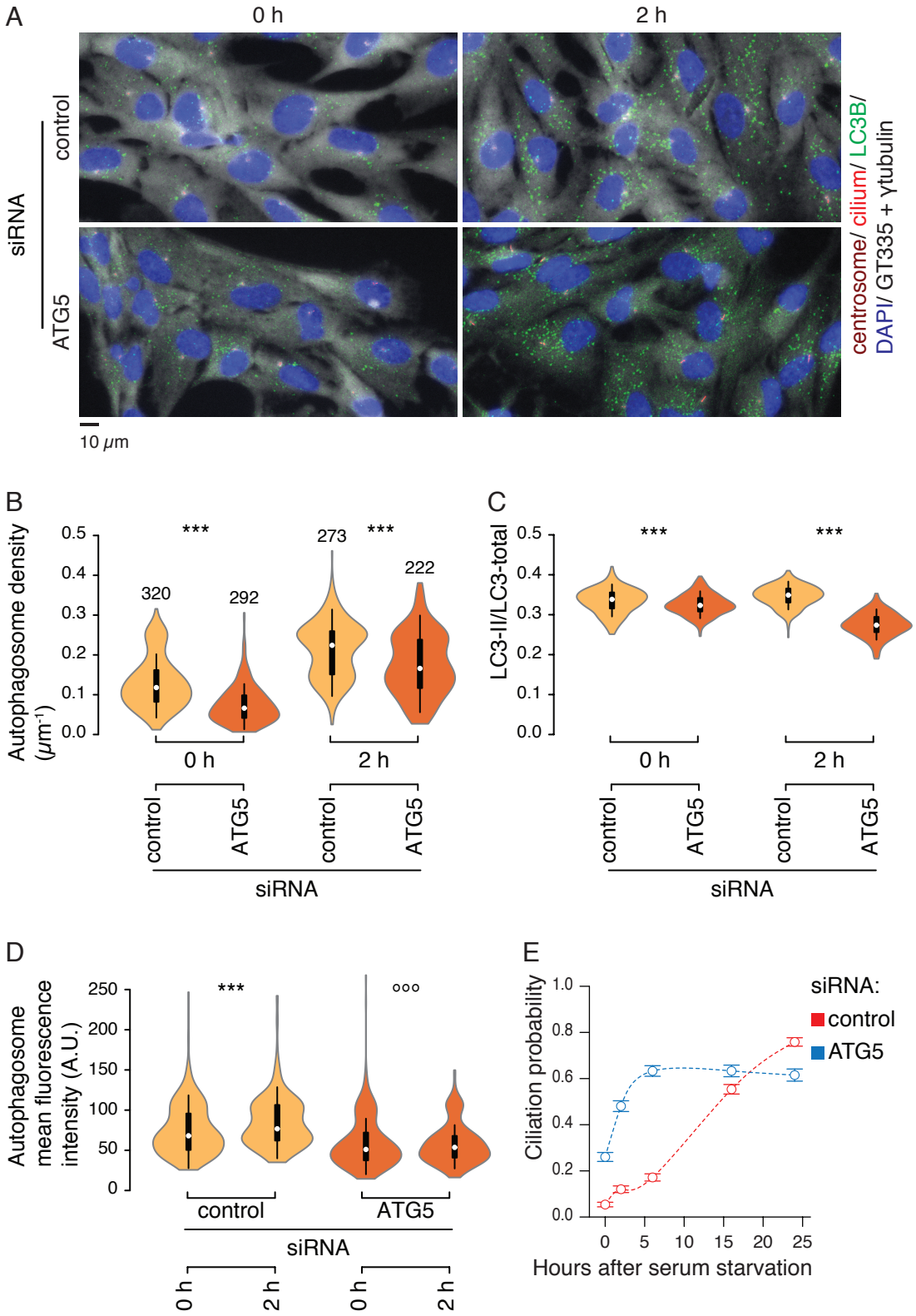

Figure 34: **Ciliogenesis kinetics are enhanced in autophagy-compromised cells**. (A-E) RPE1 cells treated with control or ATG5 siRNA in the presence of serum or serum starved for 24 hours were fixed and stained against polyglutamilated tubulin (GT335), γ-tubulin (GTU88), LC3B and with DAPI. (A) Sample images of cells just before serum starvation (0h) or 2 hours after serum starvation (2h). Transformed images used by the automated image analysis pipeline described in the Material & Methods section. Due to high dynamic range, pixel intensity values of ATG5 are log transformed to allow the visualization of both the brightest and the faintest granules. (B-D) Violin plot of the (B) autophagosome density, ratio of LC3-II integrated intensity over the total cellular LC3 integrated intensity and (D) mean fluorescence per autophagosome as determined by automated image analysis protocol detailed in Materials & Methods of cells just before serum starvation (0h) or 2 hours after serum starvation (2h). *** corresponds to $p<0.001$, °°° corresponds to not significant. A.U. - arbitrary units. The number on top of the violin in panel B is N for the panels B, C and D. (A-D) Representative micrographs and quantification of one representative experiment out of three are shown. (E) Quantification of the probability of a cell to ciliate in the indicated time points. Data are means ± SEM of the combination of three independent experiments. $515<N_{control}<583$, $343<N_{ATG5}<511$.

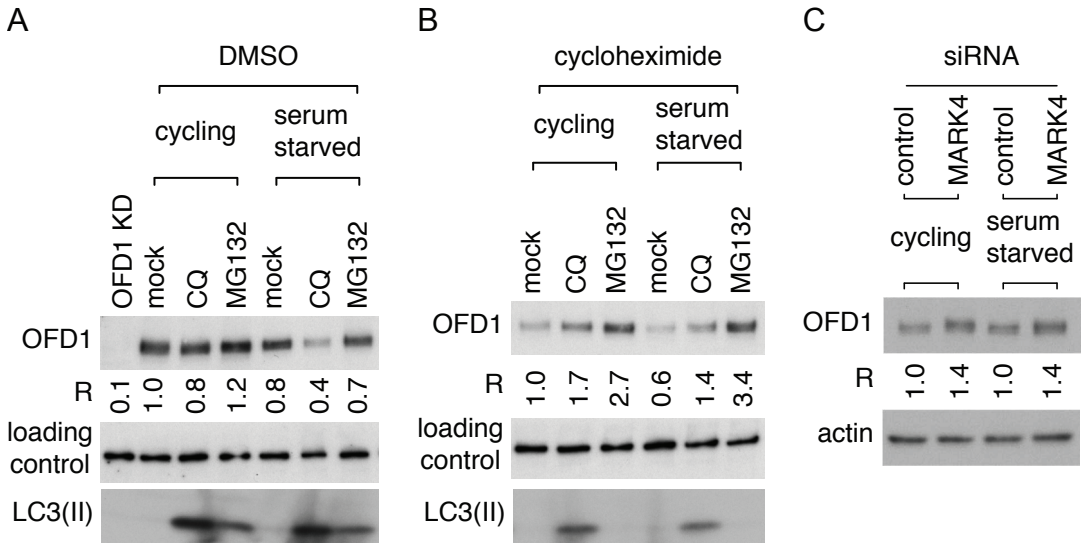

Figure 35: **OFD1 degradation upon serum starvation is compromised in MARK4 depleted cells**. (A) Total cell extracts of RPE1 cells treated with control or MARK4 siRNA in the presence of serum or without serum, treated with chloroquine (CQ) or proteasome inhibitor MG132 and in the presence of cycloheximide were analyzed by immunobloting. An unspecific band was used as loading control. (B) Total cell extracts of RPE1 cells treated with control or MARK4 siRNA in the presence of serum or without serum were analyzed by immunobloting. Actin was used as loading control. R indicates the ratio of integrated pixel intensities of OFD1 to loading control bands in the image and divided all ratios by the ratio of the "control" condition for normalization. The R values shown are means of three independent experiments.

To know if there is a variation of OFD1 abundance before and after serum starvation, we need to compare the lanes "mock" in Figure 35A. Interestingly, in RPE1 cells it appears that there is no significant difference in OFD1 protein levels between untreated cells that were cycling or serum starved. Comparison of band intensity in these conditions either by visual or computational means indicates a difference in protein levels that is within the error margins of the method. To exclude de novo OFD1 protein synthesis from the analysis, I inhibited protein synthesis by cycloheximide addition to the cell medium and serum starved the cells for 12 hours. To inhibit autophagy related degradation I used chloroquine (CQ) and to obstruct the proteasome pathway I used MG132. Figure 35B shows the result of an immunoblot performed with samples of all the conditions above. After cycloheximide addition, we can see that a difference between the OFD1 protein levels of mock treated, cycling and starved cells is noticeable: cells that were serum starved for 12h have almost half the amount of OFD1 than cells that were grown in the presence of serum (Figure 35B). Regarding which protein degradation pathway is preferred by the cell for the OFD1 breakdown, results indicate that both autophagy and proteasome pathways can be used to degrade it. We can see that the bands corresponding to OFD1, in the lanes where the proteins of CQ or MG132 treated cells were separated, are significantly more intense than of the mock treatment cells. However, in contradiction to what was published by Tang et al. for MEFs, the proteasome pathway appears to be the main responsible for OFD1 degradation in RPE1 cells, especially when cells are subjected to serum starvation.

Having established that there is OFD1 degradation upon serum starvation in RPE1 cells, it was time to inquire about the role of MARK4 in the process. As seen in Figure 35C, MARK4 knock-down cells accumulate a higher amount of OFD1 than cells treated with control siRNA. The normalized ratio of OFD1 band intensity to the intensity of the loading control band, in this case, actin, shows that MARK4-depleted cells have consistently 40% higher levels of OFD1 than control-depleted cells either when they are cultivated in the presence of serum or after 24 hours of serum starvation. Figure 35C also shows the migration pattern of

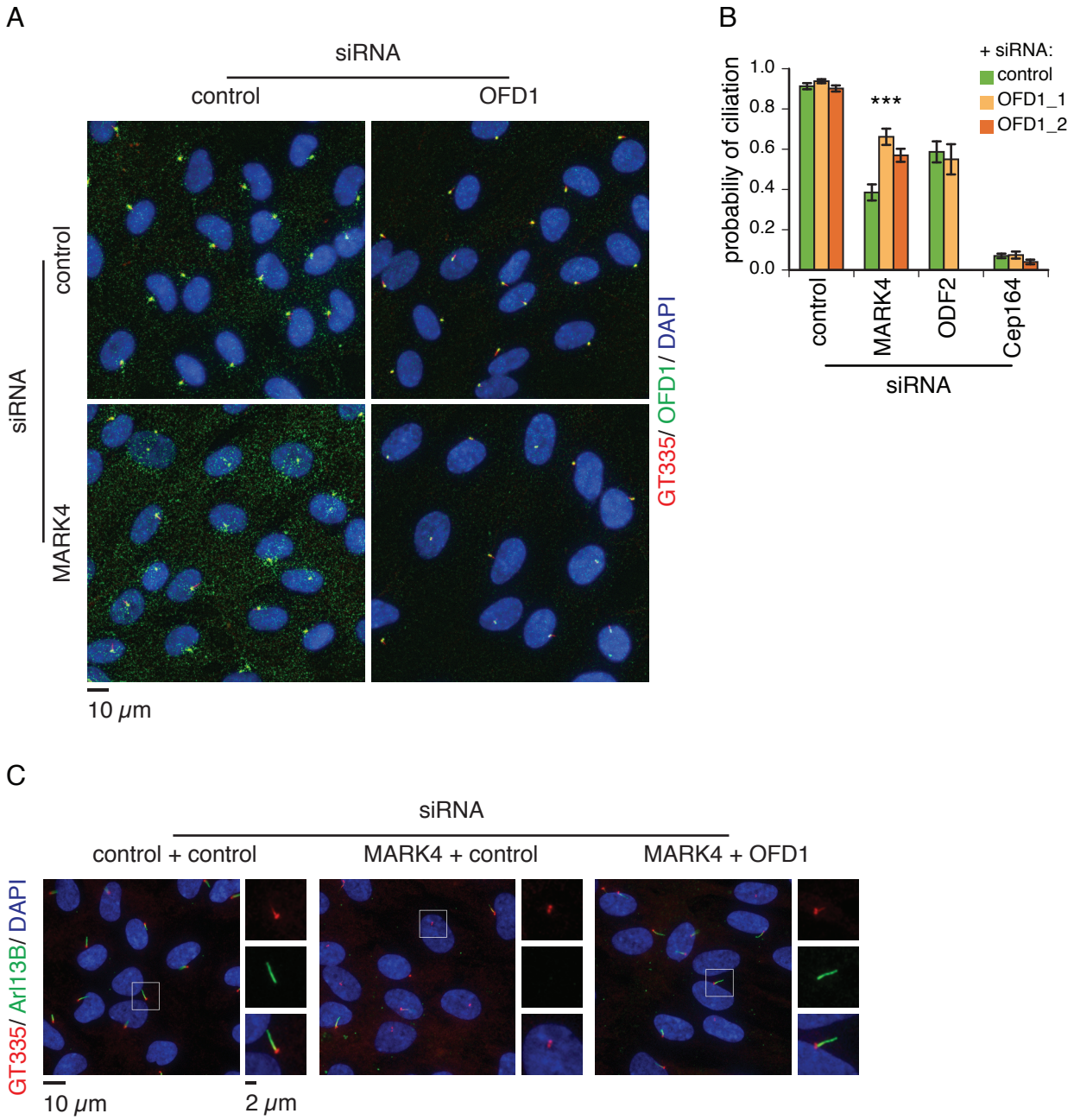

Figure 36: **Limited OFD1 co-depletion with MARK4 partially rescues MARK4 depleted cells ciliogenesis defect**. (A, B and C) RPE1 cells treated with control or MARK4 siRNA for 24 hours were further treated with control or OFD1 siRNA for 12h and serum starved for 24 hours. (A) Cells were fixed and stained against polyglutamilated tubulin (GT335), OFD1 and with DAPI. (A) Representative maximum intensity projections of fluorescence micrographs of one representative experiment out of three are shown. (B) Quantification of the probability of a cell to ciliate under the indicated treatments. *** corresponds to $p<0.001$. Data shown is the combination of three independent experiments. $N_{control}$=690, 660, 631; N_{MARK4}=527, 603, 560; N_{ODF2}=317, 251; N_{Cep164}=644, 540, 552. (C) Cells were fixed and stained against polyglutamilated tubulin (GT335), ARL13B and with DAPI. Representative micrographs of one representative experiment out of three are shown.

OFD1 in a gradient gel. Interestingly, it reveals not only higher amounts of OFD1 but also that OFD1 bands present a distinct pattern in cells treated with MARK4 siRNAs when compared to control treated cells.

IV.II.VII.Co-depletion of OFD1 rescues the loss of cilia in MARK4-depleted cells

If MARK4-depleted cells can not become ciliated due to the inability of these cells to degrade the CS pool of OFD1, an ectopic degradation of OFD1 from the CSs should bypass MARK4's role of promoting the degradation of this inhibitory pool of OFD1 and restore ciliogenesis proficiency in MARK4-deficient cells. To test this hypothesis, I performed a depletion of OFD1 so that only the satellite pool of this protein would be

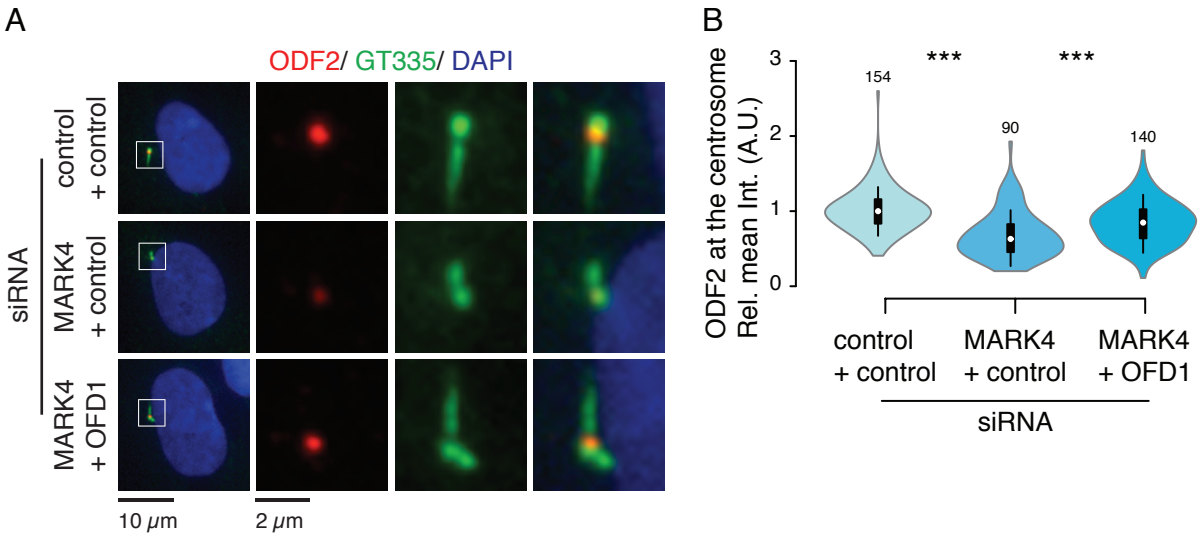

Figure 37: **OFD1 co-depletion with MARK4 partially rescues MARK4 depleted cells defective ODF2 recruitment to the centrosome**. (A, and B) RPE1 cells treated with control or MARK4 siRNA for 24 hours were further treated with control or OFD1 siRNA for 12h and serum starved for 24 hours. (A) Cells were fixed and stained against ODF2, polyglutamilated tubulin (GT335) and with DAPI. (A) Representative micrographs of one representative experiment out of three are shown. Regions within the white boxes are depicted at higher magnification on the right. (B) Violin plots show the relative ODF2 intensity at the centrosome under the indicated treatments. *** corresponds to p<0.001. Rel. mean Int. - relative mean intensity, A.U. - arbitrary units. Data from one representative experiment out of three. The number on top of the violin is N.

affected by a short exposure and low siRNA concentration transfection. The centrosomal pool reported to be essential for cilia formation (Lopes et al., 2011), would be for the most part uninfluenced by the depletion procedure. Figure 36A shows that with the transfection conditions used, the selective reduction of the CS pool of OFD1 was satisfied and only the centrosomal pool of OFD1 was left in the cell. In Figure 36A-B we can see that the treatment of MARK4-depleted cells with small doses of two different OFD1 targeting siRNAs can rescue primary cilia formation. As can be seen in Figure 36B, MARK4-depleted cells treated with control siRNA have a probability of being ciliated under 40%, but when treated with any of the OFD1 targeting siRNAs tested, the probability to be found ciliated after 24 hours of serum starvation rises to around to 60%. We can also see that OFD1 depletion from the CSs is not a general panacea for ciliogenesis defects, as depletion of OFD1 did not rescue the ability of Cep164 depleted cells to ciliate (Figure 36B).

Since OFD1 was reported to be involved in the regulation of centriole length (Singla et al., 2010), I wanted to know if the structures that we positively identified as cilia in Figure 36A-B were in reality cilia or just aberrantly over-extended centrioles. Staining against ciliary membrane specific protein ARL13B (Cantagrel et al., 2008) demonstrates that the polyglutaminated structures that we see on Figure 36C are the axonemes of primary cilia and not abnormally extended centrioles.

MARK4 notorious role in primary cilia formation has been linked with its ability to recruit sub-distal appendage protein ODF2 to the basal body (Kuhns et al., 2013). Moreover, ultra-structural analysis of the basal bodies of cells subjected to ODF2 depletion reveals a similar phenotype to MARK4-depleted cells: failure of the axoneme to extend. For these reasons, in Kuhns et al., 2013, we postulate that MARK4 could contribute to primary cilia formation by promoting the accumulation of a critical level of ODF2 at the basal body. Depletion of ODF2 has the effect of lowering the probability of a given cell to ciliate after being subjected to 24 hours of serum starvation to about 60% as can be seen in Figure 36B. However, co-depletion of OFD1 with ODF2 does not lead to a restoration of the probability of cells low on ODF2 to ciliate.

In MARK4-depleted cells, ODF2 fails to accumulate at the basal body, but its total levels are comparable to control-depleted cells (Kuhns et al., 2013). If, as can be seen in Figure 37A-B, we compare the ODF2 levels at the centrosome, we see that OFD1 co-depletion with MARK4 leads to a partial restoration of the ability of cells to accumulate ODF2 at the centrosome.

IV.III. Discussion

The working hypothesis for this part of the project was that by regulating autophagy induced by serum starvation, MARK4 contributed to the degradation of the centriolar satellite pool of OFD1 that plays an inhibitory role in ciliogenesis. If this were the case, the artificial depletion of OFD1 from the centriolar satellites would result in a rescue of the ciliogenesis defect shown by cells treated with siRNA against MARK4.

The first premise of the hypothesis is that MARK4 is necessary for the correct activation of autophagy upon serum withdrawal. Using RPE1 cells stably expressing YFP-LC3 we could compare the efficiency of autophagy activation upon serum starvation between control and MARK4-depleted cells. We saw that even though autophagy activation in MARK4-depleted cells is not completely compromised, the increase in the number of autophagic vesicles is much lower in MARK4 than in control-depleted cells. We also saw how this defect in autophagic vesicle formation translates in the inability of cells devoid of MARK4 protein to biochemically convert the cytoplasmic LC3-I into phosphatidylethanolamine-conjugated LC3-II. Even when autophagy was induced by chemical inhibition of the proteasome pathway, the amount of LC3-II relative to LC3-I in MARK4-depleted cells was lower than in control-depleted cells.

To know if this failure of MARK4-depleted cells to produce LC3-II and new autophagic vesicles upon serum starvation is caused by a defect in LC3-I to LC3-II conversion or by an increased autophagic turnover, we followed the autophagic flux during the serum starvation process using cells stably expressing mCherry-EGFP-LC3. We saw how contrary to control-depleted cells (that have an autophagy flux peak at the 6 hour mark), MARK4-depleted cells have an earlier and sudden flux increase only a couple of hours after serum starvation started. These results can be explained by a defect in MARK4-depleted cells to form early autophagosomes when stimulated by serum starvation. If so, MARK4 activity appears to influence mainly the autophagosome formation step, although a role in the LC3 recycling process can not be excluded. In control cells, the autophagic flux values are comparatively small for the first hours because the increase in autophagic degradation is balanced by the autophagic burst caused by the cell's response to serum starvation. As we previously saw in Figure 25, in MARK4-depleted cells the autophagic burst is compromised. In these cells, the increase in autophagic degradation is not counterbalanced by the formation of new autophagic vesicles and the values of autophagic flux experience a sharp increase early after serum starvation. The fact that, in MARK4-depleted cells, there is a predominance of red over yellow autophagic vesicles up to 24 hours after serum starvation indicates that the defects caused by MARK4 depletion may also affect LC3 recycling from the late autophagosomes.

MARK4 was reported to be a negative regulator of mTOR (Li and Guan, 2013), itself a negative regulator of autophagy (Ganley et al., 2009; Jung et al., 2009; Kim et al., 2011; Utani, 2010). Since mTORC1 complex localization provides an indication of its kinase activity, we compared mTOR localization in MARK4 and control-depleted cells either growing in the presence of serum or without it. We found that in MARK4-depleted cells mTOR strongly colocalizes with the lysosomal marker LAMP1 independently of the presence of serum in the growth medium. The high colocalization of mTOR with the lysosomes indicates an activated state of mTOR since it is at the surface of the lysosome that it can interact with activating GTP-loaded RHEB GTPase (Betz and Hall, 2013; Shimobayashi and Hall, 2014). That is consistent with our finding that when MARK4-depleted cells are serum starved, the mTOR residual kinase activity towards its model substrate S6K is 75% higher than when cells are treated with control siRNA. Therefore, is possible that this remaining

mTOR activity in MARK4-depleted cells after serum starvation is the cause of the incomplete autophagy activation in those cells. Regarding the claim that MARK4 is a negative regulator of mTOR through phosphorylation of the Ser792 of Raptor (Li and Guan, 2013), that is not supported by the data presented in Figure 27C. The results indicate that contrary to what happens in HEK293, in RPE1 cells, MARK4 kinase activity has an inhibitory role on Raptor's Ser792 phosphorylation. The fact that Human embryonic kidney cells 293 (HEK293) cells proliferate at much higher rates than RPE1 cells inspires the hypothesis that since mTOR is a major player in cell growth and proliferation, its activity regulation may be different in these cells.

It was previously reported that in HeLa cells subjected to growth factor starvation but not complete nutrient deprivation, the localization of mTOR on lysosomes was increased at the same time that mTOR kinase activity was lost (Korolchuk et al., 2011). Here I report that, as shown in Figure 27, the high colocalization with the lysosome but little kinase activity of mTOR upon growth factor starvation but not total nutrient deprival does not happen only in HeLa cells, but it is also observed in untransformed RPE1 cells.

In any serum condition, MARK4-depleted cells show a localization pattern of the lysosomal marker LAMP1 that differs from what is found in control-depleted cells. Instead of the uniform distribution through the cytosol of control-depleted cells, MARK4-depleted cells have their lysosomes clustered around the nucleus. With a phenotype reminiscent of MARK4-depleted cells, Styers et al. (Styers, 2004) showed that lysosomal distribution is modified in fibroblasts from vimentin-deficient mice. Moreover, it is known that cells with disrupted intermediate filament cytoskeleton, namely vimentin, have a reduced autophagosome content phenotype (Blankson, 1995; Styers, 2004; Toivola et al., 2005), similar to what we saw in cells where MARK4 expression is suppressed. The severe loss of vimentin fibers in MARK4-depleted cells is consistent with an abnormal lysosomal distribution and lowered inducible autophagic response also observed in these cells. However, the mechanism that connects vimentin with lysosomal sorting and the autophagic response is still poorly understood. This lack of knowledge makes it tough to predict the putative MARK4 substrate that is responsible for the weakened vimentin cytoskeleton solely based on a systematic literature review. For a reliable identification of the factor or factors involved in this MARK4 mediated regulation of the vimentin cytoskeleton, an unbiased screen could be performed where the MARK4 depletion induced vimentin phenotype could be rescued. Furthermore, a functional link between vimentin and microtubule structures has already been found (Whipple et al., 2008).

Reported in first hand in this study is the importance of MARK4 for the inhibition of MAP4 binding to the microtubules when cells are subjected to serum starvation. Semenova et al. (Semenova et al., 2014) propose that MAP4 regulates directed microtubule transport in two ways: it inhibits minus-end directed transport by blocking the movement of dynein motors along the microtubules and stimulates plus-end-directed transport through the interaction with cargo-bound $p150^{Glued}$ that increases the processivity of kinesin-2 motors. Since CS proteins are known dynein-dynactin cargo, I used them as probes of minus-end directed transport along the microtubules to verify if MAP4 abundance at microtubules in MARK4-depleted cells set back minus-end transport. I found out that CS markers PCM1, CEP290 and WDR8 were dispersed throughout the cell in MARK4-depleted cells, whereas in control-depleted cells CS protein localization was more concentrated around the microtubule organizing center (a microtubule minus-end abundant zone). Moreover, consistent with a failure to displace MAP4 from the microtubules, OFD1 CS dynamics upon serum starvation confirms that in MARK4-depleted cells minus-end microtubule transport dominates over minus-end transport.

It is credible that the defect of MARK4-depleted cells to displace MAP4 from the microtubules has a disruptive effect on the transport of essential ciliary components along the microtubules in a predominantly minus-end direction, therefore with the bearing of the basal body where the ciliary assembly is taking place. If we deplete MAP4 in MARK4-depleted cells, we would be removing the constraint to ciliogenesis posed by the increased inhibition of minus-end directed transport caused by MAP4 and a rescue, at least partial, of MARK4's ciliogenesis defect would be expectable. Here I could not demonstrate that MAP4 depletion has any alleviating effects on the defect of MARK4-depleted cells to ciliate. This result is explained either because the MAP4 accumulation phenotype in MARK4-depleted cells and consequent CS protein dispersal has no relation with ciliogenesis or because of the adverse effects of MAP4 depletion on ciliogenesis balance the benefits that its removal may have in an increased minus-end directed transport to the basal body. The fact that MAP4 depletion does not decrease the probability of a given cell already depleted of MARK4 to form cilia indicates that MAP4 may act downstream of MARK4 in the same ciliogenesis pathway. Further inquiries about the details of this pathway and its plausible connections with vimentin intermediate filament cytoskeleton and lysosome and autophagy functions have here preliminary data at their disposal.

Actin has also been identified as a participant in autophagosome formation (Aguilera et al., 2012; Mi et al., 2015). However, contrary to what happens with vimentin and MAP4, cells depleted of MARK4 do not appear to have an altered actin cytoskeleton compared to control-depleted cells (results not shown).

The link between autophagy and ciliogenesis was put forward in 2013 in a back-to-back publication of Pampliega et al. (Pampliega et al., 2013) and Tang et al. (Tang et al., 2013). Even though both these papers uncover a particular aspect of cell biology that appears to demonstrate a link between starvation-induced ciliogenesis and autophagy, their results are barely overlapping and sometimes even contradictory (Orhon et al., 2014). These results of our depletion of ATG5 in RPE1 cells are in agreement with the findings of Pampliega et al. (Pampliega et al., 2013). As I did here for RPE1 cells, these authors also reported an increase in the ability to ciliate of ATG5 null MEFs that were cultivated in serum rich medium and the faster kinetics of the ciliation process. Tang et al. (Tang et al., 2013), on the other hand, did not find $Atg5^{-/-}$ MEFs to be more ciliated than wild-type cells in medium supplemented with serum. They did report, however, that 24 hours after serum starvation, $Atg5^{-/-}$ MEFs were less probable to be ciliated than wild-type. The same happens with RPE1 cells. ATG5-depleted cells have in fact faster ciliogenesis kinetics but the total fraction of ciliated cells peaks at slightly above 60%. In the subsequent hours, the fraction of ciliated cells decreases gradually to slightly below 60%, which compared with 80% of ciliated cells for the control group indicates that autophagy-deficient cells have difficulties to achieve all its ciliation potential. Therefore, in RPE1 cells, autophagy plays a dual role in its dance with ciliogenesis: in normal conditions, it represses the ciliogenesis program, but it is also necessary for the cell to achieve full ciliation ability and to be capable of performing cilia maintenance.

So far we can conclude that MARK4-depleted cells have an attenuated autophagic response to serum withdrawal caused either by a defect in mTORC1 inhibition, vimentin cytoskeleton regulation or MAP4 removal from the microtubules. I proceeded to investigate if OFD1 CS degradation occurs in the same fashion in RPE1 as reported by Tang et al. (Tang et al., 2013) in MEFs. I found out that in RPE1 cells there is indeed OFD1 degradation but, contrary to what was previously reported for MEFs, the primary degradation pathway in this cell line is via proteasome degradation and not autophagy. Moreover, when de novo protein synthesis is not inhibited, the differences in protein levels are not even noticeable. What is clear in the results is that

MARK4 influences the post-translational state of OFD1, apparent in the different mobilities in an acrylamide gel of OFD1 protein bands of MARK4 and control treated total cell extracts. If we take as valid the conclusion that upon serum starvation cells respond by degrading a large pool of its OFD1 protein but we observe that the overall protein levels remain similar before or after the starvation, we are forced to conclude that, upon serum starvation, the cell undergoes a massive replacement of its OFD1 pool. Such a time coordinated massive turn-over of a CS protein is intriguing, but it is possible that has something to do with the OFD1 CSs function in inhibiting ciliogenesis reported by Tang et al. (Tang et al., 2013).

It would be very useful for further understanding of CS function to perform a characterization of OFD1 and other CS proteins post-translational modifications in different growth conditions. The understanding of how post-translational modifications of CS proteins correlate with various phases of the cell cycle or cellular proliferative states could reward valuable tools for disease diagnostics and research and reveal novel targets for therapy.

I was able to show that artificial degradation of the CS pool of OFD1 in cells depleted of MARK4 was enough to restore the capacity of these cells to ciliate. Using two distinct siRNA sequences to target OFD1 mRNA yielded similar results, with an efficient rescue of ciliation of MARK4-depleted cells but not of cells depleted of Cep164. Cep164 depletion has a strong phenotype of cilia loss caused by defects in the distal appendages of the mother centriole that render it unable to dock a ciliary vesicle and become a basal body (Schmidt et al., 2012). OFD1 does not appear to have any influence on this process since the co-depletion of Cep164, and OFD1 does not alter the probability of Cep164 depleted cells to ciliate.

The fact that OFD1 depletion does not rescue ODF2 depletion ciliogenesis phenotype indicates that either MARK4 mediated processes of degradation and correct spatial organization of OFD1 upon serum starvation and ODF2 recruitment to the basal body have no relation with each other or OFD1 at the CSs prevents ODF2 to accumulate at the basal body. If the second is true, the failure of OFD1 depletion to rescue ciliogenesis in previously ODF2-depleted cells should be expected. Overall levels of ODF2 were small in these cells and not enough to promote ciliary extension even if its recruitment to the basal body was unhindered by the disappearance of the CS pool of OFD1. This mechanism is consistent with the partial restoration of ODF2 levels at the centrosome in cells subjected to MARK4 and OFD1 double knock-down and reinforces the idea put forward in Tang et al. (Tang et al., 2013) that OFD1 at the centriolar satellites may have the role of preventing ciliation of cycling cells.

V. Chapter 3: MARK4 and TTBK2 interactions with CP110 and Cep97

V.I. Introduction

Ciliogenesis occurs in most mammalian cells (Bowser and Wheatley; Wheatley et al., 1996) when they exit the cell cycle and enter a quiescent state (Tucker et al., 1979a, 1979b). The process of bringing together the incredible structure that is a photoreceptor cone cell of the retina of an eagle for example, daunting as it is in its complexity, shares its mechanism to a significant part with the formation of the flagella of the green alga *Chlamydomonas reinhardtii*.

In the molecular biology of centrosomes and cilia lab, we have been investigating proteins that control cilia formation. After conducting a screen for identification of protein kinases positive regulators of ciliogenesis, MARK4, and TTBK2, among others, were identified as so (Kuhns et al., 2013). The particular upstream signals that activate MARK4 and TTBK2 kinases in their role in ciliogenesis are not known, and little is known about their substrates. They were put together in promoting cilia formation upstream of CP110-Cep97 complex removal from the basal body (Goetz et al., 2012; Kuhns et al., 2013) (see Introduction for more information about CP110-Cep97 complex regulation).

MARK4 is a serine/threonine kinase that phosphorylates MAPs at the KXGS motif of the microtubule-binding domain of tau and other MAPs. This phosphorylation disrupts the interaction between the MAP and the microtubule leading to a detachment of both (Drewes et al., 1995, 1997; Jenkins and Johnson, 2000). As for localization, MARK4 can be found in the nucleus, centrosomes and midbody (Kuhns et al., 2013; Magnani et al., 2009; Rovina et al., 2014; Trinczek et al., 2004). Structurally, MARK4 is a 752-residue-long polypeptide divided into the protein kinase domain, the ubiquitin-associated (UBA) domain and the kinase associated domain (Naz et al., 2013). MARK4 belongs to a family of four proteins (MARK1 to 4) which have a highly conserved sequence. The atomic coordinates of MARK 1, 2 and 3 has been determined by crystallography. Comparison of the structures, including MARK4's prediction, reveals that all the isoforms have a similar domain organization (Marx et al., 2006; Panneerselvam et al., 2006). Seemingly, it is assumed that the regulation of MARK4 is identical to that of the other MARK members. MARK4 is activated by liver kinase B1 (LKB1) and MARK Kinase (MARKK) that phosphorylate T214 in the T-loop (Brajenovic et al., 2004; Lizcano et al., 2004; Timm et al., 2003). Inhibition of MARK4 is achieved by a second phosphorylation on the T-loop, this time on S218 by the glycogen synthase kinase 3b (GSK3b). This inhibition is caused by an altered T-loop conformation, consequence of the S218 phosphorylation does not allow MARK4 to recognize its substrates (Timm et al., 2008). Inhibition of MARK4 is also achieved through ubiquitination. Polyubiquitinated MARK4 interacts with the deubiquitinating enzyme, ubiquitin-specific protease (USP)9X. Mutants of MARK4 that are not able to interact with USP9X are not phosphorylated at T214. The model of MARK4 regulation via ubiquitination proposes that MARK4's UBA domain interacts with the polyubiquitin chain and through conformational changes precludes LKB1's access to the T214 site. Polyubiquitin removal from MARK4 by USP9X allows MARK4's UBA domain to interact with the catalytic domain, making the T-loop accessible to LKB1 (Al-Hakim et al., 2008).

MARK4 knock-down experiments reveal a relative increase in the number of non-ciliated cells with two CP110 or Cep97 foci at the centrosomes (Kuhns et al., 2013). This result can have two interpretations: increased number of cells are unresponsive to the serum starvation to form cilia or, an increased number of

cells is not able to proceed with axoneme extension because of the remaining inhibitory CP110-Cep97-Kif24 complex at the distal ends of the mother centrioles. The ectopic depletion of CP110 on top of MARK4 depletion was enough to partially rescue MARK4's primary cilia loss phenotype (Kuhns et al., 2013). Therefore, we can place MARK4 upstream of CP110 removal from the mother centriole in the ciliogenesis pathway.

TTBK2 belongs to the casein kinase 1 (CK1) superfamily (Houlden et al., 2007; Manning, 2002; Sato et al., 2006). As other kinases of the superfamily, TTBK2 can phosphorylate both the MAP tau and tubulin itself (Ikezu and Ikezu, 2014; Sato et al., 2006; Takahashi et al., 1995). The primary phenotype of mutant TTBK2 is associated with a type of severe neurodegeneration called autosomal dominant spinocerebellar ataxia type 11 (SCA11) (Houlden et al., 2007). The mechanism linking the TTBK2 mutant and SCA11 is still unknown, but it is plausible that the essential role that TTBK2 plays in ciliogenesis initiation is the link to the disease (Goetz et al., 2012). TTBK2 is a centrosomal protein composed of 1244 a.a. with an N-terminal kinase domain. The C-terminal's structure and function are not well studied except for the identification of an SxIP motif (Jiang et al., 2012). Homology studies indicate that this well conserved region downstream of the kinase domain should be responsible for kinase localization and substrate recruitment(Goetz et al., 2012; Liao et al., 2015). TTBK2 is localized to the base of primary cilia or the distal end of the mother centriole where it is necessary for IFT88 recruitment and removal of CP110 before axoneme extension (Goetz et al., 2012). Genetic deletion of TTBK2 in murine cells leads to an inability to ciliate, being the persistence of CP110 at the basal bodies a distinguishing feature of these cells. Overexpression of the kinase domain of TTBK2 in these cells can partially rescue the ciliogenesis defect (Goetz et al., 2012). Additionally, recombinant TTBK2 kinase domain was reported to phosphorylate Cep97 in vitro (Oda et al., 2014).

Here I start by presenting the work performed establishing a biochemical method that proved by biochemical means that MARK4 localizes at the centrosome and that the variation of the amount of ODF2 protein recruited to that organelle depends on the MARK4 kinase activity (Kuhns et al., 2013). With the collaboration of Bachelor of Science student Evangeline Kang, I investigated if MARK4 influences CP110 removal directly by interacting with the CP110-Cep97 complex or if its activity is critical for ciliogenesis in a more indirect way. Finally, once MARK4 and TTBK2 were implicated as upstream regulators of the CP110-Cep97 complex removal from the mother centriole in the ciliogenesis process, I wanted to know more details on how these kinases interact with CP110 and Cep97 and if there is an overlap in their role upstream of axoneme extension.

V.II. Results

V.II.I. MARK4 in ciliogenesis

V.II.I.I.MARK4 is at the centrosome and controls local levels of ODF2

Based on microscopy images of cells over-expressing fluorescent proteins fused with MARK4, the localization of this kinase appears to be cytoplasmic with a particular signal on the centrosome (Kuhns et al., 2013; Trinczek et al., 2004), basal body and possibly on the ciliary axoneme (Kuhns et al., 2013). To demonstrate the presence of MARK4 at the centrosome/basal body by biochemical methods, I optimized a small scale centrosome purification protocol that allows easily and with a small amount of biological material the determination of the localization and abundance of specific proteins at the centrosome. Figure 38A shows the result of the centrosome purification process performed with the lysate of murine NIH 3T3 cells stably expressing LAP-MARK4 wild type or the kinase-dead mutant under the control of a TET-on promoter. The centrosomal fraction, labeled number 3, can be identified by the protein concentration peak on the graph and positive γ-tubulin and ODF2 signals in the immunoblot. In this fraction, but not in the adjacent ones, we can see that GFP-MARK4 is present whenever is being expressed either as wild-type or kinase-dead mutant.

This work was done in the context of the Kuhns et al. publication in 2013 where we determined MARK4 localization at the centrosome and if it's kinase activity was determinant for ODF2 recruitment to the basal body. By performing a mini centrosome prep followed by quantitative immunoblot it was possible to quantify the influence of MARK4 kinase activity in ODF2 recruitment to the basal body. In Figure 38B it is shown that the over-expression of wild type MARK4 leads to a greater accumulation of ODF2 in the centrosomal fraction of the cell lysate. This result gives support to the idea that MARK4 activity is one of the determinants of ODF2 localization at the basal body of ciliated cells. The over-expression of the kinase-dead mutant of MARK4 does not make the ODF2 concentration at the basal body to differ from control cells, where no over-expression was induced (Figure 38B).

V.II.I.II.MARK4 interacts with Cep97 in vivo

I wanted to know if MARK4 interacted in vivo with the CP110-Cep97 complex. To maximize the effects of MARK4 kinase activity all identified residues that upon phosphorylation render MARK4 a hyperactive kinase (ka) were mutated (S26E and T214E)(Wissing et al., 2007). A further mutation (K88A) was introduced in the hyperactive mutant to increase the likelihood of MARK4 to stay bound to its substrates. This mutation in the kinase catalytic site where a magnesium ion is coordinated renders the kinase dead, that is, unable to catalyze the phosphorylation reaction. Lysine 88 is one of the residues necessary for MARK4 coordination with one of the magnesium ions essential for ATP to bind the enzyme and feed the kinase catalytic activity (Jenardhanan et al., 2014; Marx et al., 2006). This MARK4 mutant labeled kinase active dead (kad) is potentially a good substrate entrapment mutant.

Co-over-expression of FLAG-tagged Cep97 with EGFP-MARK4 in HEK293T cells, followed by immunoprecipitation (IP) revealed that Cep97 interacted with MARK4-kad but not with MARK4-ka (Figure 39A-B). We can see in Figure 39B that none of the MARK4 mutants interact strongly with CP110, at least in the conditions tested. A second effect noticeable in the co-over-expression of Cep97 with MARK4 is the difference in electrophoretic mobility of Cep97 when exposed to the different kinase mutants (Figure 39A-B). When over-expressed with MARK4 ka mutant, Cep97's distinct three band pattern in an immunoblot

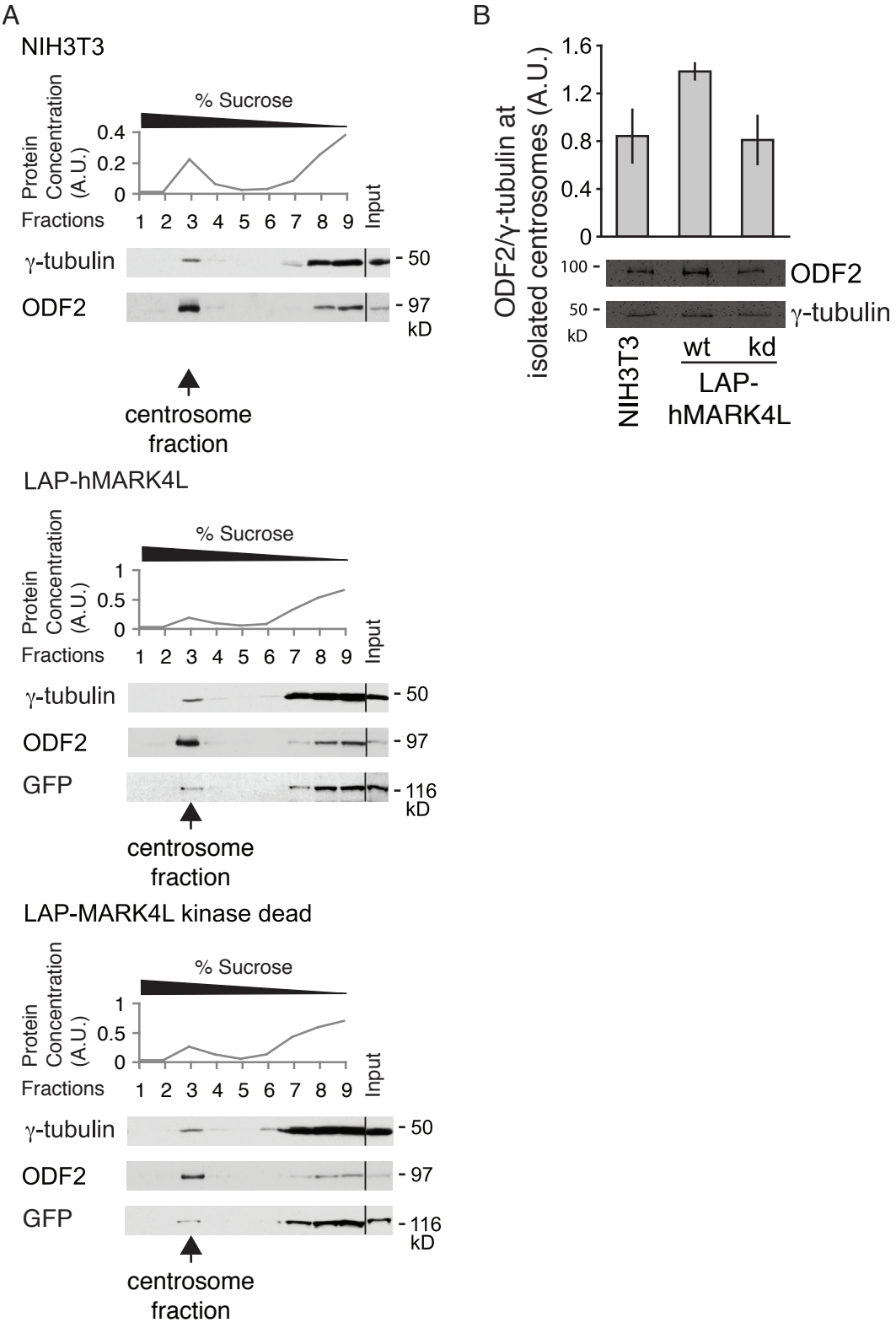

Figure 38: **MARK4 activity modulates ODF2 recruitment to the centrosome**. Centrosomes from NIH 3T3 cells stably expressing either LAP-hMARK4L wild type or kinase dead mutant under the control of the TET-on promoter were isolated by centrifugation using a discontinuous sucrose gradient. (A) immunoblot for ODF2, γ-tubulin and GFP in all the sucrose gradient fractions. (B) immunoblot for ODF2 and γ-tubulin in the centrosomal fraction. The graph shows the quantification of centrosome-associated ODF2 normalized to γ-tubulin. Data are means ± SD of three independent experiments. Published in Kuhns et al., 2013.

changes to a single inferior line. This effect can be seen already in the input lysate, the intensity of the higher bands is lower than when the MARK4 kad mutant is present (Figure 39A-B). This result indicates that the Cep97's post-translational modifications are sensitive to the expression level of MARK4. These band mobility changes are usually caused by electrostatic charge variations arising from covalent modifications of the polypeptide.

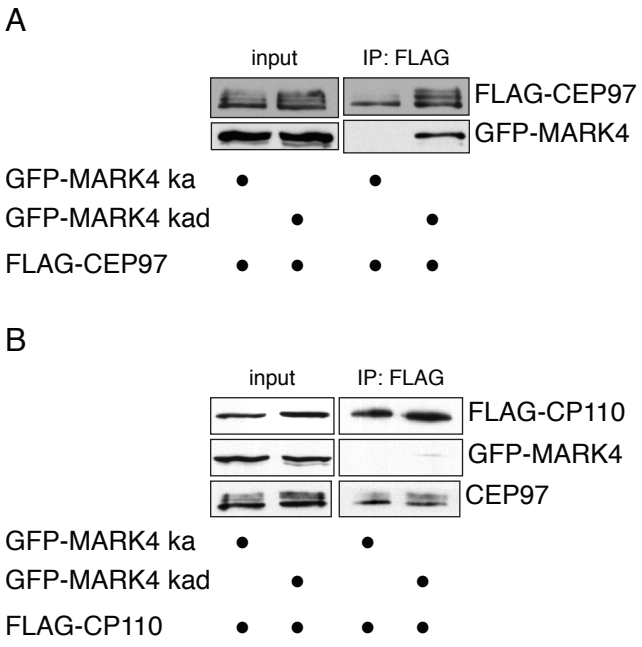

Figure 39: **Cep97 interacts preferentially with the MARK4 kinase entrapment mutant**. HEK293T cells were transiently transfected with FLAG tagged CP110, Cep97 or MARK4 and GFP tagged MARK4 as indicated. Catalytic active (ka), catalytic active and kinase dead (kad) mutants of MARK4. Immunoprecipitations (IP) were performed using anti-FLAG agarose. Interacting proteins were detected by immunoblotting.

V.II.I.III.In vitro phosphorylation of CP110 and Cep97 by MARK4 and PLK-1

To know if CP110 and Cep97 are in vitro substrates of MARK4, we purified two recombinant truncations for each CP110 and Cep97 proteins. The schematic representation of these constructs can be seen in Figure 40. For CP110, I created two GST tagged truncations comprising the N-terminus including the Cep97 binding domain (GST-CP110-N, a.a. 1-300) and the middle region that includes the site of interaction with centrosomal protein of 76 kDa (Cep76) (Tsang et al., 2009) (GST-CP110-M, a.a. 301-600). Cep97's truncations comprise the N-terminal region that harbors eight leucine rich repeats and tagged with a 6xHis (His-Cep97-N, a.a. 1-260) and the GST-tagged C-terminal region where binding of CP110 takes place. Recombinant 6xHis tagged MARK4 was purified from *Escherichia coli* (*E. coli*). A particular mutation on MARK4's already mentioned S26 to A26 was performed, to prevent MARK4 auto-phosphorylation. By doing this, we intended to prevent an auto-phosphorylation band from occurring at 80 kDa. As expected, MARK4 did not show auto-phosphorylation in the in vitro kinase assays (Figure 41, buffer lane). The T214E mutation was introduced (MARK4-ka), to increase MARK4 activity. This phospho-mimicking mutation introduced in

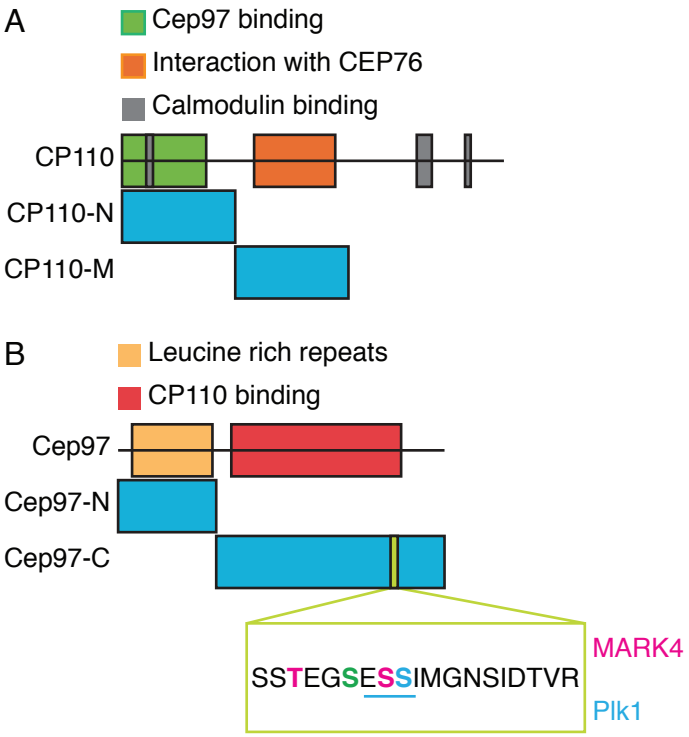

Figure 40: **CP110 and Cep97 truncations**. (A) Schematic representation of CP110 constructs used in this study. (B) Schematic representation of Cep97 constructs used in this study with inset representing MARK4 phosphorylated residues in magenta and Plk1 phosphorylations in cyan. Residue in green is phosphorylated by both kinases.

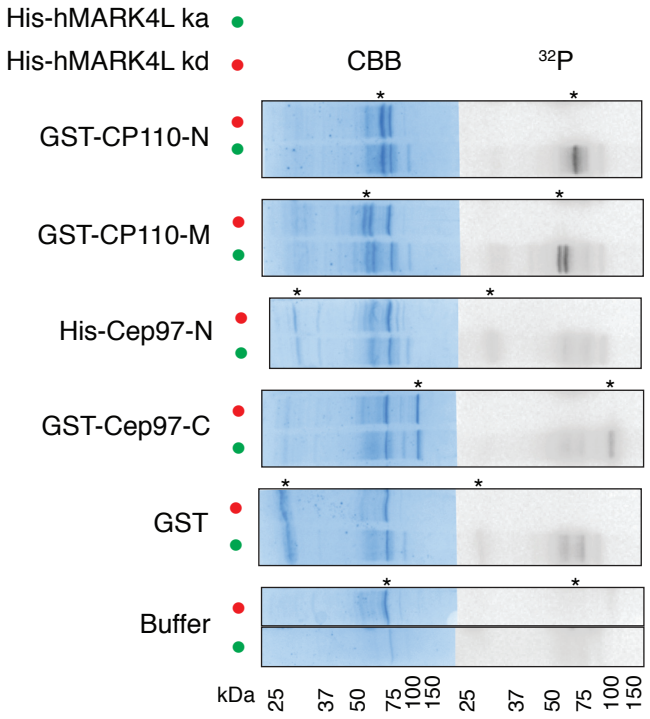

Figure 41: **CP110 and Cep97 are phosphorylated in vitro by MARK4**. Purified 6His-MARK4L, either catalytic active (ka) or kinase dead (kd), was incubated with recombinant CP110 and Cep97 truncations. GST was used as a negative control. Samples were subjected to SDS-PAGE followed by autoradiography (^{32}P) and Coomassie Brilliant blue staining (CBB). Asterists indicate the relevant bands. Experiment performed by Evangeline Kang.

MARK4 activation loop stabilizes the interaction with its partners (Kuhns et al., 2013; Matenia et al., 2005). As mentioned above, the mutation K88A was introduced to the MARK4 coding sequence (MARK4-kd), to inhibit MARK4 protein-kinase activity.

By combining the tagged CP110 and Cep97 recombinant proteins with MARK4 and radioactive ATP I could detect if any of the fragments were an in vitro MARK4 substrate. Figure 41 shows the existence of MARK4 specific phosphorylation sites in CP110, both in its N-terminal Cep97 binding domain and in the region that comprises its interaction site with Cep76. The phosphorylation was specific to GST-CP110, as GST alone was not phosphorylated by MARK4-ka. As for Cep97 phosphorylation by MARK4, we can see in Figure 41 that the Cep97 fragments do not appear to be phosphorylated by MARK4 given that the intensity of the radioactive Cep97 bands is much lower than the radioactive bands of both CP110 fragments. Considering the background phosphorylation that the His-hMARK4 ka mutant causes when it reacts with itself (Figure 41, buffer lane) or with the GST tag (Figure 41, GST lane, bands at 75 kDa), I consider that MARK4 did not specifically phosphorylate GST-Cep97 in vitro under the conditions used here.

To determine which sites MARK4 phosphorylates in the CP110-Cep97 complex, CP110 or Cep97 were pre-incubated with the hyperactive form of MARK4 in the presence of ATP and sent for mass spectrometric analysis for identification of phosphorylated residues. I included Cep97 in this analysis because Cep97 and Mark4-kd intensely interacted in vivo. Six phosphorylated sites were found in CP110 and, inter-

Table 1: **Phosphorylation sites by MARK4 kinase identified on CEP97 and CP110 peptides by mass spectrometric analysis**. Purified catalytic active 6His-MARK4L was incubated with recombinant CP110 and Cep97 truncations. Samples were subjected to SDS-PAGE, the appropriate bands were excised and the protein content was subjected to trypsin digestion followed by mass spectrometry for identification of phosphorylated residues.

Protein name	Phosphorylated peptide	Phosphorylation site
CEP97	NNFPASVHTTRY**S**R	S378
	SSTEG**S**ESSIMGNSIDTVR	S728
	SSTEGSE**S**SIMGNSIDTVR	S730
	SS**T**EGSESSIMGNSIDTVR	T725
	SSTEGSESSIMGN**S**IDTVR	S736
CP110	IQEASL**S**TESFLPAQSESISLIR	S21
	TGHPTVLE**S**NSDFK	S337
	SLTG**S**YAKLPSPEPSMSPK	S360
	LHEPYA**S**SQCIASPNFGTVSGLKPASMLEK	S510
	LHEPYAS**S**QCIASPNFGTVSGLKPASMLEK	S511
	NC**S**LQTELNK	S536

estingly, two phospho-peptides were identified in Cep97 (Table 1). Because I have used recombinant proteins (MARK4 and Cep97) in these assays, I consider as unlikely that a contaminating kinase phosphorylates Cep97. One phospho-site found in Cep97 interestingly overlaps with a PLK-1 site (Table 1, Table 2 and Figure 40B, bottom), raising the question of whether Cep97 is a PLK-1 substrate.

By performing a radioactive labeling assay using CP110 and Cep97 truncations as substrates and GST-PLK-1 as the kinase, it was possible to identify the C-terminal domain of Cep97 as an in vitro substrate of PLK-1 (Figure 42). Regarding CP110 phosphorylation by PLK-1 is more unclear. There is just some background noise coming from the region where the purified GST-CP110-N runs on a 10% SDS-PAGE gel. This signal is consistent across experiments but not strong enough to support the claim that CP110 is a substrate of PLK-1.

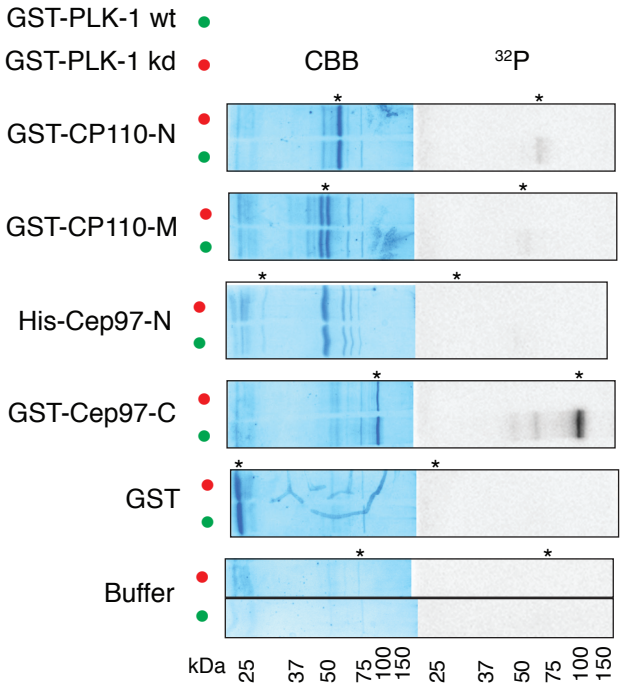

Figure 42: **Cep97 is phosphorylated in vitro by PLK-1**. Purified GST-PLK-1, either wild type (wt) or kinase dead (kd), was incubated with recombinant CP110 and Cep97 truncations. GST was used as a negative control. Samples were subjected to SDS-PAGE followed by autoradiography (^{32}P) and Coomassie Brilliant blue staining (CBB).

Mass spectrometry of Cep97 pre-phosphorylated with recombinant PLK-1 shows that Cep97 can be phosphorylated by PLK-1 in the pleiad of sites, shown in Table 2. The overlap of one PLK-1 and MARK4 phospho-site opens the possibility for the existence of a regulatory cross-talk between the two kinases.

Table 2: **Phosphorylation sites by PLK1 kinase identified on CEP97 peptides by mass spectrometric analysis**. Purified GST-PLK1 was incubated with recombinant Cep97 truncation. Samples were subjected to SDS-PAGE, the appropriate bands were excised and the protein content was subjected to trypsin digestion followed by mass spectrometry for identification of phosphorylated residues.

Protein name	Phosphorylated peptide	Phosphorylation site
CEP97	ESDLGDV**S**EEHGEWNK	S8
	ESSNNEQDN**S**LLEQYLTSVQQLEDADER	S770
	NDLHLEDIQTDEDKLNC**S**LLSSES**T**FMPVASGLSPLSPTVELR	S397 – T404
	QLMNQ**S**QNEELSPLVPVETR	S308
	SSTEG**S**ES**S**IMGNSIDTVR	S728 – S731

V.II.II. TTBK2 in ciliogenesis

V.II.II.I.TTBK2 centrosomal localization is Cep164 and Cep123 dependent

To be able to compare the role of MARK4 and TTBK2 in ciliogenesis, it was necessary to perform a preliminary characterization of TTBK2 in RPE1 cells. TTBK2 is localized at the centrosome and/or at the base of the primary cilium (Figure 43C). A close-up analysis (Figure 43A) indicates that TTBK2 localizes at the distal appendages of the mother centriole. Its signal overlaps with Cep164 fluorescence but less so with sub-distal or transition zone proteins ODF2 and NPHP1 respectively. Regarding antibody specificity, panels C and D of Figure 43 shows that the TTBK2 signal significantly decreases upon treatment with TTBK2 tar-

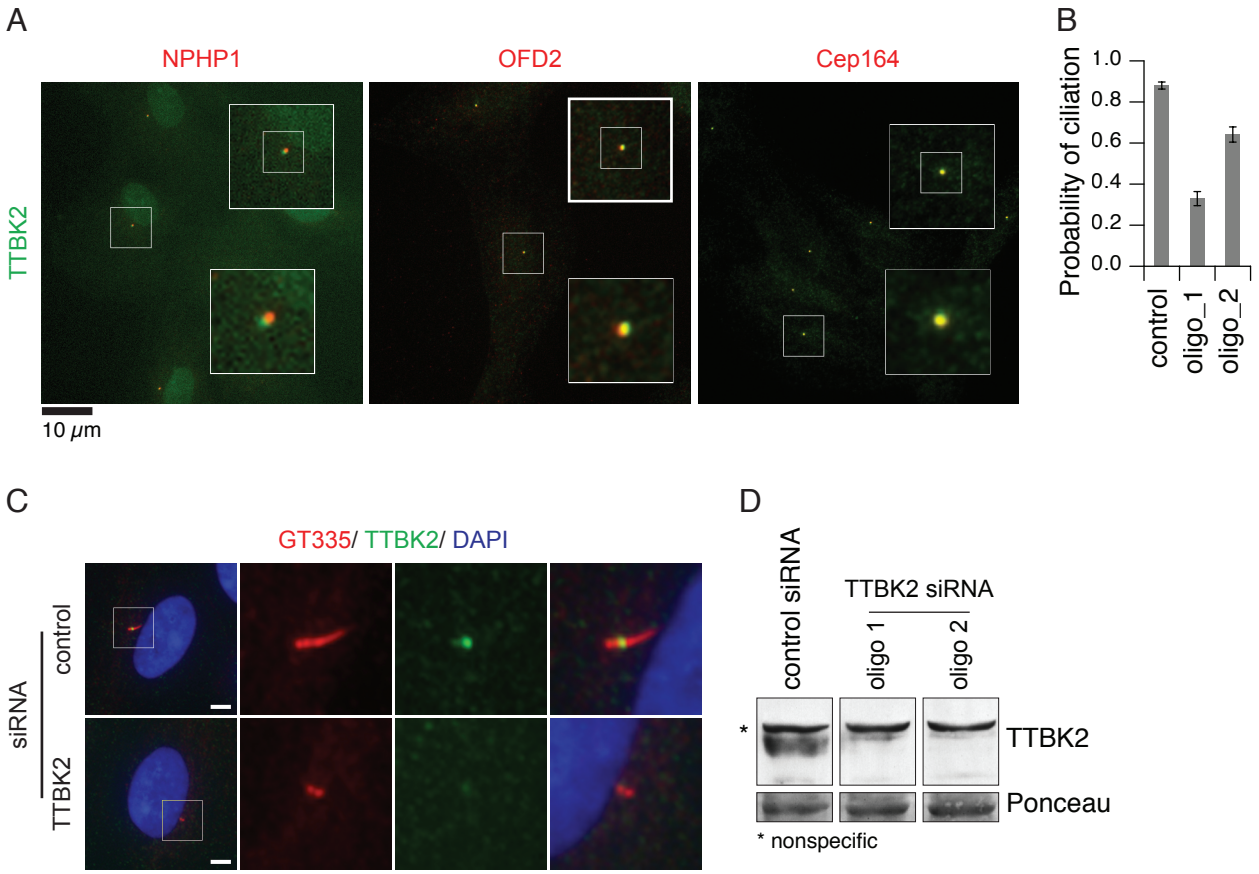

Figure 43: **TTBK2 is a positive regulator of ciliogenesis and localizes to the distal appendages of the mother centriole**. RPE1 cells, treated with control or TTBK2 siRNA, were serum starved for 48 h. (A and C) Cells were stained for TTBK2, polyglutamylated tubulin (GT335), Cep164, NPHP1, ODF2 and DAPI. Regions within the white boxes are depicted with higher magnification on the right and bottom. Scale bar is 5 μm. (B) Percentage of ciliated cells based on polyglutamylated tubulin staining. Data are means ± SEM of three independent experiments. $N_{control}$=300; N_{oligo_1}=255; N_{oligo_2}=212. (D) Total cell extracts of control and TTBK2-depleted RPE1 cells were analysed by immunoblot. Ponceau-S staining served as a loading control.

geting siRNA. TTBK2 depletion leads to ciliogenesis defects as shown in Figure 43B and Figure 46A and as has been previously reported (Goetz et al., 2012).

The presence of TTBK2 at the centrosomes varies along the cell cycle (Figure 44A). Its signal is active in cells undergoing G1 phase but absent in G2, metaphase or telophase (Figure 44A). A high TTBK2 presence can also be detected in the midbody (Figure 44A) which is in agreement with published results (Chaki et al., 2012). The centrosomal localization dynamics of TTBK2 along the cell cycle resemble those of Cep164 (Schmidt et al., 2012). TTBK2 co-immunoprecipitates with Cep164 when both proteins are over-expressed in HEK293T (Figure 44C). GFP-tagged Cep164 interacted with FLAG-tagged TTBK2 only when the expressed GFP construct carried an entire WW domain harbored in the N-terminus (Figure 44B-C). The fact that this WW domain has been shown to be crucial for ciliogenesis (Schmidt et al., 2012) indicates that Cep-164-TTBK2 interaction is critical for primary cilia formation.

I wanted to know if TTBK2 localization depended only on the Cep164 interaction or if there were additional components involved in its targeting to the distal appendages of the mother centriole. Analyzing the distal appendages protein assembly pathway, I decided to investigate if Cep123 had any role in TTBK2 recruitment. Both Cep164 and Cep123 assembly in the distal appendages is made via the Cep83 branch, but Cep164 assembly requires that SCLT1 is present whereas Cep123 just requires Cep83 (Tanos et al., 2013). The localization of Cep123 and Cep164 is mutually independent, and both proteins are required for ciliary

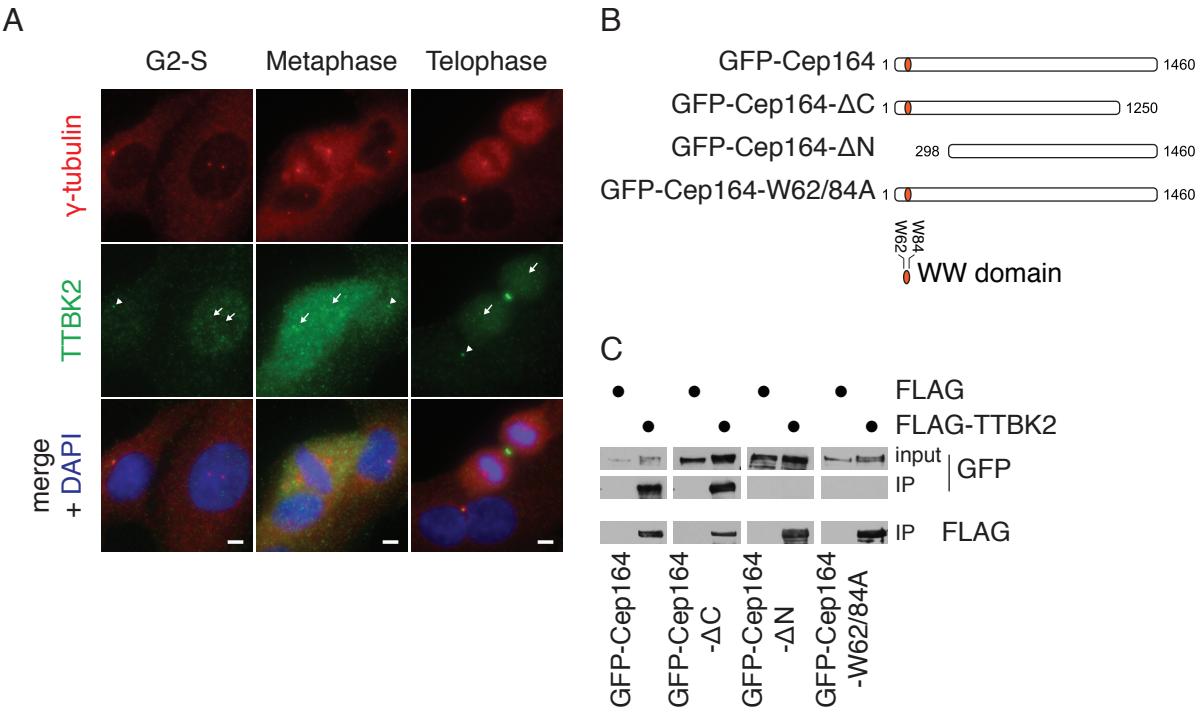

Figure 44: **TTBK2 interacts with Cep164**. (A) RPE1 cells were serum starved for 48 h and stained for TTBK2, γ-tubulin and DAPI. Centrosomes of representative cells in G1 (arrowheads) and other stages of the cell cycle (arrows) are indicated. (B) Schematic representation of Cep164 constructs used in this study. (C) HEK293T cells were transiently cotransfected with the indicated Cep164 constructs fused to GFP and FLAG tagged TTBK2. Immunoprecipitations (IP) were performed using anti-FLAG agarose and interacting proteins were detected by immunoblot. Images in (A) are maximum intensity projections. Scale bar is 5 μm.

vesicle docking (Sillibourne et al., 2013). By depleting Cep164 or Cep123, I found that the knock-down of either Cep164 or Cep123 resulted in a marked decrease in TTBK2 intensity at the centrosome (Figure 45B and D). Therefore, TTBK2 centrosomal localization is dependent on Cep164 and Cep123 (Figure 45A-D).

V.II.II.II.Ectopic removal of CP110 partially rescues TTBK2 depletion ciliation defect

It was previously shown that ectopic depletion of CP110 rescues the ciliogenesis defect of MARK4 depletion (Kuhns et al., 2013). If TTBK2 plays a similar role in CP110 removal, I expected that CP110 depletion would also be able to rescue ciliogenesis in cells lacking TTBK2. Indeed, as shown in Figure 46 for TTBK2, I could also partially rescue the ciliogenesis defect of TTBK2 depletion by co-depleting CP110.

V.II.II.III.IFT88 recruitment to the cilium depends on TTBK2 activity

To investigate further the role of TTBK2 in cilia formation I looked into its role in the recruitment of factors essential for cilia formation. It was previously reported (Goetz et al., 2012) that TTBK2 was necessary for IFT88 recruitment to the mother centriole and cilia elongation. I found that TTBK2 depletion was enough for ultimately prevent IFT88 binding to the mother centriole and consequently to localize in the cilium (Figure 47A-B). Cells, in which FLAG-TTBK2 was over-expressed, were able to form cilia, and localize IFT88, whereas cells overexpressing the kinase-dead TTBK2 mutant were not able to ciliate or to recruit IFT88 to the mother centriole (Figure 47C). This result indicates that TTBK2 kinase activity is necessary for IFT88 recruitment to the mother centriole and that this kinase dead is a dominant negative mutation.

Since TTBK2 localization is also determined by Cep123, I investigated if the depletion of this distal appendage protein had an impact on IFT88 recruitment to the centrosome. Cells depleted of Cep123 saw a

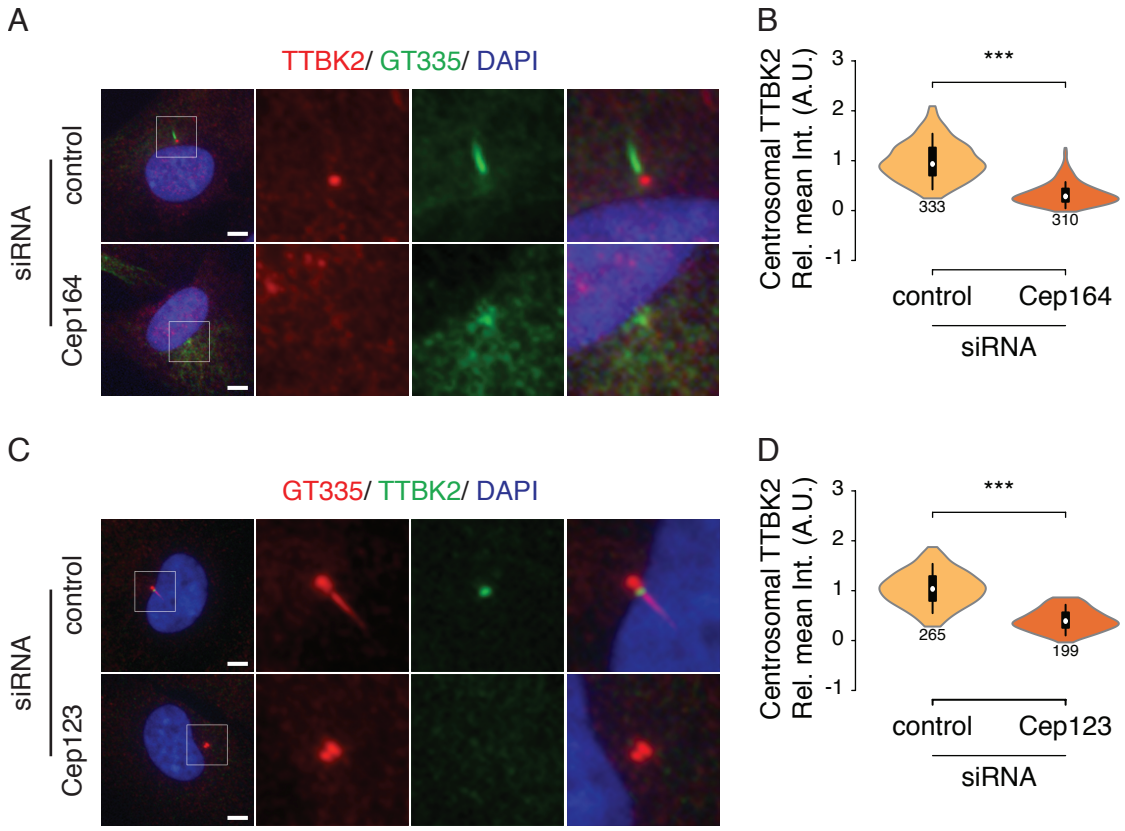

Figure 45: **TTBK2 localisation is Cep164 and Cep123 dependent**. (A andC) RPE1 cells, treated with control, Cep164 or Cep123 siRNAs, were serum starved for 48h and stained for TTBK2, polyglutamylated tubulin (GT335) and DAPI. (B and D) Violin plots show the relative TTBK2 intensity at the centrosome after control, Cep164 and Cep123 depletion in RPE1 cells in three independent experiments. *** corresponds to p<0.001. (B and D) Rel. mean Int. (A.U.), relative mean intensity (arbitrary units). Data shown is the combination of three independent experiments. The number under the violin is N. (A and C) regions within the white boxes are depicted at higher magnification on the right. Scale bar is 5 μm.

reduction in the IFT88 intensity at the centrosome but not as severely as with Cep164 or TTBK2 depletion (Figure 47D-E and A-B respectively).

V.II.III.Conjunct role of MARK4 and TTBK2 in ciliogenesis

V.II.III.I.The combined activities of MARK4 and TTBK2 contribute to cilia formation

To understand if MARK4 and TTBK2 activities could be complementary in the removal of CP110 from the distal end of the mother centriole I took advantage of the fact that for both cases, after treatment with MARK4 or TTBK2 siRNAs, circa 35% of the cells could still form cilia (Figure 48A). By performing a double knock-down of MARK4 and TTBK2, the number of ciliated cells dropped to approximately 10% of the total number of cells (Figure 48A).

When we look at the effect on CP110 removal from the mother centriole, the cells treated with the MARK4 and TTBK2 siRNA combination show an increase in the proportion of cells that have their centrosomes decorated with one or two CP110 signals and a decrease in the percentage of cells with a cilium (Figure 48B-C).

V.II.III.II. Rab8a ciliary vesicle docking is compromised in cells depleted of MARK4 and TTBK2

Cep164 and Cep123 have been reported as essential proteins involved in the process of vesicle docking to the mother centriole (Schmidt et al., 2012; Sillibourne et al., 2013; Tanos et al., 2013). The mechanism

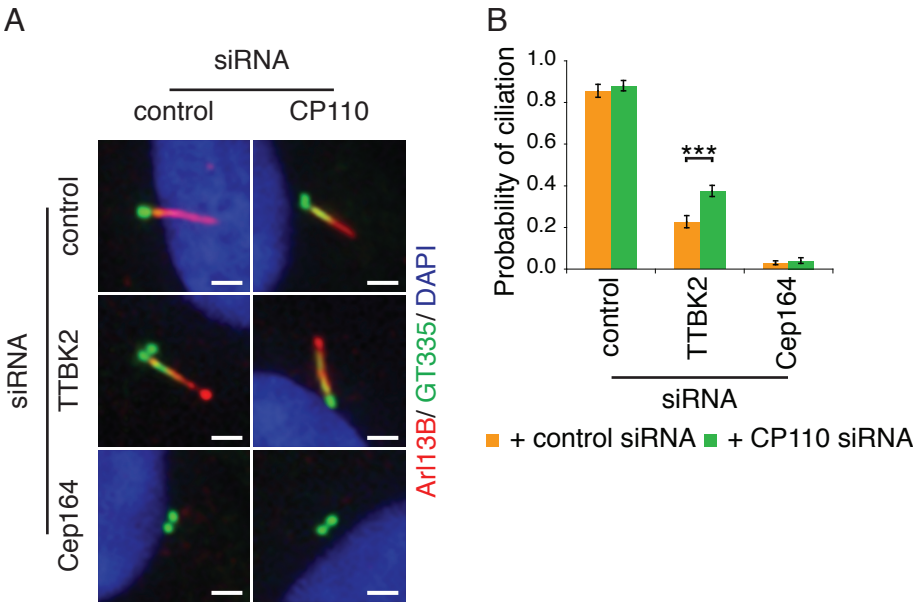

Figure 46: **Co-depletion of CP110 rescues TTBK2 depletion ciliogenesis defect**. (A and B) After treatment with control, TTBK2, or Cep164 siRNA for 24 h, RPE1 cells were subjected to control or CP110 depletion for 24 h, subsequent serum starvation for 24 h and stained for polyglutamylated tubulin (GT335), Arl13B and DAPI. (A) Scale bar is 2 μm. (B) Percentage of ciliated cells based on polyglutamylated tubulin and Arl13B staining. Data are means ± SEM of three independent experiments. *** corresponds to $p<0.001$. $N_{control}$=335, 412; N_{TTBK2}=311, 381; N_{Cep164}=360, 260.

of Cep164 action involves the binding of the GEF Rabin8 and the GTPase Rab8, mediating the association of the mother centriole and the ciliary membrane biogenesis machinery (Schmidt et al., 2012). For Cep123 no mechanistic insight has been produced so far, but published results show that ciliary vesicles fail to form when Cep123 is absent (Sillibourne et al., 2013). Currently, it is still unknown if TTBK2 plays a role in the vesicle docking process or its facilitating action towards ciliogenesis is reflected exclusively on the removal of inhibitory CP110 from the distal ends of the mother centriole to allow axoneme extension. I performed siRNA knock-down experiments using an RPE1 stable cell line that stably overexpresses Rab8a fused with an EGFP protein (Schmidt et al., 2012). As shown in Figure 49A-B, in control cells 16 hours after serum starvation, the majority of the cells presented cilia decorated with EGFP-Rab8a and polyglutamylated tubulin. Due to the small time of serum starvation, I could still find cells that had just a small EGFP-Rab8a rich vesicle associated with the centrosome and cells with no vesicle decorating either centrosomes or cilia (Figure 49A). For MARK4 and TTBK2, the depletion of the single proteins caused either the cells to reveal the association of a small vesicle with the centrosome, but had no axoneme extension, or did not show any EGFP-Rab8a associated with the centrosome (Figure 49A-B). When the TTBK2 and MARK4 siRNAs are used together in the EGFP-Rab8a stable cell line, the fraction of cells able to assemble a ciliary vesicle drops and the vast majority of cells do not have any association of Rab8a with the centrosome or cilia formation (Figure 49A-B). The results for Cep123 depletion indicate a vesicle docking defect phenotype (Figure 49A-B). The effect of Cep123 subtraction appears to be less severe as Cep164's (Schmidt et al., 2012) but it is nevertheless noteworthy.

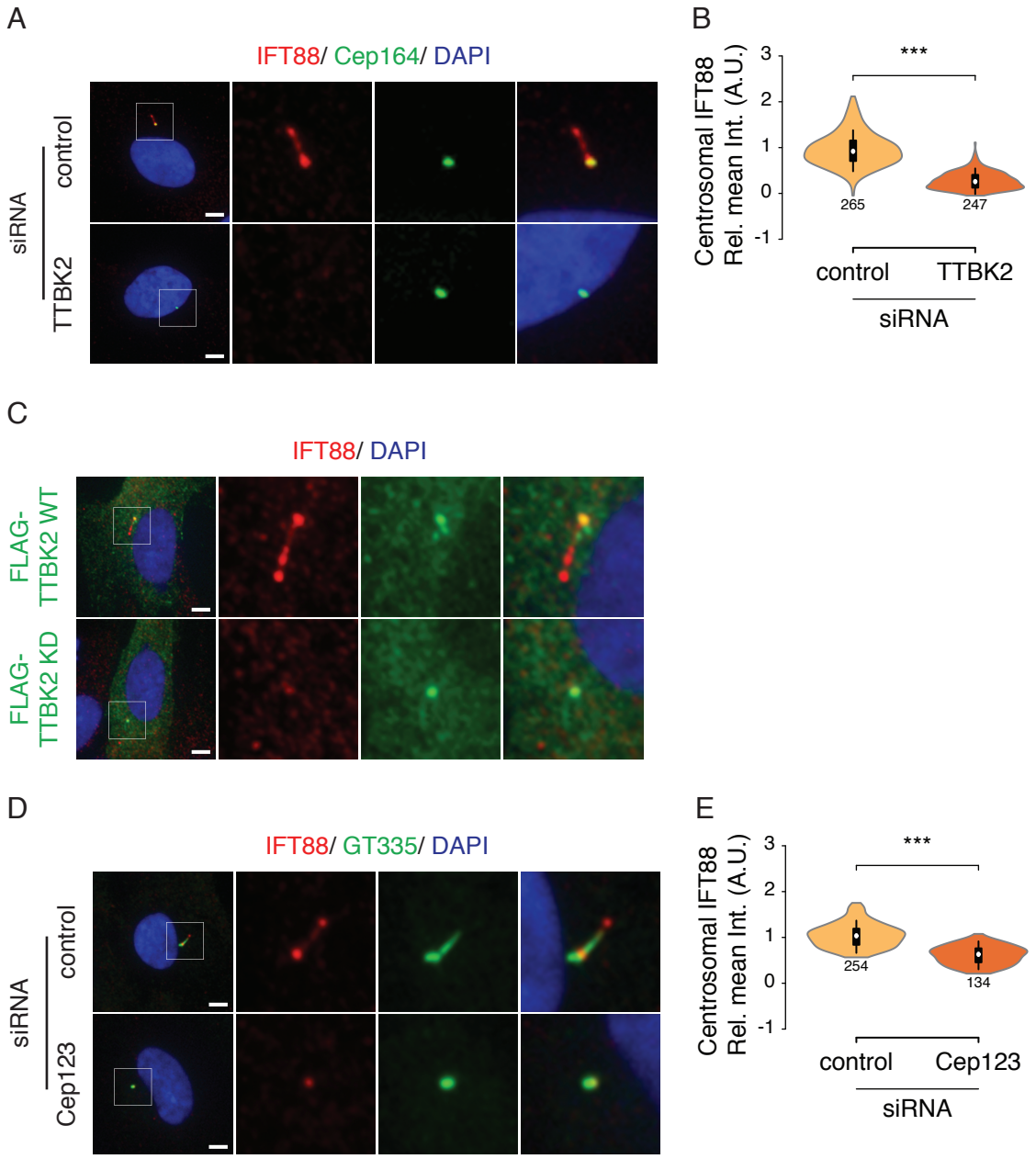

Figure 47: **IFT88 localization at the basal body is TTBK2 kinase activity dependent**. (A) RPE1 cells, treated with control or TTBK2 siRNA, were serum starved for 48 h and stained for IFT88, Cep164 and DAPI. (B) Violin plot shows the relat ive IFT88 intensity at the centrosome after control and TTBK2 depletion in RPE1 cells in three independent experiments. (C) RPE1 cells were transiently transfected with FLAG-TTBK2 WT (wild type) or FLAG-TTBK2 KD (kinase dead) constructs for 24 h, serum starved for 24 h and stained for IFT88, FLAG and DAPI. (D) RPE1 cells, treated with control or Cep123 siRNA, were serum starved for 48 h and stained for IFT88, Cep164, polyglutamylated tubulin (GT335) and DAPI. (E) violin plot shows the relative IFT88 intensity at the centrosome after control and Cep123 depletion in RPE1 cells in three independent experiments. (B and E) The number under the violin is N. (A, C and D) Regions within the white boxes are depicted at higher magnification on the right. Scale bar is 5 μm. (B and E) Rel. mean Int. (A.U.), relative mean intensity (arbitrary units).

V.II.III.III.MARK4 or TTBK2 depletions lead to transition zone anomalies

A possible consequence of the failure of the cells to successfully dock a ciliary vesicle to its mother centriole and remove the inhibitory pool of CP110 is the emergence of defects in transition zone structure and composition. It is known that if Cep164 is not present, distal appendage and transition zone protein NPHP1 fails to accumulate at these locations (Schmidt et al., 2012). To unveil if this effect manifests itself trough a direct role of Cep164 or if it is related to its interaction with TTBK2, I measured NPHP1 intensity at the centrosome upon kinase depletion. Because MARK4 may also have a role in transition zone maturation

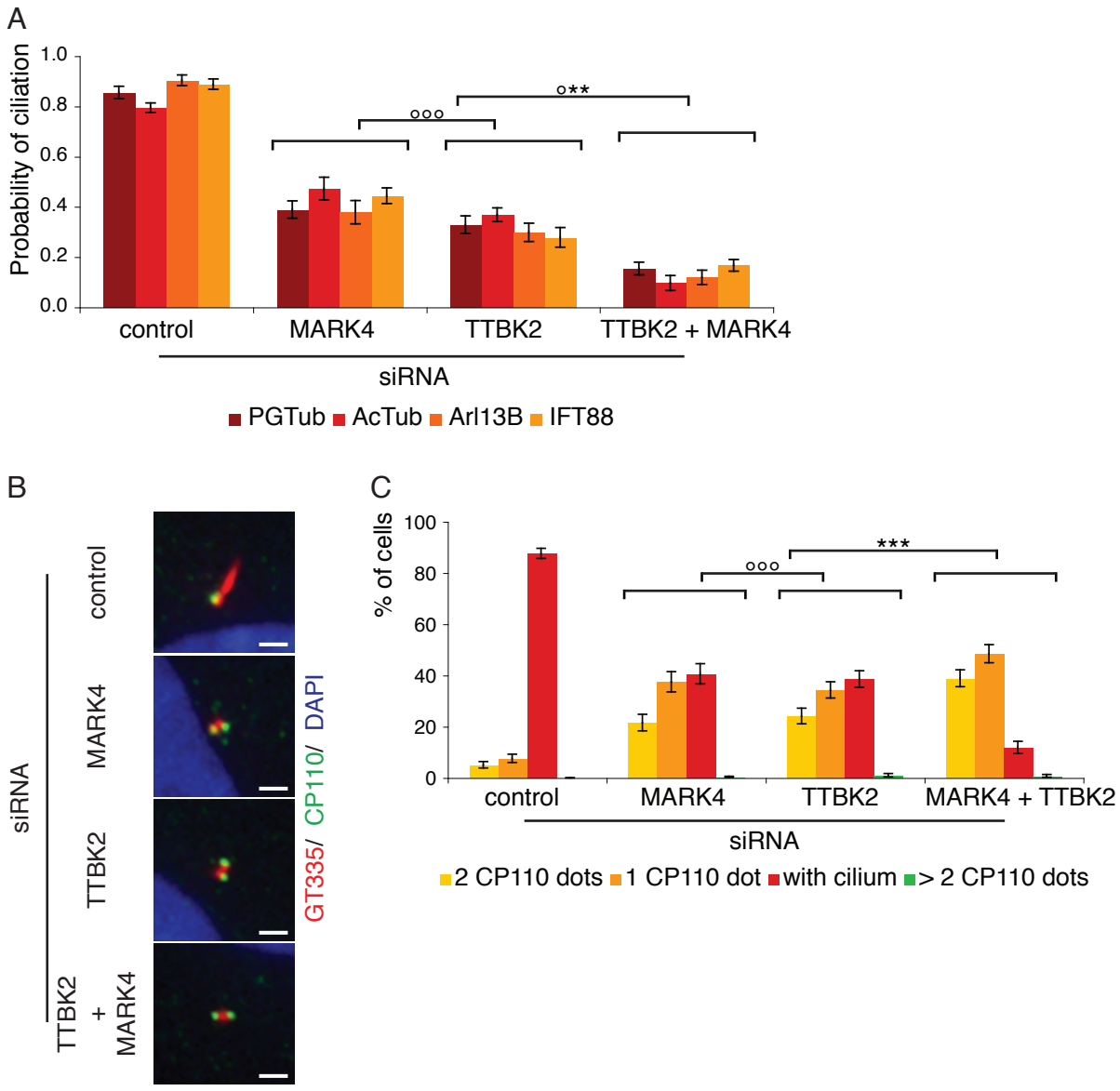

Figure 48: **MARK4 and TTBK2 have a synergistic effect on cilia formation and in the removal of CP110 from the basal body**. (A, B and C) RPE1 cells, treated with control, MARK4, TTBK2 or MARK4 and TTBK2 siRNA, were serum starved for 48 h. (A) Percentage of ciliated cells based on polyglutamylated tubulin (PGTub), acetylated tubulin (AcTub) Arl13B and IFT88 staining. 232<N<348. (B) Staining for polyglutamylated tubulin (GT335), CP110 and DAPI. (C) The number of ciliated cells and CP110 dots per centrosome in non-ciliated cells are indicated. $N_{control}$=475, N_{MARK4}=283, N_{TTBK2}=394, $N_{MARK4+TTBK2}$=260. (A and C) Data are means ± SEM of three independent experiments. *** corresponds to p<0.001, °** corresponds to p<0.01, °°°, not statistically significant. (B) Scale bar is 2 μm.

and because the functions of MARK4 and TTBK2 in ciliogenesis seem to overlap I also performed MARK4 and double kinase knock-downs. Fluorescence microscopy shows that NPHP1 localization is more severely affected upon MARK4 and MARK4+TTBK2 depletions (Figure 50A). TTBK2 depletion appears to affect not so much the recruitment of NPHP1 to the centrosome, but the levels of NPHP1 assembled at this location. The quantification of the NPHP1 signal upon TTBK2 knock-down exhibits a much bigger variance than the other experimental groups (Figure 50B). Even though the median of NPHP1 intensity at the centrosome is identical in control and TTBK2 siRNA treatments, the TTBK2 depleted cells presented the widest distribution of intensity values (Figure 50B). Together, these results suggest that MARK4 but not TTBK2 plays a role in NPHP1 recruitment to assure distal appendage integrity and/or in transition zone establishment.

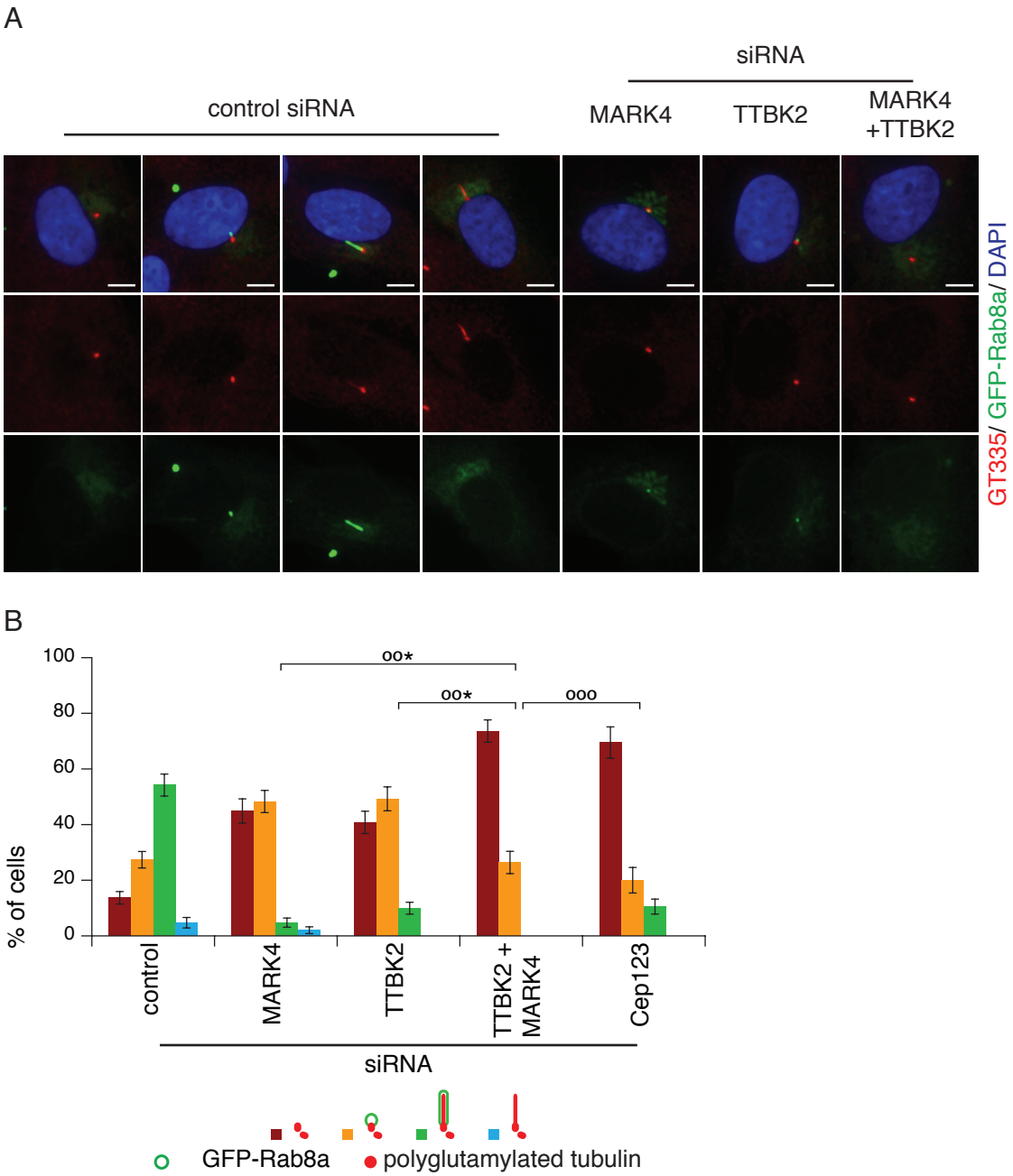

Figure 49: **MARK4 and TTBK2 double depletion leads to defects in the docking of Rab8a positive vesicles to the centrosome**. (A) RPE1 cells stably overexpressing GFP-Rab8a were treated with control MARK4, TTBK2 or MARK4 and TTBK2 siRNA, serum starved for 16 h, and stained for polyglutamylated tubulin (GT335) and DAPI. (A) Representative fluorescence micrographs are shown for the localization patterns of GFP-Rab8a. Scale bar is 5 μm. (B) Quantification of cells treated with the indicated siRNAs as described in A. Data are means ± SEM of three independent experiments. ^{oo*} corresponds to $p<0.05$, ^{ooo}, not statistically significant. $N_{control}=190$, $N_{MARK4}=147$, $N_{TTBK2}=201$, $N_{MARK4+TTBK2}=163$.

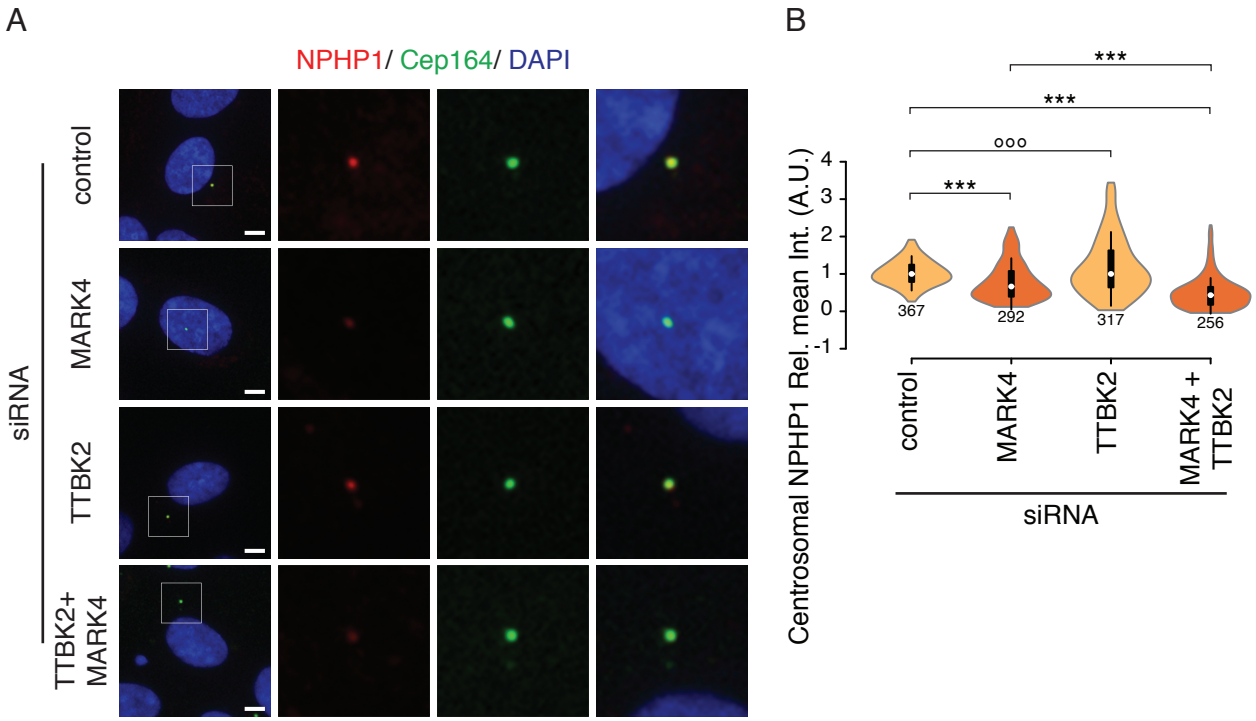

Figure 50: **MARK4 and TTBK2 double depletion leads to defects in the recruitment of NPHP1 to the transition zone**. (A) RPE1 cells, treated with control, MARK4, TTBK2 or MARK4 and TTBK2 siRNA, were serum starved for 48 h and stained for NPHP1, Cep164 and DAPI. Regions within the white boxes are depicted at higher magnification on the right. Scale bar is 5 μm. (B) Violin plot shows the relative NPHP 1 intensity at the centrosome of cells treated with the indicated siRNAs as described in A in three independent experiments. The number under the violin is N. Rel. mean Int. (A.U.), relative mean intensity (arbitrary units). *** corresponds to p<0.001, °°°, not statistically significant.

V.III. Discussion

The presence of MARK4 in the same fraction of γ-tubulin attests the centrosomal localization of MARK4. This permanence at the centrosome does not depend on MARK4's catalytic activity since both wild-type, and kinase-dead mutants can be found in the centrosomal fraction. The sensitivity of this small scale isopycnic centrifugation assay allowed to reliably quantify the amount of ODF2 that was recruited to the centrosome while over-expressing different MARK4 kinase mutants. The biochemical analysis of isolated centrosomes indicated that MARK4 is a centrosome-associated kinase that controls the levels of centrosome-associated ODF2.

Our results also suggest that the kinase-dead mutant used is not a dominant negative mutant. If the recruitment of ODF2 to the centrosome is determined by MARK4, the fact that as much ODF2 is recruited to the centrosome in kinase-dead or control cells indicates that the endogenous MARK4 may be still active. If the over-expressed MARK4 kinase-dead mutant had a dominant negative effect, it should bind to MARK4 substrates and prevent the endogenous wild-type MARK4 to fulfill its function in centrosomal ODF2 recruitment.

Regarding future directions, of note is the fact that ODF2 or MARK4 depletion and the failure to degrade trichoplein from the mother centriole share an impairment not on ciliary vesicle docking but yes on axoneme extension (Kasahara et al., 2014; Kuhns et al., 2013). Therefore, it would be easy and compelling to perform gain- or loss-of-function experiments to investigate if MARK4 is also involved in trichoplein regulation.

Since the interaction between MARK4 and Cep97 could only be stabilized and therefore detected in the MARK4-kad mutant, this indicates that MARK4 interacts very transiently with Cep97. A faint band GFP-MARK4 band can be discerned in the lane corresponding to MARK4 kad co-over-expression with CP110 (Figure 39A). However, the abundance of endogenous Cep97 that co-IPs with CP110 (Figure 39A) and the high affinity of the MARK4 kad mutant to Cep97, suggests that the little amount of MARK4 kad bound to CP110 does it indirectly through association with Cep97. The efficient binding of GFP-MARK4 kad but not the ka mutant to Cep97 attests the potency of the kinase active dead as a useful substrate entrapment mutant.

As we have seen, hyperactivity of MARK4 drives a change in Cep97's post-translation modifications. If the higher Cep97 bands in the immunoblot correspond to different phosphorylation states, this means that MARK4 phosphorylation has the effect of inhibiting the phosphorylation of the substrate by other kinases. This property of MARK4 activity resonates with the properties of the orthologous kinase Kin4 in budding yeast (Caydasi and Pereira, 2012). Kin4, a kinase involved in the spindle positioning checkpoint (SPOC), phosphorylates Bfa1 inhibiting the Cell division cycle (Cdc)5-dependent phosphorylation of Bfa1 (Caydasi and Pereira, 2009). Cdc5 is orthologous to the human PLK-1 kinase. We can speculate that Kin4-Cdc5 and MARK4-PLK-1 interaction may be a conserved regulation module. Even though the function and substrates of the control module may have changed in the course of evolution, the action of one kinase that, just on a particular pathway, blocks the activation or inhibition of one of the cellular master regulating kinases seems plausible. This regulation module would confer the cell with increased error correction abilities since when combined with the degree of redundancy inherent to a biological system the expected outcome of the system is to stop the process that the master regulator kinase is promoting until the malfunction or the error in the

system can be corrected. Examples of such process are spindle positioning checkpoint (SPOC) (Caydasi and Pereira, 2009) and possibly centrosome maturation (Kong et al., 2014).

Paradoxically Cep97 and CP110 both are excellent candidates for MARK4 substrates, but, never in the same assay. When Cep97 is a good binding partner of MARK4 entrapment mutant, CP110 is not. When CP110 serves as an in vitro MARK4 substrate, Cep97 does not. However, the results point in the same direction: MARK4 interacts with the Cep97-CP110 complex in vivo, phosphorylates CP110 in vitro and share an in vitro phosphorylated sequence in Cep97 with PLK-1. My results point to MARK4 having a role in centrosome regulation, namely the maturation from centriole to basal body and subsequent ciliary axoneme extension upstream of the removal of the CP110-Cep97 complex.

Interaction of TTBK2 with Cep164 and centrosomal localization had been previously published (Cajánek and Nigg, 2014; Chaki et al., 2012; Goetz et al., 2012) and was further confirmed by our results. I show that Cep164 is necessary for TTBK2 recruitment to the centrosome and was able to further map TTBK2 interaction with Cep164. Now we know that TTBK2 binds to the N-terminal WW domain of Cep164 and probably this interaction is determinant for TTBK2 centrosomal localization as was demonstrated by implementation experiments by Cajánek et al. 2014.

The results also show the importance of the distal appendage protein Cep123 for TTBK2 localization. We do not know if there is a direct interaction between TTBK2 and Cep123. We can speculate that, since Cep123 and Cep164 share a distal appendage localization it is plausible that TTBK2 could bind both proteins. Otherwise, it is possible that TTBK2 associates specifically with Cep164 but the binding affinity depends on distal appendage integrity, which may be compromised when Cep123 is depleted.

The depletion of Cep164 was also reported to have an adverse impact on IFT88 recruitment to the centriole that was possible to rescue by complementation experiments (Schmidt et al., 2012). Here, I could also rescue IFT88 localization at the basal body and restore ciliogenesis in cells depleted of endogenous TTBK2 by ectopically overexpressing the active form of the kinase. Since TTBK2 localization depends on Cep164, it is possible to conclude that the Cep164 acts by recruiting TTBK2 to the distal appendages of the mother centriole allowing TTBK2 to function downstream in the pathway of IFT88 recruitment. This rescue of IFT88 localization was only possible when the active form of TTBK2 was over-expressed. Over-expression of the kinase-dead version of TTBK2 had no such rescuing effect leading to the conclusion that TTBK2 kinase activity is necessary for IFT88 recruitment to the centrosome. The interaction with Cep123 also appears to be relevant for TTBK2's ability to perform the IFT88 recruitment role. However, the absence of Cep123 was not as compromising for IFT88 recruitment to the basal body as the lack of Cep164.

MARK4 and TTBK2 have very similar single phenotypes that seem to add up when their depletion is combined. Our results indicate that MARK4 and TTBK2 could be operating in synergetic parallel pathways of ciliogenesis since the additive effects of their combined knock-down can not be explained if they are part of the same branch of a pathway required for primary cilia formation. One node of the cilia formation pathway where both MARK4 and TTBK2 paths were reported to intercept, is the removal of the CP110-Cep97 complex (Goetz et al., 2012; Kuhns et al., 2013). I could partially rescue TTBK2's ciliogenesis defect by co-depleting CP110. This result demonstrates that, as it is the case of MARK4, the effect of TTBK2 depletion on ciliogenesis can be rescued by bypassing TTBK2 and artificially remove CP110 from the cells. We can conclude that at least part of the role of TTBK2 in cilia formation resides in the importance of this kinase in dissi-

pating the pool of CP110 that localizes at the distal end of the mother centriole and that prevents axoneme extension.

The partial synthetic lethality of MARK4 and TTBK2 regarding Rab8a vesicle docking to the centrosome indicates that MARK4 and TTBK2 could compensate for each other since once the action of both kinases is weakened, the cells are not proficient anymore in docking the ciliary vesicle to the mother centriole. The fact that still, 25% of the cells have docked vesicles in MARK4 and TTBK2 double depletion can be accounted by the fact GFP-Rab8a is being over-expressed in the cell line used. The ectopic expression of Rab8a is known to increases the probability of cells to ciliate and leads to longer cilia (Nachury et al., 2007; Yoshimura et al., 2007).

Previously published electron micrographs of centrosomes of cells depleted of Cep123 show small vesicles near the distal appendages of mother centrioles, but the cells appear unable to assemble a mature ciliary vesicle (Sillibourne et al., 2013). The fact that the majority of cells depleted of Cep123 can not recruit Rab8a positive vesicles to the distal appendages of the mother centriole supports the notion that Cep123 is involved in the process of ciliary vesicle docking. The parallelism of Cep123 phenotype with that of TTBK2 and MARK4 double depletion gives plausibility to the idea of a role of these kinases in the ciliary vesicle docking pathway. We can conjecture that MARK4 and TTBK2 are the links between ciliary vesicle docking and CP110 removal from the distal end of the mother centriole.

I also performed experiments where MARK4 and TTBK2 depletions are combined to investigate the role of these kinases in transition zone formation. Regarding the transition zone protein NPHP1, we found that MARK4 has probably a bigger role in NPHP1 recruitment to the mother centriole than TTBK2. Due to the high variability of NPHP1 levels when TTBK2 is missing from the cells, TTBK2 activity appears to be related not so much to the recruitment itself but more with the fine tuning of the composition and/or structure of the distal appendages and transition zone. From this, we can conclude that the defect in NPHP1 recruitment to the centrosome when Cep164 (Schmidt et al., 2012) is depleted does not happen through the agency of TTBK2.

Here I demonstrated that MARK4 interacts with the CP110-Cep97 complex and may through its phosphorylation regulate the displacement of the inhibitory complex from the basal body and allow axoneme growth. TTBK2 is at the center stage of vesicle docking due to its localization dependency on Cep164 and Cep123. Besides activating CP110 displacement from the basal body, TTBK2 may also be involved in transition zone establishment and IFT-B complex assembly.

VI. Final remarks

Centrosomes and cilia are able to gather intrinsic and extrinsic cellular information, generate an integrated response to that information and transmit that response to other cell components via cascades of specific post-translational modifications. The functions played by centrosome or cilium localized effectors such as protein kinases or ubiquitin ligases in cellular processes such as transcriptional activity, cytoskeleton regulation, autophagy or the cell cycle, among others, confer to these centriole-nucleated structures the role of central processing units of the cell. Mutations in centrosomal and ciliary proteins have been found to be the cause of developmental and metabolical pathologies. This leads to the realization that harmonious development and cellular homeostasis of an organism is dependent on the central processing role that centrosomes and cilia play in the animal cell. Although centrosomes and cilia appear to be so important in defining what is the animal cell, details about their biology have only started to be unveiled.

VII. Material & Methods

VII.I. Material

VII.I.I. Chemicals

Unless stated otherwise, all the chemicals used were acquired from Merck (Darmstadt, Germany), Roche Diagnostics (Mannheim, Germany), Roth (Karlsruhe, Germany) or Sigma- Aldrich (Taufkirchen, Germany) and were of *puriss pro analysi* grade.

VII.I.II. General buffers and solutions

Table 3: Buffers and solutions used in this study.

Buffer/Solution name	Reagents	Notes
100% TCA	500 g TCA	store at 4 ºC
	227 mL H_2O	
100x DNAse I solution	5 mM Tris-HCl	pH 7.5
	1 mg/mL DNAse I	
	75 mM NaCl	
	0.5 mM $MgCl_2$	
	50% (v/v) glycerol	
100x Lysozyme solution	10 mM Tris-HCl	pH 8.0
	20 mg/mL lysozyme	
2x HEBS	5 g HEPES-NAOH	pH 7.09
	8 g NaCl	
	0.37 g KCl	
	0.125 g Na_2HPO_4	
	1 g L-glucose	
	50 mL DPBS	
	to 500 mL	0.22 µm filter sterilize
Acid Acetone	1:39 HCl in acetone	store at -20 ºC
Borate buffer	1.25 g Boric acid	pH 8.8
	0.3725 g EDTA	

Buffer/Solution name	Reagents	Notes
	To 1 L with H_2O	
Centrosome purification lysis buffer	1 mM HEPES-NaOH	pH 7.2
	0.5% NP-40	
	0.5 mM $MgCl_2$	
	1 mM DTT	
	PMSF solution	
	Complete EDTA-free protease inhibitor cocktail	
	Phosphatase inhibitors	
Chloroquine	20 µM chloroquine	100 mM stock in H_20
Colloidal Coomassie	10% (w/v) $(NH_4)_2SO_4$	
	2% (v/v) H_3PO_4	
	0.1% (w/v) Coomassie G250	
	20% (v/v) methanol	
Complete EDTA-free protease inhibitor cocktail	1 tablet in 50 mL buffer	Diluted 1:100
Coomassie brilliant blue	0.25% Coomassie Brilliant Blue R-250	
	10% (v/v) acetic acid	
	40% (v/v) ethanol	
Destain solution	10% (v/v) acetic acid	
	40% ethanol	
DNA loading dye	0.04% (w/v) Bromophenol blue	
	0.04% (w/v) Xylen cyanol FF	
	2.5% (w/v) Ficoll 400	
	30 % glycerol	

Buffer/Solution name	Reagents	Notes
DRAQ5	Diluted 1:1000 from stock	
ECL solution 1	100 mM Tris-HCl	pH 8.5
	25 mM Luminol (3-aminophthalydrazide)	
	2.5 mM p-Coumaric acid	
ECL solution 2	100 mM Tris-HCl	pH 8.5
	61.5 µL of 30% H_2O_2	
	To 100 mL with H_2O	
ELB	50 mM HEPES-NaOH	pH 7.0
	250 mM NaCl	
	5 mM EDTA pH 8.0	
	0.1% NP-40	
	10% Glycerol	
	1 mM DTT	
	PMSF solution	
	Complete EDTA-free protease inhibitor cocktail	
	Phosphatase inhibitors	
Elution buffer	50 mM sodium phosphate	pH 8.0
	500 mM NaCl	
	500 mM Imidazole	
	1 mM DTT	
FTB	10 mM PIPES	0.22 µm filter sterilize
	55 mM $MnCl_2$	
	15 mM $MgCl_2$	
	250 mM KCl	
FTP	10 mM MOPS	0.22 µm filter sterilize
	75 mM $CaCl_2$	

Buffer/Solution name	Reagents	Notes
	10 mM RbCl	
	12% (w/v) glycerol	
GST elution buffer	50 mM Tris-HCl	pH 8.0
	150 mM NaCl	
	10 mM glutathione	
Kinase buffer	50 mM HEPES-NaOH	pH 7.4
	100 mM NaCl	
	10 mM $MgCl_2$	
	1 mM DTT	
MG132	1 µM MG132	42 mM stock in DMSO
Mini-prep solution I	50 mM glucose	
	25 mM Tris-HCl	pH 8.0
	10 mM EDTA	
	10 µg/mL RNAse I	
Mini-prep solution II	0.2 M NaOH	
	1% (w/v) SDS	
Mini-prep solution III	3 M potassium acetate	
	11.5% (v/v) acetic acid	
Nocodazole	6 µg/mL	5 mg/mL stock in DMSO
PBS	10 mM Na_2HPO_4	pH 7.2
	1.76 mM KH_2PO_4	
	2.7 mM KCl	
	137 mM NaCl	

Buffer/Solution name	Reagents	Notes
PBST	PBS	
	0.001%(v/v) Tween 20	
PBX	0.1% Triton X-100	
	PBS	
PHEM buffer	5 mM HEPES	
	60 mM PIPES-KOH	pH 7.0
	10 mM EGTA	
	2 mM $MgSO_4$	
Phosphatase inhibitors	2.5 mM Na4pyrophosphate	Diluted 1:100
	1 mM β-glycerophoaphate	
	2 mM NaF	
	0.1 mM Na_3VO_4	
PMSF solution	1 mM phenylmethane sulfonyl fluoride	Diluted 1:100
Ponceau S	0.2% (w/v) Ponceau S	
	3% (v/v) TCA	
SDS-Running buffer	25 mM Tris	
	192 mM Glycine	
	0.1% (w/v) SDS	
SDS-Sample buffer	63 mM Tris-HCl	pH 6.8
	10% (v/v) glycerol	
	2% (w/v) SDS	
	0.01% (w/v) Bromphenol-Blue	
	100 mM DTT	
Semi-dry blotting buffer	25 mM Tris	

Buffer/Solution name	Reagents	Notes
	192 mM Glycin	
	0.025% (w/v) SDS	
	5% (v/v) Methanol	
Sonication buffer	50 mM sodium phosphate	pH 8.0
	300 mM NaCl	
	10 mM Imidazole	
	0.1 mM $MgCl_2$	
	1 mM DTT	
	PMSF solution	
	Complete EDTA-free protease inhibitor cocktail	
Stripping buffer	200 mM glycine	pH 2.5
	1% (w/v) SDS	
Sucrose gradient buffer	10 mM PIPES-KOH	pH 7.2
	0.1% Triton X-100	
	1 mM DTT	
	Complete EDTA-free protease inhibitor cocktail	
	Phosphatase inhibitors	
TAE	40 mM Tris	pH 8.3
	20 mM acetic acid	
	1 mM EDTA	
TY agar medium	1 L TY medium	autoclaved
	20 g agar	
TY medium	10 g Bacto tryptone	autoclaved
	10 g Yeast extract	
	5 g NaCl	

Buffer/Solution name	Reagents	Notes
	To 1 L with H_2O	
Wash buffer	50 mM sodium phosphate	pH 8.0
	500 mM NaCl	
	30 mM Imidazole	
	1 mM DTT	
Wet blotting buffer	25 mM Tris	
	192 mM glycine	
	0.025% (w/v) SDS	

VII.I.III. Enzymes

Restriction Endonucleases	New England Biolabs
Pfu-Turbo-DNA polymerase	Stratagene
RNAse A and DNAse I	Sigma-Aldrich
T4 DNA ligase	Epicentre
Lysozyme	Sigma-Aldrich

VII.I.IV. Antibiotics

Ampicillin	100 µg/mL	100 mg/mL stock in H_2O
Kanamycin	25 µg/mL	25 mg/mL stock in H_2O
Chloramphenicol	30 µg/mL	30 mg/mL stock in ethanol
G418	800 µg/mL	200 mg/mL stock in H_2O
Doxycyclin	250 ng/mL	10 mg/mL stock in H_2O

VII.I.V. Antibodies

VII.I.V.I. Primary antibodies

Table 4: Primary antibodies used in this study.

antigene	species	source
OFD1	rabbit	kind gift from A. Fry, Lopes et al., 2011
PCM1	rabbit	kind gift from A. Merdes, Dammermann and Merdes, 2002
Cep290	rabbit	Bethyl Laboratories

antigene	species	source
γ-tubulin GTU88	mouse	Sigma-Aldrich
polyglutamylated tubulin GT335	mouse	kind gift of C. Janke, Wolff et al., 1994
actin	mouse	Chemikon
LC3B	rabbit	Novus Biologicals
LAMP1	mouse	Santa Cruz
mTOR	rabbit	Cell Signaling
S6K	rabbit	Cell Signaling
pS6K (T398)	rabbit	Cell Signaling
Raptor	rabbit	Cell Signaling
pRaptor (S792)	rabbit	Cell Signaling
γ-tubulin T5192	rabbit	Sigma-Aldrich
vimentin	rabbit	kind gift from H. Zentgraf
MAP4	rabbit	Santa Cruz
Arl13B	rabbit	Proteintech
ODF2	rabbit	lab stock, Kuhns et al., 2013
FLAG M2	mouse	Sigma-Aldrich
GFP	rabbit	kind gift from E. Schiebel
Cep97	rabbit	Bethyl Laboratories
Cep164-N	rabbit	lab stock, Schmidt et al., 2012
NPHP1	mouse	kind gift from H. Zentgraf
TTBK2	rabbit	Sigma-Aldrich
IFT88	guinea pig	lab stock, Pazour et al., 2002
CP110	rabbit	Bethyl Laboratories
acetylated tubulin C3B9	mouse	Sigma-Aldrich

VII.I.V.II.Secondary antibodies

Table 5: Secondary antibodies used in this study

antigene (conjugated with)	species	source
mouse (HRP)	goat	Dianova
rabbit (HRP)	goat	Dianova
mouse (Alexa 488)	goat	Molecular Probes
rabbit (Alexa 488)	goat	Molecular Probes

antigene (conjugated with)	species	source
guinea pig (Alexa 488)	goat	Molecular Probes
mouse (Alexa 594)	goat	Molecular Probes
rabbit (Alexa 594)	goat	Molecular Probes
guinea pig (Alexa 594)	goat	Molecular Probes
mouse (IRDye® 800CW)	goat	LI-COR
rabbit (IRDye® 800CW)	goat	LI-COR

VII.I.VI.Plasmids

Table 6: Plasmids used in this study

plasmid	codons	mutations	vector	source
GST-CP110-N	1-300		pGEX-5X-1	Evangeline Kang
GST-CP110-M	301-600		pGEX-5X-1	Evangeline Kang
His-CEP97-N	1-260		pET28a	Evangeline Kang
GST-CEP97-C	261-750		pGEX-5X-1	Evangeline Kang
GST	empty		pGEX-5X-1	GE Life Sciences
His-hMARK4L ka	full length	S26E/T214E	pET28a	Kuhns et al., 2013
His-hMARK4L kd	full length	S26A/K88A	pET28a	Kuhns et al., 2013
GST-PLK-1 WT	full length			kind gift of E. Schiebel
GST-PLK-1 KD	full length	D176N		kind gift of E. Schiebel
GFP-MARK4 ka	full length	S26E/T214E	pEGFP-C1	this study
GFP-MARK4 kad	full length	S26E/K88A/T214E	pEGFP-C1	this study
FLAG-CEP97	full length		pCMV-3Tag-1A	this study
FLAG-CP110	full length		pCMV-3Tag-1A	this study
GFP-Cep164	full length		pEGFP-C1	Schmidt et al., 2012
GFP-Cep164-ΔC	1-1250		pEGFP-C1	Schmidt et al., 2012
GFP-Cep164-ΔN	298-1250		pEGFP-C1	Schmidt et al., 2012
GFP-Cep164-W62/84A	full length	W62A/W84A	pEGFP-C1	Schmidt et al., 2012
FLAG	empty		pCMV-3Tag-1A	Agilent Technologies
FLAG-TTBK2 WT	full length		pCMV-3Tag-1A	this study
FLAG-TTBK2 KD	full length	D163A	pCMV-3Tag-1A	this study

VII.I.VII. Primers

Table 7: Primers used in this study.

name	sequence 5'-3'	restriction enzyme	purpose
FW GST-CP110-N	GATCGGATCCTC ATGGAGGAGTAT GAGAAGTTC	BamHI	Forward primer to clone CP110-N in pGEX-5X-1 and CP110 in pCMV-3Tag-1A
RV CP110-N	GATCGTCGACTT AAACATTTGATT TATTAAGGC	SalI	Reverse primer to clone CP110-N in pGEX-5X-1
FW GST-CP110-M	GATCGGATCCTC CTTCTCCAAGGT GCTTCC	BamHI	Forward primer to clone CP110-M in pGEX-5X-1
RV CP110-M	GATCGTCGACTT AGCAGTTTTCTTT TTGCAA	SalI	Reverse primer to clone CP110-M in pGEX-5X-1
FW His-Cep97-N	GATCGGATCCAT GGCGGTGGCGCG CGTG	BamHI	Forward primer to clone Cep97-N in pET28a and CEP97 in pCMV-3Tag-1A
RV Cep97-N	GATCGTCGACTT AAGGCCGATATG CTCTCCC	SalI	Reverse primer to clone Cep97-N in pET28a
FW GST-Cep97-C	GATCGGATCCTC GGCCAGCACATC CAGCTTG	BamHI	Forward primer to clone Cep97-C in pGEX-5X-1
RV Cep97-C	GATCGTCGACCT ACACAGTAACAC CAAC	SalI	Reverse primer to clone Cep97-C in pGEX-5X-1 and CEP97 in pCMV-3Tag-1A
MARK4-fw2	CTCAGATCTATGTCT TCGCGGACGGTGC	BglII	Forward primer to clone hMARK4L in pEGFP-C1
MARK4-rev2	ACCGTCGACTCAGA GCTCGAGGTCGTTG	XhoI	Reverse primer to clone hMARK4L in pEGFP-C1
RV CP110-C	GATCGTCGACTT AAATTGTCGCAA CATTTG	SalI	Reverse primer to clone CP110 in pCMV-3Tag-1A
FW TTBK2 (SalI)	GATCGTCGACATGA GTGGGGGAGGAGA G	SalI	Forward primer to clone TTBK2 in pCMV-3Tag-1A
RV TTBK2 (SalI)	GATCGTCGACCTATC TGCTGAGTTTACT	SalI	Reverse primer to clone TTBK2 in pCMV-3Tag-1A

All primers were ordered from Sigma-Aldrich in a lyophilized form, dissolved in H_2O to a stock concentration of 100 µM and stored at -20 °C.

VII.I.VIII. siRNA sequences

Table 8: small interfering RNAs used in this study.

name	target sequence (5'-3')	comment (reference)
Luciferase	AACGTACGCGGAATACTTCGA	control siRNA (Knodler et al., 2010)
Cep164 siRNA1	CAGGTGACATTTACTATTTCA	(Graser et al., 2007)
ODF2	AAAGACTAATGGAGCAACAAG	(Soung et al., 2009)

name	target sequence (5'-3')	comment (reference)
MARK4	GCATCATGAAGGGCCTAAA	(Kuhns et al., 2013)
MAP4	AACTGGCCAGAAGATACCAAC	(Ghossoub et al. 2013)
ATG5	GE Healthcare (L-004374-00-0005)	
OFD1_1	GAGCTCATAGCTATTAATTCA	(Lopes et al., 2011)
OFD1_2	GATCGATCGTTCTGTCAATGG	(Lopes et al., 2011)
TTBK2_1	CACATTGGTCATGACATGTTA	(Goetz et al. 2012)
TTBK2_2	AGGCATCACCTCAAGATGAAA	(Goetz et al. 2012)
Cep123	CACCCTGGTTGTTGGATATAA	(Sillibourne et al. 2013)
CP110	AAGCAGCATGAGTATGCCAGT	(Spektor et al., 2007)

All siRNA oligonucleotide duplexes were ordered from Life Technologies in a lyophilized form, dissolved in RNAse free H_2O to a stock concentration of 20 µM and stored at -80 °C.

VII.I.IX. *Escherichia coli* strains

DH5α	deoR endA1 gyrA96 hsdR17 (rκ-mκ-) recA1 relA1 supE44 thi-1Δ(lacZYA-argFV169) ϕ80δlacZΔM15 F- λ-
BL21 (DE3) pLysS Rosetta	F- ompT hsdSB(RB- mB-) gal dcm λ(DE3 [lacI lacUV5-T7 gene 1 ind1 sam7 nin5]) pLysSRARE (CamR)

VII.I.X. Mammalian cell lines

RPE1	human telomerase immortalized retinal pigment epithelial 1 cell line
HEK293T	human embryonic kidney cell line 293T
NIH 3T3	murine embryonic fibroblast cell line

VII.II. Methods

VII.II.I. Molecular biology

VII.II.I.I. DNA amplification

Amplification of DNA fragments by polymerase chain reaction The polymerase chain reaction (PCR) was used to copy and amplify fragments of DNA, using as template plasmid DNA. The annealing temperature of the two primers depended on their A/T and G/C content and was calculated based on this formula n(A, T) x 2°C + n(C, G) x 4 °C. All PCR reactions were run in a Thermocycler T-Personal (Biometra, Göttingen, Germany).

Reaction set up:

50 ng	DNA template
1 µM	forward primer

1 µM	reverse primer
1x Pfu-Turbo-DNA polymerase	Pfu-polymerase buffer
0.2 mM each	dNTPs
1.25 U	Pfu-Turbo-DNA polymerase
to final volume of 50 µL	H_2O

Thermocycler program:

95 ºC	2 minutes
95 ºC	30 seconds
Tm of Primers – 2 °C	30 seconds
72 ºC	1 minute / 1kb of DNA
72 ºC	10 minutes

VII.II.I.II.Site directed mutagenesis

Site directed mutagenesis was performed to replace individual base pairs in a gene sequence. The mutations were located in the middle of the primers and flanked by 15-20 bp in each side.

Reaction set up:

30 ng	Plasmid template
1 µM	forward primer
1 µM	reverse primer
1x Pfu-Turbo-DNA polymerase	Pfu-polymerase buffer
0.25 mM each	dNTPs
2.5 U	Pfu-Turbo-DNA polymerase
to final volume of 50 µL	H_2O

Thermocycler program:

95 ºC	2 minutes
95 ºC	30 seconds
55 °C	1 minute
68 ºC	2 minutes / 1kb of DNA
68 ºC	10 minutes

The template plasmid was digested by adding 20 U DpnI for 4 hours at 37 °C, which specifically digested methylated DNA. 3 µL of the digested PCR reaction were transformed into *E. coli* DH5α.

VII.II.I.III.Restriction digestion of DNA

DNA was digested with specific restriction endonucleases to generate DNA fragments for cloning, to identify positive clones or to linearize integration plasmids. Digests were carried out in the appropriate buffer system of the enzyme manufacturer (New England Biolabs, Beverly, USA). For analytical digests, 0.5 µg of DNA was digested in a final volume of 20 µL with 5-10 U restriction enzyme and incubated for 2 hours at the recommended temperature. For preparative plasmid digest, 1-5 µg of DNA was digested in a final volume of 50 µL with 10 U of restriction enzyme and incubated for 4-5 hours. PCR fragments were digested overnight. Digested DNA was analyzed by agarose gel electrophoresis.

VII.II.I.IV.Cloning of PCR products with CloneJET PCR Cloning Kit

In the cases that was necessary to enhance cloning efficiency of a PCR fragment into a vector, the high efficiency CloneJET PCR Cloning Kit (Fermentas, St. Leon-Rot, Germany) was used. Blunt-end PCR products generated by a proofreading DNA polymerase were directly ligated with the linearized pJET1.2/ blunt cloning vector, according to manufacturer's protocol.

VII.II.I.V.Agarose gel electrophoresis

DNA fragments were separated according to their size using gels with 0.8-1.5% agarose in TAE buffer. Before loading, samples were mixed with 1/5 volume of 6x DNA loading dye. As standard marker, the 1 kb ladder from Invitrogen (Karlsruhe, Germany) was used. Gels were run at 100 V for analytical gels or at 50 V for preparative gels and subsequently stained with 1 ng/mL ethidium bromide in water for 10 minutes. After destaining in water, bands were detected by UV-illumination and documented with a gel documentation system (PEQLAB Biotechnologie, Erlangen, Germany).

VII.II.I.VI.DNA extraction from agarose gels

Excised bands were transferred to Eppendorf vials, weighed and DNA was purified with QiaQuick columns (Qiagen, Hilden, Germany) following the instructions of the manufacturer.

VII.II.I.VII.Determination of DNA concentration

DNA concentrations in solutions were determined by measuring the absorbance at 260 nm (A_{260}) of the diluted sample after calibration of the photometer with a buffer control. An A_{260} of 1.0 corresponds to 50 µg/mL of DNA.

VII.II.I.VIII.Ligation of DNA into plasmid vectors

DNA fragments were integrated via cohesive ends in linearized plasmid vectors. Ligations were performed with 10 U T4 DNA ligase (Epicentre, Madison, USA) in 20 µL reactions. 50-200 ng of linearized vector was mixed with the insert in a 1:3-5 molar ratio in the recommended ligase buffer and incubated for 4 hours at RT.

Reaction set up:

1 part	linearized vector

3 to 5 parts	DNA insert
10 U	T4 DNA ligase
1x	T4 DNA ligase buffer
1.25 mM	ATP
to 10 µL	H_2O

The ligation was incubated for 4 hours at RT and 2 µL were transformed into *E. coli* DH5α.

VII.II.I.IX.Generation of chemically competent *E. coli*

Chemically competent *E. coli* cells were used for transformation by heat shock. To prepare chemically competent *E. coli*, a 250 mL culture was inoculated with an overnight pre-culture and grown at 18°C with shaking to an optical density at 600 nm (OD_{600}) of 0.6. The culture was pelleted at 1,000 g at 4°C and the pellet was gently resuspended in 1/3 of the original volume in chilled FTB. After incubation on ice for 10 minutes, the cells were again pelleted at 1,000 g and the pellet was resuspended in 1/12 of the original volume in chilled FTP. After the addition of 7% DMSO, the cells were incubated for 10 minutes on ice and snap-frozen in liquid nitrogen to be stored at -80°C.

VII.II.I.X.Heat shock transformation of chemically competent *E. coli*

100 µL of chemically competent *E. coli* suspension was thawed on ice and mixed with 0.1-1 µg of plasmid DNA or a ligation reaction and incubated for 30 minutes on ice. After heat shock for 90 seconds at 42°C, the suspension was chilled on ice. 900 µL of TY-media were added, *E. coli* were incubated for 30-60 minutes at 37 °C, plated on TY-agar plates containing the appropriate antibiotic(s) and incubated at 37 °C over night.

VII.II.I.XI.Isolation of plasmid DNA from *E. coli*

Colonies were inoculated in TY-medium supplemented with the appropriate antibiotics and grown under shaking overnight at 37 °C. Cells were pelleted for 1 minute at 14,000 rpm and plasmid isolation was performed using the appropriate Qiagen Plasmid Kit (Mini, Midi, or Maxi) (Qiagen, Hilden, Germany) according to the manufacturer's protocol. The isolated plasmids were analyzed by restriction digestion and agarose gel electrophoresis.

VII.II.I.XII.Sequencing of DNA

DNA plasmids were sent for sequencing at GATC Biotech AG (Konstanz, Germany). All plasmids mentioned in this study were subjected to DNA sequencing.

VII.II.II.Cell culture

VII.II.II.I.Cultivation and preservation of mammalian cells

All cells were grown at 37 °C in a 5% CO_2 atmosphere. HEK293T cells were grown in Dulbecco's modified Eagle's medium (DMEM) (Lonza, Cologne, Germany), supplemented with 10% fetal calf serum (FCS) (Biochrom, Berlin, Germany). RPE1 cells were cultured in DMEM Nutrient Mixture F-12 Ham (Sigma-

Aldrich, München, Germany) supplemented with 10% FCS, 2 mM L-glutamine and 0.348% sodium bicarbonate (Gibco, Karlsruhe, Germany). NIH 3T3 cells were cultured in DMEM (Lonza, Cologne, Germany) supplemented with 10% newborn calf serum (Pan Biotech, Aidenbach, Germany).

The RPE1 cell line expressing GFP-Rab8 cells was kept with G418 and the cell line expressing YFP-LC3 was kept with puromycin to maintain a stable expression of the tagged proteins. Protein expression was induced in NIH 3T3 cells by adding doxycycline for 16 hours. Cilia formation was induced by serum starvation in RPE1 and NIH 3T3 cells.

Mammalian cells were frozen in medium supplemented with 10% DMSO. For RPE1 cells, the freezing medium contained 70% FCS, for NIH 3T3 cells 30% and for HEK293T cells no medium was added and the cells were frozen in 90% serum. The cells were trypsinized, centrifuged, resuspended in freezing medium and chilled on ice for 30 minutes before transferring to -80°C. Cells were either stored at -80°C or transferred to a liquid nitrogen tank.

VII.II.II.II.Transfection of HEK293T cells

HEK293T cells were transiently transfected with plasmid DNA using the calcium phosphate precipitation method. In the evening before transfection, HEK293T cells were passaged from 80% confluent dishes with a 1:8 split ration to 10 cm cell culture dishes. In the next morning, 1-5 µg plasmid DNA was added to 500 µL 0.25 M $CaCl_2$. 500 µL of 2xHEBS were added under vortexing and the mixture was dropwise added to the cells. After 8 hours, medium was replaced with fresh medium. 24-32 hours after transfection, cells were harvested and further processed.

VII.II.II.III.siRNA-mediated protein depletion

To transiently deplete proteins in 100,000 RPE1 cells, these were seeded in 800 µL medium in a single well of a 12-well plate containing two glass coverslips. The reverse siRNA transfection was performed using LipofectamineRNAiMAX (Invitrogen, Karlsruhe, Germany) as transfection reagent. 2.5 µL siRNA duplex (final concentration of 50 nM) were added to 100 µL OptiMEM medium, and 1.8 µL LipofectamineRNAiMax were added to a second vial containing equally 100 µL OptiMEM. Both vials were combined by adding the mixture containing the siRNA duplex to the vial containing the mixture with the transfection reagent. The obtained mixture was incubated for 15 minutes at room temperature (RT) and added to the cells. 24-72 hours after addition of the siRNA duplexes, cells were further processed. Reactions for higher amounts of cells were proportionally upscaled.

VII.II.II.IV.Harvesting of mammalian cells

Cells were washed once with chilled PBS. HEK293T cells were harvested by pipetting them up and down in chilled PBS. RPE1 and NIH 3T3 cells were scrapped from the dish in chilled PBS. The suspension was transferred to a Falcon tube and the cells were pelleted at 1,000 rpm for 5 minutes at 4°C. The supernatant was discarded and the cell pellet either directly processed or snap-frozen in liquid nitrogen and stored at -80°C.

VII.II.III.General protein biochemical and immunological techniques

VII.II.III.I.SDS-Polyacrylamide gel electrophoresis (PAGE)

Proteins were separated according to their sizes by discontinuous SDS-PAGE system. The Bio-Rad Mini-PROTEAN II gel system was used for running acrylamide gels of 6, 8, 10, 12 and 15% according to the expected size of the proteins. Acrylamide solution for separating gel (5 mL/gel) and stacking gel (2 mL/gel) were prepared as follows:

Table 9: Formulations of polyacrylamide gels.

	Separating gel					Stacking gel
percentage	**6 %**	**8 %**	**10 %**	**12 %**	**15 %**	**4 %**
H_2O (mL)	2.68	2.38	2	1.7	1.175	1.55
30% acrylamide (mL)	1	1.3	1.68	2	2.5	0.325
1.5 M Tris-HCl, pH 8.8 (mL)	1.25	1.25	1.25	1.25	1.25	-
0.5 M Tris-HCl, pH 6.8 (mL)	-	-	-	-	-	0.625
10% SDS (µL)	50	50	50	50	50	25
10% APS (µL)	25	25	25	25	25	12.5
TEMED (µL)	5	5	5	5	5	2.5

Protein samples were dissolved in SDS sample buffer and heated for 15 minutes at 65 °C before loading on the gel. Mini gels were run in SDS-running buffer at 20 mA per gel. Prestained (Bio-Rad, München, Deutschland) or unstained molecular markers (Fermentas, St. Leon Rot, Germany) were used as protein standard. Separated proteins were either stained with Coomassie Brilliant Blue, Colloidal Coomassie or transferred onto a nitrocellulose or PVDF membrane.

VII.II.III.II.Semi-dry immunoblot

After SDS-PAGE, the separating gel, a nitrocellulose membrane (Schleicher and Schuell, Dassel, Deutschland) and 6 Whatman 3MM papers were immersed in semi-dry blotting buffer. A sandwich, consisting of 3 Whatman papers, the nitrocellulose membrane, the SDS-PAGE gel and another 3 Whatman papers, was assembled between the two electrodes of a semi-dry blotting apparatus. The standard blotting conditions were 110 mA for 1-1.5 hours. Transferred proteins were visualized by staining with Ponceau S solution for 1 minute before the background was reduced by washing with H_2O. Membranes were blocked with 5% milk in PBS-T for 1 hour at RT or overnight at 4°C and then incubated with the primary antibody diluted in 3% milk/PBS-T at RT for 1 hour or at 4°C overnight. The membrane was washed 3 times in PBS-T before incubating with the secondary antibody diluted in 3% milk/PBS-T for 30 minutes. The membrane was washed 3 times with PBS-T and the Western blots were probed with the enhanced chemiluminescence (ECL) solution 1 and 2 for 90 s for visualization. The signals were detected on X-ray film (FUJIFILM).

VII.II.III.III.Wet immunoblot

The PVDF membrane (Bio-Rad, München, Germany) was activated in methanol for 2 minutes before it was rinsed in chilled wet-blotting buffer. The separating gel as well as 6 Whatman paper and 2 tissues

were immersed in the same buffer. The blotting sandwich was assembled between the two electrodes. Blotting was performed at 350 mA for 2.5 hours. The transfer apparatus was cooled during the whole transfer. The membrane was blocked and stained as above described for nitrocellulose membranes.

VII.II.III.IV.Membrane stripping

Stripping was used occasionally for the detection of more than one protein on the same western blot. For removal of primary and secondary antibodies after the first probing the nitrocellulose membrane was incubated in stripping buffer for 1 hour. After washing the membrane several times with PBS, it was blocked again and re-probed with the next antibody.

VII.II.III.V.Detection of proteins with Coomassie Brilliant Blue

Coomassie Brilliant Blue staining was used as standard method to stain proteins in SDS-PAGE. The gel was incubated in staining solution for 1 hour with gentle tumbling. The gel was briefly rinsed in H_2O and destained by repeated washes in destaining solution.

VII.II.III.VI.Detection of proteins with Colloidal Coomassie

Proteins in SDS-PAGE gels were detected with Colloidal Coomassie when a more sensitive method was required that was suitable for later mass spectrometric analysis of separated proteins. Gels were fixed for 1 hour in fixing solution (10% TCA) and subsequently washed 3 times for 10 minutes in H_2O. The gel was stained in Colloidal Coomassie staining solution for 24-48 hours. Unbound color was removed by several washes in H_2O.

VII.II.III.VII.Co-immunoprecipitations

Proteins were overexpressed in HEK293T cells to test whether they co-immunoprecipitate. One of the two proteins was fused to a FLAG-tag, while the other protein was fused to a GFP-tag. HEK293T cells were lysed in 1.4 mL ELB buffer rotating at 4°C for 20 minutes. To pellet the cell debris, the total cell extracts were centrifuged at 21,000 g for 15 minutes and further clarified by centrifugation at 27,000 g for 30 minutes. The protein concentrations were adjusted and the FLAG-tagged proteins were immunoprecipitated using anti-FLAG M2 Agarose (Sigma-Aldrich, Taufkirchen, Germany) for 1-2 hours. The agarose beads were washed three times in ELB buffer. Bound proteins were eluted in SDS sample buffer and subjected to SDS-PAGE.

VII.II.III.VIII.Determination of protein concentrations

A defined volume of a bacterially expressed and purified protein was subjected to SDS- PAGE with subsequent Coomassie Brilliant Blue staining. The protein concentration was estimated based on a bovine serum albumin (BSA) standard loaded into the same gel. After scanning the gel, the intensity of the BSA bands was measured using ImageJ. The protein concentration was estimated based on the generated linear BSA standard curve. Protein concentrations of HEK293T cell lysates were measured using Advanced Protein Assay 01 reagent (Cytoskeleton, Denver, CO, USA), according to manufacturer's protocol.

VII.II.III.IX.In vitro kinase assay

The substrate and kinase were mixed together in kinase buffer. An equal volume of 16 mM ATP and 5µCi [γ-32P] were mixed and 1µl was added to each reaction. The reactions were incubated with light shaking for 30 minutes at 30°C. Sample buffer was added to each sample to stop the kinase reaction before boiling at 95°C for 5 minutes. The samples were subjected to SDS- PAGE, followed by autoradiography and Coomassie Blue staining. Gels were dried in a gel dryer (Bio-Rad) and then exposed to a phosphoimager screen (FUJIFILM) for 1-2 hours. Radioactivity was detected by phosphoimager FLA-300.

VII.II.III.X.Protein expression with IPTG induction

Both His-fusion and GST-fusion proteins were expressed in BL21 (DE3) pLysS Rosetta *E. coli* cells. *E. coli* were transformed by heat shock and plated on agar plates with the appropriate antibiotics in the evening before. The next day, 5 mL of TY medium was pipetted directly to the agar plate and a glass pipette was used to re-suspend the colonies. The resuspended colonies were then inoculated in 500 mL TY medium with antibiotic and grown shaking at 37 ºC to OD600 0.5. Protein expression was induced by adding 0.1 mM IPTG. After induction, the cells were harvested by centrifugation for 20 minutes at 6000 rpm. The pellet was resuspended in 50 mL PBS, transferred to a 50 mL falcon tube and centrifuged for 15 minutes at 6000 rpm before storing at -20 ºC.

VII.II.III.XI.Purification of GST-fusion proteins from *E.coli*

The cell pellet was resuspended in 20 mL of cold PBS with the addition of lysozyme, DNAse I, PMSF, 1 mM DTT and protease inhibitors followed by incubation in ice for 15 minutes. The cells were then lysed on ice using an ultra-sonicator in 8 rounds (40% output, 30 s pulsed, 30 s pause, cycle 3). PBS/ 1% TX-100 was added before incubating for 30 minutes in ice. The cell lysate was centrifuged (45 minutes, 20,000 rpm, 4 ºC). The cleared lysate was diluted in 480 mL of PBS/1% TX-100 in an Erlenmeyer flask. 1 mL of gluthathione-sepharose resin slurry was equilibrated by washing twice with PBS and twice with PBS/1% TX-100 before adding it to the diluted supernatant. Binding to the beads was allowed by incubation for 1 hour at 4 ºC by slow stirring on a magnetic stirrer with a stir bar. The beads were collected and separated from the flow-through by centrifugation (3 minutes, 2,000 rpm, 4 ºC). After that, the beads were washed twice with 10 mL of PBS/0.1% TX-100 and incubated 20 minutes on ice with 10 mM $MgCl_2$ and 2 mM ATP before washing twice with 10 mL PBS. The beads were resuspended in 2 mL PBS before loading into a column and eluted with GST elution buffer in 1 mL fractions.

VII.II.III.XII.Purification of His-fusion proteins from *E. coli*

The cell pellet was resuspended in 20 mL sonication buffer and lysed as described for GST-fusion proteins. The cell lysate was cleared by centrifugation (20 minutes, 10,000 rpm, 4 ºC). The cleared lysate was added to 1mL of Ni-NTA agarose that was previously equilibrated in sonication buffer. The lysate and slurry mixture was incubated stirring for 2 hours at 4 ºC. After incubation, the beads were washed 2 times with 20 mL of wash buffer before resuspension and incubation for 20 minutes on ice with 10 mM $MgCl_2$ and 2 mM ATP. The beads were washed 2 times with 20 mL of wash buffer. Protein elution was performed in elution buffer in 1 mL fractions.

VII.II.III.XIII.Centrosome purification

NIH 3T3 cells and NIH 3T3 cells stably carrying inducible LAP-hMARK4L wild-type or kinase dead constructs were grown to a density of ~80%. The TET-on constructs were induced by addition of 250 ng/mL of doxycycline in serum-free medium overnight. After washing with ice-cold PBS, the cells were harvested by scraping, pelleted for 5 minutes at 4 °C and 1,200 g, washed with 10 mL of 8% sucrose (BDH) in PBS, and sedimented at 1,200 g for 5 minutes. The cell pellet was resuspended in 250 µL of 8% sucrose and frozen in liquid nitrogen for further processing. Centrosomes were isolated by centrifugation using a discontinuous sucrose gradient (Mitchison and Kirschner, 1984). Cells were lysed for 10 minutes in 1.5 mL centrosome purification lysis buffer. Swollen nuclei and cell debris were sedimented at 1,200 g for 10 minutes, and 1.2 mL of the supernatant was supplemented with 1 M Hepes-NaOH, pH 7.2, and 2 mg/mL DNase I to a final concentration of 10 mM and 10 µg/mL, respectively. After incubation at 4 °C for 30 minutes, 1 mL lysis supernatant was overlaid on a discontinuous sucrose gradient set in one 11 × 34 mm polyallomer tube (Beckman Coulter), with 300 µL of 70% sucrose (wt/wt), 200 µL of 50% sucrose (wt/wt), and 400 µL of 40% sucrose (wt/wt) prepared in sucrose gradient buffer. Gradients were run at 100,000 g at 4 °C for 1 hour in a TLS-55 Beckman Coulter rotor. Fractions of four drops (~100 µL) were collected from the bottom of the gradient, and the protein concentration was determined. The protein content of each fraction was precipitated with TCA before SDS-PAGE and immunoblot analysis. For protein quantification, samples corresponding to the centrosomal fractions were separated by SDS-PAGE and analyzed using anti–γ-tubulin and anti-ODF2 primary antibodies and IRDye 800–conjugated secondary antibodies. Membranes were scanned with an imaging system (Odyssey Imager; LI-COR Biosciences), and band intensities were quantified using ImageJ software. The background measured in an empty area of the membrane was subtracted from all measured values. The amount of ODF2 in centrosomal fractions was normalized to the γ-tubulin amount, and the ratio of ODF2/γ-tubulin in each individual sample was calculated as the percentage within each experimental set to allow the comparison of independent experiments.

VII.II.III.XIV.TCA precipitation

Add 250 µL of 100% TCA to 1 mL sample and place on ice for 1h. Centrifuge at 13,000 rpm at 4 ºC for 10 minutes, remove supernatant and rinse the pellet with 200 µL of acid acetone kept at -20 ºC. Centrifuge again at 13,000 rpm at 4 ºC for 10 minutes, remove supernatant, air dry the pellet and resuspend in the buffer of choice.

VII.II.IV.Microscopy and image analysis

VII.II.IV.I.Cell fixation and immunofluorescence staining

Cells were grown on coverslips and either fixed in PFA, methanol or PFA and methanol. For methanol fixation, the cells were kept in ice cold methanol for 3 minutes and permeabilized in ice cold acetone for 20 s. For PFA fixation, the cells were incubated in 3% (w/v) PFA (in PBS) for 20 minutes at 37 ºC. PFA fixation was followed by a 10 minutes quenching step in 50 mM NH_4Cl (in PBS) and a 5 minutes permeabilization step in 0.1% (v/v) Triton X-100/PBS. PFA and methanol fixation was performed by incubating cells in 3% (w/v) PFA (in PBS) for 2 minutes followed by a rinsing step with 50 mM NH_4Cl (in PBS) and incubation on ice cold

methanol for 3 minutes. After washing the methanol with PBS, cells were permeabilized with 0.1% (v/v) Triton X-100/PBS. Cells were blocked with 3% (w/v) BSA in 0.1% (v/v) Triton X-100/PBS for 30 minutes at RT followed by the incubation with primary antibodies at 37 °C for 1 hour or 4 ºC overnight. Primary antibodies were detected with secondary antibodies for 30-60 minutes at RT. DAPI (Sigma-Aldrich) was included with the secondary antibodies for DNA staining. All antibodies were diluted in blocking solution. Coverslips were mounted on glass slides in Mowiol (EMD Millipore).

VII.II.IV.II.Immunofluorescence microscopy

Images were acquired using a Zeiss Axiophot microscope (Carl Zeiss) equipped with a 40× (0.75 NA, Plan-NEOFLUAR) a 63x (1.4 NA, Plan-APOCHROMAT, oil immersion) or a 100× (1.45 NA, Plan-FLUAR, oil immersion) objective lenses (Carl Zeiss), an EM-CCD camera (Cascade 1K; Photometrics), and MetaMorph software (Universal Imaging Corp.).

VII.II.IV.III.Batch processing of images for Autophagy related analysis

Immunofluorescence microscopy images were acquired with a 40× objective in 11 z-stacks spaced 0.5 µm from each other. Channels were separated by wavelength and processed in imageJ as follows: all images in the DAPI channel were subtracted of its minimum gray value and the z-stacks were maximum intensity projected; all images in the 488 nm channel (autophagosomes) were both subjected to a tophat filter with a diameter of 3 pixels and the z-stacks were maximum intensity projected and subtracted of its minimum gray value and the z-stacks were maximum intensity projected; all images in the 594 nm channel (centrosomes and cilia) were both subjected to a tophat filter with diameter of 5 pixels and the z-stacks were maximum intensity projected and subtracted of its minimum gray value and the z-stacks were median intensity projected. All this transformations were made in batch using imageJ macros.

VII.II.IV.IV.Batch processing of images for CS and lysosome related analysis

Immunofluorescence microscopy images were acquired with a 63x or a 100× objective in 15 z-stacks spaced 0.214 µm from each other. Channels were separated by wavelength and processed in imageJ as follows: all images in the DAPI channel were subtracted of its minimum gray value and the z-stacks were maximum intensity projected; all images in the 488 nm channel (CSs or lysosomes) were both subjected to a tophat filter with a diameter of 3 pixels and the z-stacks were maximum intensity projected and subtracted of its minimum gray value and the z-stacks were maximum intensity projected; all images in the 594 nm channel (centrosomes and cilia) were both subjected to a tophat filter with diameter of 10 pixels and the z-stacks were maximum intensity projected and subtracted of its minimum gray value and the z-stacks were median intensity projected. All this transformations were made in batch using imageJ macros.

VII.II.IV.V.Automated cilia and centrosome segmentation and classification

Cilia and centrosome segmentation was done using open-source software ilastik and Cell profiler. The binary images with the centrosomes and cilia masks resulting from the ilastik segmentation were used in Cell profiler using the IdentifyPrimaryObjects module for object identification and further analysis of cilia and cen-

trosomes such as measuring intensity values or geometric parameters regarding their shape and position within the cell.

VII.II.IV.VI.Automated cell segmentation

In order to segment the cells I used the open-source software Cell profiler. As seeds for image based identification of the cell boundaries I used the maximum intensity projected images of the DAPI channel and using the IdentifyPrimaryObjects module to identify the nuclei. Using the nuclei as input objects and the median intensity projection of the 594 nm channel as input image, I identified the cell boundaries using the IdentifySecondaryObjects module. As methods to identify secondary objects I used the Propagation method for low magnification images and Watershed – Image method for high magnification images. The threshold strategy was set to Adaptive, the threshold method to RobustBackground. It is critical for the correct identification of the cell borders in any given dataset to manually optimize the Threshold correction factor, Lower and upper bounds on the threshold and if the Propagation method was used to identify secondary objects, the Regularization factor to the specific image characteristics of the dataset. To exclude the maximum amount of segmentation errors, the identified objects were further filtered to exclude too small or too big cells and cells with abnormal numbers of centrosomes and cilia.

VII.II.IV.VII.Automated autophagosome and centriolar satellite segmentation

To segment dot like structures as the autophagosomes, lysosomes and CSs I used Cell profiler's IdentifyPrimaryObjects module. I used the predetermined cell shapes as Masking objects and the tophat filtered, maximum intensity projected 488 nm as input image. The thresholding method used was RobustBackground and the Method to distinguish clumped objects was Laplacian of Gaussian. In this module, the values of the Threshold correction factor, Lower and upper bounds on threshold and parameters related to the Laplacian of Gaussian filter must be empirically optimized for each dataset.

VII.II.IV.VIII.Voronoi tilling of the cell area and determination of Wiener entropy values

Having previously segmented the cells and CS it is possible to create a Voronoi tilling of the cell area using the CS as input objects. I used Cell profiller's IdentifySecondaryObjects module Distance – B method to calculate the Voronoi tilling of the cell area and MeasureObjectSizeShape module to measure the area of each tile nucleated by the centriolar satellites. To calculate the Wiener entropy value for each cell I divided the geometric mean of the Voronoi tiles area by the arithmetic mean of the Voronoi tiles area and determined the logarithm base 10 of the resulting value.

VII.II.IV.IX.Live cell imaging

RPE1 cells were grown in 8 well, glass bottom slides (Ibidi) with DMEM/F12 without phenol red. The cell nucleus was stained with DRAQ5 and images were acquired using an Olympus IX81 microscope (Olympus) equipped with a 60x 1.35 NA, UPLSAPO oil immersion objective lens (Olympus), a CCD camera (Hamamatsu ORCA-R2), ZDC hardware autofocus, microscope stage incubation system (Okolab), and Olympus xcellence software (Olympus).

VII.II.V.Statistical analysis

VII.II.V.I.Violin plots

White circles show the medians; box limits indicate the 25th and 75th percentiles as determined by R software; whiskers extend 1.5 times the interquartile range from the 25th and 75th percentiles; polygons represent density estimates of data and extend to extreme values.

VII.II.V.II.Significance

Statistical significance was determined using pairwise χ^2 tests in Figures:

Figure	Panel
33	B
36	B
43	B
46	B
48	A and C
49	B

A Wilcoxon–Mann–Whitney test (2 samples) or Kruskal-Wallis test with Dunn's post hoc with Bonferroni correction analysis were used in Figures:

Figure	Panel
19	B
20	B, C and D
21	
23	
27	B
28	B
31	B, D and F
32	B
34	B, C and D
37	B
45	B and D
48	B and E
50	B

VIII.Bibliography

Afzelius, B. (1976). A human syndrome caused by immotile cilia. Science 193, 317–319.

Aguilera, M.O., Berón, W., and Colombo, M.I. (2012). The actin cytoskeleton participates in the early events of autophagosome formation upon starvation induced autophagy. Autophagy 8, 1590–1603.

Al-Hakim, A.K., Zagorska, A., Chapman, L., Deak, M., Peggie, M., and Alessi, D.R. (2008). Control of AMPK-related kinases by USP9X and atypical Lys(29)/Lys(33)-linked polyubiquitin chains. The Biochemical Journal 411, 249–260.

Aldaz, J.M. (2010). Concentration of the ratio between the geometric and arithmetic means. Journal of Theoretical Probability 23, 498–508.

Alers, S., Loffler, a. S., Wesselborg, S., and Stork, B. (2012). Role of AMPK-mTOR-Ulk1/2 in the Regulation of Autophagy: Cross Talk, Shortcuts, and Feedbacks. Molecular and Cellular Biology 32, 2–11.

Alpadi, K., Kulkarni, A., Comte, V., Reinhardt, M., Schmidt, A., Namjoshi, S., Mayer, A., and Peters, C. (2012). Sequential analysis of trans-SNARE formation in intracellular membrane fusion. PLoS Biology 10, 445–544.

Anderson, R.G., and Brenner, R.M. (1971). The formation of basal bodies (centrioles) in the Rhesus monkey oviduct. The Journal of Cell Biology 50, 10–34.

Andronov, L., Orlov, I., Lutz, Y., Vonesch, J.-L., and Klaholz, B.P. (2016). ClusterViSu, a method for clustering of protein complexes by Voronoi tessellation in super-resolution microscopy. Scientific Reports 6, 24084.

Azimzadeh, J., and Marshall, W.F. (2010). Building the centriole. Current Biology 20, R816–R825.

Badr, C.E., Wurdinger, T., Nilsson, J., Niers, J.M., Whalen, M., Degterev, A., and Tannous, B.A. (2011). Lanatoside C sensitizes glioblastoma cells to tumor necrosis factor-related apoptosisinducing ligand and induces an alternative cell death pathway. Neuro-Oncology 13, 1213–1224.

Balczon, R., Bao, L., and Zimmer, W.E. (1994). PCM-1, A 228-kD centrosome autoantigen with a distinct cell cycle distribution. The Journal of Cell Biology 124, 783–793.

Bärenz, F., Mayilo, D., and Gruss, O.J. (2011). Centriolar satellites: Busy orbits around the centrosome. European Journal of Cell Biology 90, 983–989.

Benmerah, A. (2013). The ciliary pocket. Current Opinion in Cell Biology 25, 1–7.

Bernhard, W., and de Harven, E. (1960). L'ultrastructure du centriole et d'autres éléments de l'appareil achromatique. In Vierter Internationaler Kongress Für Elektronenmikroskopie / Fourth International Conference on Electron Microscopy / Quatrième Congrès International de Microscopie Électronique, W. Bargmann, G. Möllenstedt, H. Niehrs, D. Peters, E. Ruska, and C. Wolpers, eds. (Berlin, Heidelberg: Springer Berlin Heidelberg), pp. 217–227.

Bertran, M.T., Sdelci, S., Regué, L., Avruch, J., Caelles, C., and Roig, J. (2011). Nek9 is a PLK-1-activated kinase that controls early centrosome separation through Nek6/7 and Eg5. The EMBO Journal 30, 2634–2647.

Bettencourt-Dias, M., and Carvalho-Santos, Z. (2008). Double life of centrioles: CP110 in the spotlight. Trends in Cell Biology 18, 8–11.

Bettencourt-Dias, M., and Glover, D.M. (2007). Centrosome biogenesis and function: centrosomics brings new understanding. Nature Reviews. Molecular Cell Biology 8, 451–463.

Betz, C., and Hall, M.N. (2013). Where is mTOR and what is it doing there? Journal of Cell Biology 203, 563–574.

Blankson, H. (1995). Disruption of the Cytokeratin Cytoskeleton and Inhibition of Hepatocytic Autophagy by Okadaic Acid. Experimental Cell Research 218, 522–530.

Boveri, T. (1887). Ueber den Antheil des Spermatozoon an der Teilung des Eies. Sitzungsber. Ges. Morph. Physiol. Munchen 151–164.

Bowser, S.S., and Wheatley, D.N. Where are Primary Cilia Found?

Brajenovic, M., Joberty, G., Küster, B., Bouwmeester, T., and Drewes, G. (2004). Comprehensive Proteomic Analysis of Human Par Protein Complexes Reveals an Interconnected Protein Network. Journal of Biological Chemistry 279, 12804–12811.

Braun, D.A., and Hildebrandt, F. (2016). Ciliopathies. Cold Spring Harbor Perspectives in Biology a028191.

van Breugel, M., Hirono, M., Andreeva, A., Yanagisawa, H.A., Yamaguchi, S., Nakazawa, Y., Morgner, N., Petrovich, M., Ebong, I.O., Robinson, C. V, et al. (2011). Structures of SAS-6 suggest its organization in centrioles. Science 331, 1196–1199.

Briscoe, J., and Thérond, P.P. (2013). The mechanisms of Hedgehog signalling and its roles in development and disease. Nature Reviews Molecular Cell Biology 14, 418–431.

Brito, D.A., Gouveia, S.M., and Bettencourt-Dias, M. (2012). Deconstructing the centriole: Structure and number control. Current Opinion in Cell Biology 24, 4–13.

Bulinski, J.C., McGraw, T.E., Gruber, D., Nguyen, H.L., and Sheetz, M.P. (1997). Overexpression of MAP4 inhibits organelle motility and trafficking in vivo. Journal of Cell Science 110 (Pt 2, 3055–3064.

Burakov, A., Nadezhdina, E., Slepchenko, B., and Rodionov, V. (2003). Centrosome positioning in interphase cells. Journal of Cell Biology 162, 963–969.

Burke, M.C., Li, F.Q., Cyge, B., Arashiro, T., Brechbuhl, H.M., Chen, X., Siller, S.S., Weiss, M.A., O'-Connell, C.B., Love, D., et al. (2014). Chibby promotes ciliary vesicle formation and basal body docking during airway cell differentiation. Journal of Cell Biology 207, 123–137.

Burkhardt, J.K., Echeverri, C.J., Nilsson, T., and Vallee, R.B. (1997). Overexpression of the dynamitin (p50) subunit of the dynactin complex disrupts dynein-dependent maintenance of membrane organelle distribution. Journal of Cell Biology 139, 469–484.

Cajánek, L., and Nigg, E. a (2014). Cep164 triggers ciliogenesis by recruiting Tau tubulin kinase 2 to the mother centriole. Proceedings of the National Academy of Sciences of the United States of America 111, E2841-50.

Cantagrel, V., Silhavy, J.L., Bielas, S.L., Swistun, D., Marsh, S.E., Bertrand, J.Y., Audollent, S., Attié-Bitach, T., Holden, K.R., Dobyns, W.B., et al. (2008). Mutations in the Cilia Gene ARL13B Lead to the Classical Form of Joubert Syndrome. American Journal of Human Genetics 83, 170–179.

Carvalho-Santos, Z., Azimzadeh, J., Pereira-Leal, J.B., and Bettencourt-Dias, M. (2011). Tracing the origins of centrioles, cilia, and flagella. Journal of Cell Biology 194, 165–175.

Caspary, T., Larkins, C.E., and Anderson, K. V. (2007). The Graded Response to Sonic Hedgehog Depends on Cilia Architecture. Developmental Cell 12, 767–778.

Cauda, F., Costa, T., Torta, D.M.E., Sacco, K., D'Agata, F., Duca, S., Geminiani, G., Fox, P.T., and Vercelli, A. (2012). Meta-analytic clustering of the insular cortex. Characterizing the meta-analytic connectivity of the insula when involved in active tasks. NeuroImage 62, 343–355.

Caydasi, A.K., and Pereira, G. (2009). Spindle Alignment Regulates the Dynamic Association of Checkpoint Proteins with Yeast Spindle Pole Bodies. Developmental Cell 16, 146–156.

Caydasi, A.K., and Pereira, G. (2012). SPOC alert-When chromosomes get the wrong direction. Experimental Cell Research 318, 1421–1427.

Chaki, M., Airik, R., Ghosh, A.K., Giles, R.H., Chen, R., Slaats, G.G., Wang, H., Hurd, T.W., Zhou, W., Cluckey, A., et al. (2012). Exome capture reveals ZNF423 and Cep164 mutations, linking renal ciliopathies to DNA damage response signaling. Cell 150, 533–548.

Chang, P., Giddings Jr., T.H., Winey, M., and Stearns, T. (2003). Epsilon-tubulin is required for centriole duplication and microtubule organization. Nat Cell Biol 5, 71–76.

Chin, L.-S., Olzmann, J. a, and Li, L. (2010). Parkin-mediated ubiquitin signalling in aggresome formation and autophagy. Biochemical Society Transactions 38, 144–149.

Christensen, S.T., Clement, C. a, Satir, P., and Pedersen, L.B. (2011). Primary cilia and coordination of Receptor Tyrosine Kinase (RTK) signaling. The Journal of Pathology 172–184.

Chung, K.K., Zhang, Y., Lim, K.L., Tanaka, Y., Huang, H., Gao, J., Ross, C. a, Dawson, V.L., and Dawson, T.M. (2001). Parkin ubiquitinates the alpha-synuclein-interacting protein, synphilin-1: implications for Lewy-body formation in Parkinson disease. Nat.Med. 7, 1144–1150.

Clement, C., Ajbro, K., Koefoed, K., Vestergaard, M., Veland, I., HenriquesdeJesus, M., Pedersen, L., Benmerah, A., Andersen, C., Larsen, L., et al. (2013). TGF-β Signaling Is Associated with Endocytosis at the Pocket Region of the Primary Cilium. Cell Reports 3, 1806–1814.

Conduit, P.T., Wainman, A., and Raff, J.W. (2015). Centrosome function and assembly in animal cells. Nature Reviews. Molecular Cell Biology 16, 611–624.

Corbit, K.C., Aanstad, P., Singla, V., Norman, A.R., Stainier, D.Y.R., and Reiter, J.F. (2005). Vertebrate Smoothened functions at the primary cilium. Nature 437, 1018–1021.

Corboy, M.J., Thomas, P.J., and Wigley, W.C. (2005). Aggresome formation. Methods in Molecular Biology (Clifton, N.J.) 301, 305–327.

Cottee, M.A., Muschalik, N., Johnson, S., Leveson, J., Raff, J.W., and Lea, S.M. (2015). The homo-oligomerisation of both Sas-6 and Ana2 is required for efficient centriole assembly in flies. eLife 4, 1–65.

Craige, B., Tsao, C.-C., Diener, D.R., Hou, Y., Lechtreck, K.-F., Rosenbaum, J.L., and Witman, G.B. (2010). CEP290 tethers flagellar transition zone microtubules to the membrane and regulates flagellar protein content. The Journal of Cell Biology 190, 927–940.

Dammermann, A., and Merdes, A. (2002). Assembly of centrosomal proteins and microtubule organization depends on PCM-1. Journal of Cell Biology 159, 255–266.

de-Thé, G. (1964). CYTOPLASMIC MICROTUBULES IN DIFFERENT ANIMAL CELLS. The Journal of Cell Biology 23, 265–275.

Delgehyr, N., Sillibourne, J., and Bornens, M. (2005). Microtubule nucleation and anchoring at the centrosome are independent processes linked by ninein function. Journal of Cell Science 118, 1565–1575.

Demetriades, C., Doumpas, N., and Teleman, A.A. (2014). Regulation of TORC1 in response to amino acid starvation via lysosomal recruitment of TSC2. Cell 156, 786–799.

Doxsey, S.J., Stein, P., Evans, L., Calarco, P.D., and Kirschner, M. (1994). Pericentrin, a highly conserved centrosome protein involved in microtubule organization. Cell 76, 639–650.

Drewes, G., Trinczek, B., Illenberger, S., Biernat, J., Schmitt-Ulms, G., Meyer, H.E., Mandelkow, E.M., and Mandelkow, E. (1995). Microtubule-associated protein/microtubule affinity-regulating kinase (p110mark): A novel protein kinase that regulates tau-microtubule interactions and dynamic instability by phosphorylation at the Alzheimer-specific site serine 262. Journal of Biological Chemistry 270, 7679–7688.

Drewes, G., Ebneth, A., Preuss, U., Mandelkow, E.M., and Mandelkow, E. (1997). MARK, a novel family of protein kinases that phosphorylate microtubule-associated proteins and trigger microtubule disruption. Cell 89, 297–308.

Ebato, C., Uchida, T., Arakawa, M., Komatsu, M., Ueno, T., Komiya, K., Azuma, K., Hirose, T., Tanaka, K., Kominami, E., et al. (2008). Autophagy Is Important in Islet Homeostasis and Compensatory Increase of Beta Cell Mass in Response to High-Fat Diet. Cell Metabolism 8, 325–332.

Egan, D.F., Shackelford, D.B., Mihaylova, M.M., Gelino, S., Kohnz, R. a., Mair, W., Vasquez, D.S., Joshi, A., Gwinn, D.M., Taylor, R., et al. (2011). Phosphorylation of ULK1 (hATG1) by AMP-Activated Protein Kinase Connects Energy Sensing to Mitophagy. Science 331, 456–461.

Ezratty, E.J., Stokes, N., Chai, S., Shah, A.S., Williams, S.E., and Fuchs, E. (2011). A role for the primary cilium in notch signaling and epidermal differentiation during skin development. Cell 145, 1129–1141.

Feng, S., Knödler, A., Ren, J., Zhang, J., Zhang, X., Hong, Y., Huang, S., Peränen, J., and Guo, W. (2012). A Rab8 guanine nucleotide exchange factor-effector interaction network regulates primary ciliogenesis. Journal of Biological Chemistry 287, 15602–15609.

Ferrante, M.I., Giorgio, G., Feather, S.A., Bulfone, A., Wright, V., Ghiani, M., Selicorni, A., Gammaro, L., Scolari, F., Woolf, A.S., et al. (2001). Identification of the gene for oral-facial-digital type I syndrome. Am J Hum Genet 68, 569–576.

Fisch, C., and Dupuis-Williams, P. (2011). Ultrastructure of cilia and flagella – back to the future! Biol. Cell 103, 249–270.

Fisher, S.K., and Steinberg, R.H. (1982). Origin and organization of pigment epithelial apical projections to cones in cat retina. The Journal of Comparative Neurology 206, 131–145.

Fırat-karalar, E.N., and Stearns, T. (2014). The centriole duplication cycle. Philosophical Transactions of the Royal Society of London. Series B, Biological Sciences 369, 1–10.

Follit, J.A. (2006). The Intraflagellar Transport Protein IFT20 Is Associated with the Golgi Complex and Is Required for Cilia Assembly. Molecular Biology of the Cell 17, 3781–3792.

Follit, J.A., Xu, F., Keady, B.T., and Pazour, G.J. (2009). Characterization of mouse IFT complex B. Cell Motility and the Cytoskeleton 66, 457–468.

Fry, A.M., Mayor, T., Meraldi, P., Stierhof, Y.D., Tanaka, K., and Nigg, E.A. (1998). C-Nap1, a novel centrosomal coiled-coil protein and candidate substrate of the cell cycle-regulated protein kinase Nek2. Journal of Cell Biology 141, 1563–1574.

Fu, J., and Glover, D.M. (2012). Structured illumination of the interface between centriole and pericentriolar material. Open Biology 2, 120104.

Ganley, I.G., Lam, D.H., Wang, J., Ding, X., Chen, S., and Jiang, X. (2009). ULK1·ATG13·FIP200 complex mediates mTOR signaling and is essential for autophagy. Journal of Biological Chemistry 284, 12297–12305.

Garcia-Gonzalo, F.R., and Reiter, J.F. (2016). Open Sesame: How Transition Fibers and the Transition Zone Control Ciliary Composition. Cold Spring Harbor Perspectives in Biology.

Gerdes, J.M., Davis, E.E., and Katsanis, N. (2009). The Vertebrate Primary Cilium in Development, Homeostasis, and Disease. Cell 137, 32–45.

Ghossoub, R., Hu, Q., Failler, M., Rouyez, M.-C., Spitzbarth, B., Mostowy, S., Wolfrum, U., Saunier, S., Cossart, P., Jamesnelson, W., et al. (2013). Septins 2, 7 and 9 and MAP4 colocalize along the axoneme in the primary cilium and control ciliary length. Journal of Cell Science 126, 2583–2594.

Gilula, N.B., and Satir, P. (1972). The ciliary necklace. A ciliary membrane specialization. The Journal of Cell Biology 53, 494–509.

Goetz, S.C., and Anderson, K. V (2010). The primary cilium: a signalling centre during vertebrate development. Nature Reviews. Genetics 11, 331–344.

Goetz, S.C., Liem, K.F., and Anderson, K. V. (2012). The spinocerebellar ataxia-associated gene tau tubulin kinase 2 controls the initiation of ciliogenesis. Cell 151, 847–858.

Gönczy, P. (2012). Towards a molecular architecture of centriole assembly. Nature Reviews Molecular Cell Biology 13, 425–435.

Goto, H., Inaba, H., and Inagaki, M. (2016). Mechanisms of ciliogenesis suppression in dividing cells. Cellular and Molecular Life Sciences 1–10.

Gould, R. (1977). The pericentriolar material in Chinese hamster ovary cells nucleates microtubule formation. The Journal of Cell Biology 73, 601–615.

Graser, S., Stierhof, Y.D., Lavoie, S.B., Gassner, O.S., Lamla, S., Le Clech, M., and Nigg, E.A. (2007). Cep164, a novel centriole appendage protein required for primary cilium formation. Journal of Cell Biology 179, 321–330.

Gromley, A., Jurczyk, A., Sillibourne, J., Halilovic, E., Mogensen, M., Groisman, I., Blomberg, M., and Doxsey, S. (2003). A novel human protein of the maternal centriole is required for the final stages of cytokinesis and entry into S phase. Journal of Cell Biology 161, 535–545.

Guarguaglini, G., Duncan, P.I., Stierhof, Y.D., Holmstro¨m, T., Duensing, S., and Nigg, E.A. (2005). The Forkhead-associated Domain Protein Cep170 Interacts with Polo-like Kinase 1 and Serves as a Marker for Mature Centrioles. Molecular Biology of the Cell 16, 1095–1107.

Gupta, G.D., Coyaud, É., Gonçalves, J., Mojarad, B.A., Liu, Y., Wu, Q., Gheiratmand, L., Comartin, D., Tkach, J.M., Cheung, S.W.T., et al. (2015). A Dynamic Protein Interaction Landscape of the Human Centrosome-Cilium Interface. Cell 163, 1484–1499.

Gwinn, D.M., Shackelford, D.B., Egan, D.F., Mihaylova, M.M., Mery, A., Vasquez, D.S., Turk, B.E., and Shaw, R.J. (2008). AMPK Phosphorylation of Raptor Mediates a Metabolic Checkpoint. Molecular Cell 30, 214–226.

Hames, R.S., Crookes, R.E., Straatman, K.R., Merdes, A., Hayes, M.J., Faragher, A.J., and Fry, A.M. (2005). Dynamic recruitment of Nek2 kinase to the centrosome involves microtubules, PCM-1, and localized proteasomal degradation. Molecular Biology of the Cell 16, 1711–1724.

Hardie, D.G. (2007). AMP-activated/SNF1 protein kinases: conserved guardians of cellular energy. Nature Reviews. Molecular Cell Biology 8, 774–785.

Hardie, D.G., Ross, F. a., and Hawley, S. a. (2012). AMPK: a nutrient and energy sensor that maintains energy homeostasis. Nature Reviews Molecular Cell Biology 13, 251–262.

Haycraft, C.J., Banizs, B., Aydin-Son, Y., Zhang, Q., Michaud, E.J., and Yoder, B.K. (2005). Gli2 and Gli3 localize to cilia and require the intra flagellar transport protein polaris for processing and function. PLOS Genetics 1, e53.

Heitman, J., Movva, N., and Hall, M. (1991). Targets for cell cycle arrest by the immunosuppressant rapamycin in yeast. Science 253, 905–909.

Heller, R.F., and Gordon, R.E. (1986). Chronic Effects of Nitrogen Dioxide on Cilia in Hamster Bronchioles. Experimental Lung Research 10, 137–152.

Helps, N.R., Luo, X., Barker, H.M., and Cohen, P.T. (2000). NIMA-related kinase 2 (Nek2), a cell-cycle-regulated protein kinase localized to centrosomes, is complexed to protein phosphatase 1. The Biochemical Journal 349, 509–518.

Hilgendorf, K.I., Johnson, C.T., and Jackson, P.K. (2016). The primary cilium as a cellular receiver: Organizing ciliary GPCR signaling. Current Opinion in Cell Biology 39, 84–92.

Hori, A., and Toda, T. (2016). Regulation of centriolar satellite integrity and its physiology. Cellular and Molecular Life Sciences 1–17.

Houlden, H., Johnson, J., Gardner-Thorpe, C., Lashley, T., Hernandez, D., Worth, P., Singleton, A.B., Hilton, D.A., Holton, J., Revesz, T., et al. (2007). Mutations in TTBK2, encoding a kinase implicated in tau phosphorylation, segregate with spinocerebellar ataxia type 11. Nature Genetics 39, 1434–1436.

Hu, Q., and Nelson, W.J. (2011). Ciliary diffusion barrier: The gatekeeper for the primary cilium compartment. Cytoskeleton 68, 313–324.

Hu, Q., Milenkovic, L., Jin, H., Scott, M.P., Nachury, M. V, Spiliotis, E.T., and Nelson, W.J. (2010). A septin diffusion barrier at the base of the primary cilium maintains ciliary membrane protein distribution. Science (New York, N.Y.) 329, 436–439.

Ibi, M., Zou, P., Inoko, A., Shiromizu, T., Matsuyama, M., Hayashi, Y., Enomoto, M., Mori, D., Hirotsune, S., Kiyono, T., et al. (2011). Trichoplein controls microtubule anchoring at the centrosome by binding to Odf2 and ninein. J Cell Sci 124, 857–864.

Ikezu, S., and Ikezu, T. (2014). Tau-tubulin kinase. Frontiers in Molecular Neuroscience 7, 33.

Inoki, K., Li, Y., Xu, T., and Guan, K.L. (2003a). Rheb GTpase is a direct target of TSC2 GAP activity and regulates mTOR signaling. Genes and Development 17, 1829–1834.

Inoki, K., Zhu, T., and Guan, K.-L. (2003b). TSC2 Mediates Cellular Energy Response to Control Cell Growth and Survival. Cell 115, 577–590.

Inoko, A., Matsuyama, M., Goto, H., Ohmuro-Matsuyama, Y., Hayashi, Y., Enomoto, M., Ibi, M., Urano, T., Yonemura, S., Kiyono, T., et al. (2012). Trichoplein and Aurora A block aberrant primary cilia assembly in proliferating cells. Journal of Cell Biology 197, 391–405.

Ishikawa, H., and Marshall, W.F. (2011). Ciliogenesis: building the cell's antenna. Nature Reviews. Molecular Cell Biology 12, 222–234.

Ishikawa, H., Kubo, A., Tsukita, S., and Tsukita, S. (2005). Odf2-deficient mother centrioles lack distal/subdistal appendages and the ability to generate primary cilia. Nature Cell Biology 7, 517–524.

Iwata, A., Christianson, J.C., Bucci, M., Ellerby, L.M., Nukina, N., Forno, L.S., and Kopito, R.R. (2005a). Increased susceptibility of cytoplasmic over nuclear polyglutamine aggregates to autophagic degradation. Proc Natl Acad Sci U S A 102, 13135–13140.

Iwata, A., Riley, B.E., Johnston, J.A., and Kopito, R.R. (2005b). HDAC6 and microtubules are required for autophagic degradation of aggregated Huntingtin. Journal of Biological Chemistry 280, 40282–40292.

Izawa, I., Goto, H., Kasahara, K., and Inagaki, M. (2015). Current topics of functional links between primary cilia and cell cycle. Cilia 4, 12.

Jafari-mamaghani, M., Andersson, M., Krieger, P., and Luciano, F. (2010). Spatial point pattern analysis of neurons using Ripley ' s K-function in 3D. 4, 1–10.

Janke, C., Bulinski, J.C., and Chloë Bulinski, J. (2011). Post-translational regulation of the microtubule cytoskeleton: mechanisms and functions. Nature Reviews Molecular Cell Biology 12, 773–786.

Jenardhanan, P., Mannu, J., and Mathur, P.P. (2014). The structural analysis of MARK4 and the exploration of specific inhibitors for the MARK family: a computational approach to obstruct the role of MARK4 in prostate cancer progression. Molecular bioSystems 10, 1845–1868.

Jenkins, S.M., and Johnson, G.V.W. (2000). Microtubule/MAP-affinity regulating kinase (MARK) is activated by phenylarsine oxide in situ and phosphorylates tau within its microtubule- binding domain. Journal of Neurochemistry 74, 1463–1468.

Jiang, K., Toedt, G., Montenegro Gouveia, S., Davey, N.E., Hua, S., Van Der Vaart, B., Grigoriev, I., Larsen, J., Pedersen, L.B., Bezstarosti, K., et al. (2012). A proteome-wide screen for mammalian SxIP motif-containing microtubule plus-end tracking proteins. Current Biology 22, 1800–1807.

Joo, K., Kim, C.G., Lee, M.-S., Moon, H.-Y., Lee, S.-H., Kim, M.J., Kweon, H.-S., Park, W.-Y., Kim, C.-H., Gleeson, J.G., et al. (2013). CCDC41 is required for ciliary vesicle docking to the mother centriole. Proceedings of the National Academy of Sciences of the United States of America 110, 5987–5992.

Jung, C.H., Jun, C.B., Ro, S.-H., Kim, Y.-M., Otto, N.M., Cao, J., Kundu, M., and Kim, D.-H. (2009). ULK-Atg13-FIP200 complexes mediate mTOR signaling to the autophagy machinery. Molecular Biology of the Cell 20, 1992–2003.

Kabeya, Y., Mizushima, N., Ueno, T., Yamamoto, A., Kirisako, T., Noda, T., Kominami, E., Ohsumi, Y., and Yoshimori, T. (2003). Erratum: LC3, a mammalian homolog of yeast Apg8p, is localized in autophagosome membranes after processing (EMBO Journal (2000) 19 (5720-5728)). EMBO Journal 22, 4577.

Kamada, Y., Yoshino, K., Kondo, C., Kawamata, T., Oshiro, N., Yonezawa, K., and Ohsumi, Y. (2010). Tor directly controls the Atg1 kinase complex to regulate autophagy. Molecular and Cellular Biology 30, 1049–1058.

Kasahara, K., Kawakami, Y., Kiyono, T., Yonemura, S., Kawamura, Y., Era, S., Matsuzaki, F., Goshima, N., and Inagaki, M. (2014). Ubiquitin-proteasome system controls ciliogenesis at the initial step of axoneme extension. Nature Communications 5, 5081.

Kato, T., Satoh, S., Okabe, H., Kitahara, O., Ono, K., Kihara, C., Tanaka, T., Tsunoda, T., Yamaoka, Y., Nakamura, Y., et al. (2001). Isolation of a Novel Human Gene, MARKL1, Homologous to MARK3 and Its Involvement in Hepatocellular Carcinogenesis1. Neoplasia (New York, N.Y.) 3, 4–9.

Kaur, J., and Debnath, J. (2015). Autophagy at the crossroads of catabolism and anabolism. Nature Reviews. Molecular Cell Biology 16, 461–472.

Kim, E., Goraksha-Hicks, P., Li, L., Neufeld, T.P., and Guan, K.-L. (2008a). Regulation of TORC1 by Rag GTPases in nutrient response. Nature Cell Biology 10, 935–945.

Kim, J., Krishnaswami, S.R., and Gleeson, J.G. (2008b). CEP290 interacts with the centriolar satellite component PCM-1 and is required for Rab8 localization to the primary cilium. Human Molecular Genetics 17, 3796–3805.

Kim, J., Kundu, M., Viollet, B., and Guan, K.-L. (2011). AMPK and mTOR regulate autophagy through direct phosphorylation of Ulk1. Nature Cell Biology 13, 132–141.

Kim, J.C., Badano, J.L., Sibold, S., Esmail, M. a, Hill, J., Hoskins, B.E., Leitch, C.C., Venner, K., Ansley, S.J., Ross, A.J., et al. (2004). The Bardet-Biedl protein BBS4 targets cargo to the pericentriolar region and is required for microtubule anchoring and cell cycle progression. Nature Genetics 36, 462–470.

Kim, T.-S., Park, J.-E., Shukla, A., Choi, S., Murugan, R.N., Lee, J.H., Ahn, M., Rhee, K., Bang, J.K., Kim, B.Y., et al. (2013). Hierarchical recruitment of Plk4 and regulation of centriole biogenesis by two centrosomal scaffolds, Cep192 and Cep152. Proceedings of the National Academy of Sciences of the United States of America 110, E4849-57.

Kimura, S., Noda, T., and Yoshimori, T. (2008). Dynein-dependent movement of autophagosomes mediates efficient encounters with lysosomes. Cell Structure and Function 33, 109–122.

Kiskowski, M.A., Hancock, J.F., and Kenworthy, A.K. (2009). On the use of Ripley's K-function and its derivatives to analyze domain size. Biophysical Journal 97, 1095–1103.

Kitagawa, D., Vakonakis, I., Olieric, N., Hilbert, M., Keller, D., Olieric, V., Bortfeld, M., Erat, M.C., Flückiger, I., Gönczy, P., et al. (2011). Structural basis of the 9-fold symmetry of centrioles. Cell 144, 364–375.

Kleylein-Sohn, J., Westendorf, J., Le Clech, M., Habedanck, R., Stierhof, Y.D., and Nigg, E.A. (2007). Plk4-Induced Centriole Biogenesis in Human Cells. Developmental Cell 13, 190–202.

Knödler, A., Feng, S., Zhang, J., Zhang, X., Das, A., Peränen, J., and Guo, W. (2010). Coordination of Rab8 and Rab11 in primary ciliogenesis. Proceedings of the National Academy of Sciences of the United States of America 107, 6346–6351.

Kobayashi, T., Tsang, W.Y., Li, J., Lane, W., and Dynlacht, B.D. (2011). Centriolar kinesin Kif24 interacts with CP110 to remodel microtubules and regulate ciliogenesis. Cell 145, 914–925.

Kobayashi, T., Kim, S., Lin, Y.C., Inoue, T., and Dynlacht, B.D. (2014). The CP110-interacting proteins talpid3 and cep290 play overlapping and distinct roles in cilia assembly. Journal of Cell Biology 204, 215–229.

Kohlmaier, G., Lončarek, J., Meng, X., McEwen, B.F., Mogensen, M.M., Spektor, A., Dynlacht, B.D., Khodjakov, A., and Gönczy, P. (2009). Overly Long Centrioles and Defective Cell Division upon Excess of the SAS-4-Related Protein CPAP. Current Biology 19, 1012–1018.

Komatsu, M., Waguri, S., Ueno, T., Iwata, J., Murata, S., Tanida, I., Ezaki, J., Mizushima, N., Ohsumi, Y., Uchiyama, Y., et al. (2005). Impairment of starvation-induced and constitutive autophagy in Atg7-deficient mice. Journal of Cell Biology 169, 425–434.

Kong, D., Farmer, V., Shukla, A., James, J., Gruskin, R., Kiriyama, S., and Loncarek, J. (2014). Centriole maturation requires regulated PLK-1 activity during two consecutive cell cycles. Journal of Cell Biology 206, 855–865.

Korolchuk, V.I., Saiki, S., Lichtenberg, M., Siddiqi, F.H., Roberts, E.A., Imarisio, S., Jahreiss, L., Sarkar, S., Futter, M., Menzies, F.M., et al. (2011). Lysosomal positioning coordinates cellular nutrient responses. Nature Cell Biology 13, 453–460.

Kozminski, K.G., Johnson, K.A., Forscher, P., and Rosenbaum, J.L. (1993). A motility in the eukaryotic flagellum unrelated to flagellar beating. Cell Biology 90, 5519–5523.

Kraft, C., Peter, M., and Hofmann, K. (2010). Selective autophagy: ubiquitin-mediated recognition and beyond. Nature Cell Biology 12, 836–841.

Kubo, A., Sasaki, H., Yuba-Kubo, A., Tsukita, S., and Shiina, N. (1999). Centriolar satellites: molecular characterization, ATP-dependent movement toward centrioles and possible involvement in ciliogenesis. The Journal of Cell Biology 147, 969–980.

Kuhns, S., Schmidt, K.N., Reymann, J., Gilbert, D.F., Neuner, A., Hub, B., Carvalho, R., Wiedemann, P., Zentgraf, H., Erfle, H., et al. (2013). The microtubule affinity regulating kinase MARK4 promotes axoneme extension during early ciliogenesis. Journal of Cell Biology 200, 505–522.

Lam, H.C., Cloonan, S.M., Bhashyam, A.R., Haspel, J.A., Singh, A., Sathirapongsasuti, J.F., Cervo, M., Yao, H., Chung, A.L., Mizumura, K., et al. (2013). Histone deacetylase 6–mediated selective autophagy regulates COPD-associated cilia dysfunction. Journal of Clinical Investigation 123, 5212–5230.

Lamb, C.A., Yoshimori, T., and Tooze, S.A. (2013). The autophagosome: origins unknown, biogenesis complex. Nature Reviews Molecular Cell Biology 14, 759–774.

Lambacher, N.J., Bruel, A.-L., van Dam, T.J.P., Szymańska, K., Slaats, G.G., Kuhns, S., McManus, G.J., Kennedy, J.E., Gaff, K., Wu, K.M., et al. (2015). TMEM107 recruits ciliopathy proteins to subdomains of the ciliary transition zone and causes Joubert syndrome. Nature Cell Biology 18, 122–131.

Lawo, S., Hasegan, M., Gupta, G.D., and Pelletier, L. (2012). Subdiffraction imaging of centrosomes reveals higher-order organizational features of pericentriolar material. Nature Cell Biology 12, 308–317.

Lechtreck, K.F. (2015). IFT-Cargo Interactions and Protein Transport in Cilia. Trends in Biochemical Sciences 40, 765–778.

Lee, J.W., Park, S., Takahashi, Y., and Wang, H.-G. (2010). The Association of AMPK with ULK1 Regulates Autophagy. PLoS ONE 5, e15394.

Levet, F., Hosy, E., Kechkar, A., Butler, C., Beghin, A., Choquet, D., and Sibarita, J.-B. (2015). SR-Tesseler: a method to segment and quantify localization-based super-resolution microscopy data. Nature Methods 12, 1065–1071.

Li, L., and Guan, K.L. (2013). Microtubule-associated protein/microtubule affinity-regulating kinase 4 (MARK4) is a negative regulator of the mammalian target of rapamycin complex 1 (mTORC1). Journal of Biological Chemistry 288, 703–708.

Liao, J., Yang, T.T., Weng, R.R., Kuo, C., and Chang, C. (2015). TTBK2: A Tau Protein Kinase beyond Tau Phosphorylation. BioMed Research International 2015, 1–10.

Lindemann, C.B., and Lesich, K.A. (2010). Flagellar and ciliary beating: the proven and the possible. J Cell Sci 123, 519–528.

Lizcano, J.M., Göransson, O., Toth, R., Deak, M., Morrice, N.A., Boudeau, J., Hawley, S.A., Udd, L., Mäkelä, T.P., Hardie, D.G., et al. (2004). LKB1 is a master kinase that activates 13 kinases of the AMPK subfamily, including MARK/PAR-1. The EMBO Journal 23, 833–843.

Loos, B., du Toit, A., and Hofmeyr, J.-H.S. (2014). Defining and measuring autophagosome flux—concept and reality. Autophagy 10, 2087–2096.

Lopes, C. a M., Prosser, S.L., Romio, L., Hirst, R. a, O'Callaghan, C., Woolf, A.S., and Fry, A.M. (2011). Centriolar satellites are assembly points for proteins implicated in human ciliopathies, including oral-facial-digital syndrome 1. Journal of Cell Science 124, 600–612.

Lu, Q., Insinna, C., Ott, C., Stauffer, J., Pintado, P.A., Rahajeng, J., Baxa, U., Walia, V., Cuenca, A., Hwang, Y., et al. (2015). Early steps in primary cilium assembly require EHD1- and EHD3- dependent ciliary vesicle formation. Nature Cell Biology 17, 228–240.

Lupas, A., Van Dyke, M., and Stock, J. (1991). Predicting coiled coils from protein sequences. Science 252, 1162–1164.

Magnani, I., Novielli, C., Bellini, M., Roversi, G., Bello, L., and Larizza, L. (2009). Multiple localization of endogenous MARK4L protein in human glioma. Cellular Oncology 31, 357–370.

Malicki, J.J., and Johnson, C.A. (2016). The Cilium: Cellular Antenna and Central Processing Unit. Trends in Cell Biology xx, 1–15.

Manning, G. (2002). The Protein Kinase Complement of the Human Genome. Science 298, 1912–1934.

Mardin, B.R., Agircan, F.G., Lange, C., and Schiebel, E. (2011). PLK-1 Controls the Nek2A-PP1γ Antagonism in Centrosome Disjunction. Current Biology 21, 1145–1151.

Marx, A., Nugoor, C., Müller, J., Panneerselvam, S., Timm, T., Bilang, M., Mylonas, E., Svergun, D.I., Mandelkow, E.M., and Mandelkow, E. (2006). Structural variations in the catalytic and ubiquitin-associated domains of microtubule-associated protein/microtubule affinity regulating kinase (MARK) 1 and MARK2. Journal of Biological Chemistry 281, 27586–27599.

Masyuk, A.I., Gradilone, S. a, Banales, J.M., Huang, B.Q., Masyuk, T. V, Lee, S.-O., Splinter, P.L., Stroope, A.J., and Larusso, N.F. (2008). Cholangiocyte primary cilia are chemosensory organelles that detect biliary nucleotides via P2Y12 purinergic receptors. American Journal of Physiology. Gastrointestinal and Liver Physiology 295, G725–G734.

Matenia, D., Griesshaber, B., Li, X., Thiessen, A., Johne, C., Jiao, J., Mandelkow, E., and Mandelkow, E.-M. (2005). PAK5 kinase is an inhibitor of MARK/Par-1, which leads to stable microtubules and dynamic actin. Molecular Biology of the Cell 16, 4410–4422.

May-Simera, H.L., and Kelley, M.W. (2012). Cilia, Wnt signaling, and the cytoskeleton. Cilia 1, 7.

Mazo, G., Soplop, N., Wang, W.-J., Uryu, K., and Tsou, M.-F.B. (2016). Spatial Control of Primary Ciliogenesis by Subdistal Appendages Alters Sensation-Associated Properties of Cilia. Developmental Cell 39, 424–437.

McGlashan, S.R. (2006). Localization of Extracellular Matrix Receptors on the Chondrocyte Primary Cilium. Journal of Histochemistry and Cytochemistry 54, 1005–1014.

Mennella, V., Keszthelyi, B., McDonald, K.L., Chhun, B., Kan, F., Rogers, G.C., Huang, B., and Agard, D.A. (2012). Subdiffraction-resolution fluorescence microscopy reveals a domain of the centrosome critical for pericentriolar material organization. Nature Cell Biology 14, 1159–1168.

Mi, N., Chen, Y., Wang, S., Chen, M., Zhao, M., Yang, G., Ma, M., Su, Q., Luo, S., Shi, J., et al. (2015). CapZ regulates autophagosomal membrane shaping by promoting actin assembly inside the isolation membrane. Nature Cell Biology 17, 1112–1123.

Mihaylova, M.M., and Shaw, R.J. (2011). The AMPK signalling pathway coordinates cell growth, autophagy and metabolism. Nature Cell Biology 13, 1016–1023.

Mikule, K., Delaval, B., Kaldis, P., Jurcyzk, A., Hergert, P., and Doxsey, S. (2007). Loss of centrosome integrity induces p38-p53-p21-dependent G1-S arrest. Nature Cell Biology 9, 160–170.

Mitchison, T., and Kirschner, M. (1984). Microtubule assembly nucleated by isolated centrosomes. Nature 312, 232–237.

Mizushima, N., and Hara, T. (2006). Intracellular quality control by autophagy: How does autophagy prevent neurodegeneration? Autophagy 2, 302–304.

Mogensen, M.M., Malik, A., Piel, M., Bouckson-Castaing, V., and Bornens, M. (2000). Microtubule minus-end anchorage at centrosomal and non-centrosomal sites: the role of ninein. Journal of Cell Science 113 (Pt 1, 3013–3023.

Moritz, M., Braunfeld, M.B., Sedat, J.W., Alberts, B., and Agard, D.A. (1995). Microtubule nucleation by gamma-tubulin-containing rings in the centrosome. Nature 378, 638–640.

Murrow, L., and Debnath, J. (2012). Autophagy as a Stress-Response and Quality-Control Mechanism: Implications for Cell Injury and Human Disease. Annual Review of Pathology: Mechanisms of Disease 8, 121016121742000.

Nachury, M. V (2014). How do cilia organize signalling cascades? Philosophical Transactions of the Royal Society of London. Series B, Biological Sciences 369, 20130465-.

Nachury, M. V, Seeley, E.S., and Jin, H. (2010). Trafficking to the ciliary membrane: how to get across the periciliary diffusion barrier? Annual Review of Cell and Developmental Biology 26, 59–87.

Nachury, M. V., Loktev, A. V., Zhang, Q., Westlake, C.J., Peränen, J., Merdes, A., Slusarski, D.C., Scheller, R.H., Bazan, J.F., Sheffield, V.C., et al. (2007). A Core Complex of BBS Proteins Cooperates with the GTPase Rab8 to Promote Ciliary Membrane Biogenesis. Cell 129, 1201–1213.

Nakagawa, Y., Yamane, Y., Okanoue, T., Tsukita, S., and Tsukita, S. (2001). Outer dense fiber 2 is a widespread centrosome scaffold component preferentially associated with mother centrioles: its identification from isolated centrosomes. Molecular Biology of the Cell 12, 1687–1697.

Nakazawa, Y., Hiraki, M., Kamiya, R., and Hirono, M. (2007). SAS-6 is a Cartwheel Protein that Establishes the 9-Fold Symmetry of the Centriole. Current Biology 17, 2169–2174.

Naz, F., Anjum, F., Islam, A., Ahmad, F., and Hassan, M.I. (2013). Microtubule Affinity-Regulating Kinase 4: Structure, Function, and Regulation. Cell Biochemistry and Biophysics 67, 485–499.

Nigg, E.A., and Raff, J.W. (2009). Centrioles, Centrosomes, and Cilia in Health and Disease. Cell 139, 663–678.

Nigg, E.A., and Stearns, T. (2011). The centrosome cycle: Centriole biogenesis, duplication and inherent asymmetries. Nat Cell Biol 13, 1154–1160.

Oda, T., Chiba, S., Nagai, T., and Mizuno, K. (2014). Binding to Cep164, but not EB1, is essential for centriolar localization of TTBK2 and its function in ciliogenesis. Genes to Cells 19, 927–940.

Ohta, M., Ashikawa, T., Nozaki, Y., Kozuka-Hata, H., Goto, H., Inagaki, M., Oyama, M., and Kitagawa, D. (2014). Direct interaction of Plk4 with STIL ensures formation of a single procentriole per parental centriole. Nature Communications 5, 5267.

Omori, Y., Zhao, C., Saras, A., Mukhopadhyay, S., Kim, W., Furukawa, T., Sengupta, P., Veraksa, A., and Malicki, J. (2008). Elipsa is an early determinant of ciliogenesis that links the IFT particle to membrane-associated small GTPase Rab8. Nature Cell Biology 10, 437–444.

Orhon, I., Dupont, N., Pampliega, O., Cuervo, a M., and Codogno, P. (2014). Autophagy and regulation of cilia function and assembly. Cell Death and Differentiation 22, 1–9.

Orhon, I., Dupont, N., Zaidan, M., Boitez, V., Burtin, M., Schmitt, A., Capiod, T., Viau, A., Beau, I., Wolfgang Kuehn, E., et al. (2016). Primary-cilium-dependent autophagy controls epithelial cell volume in response to fluid flow. Nature Cell Biology i, 657–667.

Pampliega, O., Orhon, I., Patel, B., Sridhar, S., Díaz-Carretero, A., Beau, I., Codogno, P., Satir, B.H., Satir, P., and Cuervo, A.M. (2013). Functional interaction between autophagy and ciliogenesis. Nature 502, 194–200.

Panneerselvam, S., Marx, A., Mandelkow, E.M., and Mandelkow, E. (2006). Structure of the catalytic and ubiquitin-associated domains of the protein kinase MARK/Par-1. Structure 14, 173–183.

Pazour, G.J., Dickert, B.L., Vucica, Y., Seeley, E.S., Rosenbaum, J.L., Witman, G.B., and Cole, D.G. (2000). Chlamydomonas IFT 88 and Its Mouse Homologue , Polycystic Kidney Disease Gene Tg 737 , Are Required for Assembly of Cilia and Flagella. The Journal of Cell Biology 151, 709–718.

Pearson, C.G., Giddings, T.H., and Winey, M. (2008). Basal Body Components Exhibit Differential Protein Dynamics during Nascent Basal Body Assembly. Molecular Biology of the Cell 20, 904–914.

Pedersen, L.B., and Rosenbaum, J.L. (2008). Chapter Two Intraflagellar Transport (IFT). Role in Ciliary Assembly, Resorption and Signalling (Elesvier Inc.).

Pelletier, L., Özlü, N., Hannak, E., Cowan, C., Habermann, B., Ruer, M., Müller-Reichert, T., and Hyman, A.A. (2004). The Caenorhabditis elegans Centrosomal Protein SPD-2 Is Required for both Pericentriolar Material Recruitment and Centriole Duplication. Current Biology 14, 863–873.

Peterson, S.P., and Berns, M.W. (1978). Evidence for centriolar region RNA functioning in spindle formation in dividing PTK2 cells. Journal of Cell Science 34, 289–301.

Phua, S.C., Lin, Y.C., and Inoue, T. (2015). An intelligent nano-antenna: Primary cilium harnesses TRP channels to decode polymodal stimuli. Cell Calcium 58, 415–422.

Prodanov, D., Nagelkerke, N., and Marani, E. (2007). Spatial clustering analysis in neuroanatomy: Applications of different approaches to motor nerve fiber distribution. Journal of Neuroscience Methods 160, 93–108.

Quintyne, N.J., Gill, S.R., Eckley, D.M., Crego, C.L., Compton, D.A., and Schroer, T.A. (1999). Dynactin is required for microtubule anchoring at centrosomes. Journal of Cell Biology 147, 321–334.

Raben, N., Hill, V., Shea, L., Takikita, S., Baum, R., Mizushima, N., Ralston, E., and Plotz, P. (2008). Suppression of autophagy in skeletal muscle uncovers the accumulation of ubiquitinated proteins and their potential role in muscle damage in Pompe disease. Human Molecular Genetics 17, 3897–3908.

Rattner, J.B., Sciore, P., Ou, Y., Van Der Hoorn, F.A., and Lo, I.K.Y. (2010). Primary cilia in fibroblast-like type B synoviocytes lie within a cilium pit: A site of endocytosis. Histology and Histopathology 25, 865–875.

Reiter, J.F., Blacque, O.E., and Leroux, M.R. (2012). The base of the cilium: roles for transition fibres and the transition zone in ciliary formation, maintenance and compartmentalization. EMBO Reports 13, 608–618.

Ringo, D.L. (1967). Flagellar motion and fine structure of the flagellar apparatus in Chlamydomonas. The Journal of Cell Biology 33, 543–571.

Rohatgi, R., and Snell, W.J. (2010). The ciliary membrane. Current Opinion in Cell Biology 22, 541–546.

Romio, L., Wright, V., Price, K., Winyard, P.J., Donnai, D., Porteous, M.E., Franco, B., Giorgio, G., Malcolm, S., Woolf, A.S., et al. (2003). OFD1, the Gene Mutated in Oral-Facial-Digital Syndrome Type 1, Is Expressed in the Metanephros and in Human Embryonic Renal Mesenchymal Cells. Journal of the American Society of Nephrology : JASN 14, 680–689.

Ross, L., and Normark, B.B. (2015). Evolutionary problems in centrosome and centriole biology. Journal of Evolutionary Biology 28, 995–1004.

Rovina, D., Fontana, L., Monti, L., Novielli, C., Panini, N., Sirchia, S.M., Erba, E., Magnani, I., and Larizza, L. (2014). Microtubule-associated protein/microtubule affinity-regulating kinase 4 (MARK4) plays a role in cell cycle progression and cytoskeletal dynamics. European Journal of Cell Biology 93, 355–365.

Sancak, Y., Peterson, T.R., Shaul, Y.D., Lindquist, R.A., Thoreen, C.C., Bar-Peled, L., and Sabatini, D.M. (2008). The Rag GTPases bind raptor and mediate amino acid signaling to mTORC1. Science (New York, N.Y.) 320, 1496–1501.

Sancak, Y., Bar-Peled, L., Zoncu, R., Markhard, A.L., Nada, S., and Sabatini, D.M. (2010). Ragulator-rag complex targets mTORC1 to the lysosomal surface and is necessary for its activation by amino acids. Cell 141, 290–303.

Sato, S., Cerny, R.L., Buescher, J.L., and Ikezu, T. (2006). Tau-tubulin kinase 1 (TTBK1), a neuron-specific tau kinase candidate, is involved in tau phosphorylation and aggregation. Journal of Neurochemistry 98, 1573–1584.

Schmidt, K.N., Kuhns, S., Neuner, A., Hub, B., Zentgraf, H., and Pereira, G. (2012). Cep164 mediates vesicular docking to the mother centriole during early steps of ciliogenesis. Journal of Cell Biology 199, 1083–1101.

Schmidt, T.I., Kleylein-Sohn, J., Westendorf, J., Le Clech, M., Lavoie, S.B., Stierhof, Y.D., and Nigg, E.A. (2009). Control of Centriole Length by CPAP and CP110. Current Biology 19, 1005–1011.

Schnackenberg, B., Khodjakov, A., Rieder, C., and Palazzo, R. (1998). The disassembly and reassembly of functional centrosomes in vitro. Proceedings of the National Academy of Sciences 95, 9295–9300.

Schou, K.B., Pedersen, L.B., and Christensen, S.T. (2015). Ins and outs of GPCR signaling in primary cilia. EMBO Reports 16, 1099–1113.

Seeger-Nukpezah, T., and Golemis, E.A. (2012). The extracellular matrix and ciliary signaling. Current Opinion in Cell Biology 24, 652–661.

Seeley, E.S., and Nachury, M. V (2010). The perennial organelle: assembly and disassembly of the primary cilium. Journal of Cell Science 123, 511–518.

Semenova, I., Ikeda, K., Resaul, K., Kraikivski, P., Aguiar, M., Gygi, S., Zaliapin, I., Cowan, A., and Rodionov, V. (2014). Regulation of microtubule-based transport by MAP4. Molecular Biology of the Cell 25, 3119–3132.

Shang, L., Chen, S., Du, F., Li, S., Zhao, L., and Wang, X. (2011). Nutrient starvation elicits an acute autophagic response mediated by Ulk1 dephosphorylation and its subsequent dissociation from AMPK. Proceedings of the National Academy of Sciences 108, 4788–4793.

Shimobayashi, M., and Hall, M.N. (2014). Making new contacts: the mTOR network in metabolism and signalling crosstalk. Nature Reviews. Molecular Cell Biology 15, 155–162.

Sillibourne, J.E., Specht, C.G., Izeddin, I., Hurbain, I., Tran, P., Triller, A., Darzacq, X., Dahan, M., and Bornens, M. (2011). Assessing the localization of centrosomal proteins by PALM/STORM nanoscopy. Cytoskeleton 68, 619–627.

Sillibourne, J.E., Hurbain, I., Grand-Perret, T., Goud, B., Tran, P., and Bornens, M. (2013). Primary ciliogenesis requires the distal appendage component Cep123. Biology Open 2, 535–545.

Silverman, M.A., and Leroux, M.R. (2009). Intraflagellar transport and the generation of dynamic, structurally and functionally diverse cilia. Trends in Cell Biology 19, 306–316.

Singla, V., and Reiter, J.F. (2006). The primary cilium as the cell's antenna: signaling at a sensory organelle. Science 313, 629–633.

Singla, V., Romaguera-Ros, M., Garcia-Verdugo, J.M., and Reiter, J.F. (2010). Ofd1, a Human Disease Gene, Regulates the Length and Distal Structure of Centrioles. Developmental Cell 18, 410–424.

Sonnen, K.F., Schermelleh, L., Leonhardt, H., and Nigg, E.A. (2012). 3D-structured illumination microscopy provides novel insight into architecture of human centrosomes. Biology Open 1, 965–976.

Sorokin, S. (1962). Centrioles and the formation of rudimentary cilia by fibroblasts and smooth muscle cells. Cell Biology 15, 363–377.

Sorokin, S.P. (1968). Reconstructions of centriole formation and ciliogenesis in mammalian lungs. Journal of Cell Science 3, 207–230.

Spektor, A., Tsang, W.Y., Khoo, D., and Dynlacht, B.D. (2007). Cep97 and CP110 Suppress a Cilia Assembly Program. Cell 130, 678–690.

Steinman, R.M. (1968). An electron microscopic study of ciliogenesis in developing epidermis and trachea in the embryo of Xenopus laevis. American Journal of Anatomy 122, 19–55.

Stevens, N.R., Roque, H., and Raff, J.W. (2010). DSas-6 and Ana2 Coassemble into Tubules to Promote Centriole Duplication and Engagement. Developmental Cell 19, 913–919.

Stolz, A., Ernst, A., and Dikic, I. (2014). Cargo recognition and trafficking in selective autophagy. Nature Cell Biology 16, 495–501.

Stowe, T.R., Wilkinson, C.J., Iqbal, A., and Stearns, T. (2012). The centriolar satellite proteins Cep72 and Cep290 interact and are required for recruitment of BBS proteins to the cilium. Molecular Biology of the Cell 23, 3322–3335.

Styers, M.L. (2004). The Endo-Lysosomal Sorting Machinery Interacts with the Intermediate Filament Cytoskeleton. Molecular Biology of the Cell 15, 5369–5382.

Takahashi, M., Tomizawa, K., Sato, K., Ohtake, A., and Omori, A. (1995). A novel tau-tubulin kinase from bovine brain. FEBS Letters 372, 59–64.

Tang, C.J., Fu, R.H., Wu, K.S., Hsu, W.B., and Tang, T.K. (2009). CPAP is a cell-cycle regulated protein that controls centriole length. Nat Cell Biol 11, 825–831.

Tang, Z., Lin, M.G., Stowe, T.R., Chen, S., Zhu, M., Stearns, T., Franco, B., and Zhong, Q. (2013). Autophagy promotes primary ciliogenesis by removing OFD1 from centriolar satellites. Nature 502, 254–257.

Tanos, B.E., Yang, H.J., Soni, R., Wang, W.J., Macaluso, F.P., Asara, J.M., and Tsou, M.F.B. (2013). Centriole distal appendages promote membrane docking, leading to cilia initiation. Genes and Development 27, 163–168.

Taschner, M., and Lorentzen, E. (2016). The Intraflagellar Transport Machinery. Cold Spring Harbor Perspectives in Biology 1–20.

Tchernichovski, O., Nottebohm, F., Ho, C.E., Pesaran, B., and Mitra, P.P. (2000). A procedure for an automated measurement of song similarity. Animal Behaviour 59, 1167–1176.

Tee, A.R., Manning, B.D., Roux, P.P., Cantley, L.C., and Blenis, J. (2003). Tuberous Sclerosis Complex gene products, Tuberin and Hamartin, control mTOR signaling by acting as a GTPase-activating protein complex toward Rheb. Current Biology 13, 1259–1268.

Timm, T., Li, X.Y., Biernat, J., Jiao, J., Mandelkow, E., Vandekerckhove, J., and Mandelkow, E.M. (2003). MARKK, a Ste20-like kinase, activates the polarity-inducing kinase MARK/PAR-1. EMBO Journal 22, 5090–5101.

Timm, T., Balusamy, K., Li, X., Biernat, J., Mandelkow, E., and Mandelkow, E.-M. (2008). Glycogen Synthase Kinase (GSK) 3 Directly Phosphorylates Serine 212 in the Regulatory Loop and Inhibits Microtubule Affinity-regulating Kinase (MARK) 2. Journal of Biological Chemistry 283, 18873–18882.

Toivola, D.M., Tao, G.Z., Habtezion, A., Liao, J., and Omary, M.B. (2005). Cellular integrity plus: Organelle-related and protein-targeting functions of intermediate filaments. Trends in Cell Biology 15, 608–617.

Tollenaere, M.A.X., Mailand, N., and Bekker-Jensen, S. (2015). Centriolar satellites: Key mediators of centrosome functions. Cellular and Molecular Life Sciences 72, 11–23.

Trinczek, B., Brajenovic, M., Ebneth, A., and Drewes, G. (2004). MARK4 Is a Novel Microtubule-associated Proteins/Microtubule Affinity-regulating Kinase That Binds to the Cellular Microtubule Network and to Centrosomes. Journal of Biological Chemistry 279, 5915–5923.

Tsang, W.Y., and Dynlacht, B.D. (2013). CP110 and its network of partners coordinately regulate cilia assembly. Cilia 2, 9.

Tsang, W.Y., Spektor, A., Vijayakumar, S., Bista, B.R., Li, J., Sanchez, I., Duensing, S., and Dynlacht, B.D. (2009). Cep76, a Centrosomal Protein that Specifically Restrains Centriole Reduplication. Developmental Cell 16, 649–660.

Tsou, M.-F.B., and Stearns, T. (2006). Mechanism limiting centrosome duplication to once per cell cycle. Nature 442, 947–951.

Tsou, M.F.B., Wang, W.J., George, K.A., Uryu, K., Stearns, T., and Jallepalli, P. V. (2009). Polo Kinase and Separase Regulate the Mitotic Licensing of Centriole Duplication in Human Cells. Developmental Cell 17, 344–354.

Tsukita, S., Kunimoto, K., Yamazaki, Y., Nishida, T., Shinohara, K., Ishikawa, H., Hasegawa, T., Okanoue, T., Hamada, H., Noda, T., et al. (2012). Coordinated ciliary beating requires Odf2-mediated polarization of basal bodies via basal feet. Cell 148, 189–200.

Tucker, R.W., Pardee, A.B., and Fujiwara, K. (1979a). Centriole ciliation is related to quiescence and DNA synthesis in 3T3 cells. Cell 17, 527–535.

Tucker, R.W., Scher, C.D., and Stiles, C.D. (1979b). Centriole deciliation associated with the early response of 3T3 cells to growth factors but not to SV40. Cell 18, 1065–1072.

Utani, A. (2010). Laminin ??3 chain-derived peptide promotes keratinocyte migration and wound closure: Clustering of syndecan-4 and integrin ??1. Seikagaku 82, 327–331.

Vaizel-Ohayon, D., and Schejter, E.D. (1999). Mutations in centrosomin reveal requirements for centrosomal function during early Drosophila embryogenesis. Current Biology 9, 889–898.

Valente, E.M., Silhavy, J.L., Brancati, F., Barrano, G., Krishnaswami, S.R., Castori, M., Lancaster, M.A., Boltshauser, E., Boccone, L., Al-Gazali, L., et al. (2006). Mutations in CEP290, which encodes a centrosomal protein, cause pleiotropic forms of Joubert syndrome. Nature Genetics 38, 623–625.

Valente, E.M., Rosti, R.O., Gibbs, E., and Gleeson, J.G. (2013). Primary cilia in neurodevelopmental disorders. Nature Reviews Neurology 10, 27–36.

Varmark, H., Llamazares, S., Rebollo, E., Lange, B., Reina, J., Schwarz, H., and Gonzalez, C. (2007). Asterless Is a Centriolar Protein Required for Centrosome Function and Embryo Development in Drosophila. Current Biology 17, 1735–1745.

Veland, I.R., Awan, A., Pedersen, L.B., Yoder, B.K., and Christensen, S.T. (2009). Primary cilia and signaling pathways in mammalian development, health and disease. Nephron - Physiology 111, 39–53.

Voronoi, M.G. (1908). Recherches sur les pasallelloedres primitifs. Journal Für Die Reine Und Angewandte Mathematik 134, 198–287.

Waters, A.M., and Beales, P.L. (2011). Ciliopathies: an expanding disease spectrum. Pediatric Nephrology 26, 1039–1056.

Webb, J.L., Ravikumar, B., and Rubinsztein, D.C. (2004). Microtubule disruption inhibits autophagosome-lysosome fusion: Implications for studying the roles of aggresomes in polyglutamine diseases. International Journal of Biochemistry and Cell Biology 36, 2541–2550.

Wei, Q., Xu, Q., Zhang, Y., Li, Y., Zhang, Q., Hu, Z., Harris, P.C., Torres, V.E., Ling, K., and Hu, J. (2013). Transition fibre protein FBF1 is required for the ciliary entry of assembled intra flagellar transport complexes. Nature Communications 4, 2750.

Westlake, C.J., Baye, L.M., Nachury, M. V, Wright, K.J., Ervin, K.E., Phu, L., Chalouni, C., Beck, J.S., Kirkpatrick, D.S., Slusarski, D.C., et al. (2011). Primary cilia membrane assembly is initiated by Rab11 and transport protein particle II (TRAPPII) complex-dependent trafficking of Rabin8 to the centrosome. Proceedings of the National Academy of Sciences of the United States of America 108, 2759–2764.

Wheatley, D.N., Wang, a M., and Strugnell, G.E. (1996). Expression of primary cilia in mammalian cells. Cell Biology International 20, 73–81.

Whipple, R.A., Balzer, E.M., Cho, E.H., Matrone, M.A., Yoon, J.R., and Martin, S.S. (2008). Vimentin filaments support extension of tubulin-based microtentacles in detached breast tumor cells. Cancer Research 68, 5678–5688.

Winey, M., and O'Toole, E. (2014). Centriole structure. Philosophical Transactions of the Royal Society of London. Series B, Biological Sciences 369, 20130457-.

Wissing, J., Jansch, L., Nimtz, M., Dieterich, G., Hornberger, R., Keri, G., Wehland, J., and Daub, H. (2007). Proteomics analysis of protein kinases by target class-selective prefractionation and tandem mass spectrometry. Mol Cell Proteomics 6, 537–547.

Woodhouse, I.H. (2001). The ratio of the arithmetic to the geometric mean: a cross-entropy interpretation. IEEE Transactions on Geoscience and Remote Sensing 39, 188–189.

Woodruff, J., Wueseke, O., and Hyman, A. (2014). Pericentriolar material structure and dynamics. Philosophical Transactions of the Royal Society of London B: Biological Sciences 369, 20130459.

Yang, J., Liu, X., Yue, G., Adamian, M., Bulgakov, O., and Li, T. (2002). Rootletin, a novel coiled-coil protein, is a structural component of the ciliary rootlet. Journal of Cell Biology 159, 431–440.

Ye, X., Zeng, H., Ning, G., Reiter, J.F., and Liu, A. (2014). C2cd3 is critical for centriolar distal appendage assembly and ciliary vesicle docking in mammals. Proceedings of the National Academy of Sciences of the United States of America 111, 2164–2169.

Yoshimura, S.I., Egerer, J., Fuchs, E., Haas, A.K., and Barr, F.A. (2007). Functional dissection of Rab GTPases involved in primary cilium formation. Journal of Cell Biology 178, 363–369.

Zaarur, N., Meriin, A.B., Bejarano, E., Xu, X., Gabai, V.L., Cuervo, A.M., and Sherman, M.Y. (2014). Proteasome failure promotes positioning of lysosomes around the aggresome via local block of microtubule-dependent transport. Molecular and Cellular Biology 34, 1336–1348.

IX. Abbreviations

a.a.	amino acid
A.U.	arbitrary unit
ADP	Adenosine diphosphate
ALMS	Alström syndrome
AM	arithmetic mean
AMP	adenosine monophosphate
AMPK	AMP-activated protein kinase
APS	ammonium peroxodisulfate
Arf	ADP-ribosylation factor
Arl	Arf-like
ARL13B	ADP-ribosylation factor-like protein 13B
ATG	autophagy-related protein
ATP	Adenosine triphosphate
BBS	Bardel Biedl syndrome
BBSome	Bardet–Biedl syndrome complex
bp	base pair
C-	carboxyl-
C-Nap1	centrosomal Nek2-associated protein 1
Cdc	cell division cycle
Cep123	centrosomal protein 123
Cep152	centrosomal protein of 152 kDa
Cep164	centrosomal protein of 164 kD
Cep170	centrosomal protein of 170 kDa
Cep290	centrosomal protein of 290 kDa
Cep76	centrosomal protein of 76 kDa
Cep83	centrosomal protein of 83 kDa
Cep97	centrosomal protein of 97 kDa
CK1	casein kinase 1
corrACS	correlation between cell area and the number of CS foci
CP110	centriolar coiled-coil protein of 110 kDa
CPAP	centrosomal P4.1-associated protein
CQ	chloroquine

CS	centriolar satellites
DAPI	4',6-diamidino-2-phenylindole
DMSO	Dimethyl sulfoxide
DNA	Deoxyribonucleic acid
dNTP	deoxynucleosid 5´-triphosphate
DTT	dithiothreitol
E. coli	*Escherichia coli*
EDTA	ethylendiaminetetraacetic acid
EGFP	Enhanced Green Fluorescent Protein
EM	electron microscopy
EM-CCD	Electron Multiplying Charge Coupled Device
FBF-1	fas-binding factor 1
FCS	fetal calf serum
FIP200	FAK family kinase interacting protein of 200 kDa
FRET	Förster resonance energy transfer
G0	exit of G1
G1	first gap phase
G2	second gap phase
GDP	guanosine-5'-diphosphate
GFP	Green Fluorescent Protein
Gli	Glioma transcription factors
GM	geometric mean
GPCR	G protein-coupled receptor
GSK3b	glycogen synthase kinase 3b
GST	Glutathione S-transferase
HEK293	Human embryonic kidney cells 293
HeLa	Henrietta Lacks
HEPES	N-2-hydroxyethylpiperazine-N'-2-ethanesulfonic
Hh	Hedgehog
His	histidine
HRP	horse radish peroxidase
IFT	intra flagellar transport
IP	immunoprecipitation

IPTG	isopropyl-β,D-thiogalactopyranoside
JS	Joubert syndrome
KCTD17	BTB/POZ domain-containing protein KCTD17
kDa	kilo Dalton
Kif24	kinesin-like protein Kif24
kd	kinase dead
LAMP1	Lysosomal-associated membrane protein 1
LAP	Localization and Affinity Purification
LC3	light chain 3
LKB1	liver kinase B1
M	mitotic phase
MAP	microtubule-associated protein
MARK4	MAP/microtubule affinity-regulating kinase 4
MARKK	MARK Kinase
MEFs	mouse embryonic fibroblasts
MKS	Meckel syndrome
MOPS	3-morpholinopropanesulfonic acid
MTOC	microtubule organizing center
N-	amino-
NA	numerical aperture
NEK2	never in mitosis A-related kinase 2
NPHP	nephronophthisis
NPHP1	nephrocystin-1
NPHP4	nephrocystin-4
OD_{600}	optical density at 660 nm
ODF2	Outer dense fibre protein 2
OFD	orofaciodigital syndrome
OFD1	oral-facial-digital syndrome 1
p150	protein of 150 kDa
PAS	phagophore assembly site
PCD	primary ciliary dyskinesia
PCM	pericentriolar material
PCM1	Pericentriolar material 1

PI3K	class III phosphatidylinositol-3-kinase
PIPES	piperazine-N,N′-bis(2-ethanesulfonic acid)
PKD	polycystic kidney disease
PLK-1	polo-like kinase 1
PLK-4	Polo-like kinase 4
PSF	point spread function
PTCH1	protein patched homolog 1
r^2	coefficient of determination
Rab8A	Ras-related protein Rab-8A
Rabin8	Rab-3A-interacting protein
Rag	Ras-related GTP-binding protein
Raptor	Regulatory-associated protein of mTOR
Ras	Rat sarcoma
Rheb	Ras homolog enriched in brain
RNA	Ribonucleic acid
RNAi	RNA interference
ROI	region of interest
RPE1	human retinal pigment epithelium cells immortalized with telomerase reverse transcriptase
RPGR	retinal degeneration
RPGRIP1L	RPGR-interacting protein 1-like protein
rpm	revolutions per minute
S	synthesis phase
S6K	Ribosomal protein S6 kinase
SAS6	spindle assembly abnormal protein 6 homolog
SCA11	spinocerebellar ataxia type 11
SCLT1	sodium channel and clathrin linker 1
SDS-PAGE	sodium dodecyl sulfate polyacrylamide gel electrophoresis
SEM	standard error of the mean
Shh	Sonic hedgehog
siRNA	Small interfering RNA
Smo	Smoothened
spd-2	spindle-defective protein 2
SPOC	spindle positioning checkpoint

STIL	SCL-interrupting locus protein
SuFu	suppressor of Fused
T-loop	activation loop
TET	Tetracycline-Controlled Transcriptional Activation
TGF-β	transforming factor beta
TOR	target of rapamycin
TRP	transient receptor potential
TSC2	Tuberous Sclerosis Complex 2
TTBK2	tau-tubulin kinase 2
UBA	ubiquitin-associated
ULK	uncoordinated-51-like kinase
USP	ubiquitin-specific protease
VPS34	vacuolar protein sorting 34
w/v	weight per volume
WDR8	WD repeat-containing protein 8
WE	Wiener entropy
wt	wild-type
Wnt	Wingless/Int
YFP	Yellow fluorescent protein

Publications from this thesis

Panels of Figure 38 of this thesis have been published in the following article:

Kuhns, S., Schmidt, K.N., Reymann, J., Gilbert, D.F., Neuner, A., Hub, B., Carvalho, R., Wiedemann, P., Zentgraf, H., Erfle, H., et al. (2013). The microtubule affinity regulating kinase MARK4 promotes axoneme extension during early ciliogenesis. Journal of Cell Biology 200, 505–522.

Poster presentations

R. Carvalho, P. Wiedemann and G. Pereira

“MARK4 contributes to cilia formation by regulating the degradation of inhibitory OFD1 from the centriolar satellites”. Cilia 2014 - Second International Conference, Paris, France, 17-21 November 2014.

Acknowledgements

I would like to thank Dr. Gislene Pereira and Prof. Dr. Philipp Wiedemann for the opportunity to pursue my doctoral studies in their laboratories. The material, technical and scientific support that you provided was invaluable for the success of this project.

I wish to express my gratitude to my Thesis Advisory Committee members, Prof. Dr. Elmar Schiebel and Prof. Dr. Oliver Gruss for the constructive feedback on the progress of my work and helpful suggestions regarding future directions and experimental approaches.

I am grateful to Dr. Stefanie Kuhns and Dr. Kerstin Schmidt for the time they spent training me when I joined the lab. I would like to call attention to the excellent technical assistance provided by Astrid Hofmann and Dorothee Albrecht. I also wish to acknowledge the contributions of all the students I supervised: Marina, Horace, Lora and especially Evangeline. I'm thankful to all my colleagues with whom I worked in the Molecular Biology of Centrosomes and Cilia lab. Your friendship made very enjoyable the time we spent together.

My gratitude also goes to HBIGS for all the training and support provided as well as to all the facilities in all the institutes that I had the luck to contact. You were always super helpful and friendly.

Thank you to the friends I meet when climbing, dancing or just for a conversation for helping me keeping the necessary balance between my work and personal life.

I thank also my parents. Even though you are far away, I receive all you love, support and encouragement.

Finally and most importantly, big special thanks go to Eva Hasel and Olivia de Carvalho for bearing with me every day and being on my side when I need the most. I love you!

Thanks, Danke, bem hajam.